Analysis of heat transfer and flow patterns in a loop heat pipe : Modelling by analytical and numerical approaches and experimental observations

Benjamin Siedel

To cite this version:

Benjamin Siedel. Analysis of heat transfer and flow patterns in a loop heat pipe : Modelling by analytical and numerical approaches and experimental observations. Other [cond-mat.other]. INSA de Lyon, 2014. English. NNT : 2014ISAL0092 . tel-01175850

HAL Id: tel-01175850
https://theses.hal.science/tel-01175850v1

Submitted on 13 Jul 2015

Nº d'ordre : Année 2014

Thèse

ANALYSIS OF HEAT TRANSFER AND FLOW PATTERNS IN A LOOP HEAT PIPE: MODELLING BY ANALYTICAL AND NUMERICAL APPROACHES AND EXPERIMENTAL OBSERVATIONS

présentée devant

L'INSTITUT NATIONAL DES SCIENCES APPLIQUÉES DE LYON

pour obtenir le grade de

Docteur

Formation doctorale : Thermique et Énergétique
École doctorale : MEGA (Mécanique, Énergétique, Génie civil et Acoustique)

par

Benjamin SIEDEL

Soutenue le 26 Septembre 2014, devant la commission d'examen :

Yves BERTIN	Professeur (ENSMA, Poitiers)	Rapporteur
Manfred GROLL	Professeur Émérite (Université de Stuttgart)	Examinateur
Vincent PLATEL	Maître de Conférences, HDR (Université de Pau)	Examinateur
Marc PRAT	Directeur de Recherche CNRS (IMFT, Toulouse)	Rapporteur
Valérie SARTRE	Maître de Conférences, HDR (INSA, Lyon)	Directeur de thèse
Frédéric LEFÈVRE	Professeur (INSA, Lyon)	Directeur de thèse

Thèse préparée au Centre d'Énergétique et de Thermique de Lyon
CETHIL UMR5008
Université de Lyon

INSA Direction de la Recherche - Ecoles Doctorales – Quinquennal 2011-2015

SIGLE	ECOLE DOCTORALE	NOM ET COORDONNEES DU RESPONSABLE
CHIMIE	**CHIMIE DE LYON** **http://www.edchimie-lyon.fr** Sec : Renée EL MELHEM Bat Blaise Pascal 3e etage 04 72 43 80 46 Insa : R. GOURDON	M. Jean Marc LANCELIN Université de Lyon – Collège Doctoral Bât ESCPE 43 bd du 11 novembre 1918 69622 VILLEURBANNE Cedex Tél : 04.72.43 13 95 directeur@edchimie-lyon.fr
E.E.A.	**ELECTRONIQUE, ELECTROTECHNIQUE, AUTOMATIQUE** **http://edeea.ec-lyon.fr** Sec : M.C. HAVGOUDOUKIAN eea@ec-lyon.fr	M. Gérard SCORLETTI Ecole Centrale de Lyon 36 avenue Guy de Collongue 69134 ECULLY Tél : 04.72.18 60.97 Fax : 04 78 43 37 17 Gerard.scorletti@ec-lyon.fr
E2M2	**EVOLUTION, ECOSYSTEME, MICROBIOLOGIE, MODELISATION** **http://e2m2.universite-lyon.fr** Sec : Safia AIT CHALAL Bat Darwin - UCB Lyon 1 04.72.43.28.91 Insa : H. CHARLES	Mme Gudrun BORNETTE CNRS UMR 5023 LEHNA Université Claude Bernard Lyon 1 Bât Forel 43 bd du 11 novembre 1918 69622 VILLEURBANNE Cédex Tél : 06.07.53.89.13 e2m2@ univ-lyon1.fr
EDISS	**INTERDISCIPLINAIRE SCIENCES-SANTE** **http://www.ediss-lyon.fr** Sec : Safia AIT CHALAL Hôpital Louis Pradel - Bron 04 72 68 49 09 Insa : M. LAGARDE Safia.ait-chalal@univ-lyon1.fr	Mme Emmanuelle CANET-SOULAS INSERM U1060, CarMeN lab, Univ. Lyon 1 Bâtiment IMBL 11 avenue Jean Capelle INSA de Lyon 696621 Villeurbanne Tél : 04.72.68.49.09 Fax :04 72 68 49 16 Emmanuelle.canet@univ-lyon1.fr
INFOMATHS	**INFORMATIQUE ET MATHEMATIQUES** **http://infomaths.univ-lyon1.fr** Sec :Renée EL MELHEM Bat Blaise Pascal 3e etage infomaths@univ-lyon1.fr	Mme Sylvie CALABRETTO LIRIS – INSA de Lyon Bat Blaise Pascal 7 avenue Jean Capelle 69622 VILLEURBANNE Cedex Tél : 04.72. 43. 80. 46 Fax 04 72 43 16 87 Sylvie.calabretto@insa-lyon.fr
Matériaux	**MATERIAUX DE LYON** **http://ed34.universite-lyon.fr** Sec : M. LABOUNE PM : 71.70 –Fax : 87.12 Bat. Saint Exupéry Ed.materiaux@insa-lyon.fr	M. Jean-Yves BUFFIERE INSA de Lyon MATEIS Bâtiment Saint Exupéry 7 avenue Jean Capelle 69621 VILLEURBANNE Cedex Tél : 04.72.43 83 18 Fax 04 72 43 85 28 Jean-yves.buffiere@insa-lyon.fr
MEGA	**MECANIQUE, ENERGETIQUE, GENIE CIVIL, ACOUSTIQUE** **http://mega.universite-lyon.fr** Sec : M. LABOUNE PM : 71.70 –Fax : 87.12 Bat. Saint Exupéry mega@insa-lyon.fr	M. Philippe BOISSE INSA de Lyon Laboratoire LAMCOS Bâtiment Jacquard 25 bis avenue Jean Capelle 69621 VILLEURBANNE Cedex Tél :04.72 .43.71.70 Fax : 04 72 43 72 37 Philippe.boisse@insa-lyon.fr
ScSo	**ScSo*** **http://recherche.univ-lyon2.fr/scso/** Sec : Viviane POLSINELLI Brigitte DUBOIS Insa : J.Y. TOUSSAINT	Mme Isabelle VON BUELTZINGLOEWEN Université Lyon 2 86 rue Pasteur 69365 LYON Cedex 07 Tél : 04.78.77.23.86 Fax : 04.37.28.04.48 viviane.polsinelli@univ-lyon2.fr

*ScSo : Histoire, Géographie, Aménagement, Urbanisme, Archéologie, Science politique, Sociologie, Anthropologie

Résumé

Analyse de la distribution des flux de chaleur et des écoulements au sein d'une LHP: modélisation par voies analytique et numérique et observations expérimentales

La miniaturisation toujours plus poussée des composants électroniques génère des contraintes thermiques de plus en plus importantes. Les systèmes diphasiques – et particulièrement les boucles diphasiques à pompage thermo-capillaire encore appelées Loop Heat Pipes ou LHP – suscitent actuellement un intérêt croissant en raison de leurs bonnes performances thermiques, de leur fiabilité et de leur géométrie permettant une grande souplesse d'implantation. Cependant, une meilleure compréhension des phénomènes en jeu dans ces systèmes est essentielle pour optimiser leur conception et prédire leur comportement de manière fiable.

Au cours de ce travail, un modèle analytique est développé qui intègre les paramètres de fonctionnement d'une LHP, afin d'étudier leur influence en fonction des conditions opératoires. Son originalité principale réside dans la détermination précise de la répartition des différents flux thermiques dans l'évaporateur. Une étude de sensibilité est menée pour évaluer les influences de la résistance de contact entre la structure capillaire poreuse et l'enveloppe de l'évaporateur, de la conductivité thermique équivalente du matériau poreux, du coefficient d'accommodation lié aux transferts de chaleur par évaporation et des coefficients de transfert thermique entre la paroi et le milieu ambiant ou la source froide. Cette analyse montre que les paramètres mentionnés ci-dessus peuvent être estimés individuellement, en comparant le modèle à des données expérimentales judicieusement choisies.

Un banc expérimental a également été conçu et fabriqué. L'instrumentation, qui comporte des thermocouples intrusifs, un capteur de pression et un capteur de flux, permet de caractériser le fonctionnement de la LHP. De plus, le système est partiellement transparent pour permettre l'observation de la position des phases liquide et vapeur dans le système au cours du fonctionnement. Les influences de la puissance thermique appliquée, de la présence de gaz incondensables et de la température de la source froide sont analysées. Aux puissances thermiques élevées, un régime d'ébullition nucléée est observé dans le réservoir. Ce phénomène a un effet significatif sur le comportement de la LHP, qui se traduit par une augmentation des flux parasites vers le réservoir donc une dégradation des performances de la LHP. Plusieurs phénomènes oscillatoires sont également observés et corrélés aux observations visuelles des écoulements dans les canalisations. Enfin, différents régimes de condensation sont observés et les mécanismes conduisant au détachement des bulles dans le condenseur sont décrits.

Un modèle numérique a été développé, afin de simuler le comportement du banc expérimental en se rapprochant au plus près de ses caractéristiques géométriques et thermophysiques. La comparaison entre les prédictions du modèle et les données expérimentales montre les carences des modèles de pertes de charges dans les écoulements diphasiques, pour la configuration étudiée. Les transferts de chaleur et de masse dans l'évaporateur sont analysés, ainsi que l'influence de l'apparition de l'ébullition dans le réservoir et celle de la conductivité thermique de l'enveloppe de l'évaporateur. Les résultats mettent également en évidence l'importance de la conduction thermique longitudinale dans les canalisations dans le cas d'un matériau conducteur, tel que le cuivre.

Mots-clés : *loop heat pipe, modèle numérique, modèle analytique, régime permanent, banc expérimental, validation de modèle, analyse de sensibilité*

Abstract

Analysis of heat transfer and flow patterns in a loop heat pipe: modelling by analytical and numerical approaches and experimental observations

The increasing development of electronics leads to higher constraints regarding their thermal management. Two-phase passive systems – and among these systems loop heat pipes in particular – become more and more attractive because they offer thermal efficiency, reliability and large implementation flexibility. However, a better understanding of the physical phenomena involved within them is required in order to optimise their design and predict accurately their operation.

An analytical model is developed to highlight the main parameters of a loop heat pipe and their influence depending on the operating conditions. Its main originality lies in a thorough consideration of heat transfer in the evaporator. A sensitivity analysis is conducted to study the influence of the contact thermal resistance between the wick and the body of the evaporator, of the effective thermal conductivity of the wick, of the accommodation coefficient linked to the evaporation heat transfer and of the heat transfer with the ambient and with the heat sink. This analysis shows that these parameters can be individually and separately estimated by comparing the model to a set of well-chosen experimental data.

An experimental setup is designed and built. Numerous sensors, including intrusive temperatures, pressure sensors and heat flux measurements enable an accurate characterisation of the LHP operation. Furthermore, the system is partially transparent to observe the location of the liquid and vapour phases inside the system in working conditions. The effects of the heat input, non-condensable gases and of the heat sink temperature are discussed. Nucleate boiling is observed inside the reservoir for high heat fluxes. This phenomenon impacts significantly the behaviour of the loop heat pipe, increasing the parasitic heat flux towards the reservoir and therefore decreasing the performance of the LHP. Several oscillating phenomena are also observed and correlated to the flow patterns. Finally, distinct condensation regimes are investigated and the mechanisms leading to the bubble detachment in the condenser are discussed.

A numerical model is developed in accordance with the geometrical and thermophysical characteristics of the experimental setup. The model is compared with the experimental data. The comparison shows the lack of accuracy of the two-phase pressure drops models in this configuration. Heat and mass transfer in the evaporator are discussed and the effects of boiling in the reservoir and of the thermal conductivity inside the evaporator casing are investigated. The results highlight the importance of the longitudinal thermal conduction inside the tube in the case of conductive materials such as copper.

Keywords: *loop heat pipe, numerical model, analytical model, steady-state, experimental set-up, visual study, model validation, sensitivity analysis*

Acknowledgements

This PhD thesis has been carried out at the Center for Energy and Thermal Sciences of Lyon (CETHIL UMR5008), directed by Prof. Jocelyn Bonjour. This work has been performed under the supervision of Prof. Frédéric Lefèvre and Dr. Valérie Sartre. I gratefully acknowledge the financial support of the European Commission FP7 Project PRIMAE, grant agreement 265416, that made this study possible.

I gratefully thank Valérie Sartre for her advice, expertise and scientific discussion. Her level of requirement and the time she spent supervising this investigation enabled the quality of the present manuscript. I also thank Frédéric Lefèvre for his availability, thorough supervision and scientific skills. His innovative ideas have been a key element of this thesis. Beyond our research work together, thank you for the friendly relations we could build along these years.

I would like to thank Prof. Yves Bertin and Prof. Marc Prat for being reviewers of this study. I also thank Dr. Vincent Platel and Prof. Manfred Groll for agreeing to be examiners of this thesis.

I thank the administrative staff of the lab for his help and understanding.

I am also grateful to the technicians of the CETHIL, particularly Bernard and Nicolas. Your time and skills made the design and manufacturing of the experimental setup possible. I gratefully acknowledge the extensive work of Nathanaël, who spent much time designing and building the LHP.

I thank my colleagues and particularly my office-mates Pierrick and Kévin. I enjoyed the good atmosphere, your humour and the fun we had together.

I thank my family for its support and my brother Sam for introducing me to the two-phase world.

I thank my wonderful wife Debora for her support, understanding and kindness. Du bist so großartig mein Schatz!

I finally thank my Creator for the wonderful life He gave me, His love and blessings and the relationship I can have with Him.

Contents

Nomenclature

A	Fourier series coefficient	-
a, a_0, a_1	length	m
a_{ev}	accommodation coefficient	-
B	length ratio	-
b	length	m
C	Fourier series coefficient	-
c, c_0, c_1	length	m
c_{p}	specific heat	$\mathrm{J \cdot kg^{-1} \cdot K^{-1}}$
D	length ratio	-
	diameter	m
d, d_0	length	m
E	length ratio	-
e	length, thickness	m
f	friction coefficient	-
G	Fourier series coefficient	-
g	gravitational acceleration	$\mathrm{m \cdot s^{-2}}$
H	height	m
h	heat transfer coefficient	$\mathrm{W \cdot m^{-2} \cdot K^{-1}}$
h_{lv}	enthalpy of vaporisation	$\mathrm{J \cdot kg^{-1}}$
K	analytical model coefficient	-
	wick permeability	$\mathrm{m^2}$
L	length	m
$\overline{M}$	molar mass	$\mathrm{kg \cdot mol^{-1}}$
m	mass	kg
$\dot{m}$	mass flow rate	$\mathrm{kg \cdot s^{-1}}$
P	absolute pressure	Pa
P^*	partial pressure	Pa
p	perimeter	m
Q	heat transfer rate	W
R	thermal resistance	$\mathrm{K \cdot W^{-1}}$
$\overline{R}$	universal gas constant	$\mathrm{J \cdot K^{-1} \cdot mol^{-1}}$
r	radius	m

S	cross-sectional area	m^2
S_i	absolute sensitivity	-
S_i^*	relative sensitivity	-
T	temperature	K
T^*	non-dimensional temperature	-
t	time	s
u	velocity	$\mathrm{m \cdot s^{-1}}$
V	volume	m^3
X, Y, Z	non-dimensional coordinates	-
x	vapour quality	-
	axis coordinate	m
$x_\mathrm{i,j,k}$	sensitivity parameter	-
y, z	axis coordinates	m

Greek Symbols

ε	void fraction, porosity	-
λ	thermal conductivity	$\mathrm{W \cdot m^{-1} \cdot K^{-1}}$
μ	dynamic viscosity	$\mathrm{Pa \cdot s}$
φ	heat density	$\mathrm{W \cdot m^{-2}}$
ρ	density	$\mathrm{kg \cdot m^{-3}}$
σ	surface tension	$\mathrm{N \cdot m^{-1}}$
θ	angle	rad
χ_tt	Martinelli parameter	-

Subscripts

0	constant
2φ	two-phase
316L	stainless steel 316L
air	air
b	evaporator body
c	condenser, contact, convection
cap	capillary
cond	condensation
D	diameter
e	evaporator
eff	effective
eq	equivalent
ev	evaporation
f	fluid
fric	frictional

gr	groove
h	homogeneous
heater	flat heater
hf	heat flux sensor
i	inner, inlet, internal
in	input
l	liquid
LHP	loop heat pipe
m	meniscus
m, n	discretisation step, Fourier series increment
max	maximum
mom	momentum
NCG	non-condensable gases
nuc	nucleation
num	numerical
o	outer, outlet
p	pore
par	parasitic heat flux
r	reservoir
sat	saturation
sen	sensible
sink	heat sink
static	hydrostatic
sub	subcooling
t	general solution
top	reservoir top surface
tot	total
tube	tube
v	vapour
w	wick
we	wick-fin interface
wm	wick material

Non Dimensional Numbers

$Bi = \frac{Lh}{\lambda}$	Biot number
$Bo = \left(\frac{D^2 g(\rho_\mathrm{l} - \rho_\mathrm{v})}{\sigma}\right)^{\frac{1}{2}}$	Bond number
Fr	Froude number
$Ga = \frac{gD^3\rho^2}{\mu^2}$	Galileo number

$Gz = \frac{D}{L} Re Pr$	Graetz number
Nb	Merit number
$Pr = \frac{c_\mathrm{p}\mu}{\lambda}$	Prandtl number
$Ra = \frac{g\rho^2 c_\mathrm{p} \beta (T_\mathrm{tube} - T_\mathrm{f}) L^3}{\mu\lambda}$	Rayleigh number
$Re = \frac{\rho u D}{\mu}$	Reynolds number

Introduction

The issues concerning the thermal management have become essential in numerous industrial fields. They particularly have an impact on the electronics industry as a consequence of the continuous increase of the electronic components density. This densification is described by the empirical Moore's law [1] who predicted in 1965 that the number of transistors in a dense integrated circuit would double approximately every two years, which has proved to be true so far. The direct consequence of this law is an unprecedented increase of the heat fluxes to be dissipated. They reach today several hundreds of W/cm^2, corresponding to the maximal solar irradiance on Earth concentrated more than a thousand times! Despite many efforts made to enhance traditional cooling systems, the temperatures reached at the core of the components are of major importance and restrict their life expectancy. In civil and military aviation, thermal stress represents nowadays 63 % of the failure sources of on-board electronics (Figure 0.1). For this reason, a consortium of European industrial and academic partners launched the FP7 PRIMAE[1] project in 2010. The objective is to develop a new flexible, robust and open aeronautical packaging for the next generation of electronics and particularly to Integrated Modular Avionics (IMA). The Cethil laboratory is an academic partner of this project, in charge of the design of an innovative cooling solution for the thermal management of the electronic packaging (Figure 0.2). The model presented in the chapter 4 of this manuscript was partially developed in the frame of this project.

Other industrial fields are confronted to the issues of thermal management:

- Electric energy storage in batteries that are more and more compact induces overheating problems that may have terrible consequences, as it was proven by the recent full grounding of the entire Boeing 787 fleet.
- The miniaturisation of fuel cells is restrained by the heating of the cell core.
- The space occupied by the engine cooling systems in the automotive industry becomes problematic with the reduction of the available space under the hood.

Therefore, the development of more efficient and compact cooling solutions becomes a major industrial concern. Liquid-vapour phase-change heat transfer can meet this challenge because it enables the transfer of large amounts of heat with a small temperature difference.

---

[1] PRIMAE: Packaging of futuRe Integrated ModulAr Electronics, European Commission Grant Agreement FP7-265416-Primae – www.primae.org

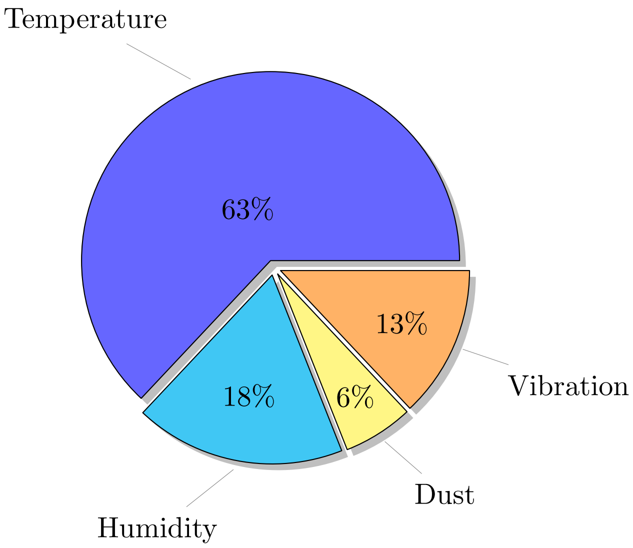

Figure 0.1: Main avionics packaging failure sources [2]

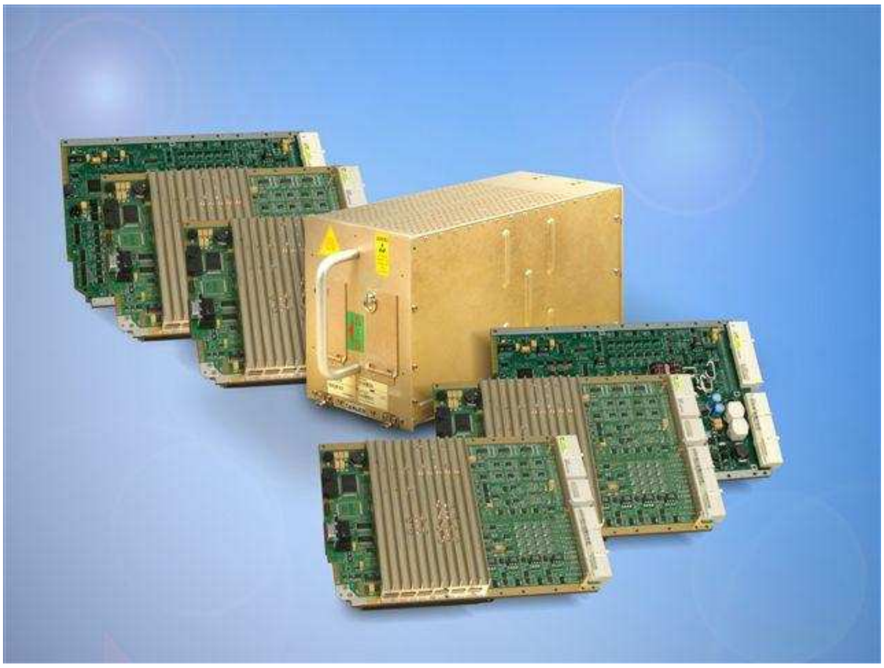

Figure 0.2: Avionics ARINC600 packaging

This mode of heat transfer is implemented in both refrigerating machines and mechanical two-phase thermal loops. However, these systems use mechanical components (pump, compressor) that consume energy, necessitate preventive maintenance and occupy a non-negligible space. These drawbacks can be avoided with the use of passive two-phase systems: the heat pipes. The development of these devices has continuously increased since the 1960's, encouraged by the spatial industry which is confronted to thermal management in an environment where heat transfer by convection is not an option. Since the first space applications, their use has spread in many fields like consumer electronics, transport or renewable energy industries.

Several types of heat pipes can be considered according to their application: conventional heat pipes [3], loop heat pipes [4] or pulsating heat pipes [5].

A conventional heat pipe consists of a hermetic thin envelope, filled with a working fluid in saturated liquid-vapour state. Liquid evaporates in a zone of the envelope in contact with a heat source (evaporator) and vapour condenses in another zone in contact with a heat sink (condenser). Vapour circulates in a unique channel in the centre of the envelope, whereas the return of liquid from the condenser to the evaporator is ensured by a peripheral capillary structure (mesh, grooves, etc.). Conventional heat pipes present operating limits induced by the capillary structure and the flow characteristics in it. Unlike conventional heat pipes, Loop Heat Pipes (LHPs) are characterised by vapour and liquid flows in separate channels and by the presence of the capillary structure exclusively in the evaporator. Nowadays, this technology is at a design stage, prototype validation stage or manufactured in limited series for the spatial industry in particular. The key operating element of such a system is the manufacturing of the capillary structure, much more complex than in a conventional heat pipe. The state of the art concerning the design of these structures is scarce, the knowledge being limited to a couple of laboratories and companies worldwide which do not share their expertise.

The Cethil laboratory has been conducting research in the field of heat pipes for more than 20 years. The first investigations about LHPs started in 2006 with the European project COSEE[2]. Its goal was to provide a cooling solution for the seat electronic boxes in commercial aircrafts. The Cethil was in charge of the design of the loops [6], while the manufacturing was ensured by the Belgian company Euro Heat Pipes (EHP) and a Russian team lead by Yuri Maydanik, the inventor of LHPs. This collaboration enabled a fast start of this activity in the laboratory. Today, the Cethil is developing its first home made experimental LHP, the first experimental data being presented in this manuscript. The laboratory is also part of a project funded by the DGA (French defence agency) to promote the emergence of the first French manufacturer of LHPs [7]. This project is coordinated by the company Atherm (manufacturer) and includes Thalès Avionics (end-user) and the Cethil (academic partner). The system, elaborated in 4 years, provides competitive thermal performance compared to the best LHPs that are fabricated worldwide and beneficiate of 40 years of development. The Cethil also patented an adsorption-based antifreeze solution combined with an LHP to enable the use of water as working fluid even if the storage conditions are below 0°C [8].

The extensive theoretical and experimental investigations from the literature highlight the complexity of LHPs and the importance of coupled phenomena on their operation. Therefore, despite detailed analyses, several mechanisms of LHPs are still not well understood and need further investigations. Moreover, the diversification of the applications for LHPs sets new constraints regarding the choice of working fluid and of materials and the design characteristics. Hence, additional experimental data and new modelling solutions are necessary for a better understanding of the LHP operation and are of major importance in the accurate

---

[2] COSEE: Cooling Of Seat Electronic box and cabin Equipment, European FP6-Project AST5–CT-2006–030800

design of LHPs.

The objective of the present study is to provide a thorough analysis of the LHP operation, through experimental, analytical and numerical investigations. Based on the works presented in the literature, a detailed theoretical study of the entire system leads to a better understanding of the coupled phenomena occurring in LHPs and enable to assess the major parameters of influence of such systems. An experimental apparatus with transparent transport lines and condenser provides experimental data for further analysis and for the validation of the theory.

This thesis is organised as follows:

- In the first chapter, an extensive bibliographic review is conducted to identify the physical mechanisms the LHP operation depends on as well as the function and the properties of every component constituting this system. Then, a thorough synthesis of the steady-state modelling works available in the literature is presented. Lastly, the potential location of the liquid-vapour interface inside the capillary structure is discussed.

- Chapter 2 presents an analytical investigation of the LHP operation. After introducing the theoretical model, a standard case is defined and a sensitivity analysis is conducted in order to identify the influential input parameters of the model. A parametric study is undertaken afterwards.

- Chapter 3 presents an experimental study on LHPs operation. First, the experimental setup is described. Then, results in steady-state and transient operations are discussed and a visual investigation of two-phase flow in the transport lines and in the condenser is developed.

- Chapter 4 introduces a numerical model of the experimental setup. This model considers accurately heat and mass transfer in the evaporator and in the transport lines. It is described and validated with experimental results. Then, heat transfer in the evaporator is discussed and the temperature profile along the transport lines and the condenser is investigated.

Chapter 1

Literature review

This chapter presents an extensive review of the operation of loop heat pipes. First, the operating principles are described and the working limits are presented. The various components constituting an LHP are then investigated and their influence on the LHP operation is discussed. An emphasis is put on the study of the evaporator/reservoir and particularly on the capillary structure since their characteristics have a major impact on the phenomena occurring in the loop heat pipe. Afterwards, a literature review about steady-state modelling works on LHPs is conducted. Complete numerical models, partial numerical analyses and analytical investigations are discussed separately and a synthesis is detailed comparing the main steady-state studies since 1999. Finally, the location of the liquid-vapour interface inside the capillary structure is investigated. The theoretical and experimental works about the development of a vapour zone in the porous element are presented in order to assess this phenomenon, its modelling potential and to discuss the relevance of its consideration in the present study.

1.1 LHP operating principles

Over the last decades, capillary two-phase heat transfer loops have gained much interest due to their robustness, flexibility and operating capability. They provide efficient heat transport from one or several heat sources to a heat sink. Unlike conventional heat pipes, the vapour and the liquid flow in separate smooth tubes between the wicked evaporator and the condenser. As shown in Figure 1.1, these loops consist mainly of an evaporator structure and a condenser connected to each other by two transport lines.

A heat load Q_{in} is supplied to the evaporator and is conducted through the evaporator wall to the vapour grooves. There, evaporation of the liquid filling the wick occurs and the vapour is evacuated through the vapour grooves. The vapour flows then through the vapour line to the condenser. The vapour entering the condenser reaches its saturation temperature and condensation takes place. Once all the vapour is condensed, the liquid is subcooled in the remaining part of the condenser, before flowing back to the evaporator through the liquid line. The liquid then enters the porous wick to replace the evaporated fluid. A hydro-

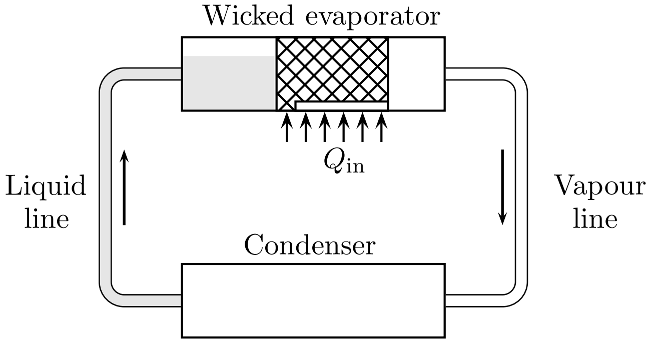

Figure 1.1: Schematic of a capillary two-phase loop

accumulator, called reservoir or compensation chamber, is also connected to the liquid line or embedded into the evaporator structure to compensate the displacement of the fluid charge in the condenser as well as the expansion of the working fluid during operation.

1.1.1 Classification of capillary two-phase heat transfer loops

Loop Heat Pipes (LHPs) were originally invented in former Soviet Union in the late 1970's. Similar two-phase systems, known as Capillary Pumped Loops (CPLs) were patented in the US in the 1960's and developed later for spatial applications, mostly by the NASA[1]. Both devices share a lot of similar characteristics. As shown in Figure 1.2, the basic distinction between a traditional architecture of a CPL and a traditional LHP can be found in the thermohydraulic link between the reservoir and the evaporator. A CPL features a reservoir plumbed into the liquid line or the evaporator and is outside the path of fluid circulation. The reservoir usually has no thermal link with the evaporator and it needs to be heated prior to start-up in order to collapse any vapour bubbles in the evaporator core and to ensure that the wick is wetted. In an LHP, the reservoir is embedded in the evaporator/reservoir structure, making the loop more robust and auto-regulating. However, as a drawback, integrating an LHP in its environment may prove to be more difficult because the reservoir location is not as flexible as in a CPL. This simple difference between both systems has great impacts on all aspects of the loop operation, including start-up, robustness, operating temperature, control heater power requirement for the reservoir, design flexibility and operation failures. For a further detailed analysis on the similarities and differences between LHPs and CPLs, the reader may refer to the works of Nikitkin and Cullimore [9] and Butler et al. [10].

Following the large development of two-phase loop systems, devices that are somewhere between the traditional designs of LHP and CPL have been studied. For instance, Lachassagne et al. [11] and the company *Euro Heat Pipes* developed a CPLIP[2] with a reservoir divided into two parts with liquid only flowing through the lower part (Figure 1.3). Such

---

[1] NASA: National Aeronautics and Space Administration

[2] CPLIP: Capillary Pumped Loop for Integrated Power. This system is also known as CPLTA: Capillary Pumped Loop for Terrestrial Application

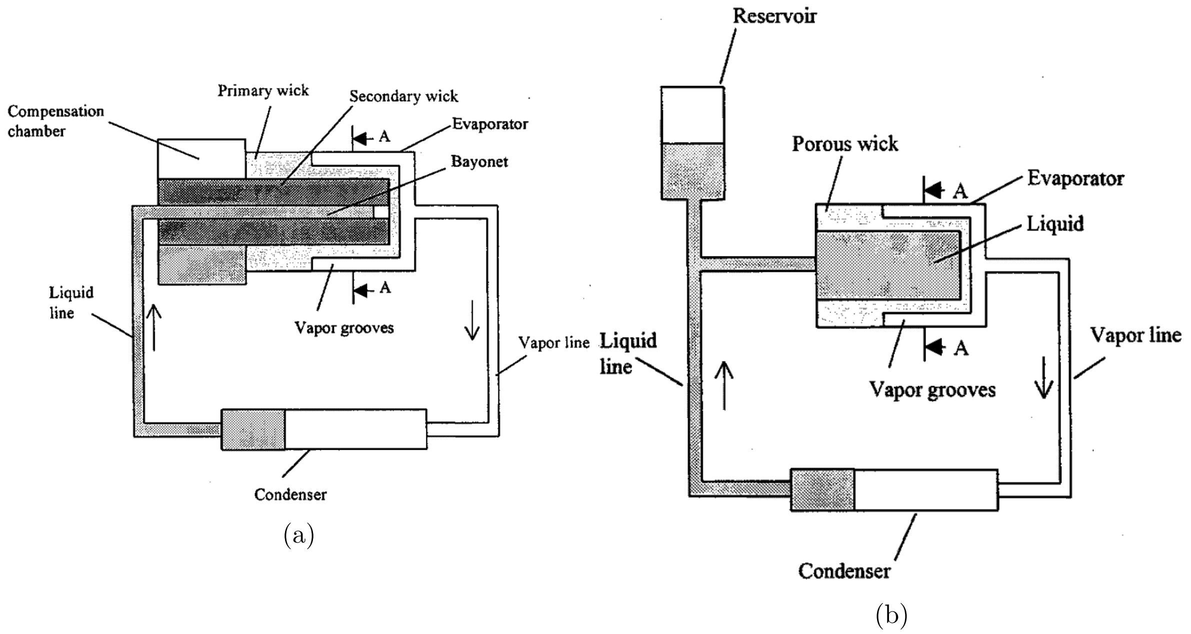

(a)

(b)

Figure 1.2: Schematic of (a) a traditional LHP and (b) a traditional CPL [10]

a feature enhances the reservoir regulation during transient states (start-up, power steps, etc.) since the reservoir higher part temperature is more stable. Like a standard CPL, the operating temperature of the device can be controlled by the reservoir. However, more like LHPs, the CPLIP design enables heat and mass transfer between the evaporator and the reservoir. Indeed, the reservoir is located above the evaporator, thus, vapour bubbles due to percolation in the wick can rise from the evaporator to the reservoir. Extensive experimental and numerical investigations on this system can be found in [11–15].

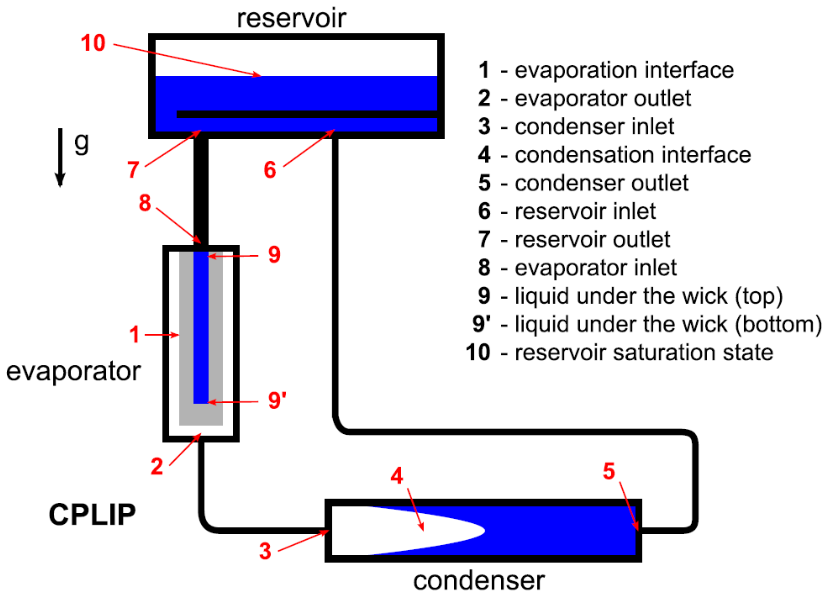

Figure 1.3: Schematic of a CPLIP [11]

Many different types of LHP exist, based on the application they are designed for and their geometrical characteristics. Although LHPs and CPLs were first integrated in satellite thermal management units, their application became diversified and designs are nowadays available for applications as wide-ranging as cryogenic telescope cooling [16], solar water heating [17], laptop thermal management [18] and cooling of high power electronics on board a train [19]. Maydanik [20] suggests the classification presented in Table 1.1 to categorize the LHP designs that can be found in the literature and in the industry.

LHP design	LHP dimensions	Evaporator shape	Evaporator design
• Conventional (diode) • Reversible • Flexible • Ramified	• Miniature • All the rest	• Cylindrical • Flat disk-shaped • Flat rectangular	• One butt-end compensation chamber • Two butt-end compensation chambers • Coaxial
Condenser design	Number of evaporators and condensers	Temperature range	Operating-temperature control
• Pipe-in-pipe • Flat coil • Collector	• One • Two or more	• Cryogenic • Low-temperature • High-temperature	• Without active control • With active control

Table 1.1: Classification of Loop Heat Pipes [20]

Although a conventional LHP is a simple loop with a defined heat flow direction from a unique evaporator to a unique condenser, other designs exist, with a condenser similar to the evaporator that can act as evaporator in case of heat flow reversal, with flexible transport lines, or even with a ramified architecture including multiple evaporators and/or condensers (Figure 1.4).

Miniature LHPs are typically used in electronic thermal management, with transport lines diameters smaller than 3 mm and an active zone area in the evaporator of several square centimetres. However, LHPs of greater dimensions are also developed for other applications. Several evaporator shapes exist, as will be further discussed in subsubsection 1.2.1.1. In traditional LHP designs, the reservoir is usually located on one side of the evaporator, but the reservoir may also be located on both sides to ensure a better wick wetting whatever the orientation of the loop, or even in the core of the wick. The core diameter may then be larger and the connections between the evaporator/reservoir and the transport lines need to be moved (Figure 1.4c). As explained in subsection 1.2.3, several designs of condenser can be implemented depending of the heat sink available and of the integration constraints. According to the application and to the working fluid of the loop, the operating temperature may vary from cryogenic temperatures to temperatures higher than 150 °C. Despite its auto-

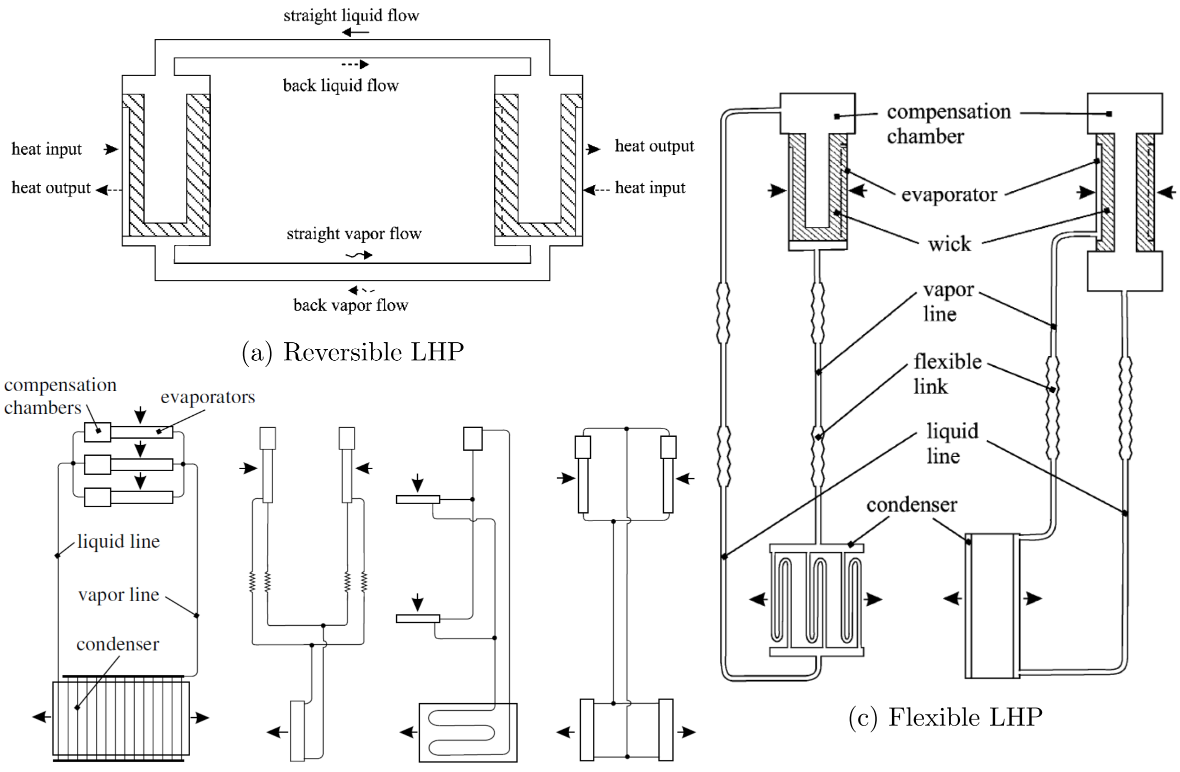

(a) Reversible LHP

(c) Flexible LHP

(b) Ramified LHP

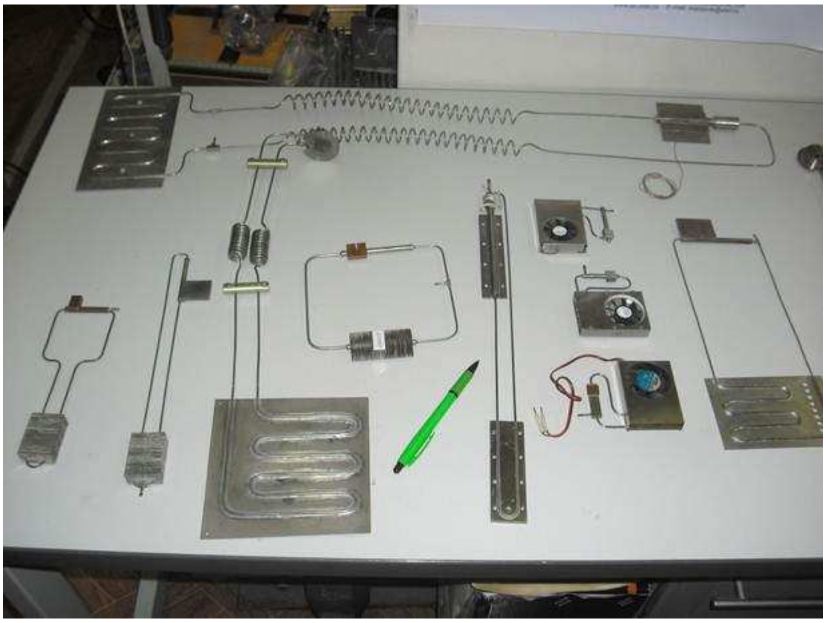

(d) LHP produced by Maydanik's research team at the Institute of Thermal Physics

Figure 1.4: Various designs of LHP [20]

regulating capability, a loop heat pipe may also be actively controlled through a heater connected to the compensation chamber [20–23]. This feature enables an accurate stability of the loop operating temperature for a wide range of power inputs.

The present study focuses on LHPs dedicated to the thermal management of electronic devices. As such, the following work will be limited to conventional LHPs of small dimensions, with one evaporator and one condenser, without active control of the system and for temperatures varying from 0 °C to 150 °C.

1.1.2 The thermodynamic cycle of an LHP

Figure 1.5 presents the typical Pressure-Temperature diagram of the thermodynamic cycle of an LHP in steady-state operation. The location of the characteristic points is also shown in Figure 1.6.

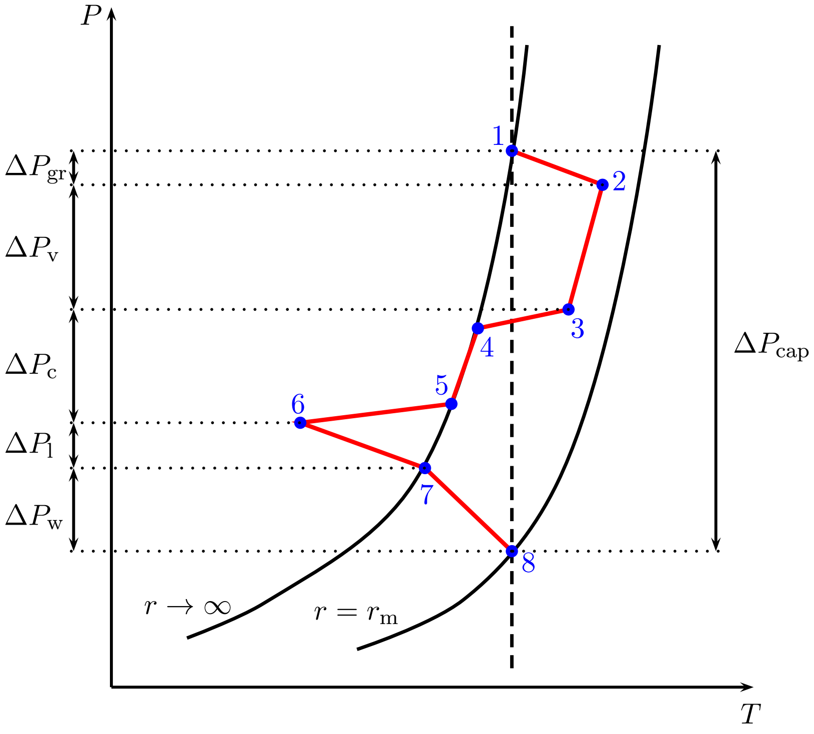

Figure 1.5: P-T diagram of an LHP operating cycle

1 → 2 In the evaporator, the liquid evaporates at the liquid-vapour interface (1) at temperature T_{gr}. It is often assumed that the evaporation takes place at the wick-groove interface. However, several authors studied the displacement of the vapour front inside the porous structure, as will be further discussed in section 1.4. The vapour is then slightly superheated in the grooves before exiting the evaporator (2).

2 → 3 The vapour flows through the vapour line and exchanges heat with the ambient if the lines are not thermally insulated. The temperature decreases if the ambient temperature is lower than the vapour temperature, as represented in the diagram. The fluid velocity is maximal in the vapour line. Therefore, the pressure drop due to the friction between the vapour and the walls, ΔP_{v}, can be high.

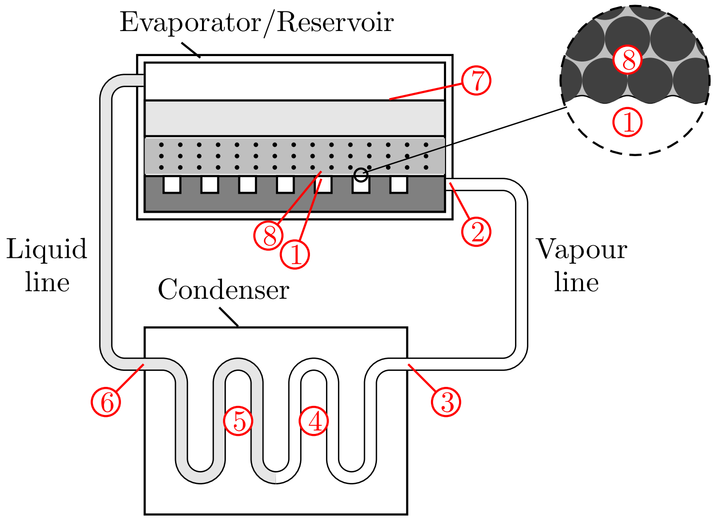

Figure 1.6: Location of the characteristic points in the LHP

3 → 6 The vapour enters the condenser and is cooled down until the saturation temperature is reached (4). Condensation then occurs between (4) and (5) and pressure drops in the two-phase zone of the condenser can be significant due to the friction at the liquid-vapour interface. In the last part of the condenser (5-6), the liquid is subcooled.

6 → 7 The liquid flows through the liquid line while dissipating heat to the ambient when the latter is not insulated. The temperature increases if the ambient temperature is higher than the liquid temperature, as shown in the figure. When it enters the reservoir, it mixes with the fluid in the reservoir which is in a two-phase equilibrium.

7 → 8 The liquid flows through the porous structure to the groove, generating additional pressure losses ΔP_{w}. When it reaches the liquid-vapour interface (8), the liquid is at the saturation temperature corresponding to the local pressure. As a meniscus forms in the pores, the equilibrium curve is shifted toward the right as shown in Figure 1.5; this equilibrium depends on the radius of curvature. In practice, a part of the liquid in the wick is even superheated, especially near the fin.

8 → 1 The pressure step ΔP_{cap} corresponds to the capillary pressure at the wick-groove interface. Indeed, the meniscus creates a pressure gradient between both sides of the liquid-vapour interface, called capillary pressure.

1.1.3 Steady-state operating performance of an LHP

To assess the operating performance of a loop heat pipe in steady-state, one generally considers the LHP temperature or its thermal resistance as a function of the heat load (Figure 1.7).

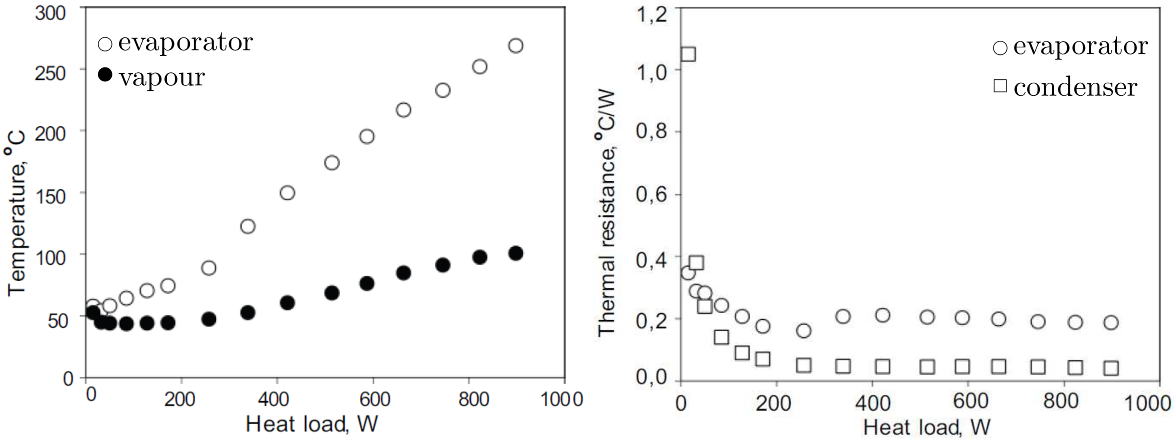

(a) (b)

Figure 1.7: Example of heat load dependence of the operating temperature (a) and the thermal resistance (b) [24]

The characteristic temperature of the LHP is often defined as the vapour groove temperature T_{v} [25–27], but one can also use the evaporator maximal temperature T_{e} [28, 29] or even the reservoir temperature [6, 23] to describe the loop operation. In electronic cooling applications design, the system requirement often concerns the electronic device maximal tolerable temperature so in that case, the use of T_{e} to describe the LHP performance has more meaning.

The LHP operating temperature as a function of the heat load may be U-shaped, flattened, or may increase linearly with the heat flux. Launay and Vallée [30] state that according to experimental results, the prediction of the operating curve shape is difficult because strongly influenced by heat transfer in the evaporator/reservoir, and therefore sensitive to the evaporator design and thermal characteristics. U-shaped curves have been most often encountered for metal wicks, with ammonia as working fluid and when the temperature difference between the ambient and the heat sink is large. Curves with flattened shapes have been observed for low thermal conductivity wicks with low-pressure fluids such as methanol, ethanol or acetone.

The literature reports two distinct LHP operating modes, namely the variable conductance mode (VCM) and the fixed conductance mode (FCM) (Figure 1.8). As explained by Launay et al. [6], the LHP operates in VCM when the portion of the area of the condenser where liquid subcooling is taking place is large enough. In that case, the liquid exits the condenser at a temperature close to the heat sink temperature. For higher heat loads, the LHP operates in FCM: the two-phase zone almost fills the condenser and the liquid enters the liquid line at a temperature close to the saturation. The LHP operating temperature increases then quasi-linearly with the heat flux.

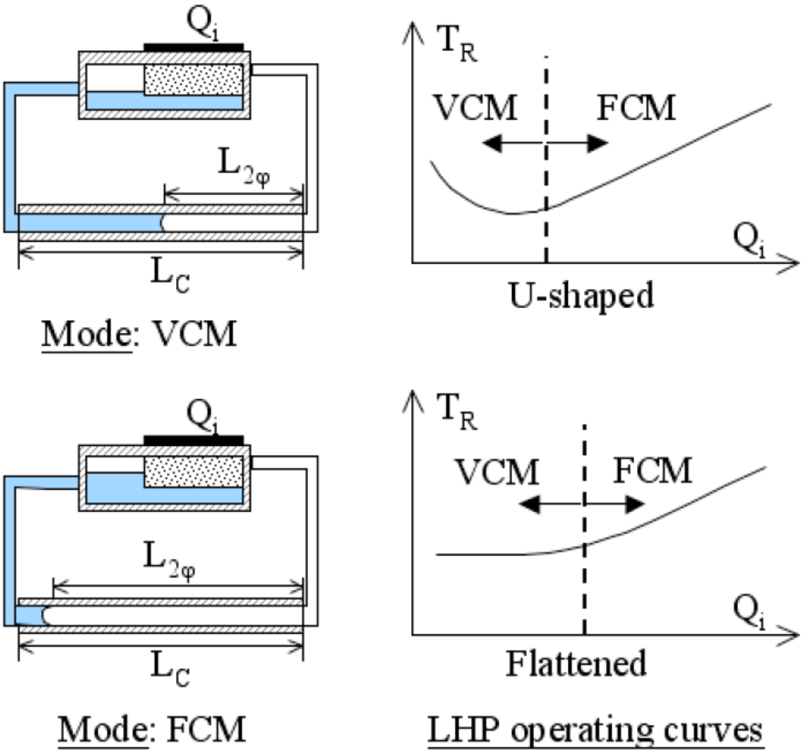

Figure 1.8: Typical LHP operating curves [6]

The total thermal resistance of an LHP R_{LHP} is generally evaluated as [24]:

$$R_{\mathrm{LHP}} = \frac{T_{\mathrm{e}} - T_{\mathrm{c}}}{Q_{\mathrm{in}}} \tag{1.1}$$

where T_{c} is the condenser temperature and Q_{in} is the heat load. It is also possible to assess the performance of the evaporator and of the condenser separately:

$$R_{\mathrm{e}} = \frac{T_{\mathrm{e}} - T_{\mathrm{v}}}{Q_{\mathrm{in}}} \tag{1.2}$$

$$R_{\mathrm{c}} = \frac{T_{\mathrm{v}} - T_{\mathrm{c}}}{Q_{\mathrm{in}}} \tag{1.3}$$

where R_{e} and R_{c} are the thermal resistances of the evaporator and of the condenser, respectively.

Such a definition may be problematic in practice. Indeed, according to Maydanik et al. [31], the calculation of the thermal resistance usually uses the average temperature of the evaporator active-zone surface and the average temperature of the condenser active-zone surface. The active surface of the evaporator can generally be considered thermally homogeneous with some uncertainty, because the use of a very conductive material such as copper enables to reduce drastically the temperature gradient in the evaporator. Therefore, a single measurement is sufficient, with the insertion of a thermocouple in contact with the evaporator wall. The measurement of the average temperature of the condenser is however much more complex. Indeed, the condenser often presents large temperature gradients between the two-phase zone and the subcooling zone. Moreover, its geometry (fins, tube-in-tube, etc.) complicates an accurate temperature measurement. Therefore, a substitution can be made, using the temperature at the surface of the liquid line at the exit of the condenser [31], the average of the temperatures at the condenser inlet and outlet [24] or the heat sink temperature [30]. This last solution includes the external heat exchange with the heat sink which is inherent to the efficiency of the LHP. However, an accurate measurement of the heat sink is often available and does not present the same uncertainty as for the condenser outlet temperature (difference between the temperature of the fluid and at the wall surface, thermal conduction in the tube wall, invasive measurement).

1.1.4 Operating limits

As explained by Launay et al. [32], a loop heat pipe is subjected to several limitations related to the physical phenomena involved during its operation, as well as to its operating specifications. These limitations have magnitudes and characteristics different from those of conventional heat pipes.

1.1.4.1 Boiling limit and superheat limit

As thoroughly explained by Kaya and Goldak [33], at large heat fluxes, nucleation may start in the porous structure of the LHP, at the wick-fin interface. Boiling can initiate at small superheat values if vapour or gas is already trapped in the small cavities. The boiling limit is then reached. With increasing heat loads, the vapour-liquid interface may then recede further into the wick and lead to a dryout. The authors report that purifying the fluid and improving the wick-fin interface prevent the entrapment of vapour embryos and non-condensable gases, thus leading to much higher nucleation superheats, at the same order of magnitude as that for homogeneous nucleation. In that case, the superheat limit can be reached: an explosive nucleation scenario can be expected, destroying the capillary meniscus drying the wick out. In practical, both the boiling and the superheat limits are very difficult to predict accurately. Furthermore, no thorough experimental study on these phenomena during LHP operation has ever been reported. A further analysis of this phenomenon will be discussed in section 1.4.

1.1.4.2 Capillary limit

As explained before, the capillary pressure must compensate the pressure drops in the LHP during operation. Assuming a static interface, this capillary pressure can be expressed with the Young-Laplace equation [34]:

$$\Delta P_{\mathrm{cap}} = \frac{2\sigma \cos\theta}{r_{\mathrm{m}}} \tag{1.4}$$

where σ is the surface tension of the working fluid, r_{m} is the radius of curvature of the meniscus in the wick and θ is the contact angle between the liquid and the wick. The radius of the meniscus adapts itself so that the capillary pressure compensates the pressure drops in the LHP at all times. The minimal value of the meniscus radius is the pore radius r_{p} which defines the maximum capillary pumping capability:

$$\Delta P_{\mathrm{cap,max}} = \frac{2\sigma\cos\theta}{r_{\mathrm{p}}} \tag{1.5}$$

As the heat load increases, the mass flow rate as well as the total pressure drops in the system increase. If pressure drops in the system exceed the capillary pressure, the liquid-vapour interface moves into the porous wick and this may eventually lead to a loop deprime, *i.e.* a failure of the system operation, due to the inability of the wick to act as a capillary lock. This operating limit has been theoretically and experimentally observed [23, 35–37].

1.1.4.3 Overheat limit

The maximal sustainable temperature for the LHP itself or for the equipment in contact with the evaporator can be a strong limitation in general experimental procedures and in design analyses. In the case of electronic thermal management, the maximal specification is often around 100 °C. Such a constraint restricts the admissible heat load range, even if the tested LHP is much capable of sustaining larger heat loads. Thus, this limit is often the most restrictive in testing and designing an LHP [38–42].

1.1.4.4 Other limits

Aside from the previously described limitations, several authors presented other operating limits [43, 44]. The *viscous limit* occurs for extremely low heat loads and in the case of high-viscous fluids that can be found in cryogenic applications or during start-up from a frozen state. In such a situation, the pressure gradients generated by the heat load are insufficient to overcome the viscous forces and no increase of the fluid flow rate (for increasing heat load) is observed. Although this situation can occur, it does not present a large interest in the present study. Chuang [43] and Hamdan [44] also suggest the *sonic limit* and the *entrainment limit*. The first mentioned corresponds to the occurrence of vapour choking when the sonic speed is reached. However, to our knowledge, no experimental study ever reported such a problem. The second limit is a major parameter of traditional heat pipes. It occurs when the vapour shear is able to carry water droplets from the liquid stream flowing back to the condenser, leading to a dryout of the evaporator. However, since the vapour and the liquid flow in separate channels in a loop heat pipe, such a limitation is not relevant in most LHPs.

1.2 Components constituting an LHP

Loop heat pipes are complex systems involving many coupled phenomena. However, extensive numerical and experimental studies have been conducted to determine the influence of specific parameters on the global system operation. This section presents the role and the importance of each LHP component. For a further analysis, the reader may refer to the experimental review of Launay and Vallée [30] and to the works of Ku [35] and Maydanik [20].

1.2.1 The evaporator-reservoir

1.2.1.1 The evaporator-reservoir shape

The evaporator-reservoir is undoubtedly the most critical and main structural element of an LHP, since its geometrical and thermal characteristics define significantly the operation of the entire system. The evaporator-reservoir basically consists of a metallic casing, a porous wick, vapour grooves and a chamber constituting the reservoir. Three main evaporator shapes exist: the cylindrical evaporator, the flat evaporator with the reservoir in the thickness, and the flat evaporator with the reservoir in the length (Figure 1.9).

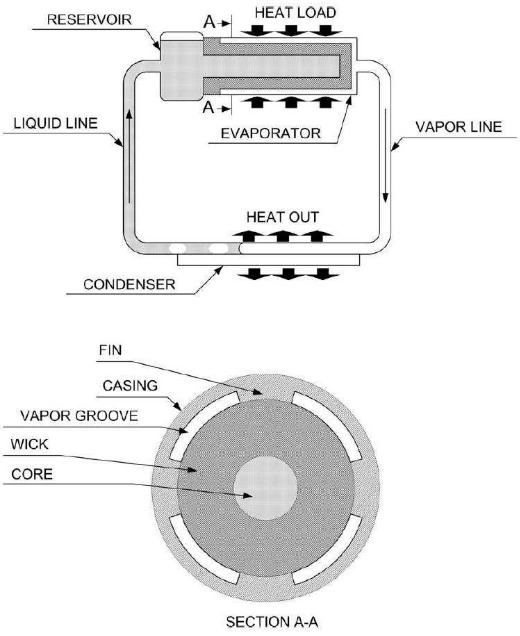

(a) Cylindrical evaporator [33]

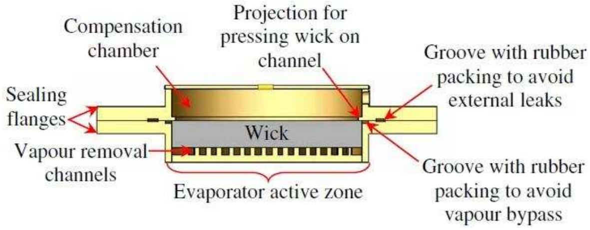

(b) Flat disk-shaped evaporator [45]

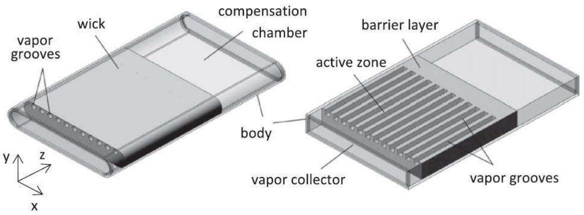

(c) Flat evaporator with reservoir in the length [46]

Figure 1.9: Various evaporator shapes

The cylindrical evaporator was the first to be developed. Therefore, most of the experimental studies focus on such shapes. However, in the past years, studies have shown a larger variety of evaporator-reservoir designs. This is mainly due to a necessity of flexibility and miniaturization attributable to the expansion of LHP applications [30]. Cylindrical evaporators provide better mechanical strength which is a decisive advantage in the use of high-pressure working fluids like ammonia. However, the device to be cooled by the LHP is generally flat and the evaporator needs a special "cylinder-plane" thermal interface located at the surface of the evaporator active zone. This leads to a degradation of the LHP thermal performances [20]. Moreover, the thickness of a cylindrical evaporator cannot be reduced as much as the flat LHP's one. This gave rise to the development of flat evaporators, where the components are stacked or where the reservoir is located next to the wick. Fore more detailed information about LHPs with flat evaporator, the reader may refer to the recent review of Maydanik et al. [47].

1.2.1.2 The primary capillary structure

The primary wick is at the heart of the evaporator. It has a double hydraulic purpose: supplying liquid for the evaporation zone from the reservoir as well as ensuring a sufficient capillary pressure to compensate for pressure losses in the LHP. Additionally, its thermal role is to promote heat transfer from the evaporator wall to the evaporation region while avoiding heat to be conducted to the reservoir [48]. These distinct needs show the necessity of a compromise in the selection of the best suitable wick characteristics like pore size, porosity, permeability and material.

Wick material

Experimental works show that plastic, metal, as well as ceramic are eligible materials for the LHP porous structure. Plastic wicks, among which polypropylene [49], PTFE [50], polyethylene [51] present the advantages of having a very low thermal conductivity. This characteristic prevents heat to flow from the evaporator to the reservoir through the wick, thus improving the LHP performances. However, the porosity of plastic wicks is quite low (about 50 %) and the maximum operating temperature of such materials is limited, restricting their use from low to moderate temperature ranges [49].

Several recent works reported test results with ceramic wicks [37, 52–54]. Ceramic wicks offer a good thermal and chemical stability, compatibility with metals and a large freedom in the choice of sizes and shapes in the microstructure. As for plastic wicks, ceramics thermal characteristics minimise parasitic heat losses through the wick. The reported results prove ceramics to be a reliable alternative for LHP applications.

Recently, Silk and Myre [55] conducted performance tests on LHPs using a carbon foam as a wick structure in an effort to reduce standard LHP fabrication costs. The initial results with compressed carbon foam wick structure indicate that they are viable materials for LHP applications.

The majority of experimental studies show the performance of metallic porous structure [30]: nickel wicks are widely used, but titanium, stainless steel, brass and iron oxyde are also tested. Several manufacturing processes can be used to provide adequate metal wicks but sintered powder is the most common process, providing high porosity and low pore size characteristics. Recent works present the performance of sintered copper wicks associated with water as working fluid [24, 39, 40, 56–59].

Contact with the evaporator envelope

To enable a good heat transport from the evaporator wall to the evaporation zone as well as to prevent any vapour leak back to the compensation chamber, the proper fitting of the capillary wick inside the evaporator casing has to be ensured. Therefore, the machining and assembly processes have to be closely adapted to minimize the contact resistance at the interface between the wick and the evaporator wall. Metallic wick structures offer the advantage of plastic deformation during the assembly process, providing a good contact between both materials. However, this deformation may lead to an open porosity obstruction, degrading the liquid flow in the porous structure [52]. Experimental tests with a conical copper wick inserted in a brass evaporator have been conducted, where the envelope is at a high temperature prior to assembly to provide expansion and sintering necessary to the metallic connection [60]. According to the authors, such a method enables a proper and tight wick fitting with no clearance, even without a high-precision fabrication. Santos et al. [52] explain that ceramic wicks are easier to machine without damaging the pores on the external surface. The chosen material and the assembly process must also ensure a good thermal and mechanical contact whatever the heat flux and the operating temperature. Indeed, differential expansion phenomena between the envelope and the porous structure may decrease the quality of the contact.

Choi et al. [61] investigated new techniques to enhance the thermal contact conductance of evaporators in LHPs. Several channel designs are tested and compared (Figure 1.10). The base plate is made of copper and sintered nickel is used for the wick. An estimation of the evaporator thermal resistance is given and values ranging from $7 \cdot 10^{-5}$ to $3 \cdot 10^{-4}\,\mathrm{m^2 \cdot K \cdot W^{-1}}$ are obtained. The interpenetrating design improves the thermal contact between the wick and the casing and decreases the evaporator resistance by about 25 %.

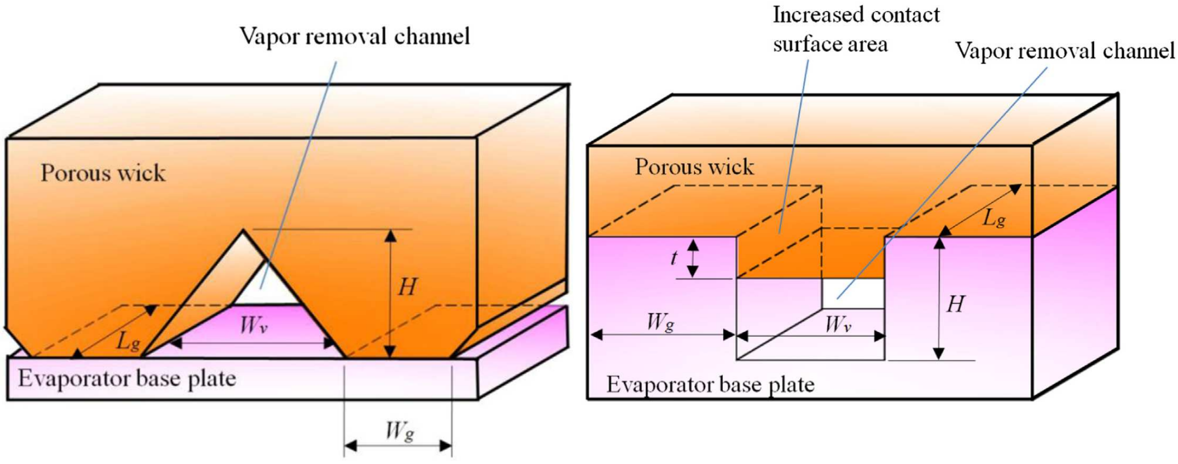

(a) Triangular design

(b) Interpenetrating design

Figure 1.10: Various channel designs to enhance the thermal contact [61]

Recently, Singh et al. [62] discussed various fabrication techniques for the capillary wick of a loop heat pipe. Three distinct methods for the insertion of the wick inside the evaporator containment tube are investigated, namely the *direct force fit*, the *thermal expansion fit* and the *cryogenic shrink fit*. The first technique consists on applying a constant mechanical force for the insertion and offers simplicity and flexibility. However, the tested samples show non-contact areas after integration. The second method consists in expanding the evaporator tube at very high temperature prior to assembly. The main issue encountered is a high temperature oxidization of both the tube and the wick. The third technique shows the best results. A prior immersion of the wick in liquid nitrogen enables a correct insertion for a good contact between both parts.

Information from the literature concerning the thermal contact between a porous structure and a solid base plate is very scarce. In addition, this parameter depends on many geometrical and manufacturing characteristics as well as on the assembly process. It is therefore very difficult to assess with accuracy the value of such a parameter in the study and the modelling of an LHP.

Wick porosity
The wick porosity, which is the ratio of the volume occupied by the wick material to the total volume, is an important parameter of the porous structure and has a decisive influence on its thermal and hydraulic characteristics. A higher porosity enables a higher mass flow rate of liquid through the wick and efficient supply of liquid to the evaporation zone. However, depending on the manufacturing process, the material chosen for the porous structure and its mechanical characteristics, the porosity is limited. Between the years 1998 and 2010, experimental works on LHPs were conducted with porous material porosities ranging from 32 % to 86 % [30]. A higher porosity can be obtained with sintered metal than with plastic materials [48]. Sintered wick structures have uniform porosity in all three axes. The porosity can be customized to requirements by using powders of different sizes and changing the sintering temperature and time during the manufacturing process [63].

Singh et al. [63] discuss in detail measurement techniques to determine the wick properties for LHP applications. The porosity of polyethylene and copper samples is measured by two distinct methods, namely the density method and the soaking method. The density method, simple and straightforward, gives results very close to the values given by the manufacturer. The soaking method seems to underestimate the porosity of the samples. However, no procedure is available to assess correctly the accuracy of each method.

Wick permeability
The permeability of the wick determines its ability to transport liquid in the presence of a pressure gradient. In an LHP, the permeability of the wick has to be as high as possible to provide a good liquid flow inside the porous structure without generating additional pressure losses. The permeability is a function of the wick structural characteristics. In common LHP applications, its value varies between 10^{-15} and $2 \cdot 10^{-12}\,\mathrm{m}^2$, depending on the material chosen and the pore radius (Figure 1.11). Several methods to measure permeability have been developed [63–65]. Most reported works use a Darcyan approach to evaluate the pressure drop, neglecting the inertial effects of the fluid in the porous medium. Darcy's law associates the pressure drop $\mathrm{d}P_\mathrm{f}/\mathrm{d}x$ across a porous material with the amount of fluid flowing through

the structure dm/dt and the properties of the fluid and the solid material [64]:

$$\frac{\mathrm{d}P_\mathrm{f}}{\mathrm{d}x} = -\frac{\mu}{K\rho_\mathrm{f}S_\mathrm{w}}\frac{\mathrm{d}m_\mathrm{f}}{\mathrm{d}t} \tag{1.6}$$

where μ is the dynamic viscosity of the fluid, K is the permeability of the porous medium, ρ_f is the fluid density and S_w is the porous material cross-sectional area. Berti et al. [65] develop a more precise method based on Forchheimer terms (a Darcyan and a non-Darcyan permeability constants), taking into account the contribution of kinetic effects on the pressure drop. The Forchheimer's law provides a more realistic evaluation of the phenomena occurring in the porous wick structures. According to the authors, the inertial effect is a relevant contribution in the pressure drop prediction.

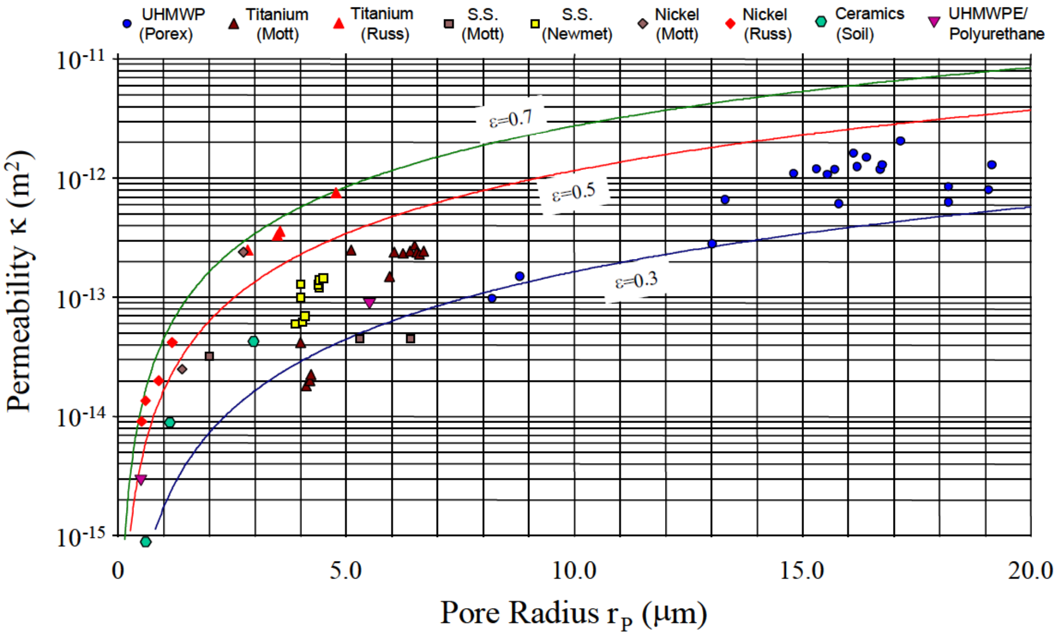

Figure 1.11: Porous characteristics of common LHP wicks [26]

Pore size

The pore size determines the maximal capillary pressure achievable by the wick. As such, a low pore diameter provides a better hydraulic lock and ensures the fluid flow in the loop even for high pressure drops and against gravitational effects. However, lowering the pore size increases the pressure losses in the porous structure and can lead to a porosity obstruction during the manufacturing process. As shown in Figure 1.11, the pore diameter generally ranges between 1 and 20 µm. However, the use of sintered copper can lead to larger pore diameters, between 16 and 140 µm [39, 40, 57, 66]. In that case, no particular performance degradation of the LHP operation is observed. When considering a porous structure of an LHP, one cannot strictly measure the pore diameter. Indeed, the manufacturing process leads to a distribution of pore diameters in a definite range, dependent on the powder size, the powder density, and the sintering temperature during processing [63]. Thus, some authors clarify their data, giving the pore size range, the mean pore radius of the wick, or the maximal pore size to be expected that can be used in the calculation of the capillary limit. The latter can be measured by the bubble point test, as explained by Singh et al. [63]. A porous material, saturated with liquid, is in contact with liquid on one side and with gas on the other side. The gas pressure is increased until bubbles are observed on the liquid side, thus determining the capillary limit and the maximal pore size. Holley and Faghri [64] present other methods: the risen meniscus test, the fallen meniscus test and the rate-of-rise method. Xu et al. [67] states that the pore size and its distribution affects the thermal conductivity of the wick. Figus et al. [68] studied the development of a liquid-vapour interface inside the porous structure of a loop heat pipe. According to the author, a smooth vapour front is to be expected in the case of an extremely narrow pore size distribution. However, some disorder in the pore size distribution results in a very irregular interface, also known as fractal type front. This phenomenon will be further discussed in section 1.4.

Wick effective thermal conductivity

The effective thermal conductivity of the porous wick saturated with liquid is of great interest for the design and performance evaluation of LHPs. This parameter determines the ability of the wick to transport heat from the evaporator envelope to the evaporation zone as well as the amount of heat that is conducted through the porous structure and given to the reservoir (parasitic heat flux). An experimental setup to measure the effective thermal conductivity of a sintered copper wick is presented by Singh et al. [63]. The test sample, a copper porous structure saturated with water, is fixed between a heater (copper block with cartridge heaters) and a fin heat exchanger. During the tests, the conditions at the heat exchanger are kept constant, while varying the input power. The temperature is monitored using thermocouples at various locations. A proper care is taken to ensure a high degree of saturation of the wick and an adequate sealing of the sample, as well as to prevent heat losses to the ambient. The results show a quasi-constant value of the effective thermal conductivity for the entire range of applied heat loads and demonstrate the reliability of the experimental method. However, the authors note a number of unaccountable factors in the experiment that can result in an inaccurate determination of the conductivity: improper thermal contact between the wick and the copper wall, trapped vapour and incomplete saturation of the copper wick with the water.

The large majority of experimental and modelling studies use a correlation to predict the effective thermal conductivity of the porous material. A large number of these correlations can be found in the literature [48, 69, 70]. This thermophysical property depends not only on the material constituting the wick but also on geometrical parameters such as the porosity, the mean pore diameter and the pore size distribution. The results are very different according to the chosen correlation (see Appendix A). Presently, the only reliable method to select a correlation is the comparison with experimental data.

Biporous wicks

As explained by Yeh et al. [71], bidispersed and biporous wicks can be differentiated by their manufacturing process. The first mentioned are fabricated through consolidation of clusters of small porous particles whereas biporous wicks are generated using both metal powder sintering and pore formers dissolving (Figure 1.12).

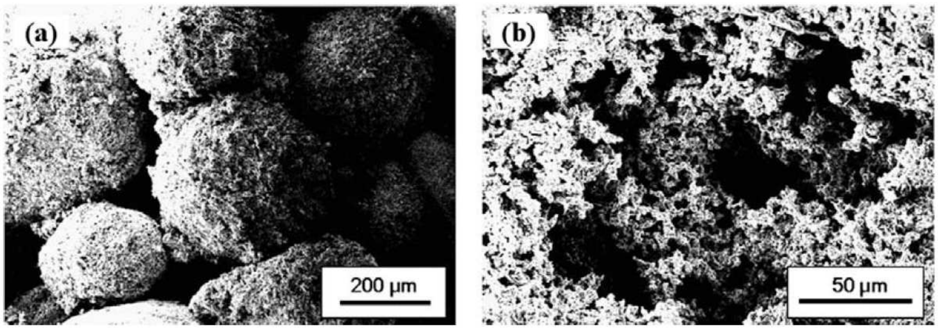

Figure 1.12: Photographs of wick structures with bimodal pore size distributions: *(a)* bidispersed wick and *(b)* biporous wick [71]

Despite different manufacturing processes, they share a common characteristic: a bimodal pore size distribution (Figure 1.13). Such a feature offers the advantage of having large pores to reduce pressure drops across the wick and to enable the evacuation of eventual vapour bubbles forming in the capillary structure and small pores that supply the returning liquid and increase the evaporative surface. In order to avoid the trapping of vapour inside the wick at high heat flux, which leads to a degradation of the system performance, wick structures with bimodal pore size distributions have been developed and first tested in LHPs by North et al. [72]. Several experimental and numerical works show that the LHP operating performance can be substantially improved by using a biporous wick instead of a monoporous structure [71, 73–75].

1.2.1.3 Secondary capillary structure

Several works from the literature report the advantage of adding a secondary wick between the reservoir and the main capillary wick [30, 35, 50, 76]. Such a feature enables to maintain the hydraulic connection between the liquid pool in the reservoir and the base of the main capillary wick whatever the orientation of the evaporator/reservoir. Additionally, it acts as a thermal barrier between the reservoir and the evaporator, reducing the parasitic heat fluxes. Vapour arteries incorporated inside the secondary wick may prevent potential vapour or gas bubbles from accumulating inside the evaporator core. An evaporator design with a secondary wick is presented in Figure 1.14. The required characteristics for the secondary wick are a high permeability and a low thermal conductivity [30]. Thus, the pores are generally much larger in the secondary wick than in the primary wick.

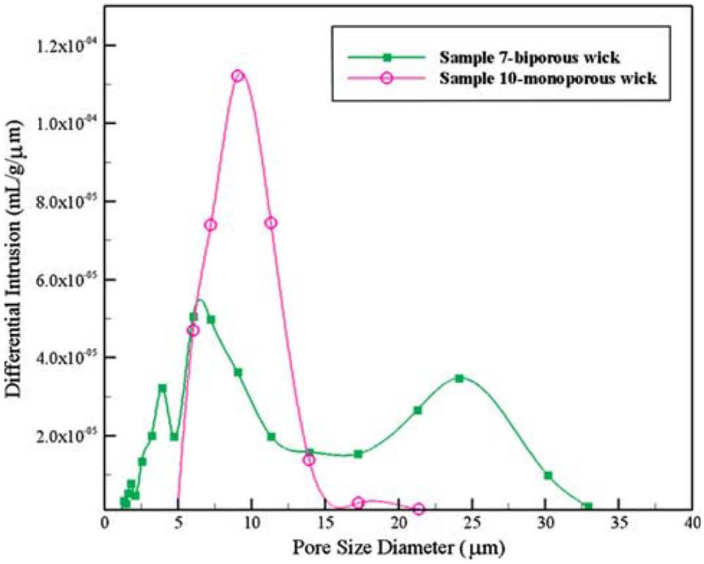

Figure 1.13: Pore size distributions of monoporous and biporous wicks (sintered nickel) [73]

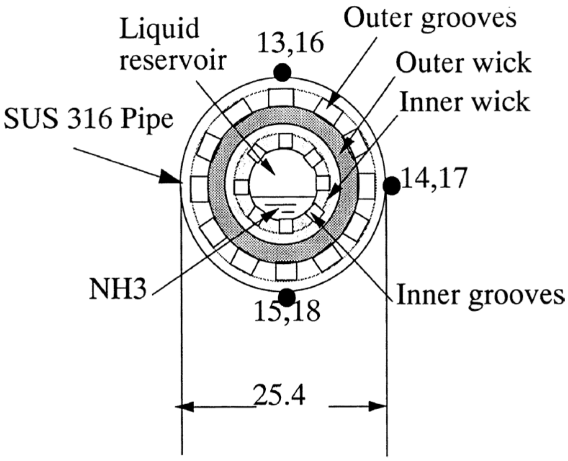

Figure 1.14: Cross-sectional view of an evaporator with a secondary wick [50]

1.2.1.4 The vapour grooves

As explained by Choi et al. [77], the vapour grooves, or vapour channels, have a double function in the LHP evaporator: to provide a thermal path for the conductive heat transfer from the evaporator base plate to the liquid-vapour interface of the wick structure as well as to collect and remove the vapour generated in the evaporation zone and to convey it to the vapour transport line. As a result, the geometrical characteristics (shape, dimension, position) of the vapour grooves are decisive parameters of the heat transfer in the evaporator/reservoir structure. The evaporation rate, the contact resistance, the evaporator envelope thermal homogeneity and the pressure drops in the vapour grooves are closely related to their geometry.

Altman et al. [78] present various LHP groove designs. As shown in Figure 1.15, vapour grooves can be machined either in the evaporator casing or directly in the wick. Combined solutions can also be considered. In experimental works from the literature, the grooves are generally machined in the evaporator envelope for manufacturing simplicity reasons. However, according to Zhang et al. [79], the loop heat pipe operates at lower temperature when the vapour grooves are located inside the wick because the evaporation area is larger in that case. Their numerical results also show that in the case of rectangular-shaped grooves, the thermal performances are maximal when the height and width of the grooves are equal.

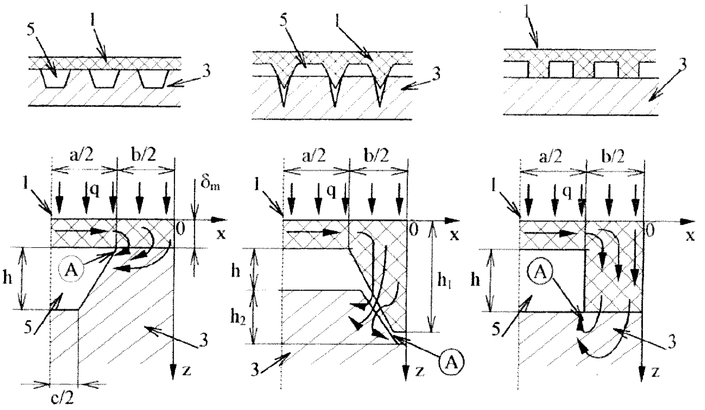

Figure 1.15: Design versions of LHP vapour grooves [78]

Kiseev et al. [80] experimentally studied different shapes of grooves (rectangular, trapezoidal and triangular) for flat circular evaporators. They conclude that, in the case of quadratic grooves, the optimum ratio between the total transversal area of the vapour grooves and the total area of the heat input wall is around $0.4 - 0.5$. They also add concentric grooves of different shapes (rectangular, trapezoidal, triangular) to the radial ones and compare different vapour grooves layouts (Figure 1.16). The decrease in the size and the distance between the concentric vapour grooves enhance heat transfer. These conclusions are in accordance with the work of Wei et al. [81], who numerically investigated the effect of geometric parameters on the wick performance. They conclude that the optimal ratio between the groove width and the fin width is close to 1.

Vlassov and Riehl [82], Riehl and dos Santos [51] and Kuroi and Nagano [83] also conducted studies on the implementation of circumferential grooves in a cylindrical evaporator. They all conclude that the presence of the additional grooves participates in providing homogeneous temperature to compensate unsymmetrical heat input from the attached saddle. According to Riehl and dos Santos [51], in a cylindrical evaporator, the circumferential grooves act as micro heat pipe, transporting heat from the hottest to the coldest part of the capillary evaporator.

1.2.1.5 Parasitic heat fluxes

Parasitic heat fluxes (or heat leaks) refer to the heat that is conducted from the evaporator to the reservoir and thus does not participate in the evaporation at the interface between the vapour grooves and the wick. Parasitic heat losses can generally be divided into two terms

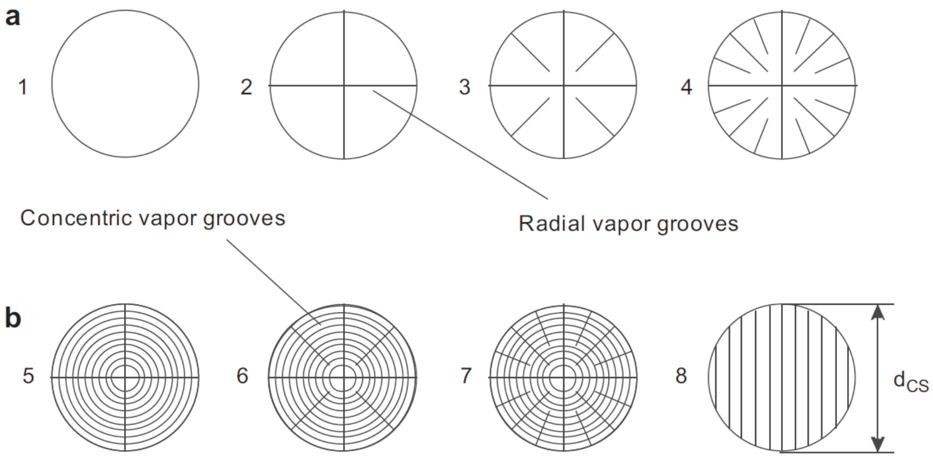

Figure 1.16: Various layouts of vapour grooves [80]

(Figure 1.17). A part of the heat never enters the wick. It is thermally conducted through the evaporator casing instead and reaches the reservoir bypassing the porous structure. This heat flux is usually referred to as the "longitudinal" (for flat evaporators) or the "axial" (for cylindrical evaporators) parasitic heat losses. Another part of the heat load reaches the reservoir by thermal conduction through the porous wick and is called "radial" or "transversal" parasitic heat flux, depending on the evaporator geometry.

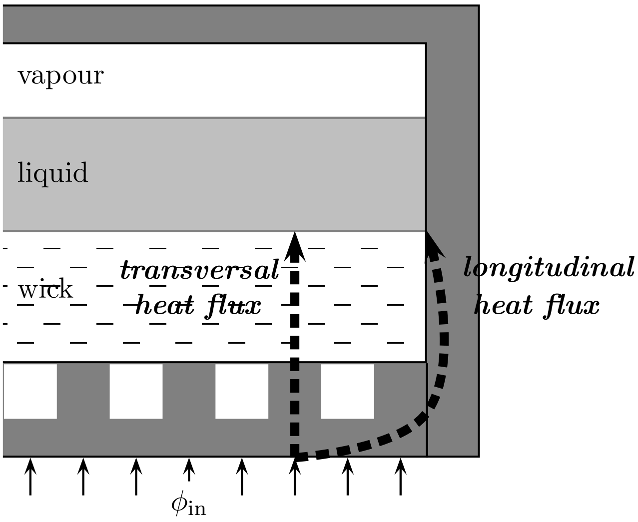

Figure 1.17: Parasitic heat fluxes in the evaporator

Longitudinal/axial heat flux

The axial heat leak refers to the heat conducted from the evaporator metal mass to the compensation chamber through the connection in between. Therefore, it mainly depends on the configuration of the compensation chamber [32], the material and the thickness of the evaporator casing and the global evaporator/reservoir design.

Radial/transversal heat flux

The radial heat flux depends on the thermal and hydrodynamic effects in the porous medium [32]. Parameters such as the effective thermal conductivity, the wick thickness, the heat transfer with the reservoir, the thermal convection with the fluid flowing through the porous medium affect the radial heat losses.

The parasitic heat fluxes have a major influence on the LHP operation. While the largest part of the total heat load is dissipated in the evaporator through evaporation, the rest is given to the ambient or transferred to the reservoir. In steady-state operation, this parasitic heat flux is compensated by the subcooling of the liquid returning to the reservoir. Therefore, parasitic heat fluxes indirectly dictate the proportion of the heat load that is actually dissipated by evaporation as well as the subcooling of the liquid at the exit of the condenser. High parasitic heat fluxes lead to a decrease of the mass flow rate and to an increase of the LHP operating temperature.

Several measures can minimise parasitic heat losses [30]: The choice of a material with low thermal conductivity for the wick (plastic, ceramic, titanium), for the evaporator-reservoir casing (stainless steel, Inconel®) or for the reservoir alone, the reduction of the wall thickness, the reduction of the conductive section between the evaporator and the reservoir. Singh et al. [42] use an O-ring seal between the evaporator and the compensation chamber to prevent heat leaks. The quality of the thermal contact between the evaporator envelope and the porous wick also influences the total amount of parasitic heat losses as well as the proportion of both heat fluxes.

1.2.2 The transport lines

The vapour and liquid lines connect the evaporator to the condenser. As explained by Launay and Vallée [30], various requirements should be met in the transport lines sizing:

- The wall thickness has to be sized to accommodate the variations of the fluid pressure, considering the mechanical properties of the tube material.
- The length of each transport line is generally defined by the position of the heat source and the heat sink, imposed by the environment in which the loop is integrated. It varies between a few centimetres and several metres.
- The diameter of both transport lines has to be large enough to reduce the pressure drops along the line. However, smaller diameters allow a better integration of the LHP and lead to a miniaturization of the reservoir. In the literature, transport lines diameters usually range between 1 and 5 mm. The number of bends and other singularities also has to be reduced in order to minimise pressure drops along the lines.

Transport lines are generally metallic tubes in copper or stainless steel. In experimental studies, they can be thermally insulated to reduce heat losses to the ambient that are particularly difficult to estimate accurately. Very few studies have been conducted to study the influence of the vapour and liquid lines on the LHP operation. Rivière et al. [84] show that the thermal conductivity of the liquid line has an impact o the liquid subcooling entering the reservoir. They also state that condensation already occurs in the vapour line before entering the condenser. These conclusions are confirmed by the work of Siedel et al. [85].

1.2.3 The condenser

The function of the condenser is to dissipate the heat from the working fluid to the heat sink. Various types of condensers can be used (Table 1.2). In the literature, the most common modes of heat transfer are the condensation in tube with heat flux evacuation through a liquid cooled plate, a tube-in-tube heat exchanger or a finned surface heat exchanger [30].

Condensation cross-section	Thermal link	Modes of external heat transfer
• circular • annular	• plate heat exchanger • finned heat exchanger • tube-in-tube heat exchanger	• air forced convection • air natural convection • liquid forced convection • radiative heat transfer

Table 1.2: Classification of condenser elements [30]

Although less studied in the literature, the condenser plays a decisive role in the LHP operation, in particular in fixed conductance mode [6]. Maydanik and Vershinin [24] explain that the main limitation for the capacity and the thermal resistance of miniature LHPs is the conditions of cooling of the condenser. Therefore, the thermal-fluidic characteristics of the condenser are of major interest and the design optimization of the condenser is necessary to enhance the LHP performance [86].

1.2.3.1 Pressure drops in the condenser

The use of sophisticated condensation models in global LHP models remains challenging. Therefore, authors generally make important assumptions on the flow regime to model the pressure drops and the heat transfer in the condensing zone. Actually, the flow regime depends on many parameters such as the diameter of the condenser, the void fraction and the vapour quality of the fluid flow, the vapour and liquid densities, the capillary length of the fluid and heat transfer with the wall. In horizontal co-current flow, the flow pattern can either be bubbly, plug, stratified, wavy, slug or annular [87]. Various experimental and numerical studies deal with the pressure and thermal characteristic of two-phase flow in tubes and many correlations can be found in the literature to evaluate condensation heat transfer and two-phase pressure drops [87, 88].

According to Thome [88], the total pressure drop of a two-phase flow P_{tot} is the sum of the static pressure drop ΔP_{static}, the momentum pressure drop ΔP_{mom} and the frictional pressure drop ΔP_{fric}:

$$\Delta P_{\text{tot}} = \Delta P_{\text{static}} + \Delta P_{\text{mom}} + \Delta P_{\text{fric}} \tag{1.7}$$

The static pressure drop is equal to:

$$\Delta P_{\text{static}} = \rho_{2\varphi} g H \sin\theta \tag{1.8}$$

where H is the vertical height, θ is the angle with respect to the horizontal and the two-phase density $\rho_{2\varphi}$ is:

$$\rho_{2\varphi} = \rho_{\text{l}}(1-\varepsilon) + \rho_{\text{v}}\varepsilon \tag{1.9}$$

and ρ_{l} and ρ_{v} are the liquid and vapour densities, respectively. The static pressure is equal to zero if condensation occurs in a horizontal tube. Numerous methods are available for calculating the void fraction ε. The simplest is the homogeneous model, considering a homogeneous pseudo-fluid that obeys the conventional equations for single-phase fluids and which properties correspond to the averaged properties of both the liquid and the vapour phases. Assuming the vapour and the liquid velocities are equal, the void fraction is then given by:

$$\varepsilon = \left[1 + \frac{1-x}{x}\left(\frac{\rho_{\text{v}}}{\rho_{\text{l}}}\right)\right]^{-1} \tag{1.10}$$

where x is the vapour quality of the fluid. The momentum pressure drop ΔP_{mom} reflects the change in kinetic energy of the flow and can be expressed as:

$$\Delta P_{\text{mom}} = \Delta\left[\frac{\dot{m}_{\text{tot}}^2}{S_{\text{tube}}^2 \rho_{2\varphi}}\right] \qquad \text{(homogeneous model)} \tag{1.11}$$

$$\Delta P_{\text{mom}} = \left(\frac{\dot{m}_{\text{tot}}}{S_{\text{tube}}}\right)^2 \Delta\left[\frac{(1-x)^2}{\rho_{\text{l}}(1-\varepsilon)} + \frac{x^2}{\rho_{\text{v}}\varepsilon}\right] \qquad \text{(separated flow model)} \tag{1.12}$$

with $\dot{m}_{\text{tot}}$ the total mass flow rate and S_{tube} the cross-section area of the tube.

The frictional pressure drop is the most difficult term to calculate. In can be determined using the homogeneous model or separate flow models. In the literature, the most used correlations are the models of Friedel, Lockhart and Martinelli, Grönnerud, Chisholm and Müller-Steinhagen and Heck [88]. These models predict the two-phase frictional pressure drop based on a two-phase multiplier for the liquid phase and in some cases for the vapour phase. This factor depends on the thermophysical properties of both phases and on the vapour quality of the fluid flow.

1.2.3.2 Heat transfer in the condenser

Several models are available in the literature to calculate the condensation heat transfer coefficient in a horizontal tube. In the case of stratified flow and low velocities, the correlation from Chato can be used to calculate the average heat transfer coefficient h_{i} [89]:

$$h_{\text{i}} = 0.555\left(\frac{g\left(h_{\text{lv}} + \frac{3}{8}c_{\text{p,l}}\left(T_{\text{sat}} - T_{\text{tube}}\right)\right)\lambda_{\text{l}}^3\left(\rho_{\text{l}} - \rho_{\text{v}}\right)\rho_{\text{l}}}{D_{\text{i}}\mu_{\text{l}}\left(T_{\text{sat}} - T_{\text{tube}}\right)}\right)^{0.25} \tag{1.13}$$

where λ_l is the thermal conductivity of the liquid, μ_l is the dynamic viscosity, $c_\mathrm{p,l}$ is the specific heat of the liquid, D_i is the internal diameter of the tube, h_lv is the latent heat of vaporization of the fluid and T_sat and T_wall are the saturation and the wall temperatures, respectively. If the flow is annular, the correlation given by Akers et al. [90] can be used:

$$\text{if } Re_\mathrm{eq} < 5 \cdot 10^4 \qquad h_\mathrm{i} = 5.03 \frac{\lambda_\mathrm{l}}{D_\mathrm{i}} Re_\mathrm{eq}^{\frac{1}{3}} Pr_\mathrm{l}^{\frac{1}{3}} \tag{1.14}$$

$$\text{if } Re_\mathrm{eq} > 5 \cdot 10^4 \qquad h_\mathrm{i} = 0.0265 \frac{\lambda_\mathrm{l}}{D_\mathrm{i}} Re_\mathrm{eq}^{\frac{4}{5}} Pr_\mathrm{l}^{\frac{1}{3}} \tag{1.15}$$

where the equivalent Reynolds number for two-phase flow Re_eq is determined from an equivalent mass flow rate:

$$\dot{m}_\mathrm{eq} = \dot{m}_\mathrm{tot} \left[(1-x) + x \left(\frac{\rho_\mathrm{l}}{\rho_\mathrm{v}} \right)^{1/2} \right] \tag{1.16}$$

In the previous equations, Pr_l is the liquid Prandt number and $\dot{m}_\mathrm{tot}$ is the total mass flow rate considering both the vapour and liquid flow rates.

Goncharov et al. [91] conducted a modelling and experimental investigation of condensation in LHPs. The flow regime is observed inside condenser quartz glass tubes with an internal diameter of 4 mm and water as working fluid. The formation and behaviour of liquid slugs are particularly of interest in the last part of the condenser. The authors also conduct a modelling analysis of the condensation flow. They conclude that pressure pulsating phenomena are generated due to the liquid slug formation. These liquid slugs are a consequence of large surface tension forces near the end of the condenser.

A fine modelling of the heat transfer associated with condensation can be found in the work of Miscevic et al. [92]. They model separately the two phases and obtained the general shapes of the interfaces, in the case of a capillary regime. This model takes into account the transient behaviour of the liquid shape inside the tube due to the capillary effects. Furthermore, this study shows the significance of the thin liquid film in the calculation of the pressure drop as well as the estimation of the heat transfer. El Achkar et al. [93] experimentally determined the hydraulic and thermal parameters in the isolated bubbles zone during the condensation flow in a circular micro channel. Negligible latent heat is dissipated compared to the one dissipated in the annular and the intermittent zones.

For further considerations on two-phase flow, the reader can refer to the extensive studies of Collier and Thome [87] or Thome [88].

1.2.4 The working fluid

1.2.4.1 Requirements on the working fluid characteristics

In addition to the design of the LHP elements, the selection of the working fluid is determinant. Indeed, it must satisfy various requirements, summarised by Soler [94] as follows:

- The operating temperature range shall correspond to limited saturation pressures, regarding the mechanical integrity of the system.

- The triple point temperature should be lower than the lowest temperature encountered in the loop operation. The critical point temperature should not be reached during the LHP operation.
- The latent heat of vaporization should be as high as possible to transfer a huge amount of energy with a small flow rate. Therefore pressure drops are reduced inside the system.
- The surface tension should be as high as possible to provide a large capillary pressure.
- The vapour density should be as high as possible to restrain the vapour velocity and thus the generated pressure losses.
- The dynamic viscosity of both the vapour and the liquid should be small to reduce the pressure drops.
- The fluid should be chemically stable, non-corrosive and as pure as possible to prevent the generation of non-condensable gases during the LHP operation.

Additional criteria may exist in accordance with environmental and safety constraints.

1.2.4.2 Working fluid selection criteria

The selection of the optimal working fluid is not simple. Indeed, some of the previously given requirements are contradictory and a compromise has to be found. Various comparative studies have been undertaken to assess the performance of several working fluids. It depends on many parameters regarding the thermophysical properties of the fluid, the operating temperature range of the LHP and the heat load range. The majority of these investigations is a comparison of several working fluids in a given configuration. Therefore, it does not provide a significant analysis about an appropriate selection criterion of the working fluid.

Kaya and Ku [95] compared the performance of an LHP using three different fluids: ammonia, water and acetone. In their experiment, the evaporator is cylindrical and the heat sink temperature is equal to 273 K. The LHP operating limits are very different depending on the working fluid characteristics. According to the authors, the water and acetone LHPs are limited by the absolute vapour pressure which is too low to overcome the pressure drops at low power levels (viscous limit). The LHP working with water shows a much higher capillary limit than the other LHPs.

Pauken and Rodriguez [96] experimentally tested an LHP with both ammonia and propylene, with a heat sink temperature ranging from $-10\,^{\circ}\mathrm{C}$ to $20\,^{\circ}\mathrm{C}$. Ammonia exhibits good heat transfer characteristics and is therefore the most used working fluid in LHP for spatial applications. Propylene makes a good comprise, because it has a lower freezing point and relatively good heat transfer properties.

Boo and Chung [49] tested a polypropylene wick with methanol, ethanol and acetone. The LHP has a flat-type evaporator. The maximal operating temperature is set according to the specification of the polypropylene wick which shape can be deformed at high temperature.

The methanol is considered as the best candidate in this particular application, based on the maximal reached heat load and the thermal resistance at high heat fluxes. However, for low to moderate heat loads, the acetone LHP operates at the lowest vapour temperature.

Hsu et al. [97] tested a micro LHP with water and methanol as working fluid. Water demonstrates a wider heat load performance range (3.3–13 W) than methanol (1.2–5.9 W) with a condenser temperature of 17 °C. Furthermore, the thermal resistance of the LHP working with water is lower than with methanol. However, the start-up temperature and power are lower with methanol than with water.

Vasiliev et al. [41] conducted tests with wicks made of nickel and titanium and acetone and water as working fluids. The LHP with titanium and water transports up to 900 W for different spatial orientations, keeping the temperature of the heated wall lower than 100 °C, with a heat sink temperature of 20 °C. For the LHP working with acetone and a nickel wick, the maximal heat load does not exceed 300 W.

Liu et al. [98] compared the transient and steady-state behaviours of an LHP with methanol and acetone as working fluid. The LHP working with acetone starts up faster and operates at a lower temperature. However, the theoretical heat transfer limitation (based on the capillary limit) is far less for the acetone LHP than with methanol.

Apart from the previous cited works, other working fluids have been tested, including pentane, R134a, neon, oxygene, nitrogen, ethane, propane, R152A, R11 and toluene [20, 30].

Despite interesting results for given configurations and requirements, these experimental investigations do not provide any useful method for the selection of the working fluid in the design of an LHP. Indeed, this choice depends on many parameters that vary from one application to another.

Mishkinis et al. [99] conducted a dimensionless analysis to examine scaling issues in LHPs. Several figures of merit are presented, as well as criteria based on general dimensionless numbers. A non-dimensional study can provide means for comparison and enable the selection of an optimal working fluid. A similar method is developed by Launay et al. [100]. The authors obtain figures of merit for LHPs to suggest selection criteria for the working fluid. Based on an analytical LHP model, they define several criteria, depending on the operating mode of the LHP (variable conductance, fixed conductance, or close to the capillary limit), that lead to an optimisation of the LHP performance (Table 1.3). In variable conductance mode, the criterion also depends on the ratio of the parasitic heat flux through the wall Q_{b} to the parasitic heat flux through the wick Q_{w}. When the LHP operates close to the capillary limit, a distinction is made, according to the ratio between the pressure drops in the vapour line ΔP_{v} and the pressure drops in the capillary structure ΔP_{w}. The merit numbers depend on the thermal ($c_{\mathrm{p,l}}$, h_{lv}, λ_{l}) and the hydraulic (ρ_{l}, ρ_{v}, μ_{l}, μ_{v}, σ) properties of the working fluid. The maximisation of the merit number leads to the selection of the best suitable fluid from a performance point of view. Such a method, coupled with an analytical model, is a useful tool for the choice and the comparison of working fluids. Furthermore, the thermophysical properties of the fluid are explicitly expressed in the merit numbers.

Operating mode	Merit number	Condition
Variable conductance	$Nb1 = \frac{c_{\mathrm{p,l}}}{h_{\mathrm{lv}}}$	$Q_{\mathrm{b}} \gg Q_{\mathrm{w}}$
	$Nb2 = \frac{\rho_{\mathrm{v}}^2 c_{\mathrm{p,l}} h_{\mathrm{lv}}^{1.75}}{\mu_{\mathrm{v}}^{0.25}}$	$Q_{\mathrm{b}} \ll Q_{\mathrm{w}}$
Fixed conductance	$Nb3 = \left(\frac{\rho_{\mathrm{l}} \left(\rho_{\mathrm{l}} - \rho_{\mathrm{v}}\right) h_{\mathrm{lv}} \lambda_{\mathrm{l}}^3}{\mu_{\mathrm{l}}}\right)^{0.25}$	
Close to the capillary limit	$Nb4 = \frac{\rho_v \sigma h_{\mathrm{lv}}^{1.75}}{\mu_{\mathrm{v}}^{0.25}}$	$\Delta P_{\mathrm{v}} \gg \Delta P_{\mathrm{w}}$
	$Nb5 = \frac{\rho_{\mathrm{l}} \sigma h_{\mathrm{lv}}}{\mu_{\mathrm{l}}}$	$\Delta P_{\mathrm{v}} \ll \Delta P_{\mathrm{w}}$

Table 1.3: Working fluid selection criteria [100]

1.2.4.3 Chemical compatibility

Mishkinis et al. [101] performed a survey of possible solutions in the selection of working fluids in compatibility with the LHP envelope and wick materials. Figure 1.18 shows a compatibility table of several wick-fluid and envelope-fluid couples. The color indicates the degree of compatibility and the numbers correspond to references listed at the end of the paper [101]. For example, the wick-fluid couple nickel-methanol is compatible according to references 1 and 13, probably compatible for reference 2 but incompatible according to reference 7. The authors note a lot of contradictory data in the literature as well as the need to consider not only both couples but also the combination of the three elements: wick, envelope and fluid. They also perform several compatibility tests to assess the generation of non-condensable gases in the system. They conclude the following: alcohols are found non compatible with nickel wicks and steel envelopes, acetone is compatible with many materials combination at high temperature, except nickel wicks and ammonia appeared to be compatible with the LHP common materials.

Anderson et al. [102] performed a survey of life tests conducted with 30 different intermediate temperature working fluids and over 60 different working fluid/envelope combinations. Fluids including water, organic fluids, halides, sulfur and mercury were investigated. However, the temperature range, from 150 °C to 700 °C, does not have a particular interest in the scope of the present study.

The chemical compatibility has to be considered in the selection of the working fluid, because non-condensable gases may be generated in the system and modify the LHP operation. However, as explained by Mishkinis et al. [101], no consensus exists in the literature and many investigations are insufficient or contradictory. Further analyses and long-term tests are necessary to confirm the available data.

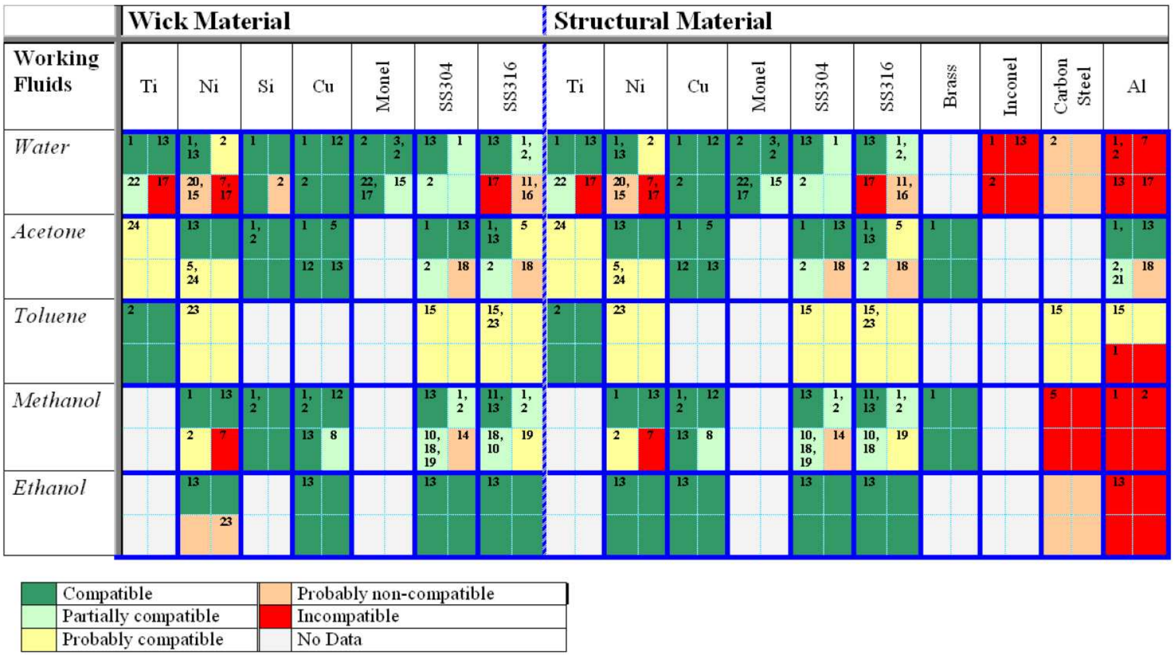

	Wick Material							Structural Material									
Working Fluids	Ti	Ni	Si	Cu	Monel	SS304	SS316	Ti	Ni	Cu	Monel	SS304	SS316	Brass	Inconel	Carbon Steel	Al
Water	🟩 1 🟩 13 ▨ 22 🟥 17	🟩 1, 13 🟨 2 🟧 20, 15 🟥 7, 17	🟩 1 🟩 🟩 🟧 2	🟩 1 🟩 12 🟩 2 🟩	🟩 2 🟩 3, 2 🟩 22, 17 ▨ 15	🟩 13 ▨ 1 ▨ 2 ▨	🟩 13 ▨ 1, 2, 🟥 17 🟧 11, 16	🟩 1 🟩 13 ▨ 22 🟥 17	🟩 1, 13 🟨 2 🟧 20, 15 🟥 7, 17	🟩 1 🟩 12 🟩 2 🟩	🟩 2 🟩 3, 2 🟩 22, 17 ▨ 15	🟩 13 ▨ 1 ▨ 2 ▨	🟩 13 ▨ 1, 2, 🟥 17 🟧 11, 16	⬜ ⬜ ⬜ ⬜	🟥 1 🟥 13 🟥 2 🟥	🟧 2 🟧 🟧 🟧	🟥 1, 2 🟥 7 🟥 13 🟥 17
Acetone	🟨 24 🟨 🟨 🟨	🟩 13 🟩 🟨 5, 24 🟨	🟩 1, 2 🟩 🟩 🟩	🟩 1 🟩 5 🟩 12 🟩 13	⬜ ⬜ ⬜ ⬜	🟩 1 🟩 13 ▨ 2 🟧 18	🟩 1, 13 🟨 5 ▨ 2 🟧 18	🟨 24 🟨 🟨 🟨	🟩 13 🟩 🟨 5, 24 🟨	🟩 1 🟩 5 🟩 12 🟩 13	⬜ ⬜ ⬜ ⬜	🟩 1 🟩 13 ▨ 2 🟧 18	🟩 1, 13 🟨 5 ▨ 2 🟧 18	🟩 1 🟩 🟩 🟩	⬜ ⬜ ⬜ ⬜	⬜ ⬜ ⬜ ⬜	🟩 1, 🟩 13 ▨ 2, 21 🟧 18
Toluene	🟩 2 🟩 🟩 🟩	🟨 23 🟨 🟨 🟨	⬜ ⬜ ⬜ ⬜	⬜ ⬜ ⬜ ⬜	⬜ ⬜ ⬜ ⬜	🟨 15 🟨 🟨 🟨	🟨 15, 23 🟨 🟨 🟨	🟩 2 🟩 🟩 🟩	🟨 23 🟨 🟨 🟨	⬜ ⬜ ⬜ ⬜	⬜ ⬜ ⬜ ⬜	🟨 15 🟨 🟨 🟨	🟨 15, 23 🟨 🟨 🟨	⬜ ⬜ ⬜ ⬜	⬜ ⬜ ⬜ ⬜	🟨 15 🟨 🟨 🟨	🟨 15 🟨 🟥 1 🟥
Methanol	⬜ ⬜ ⬜ ⬜	🟩 1 🟩 13 🟨 2 🟥 7	🟩 1, 2 🟩 🟩 🟩	🟩 1, 2 🟩 12 🟩 13 ▨ 8	⬜ ⬜ ⬜ ⬜	🟩 13 ▨ 1, 2 ▨ 10, 18, 19 🟧 14	🟩 11, 13 ▨ 1, 2 ▨ 18, 10 🟨 19	⬜ ⬜ ⬜ ⬜	🟩 1 🟩 13 🟨 2 🟥 7	🟩 1, 2 🟩 12 🟩 13 ▨ 8	⬜ ⬜ ⬜ ⬜	🟩 13 ▨ 1, 2 ▨ 10, 18, 19 🟧 14	🟩 11, 13 ▨ 1, 2 ▨ 10, 18 🟨 19	🟩 1 🟩 🟩 🟩	⬜ ⬜ ⬜ ⬜	🟥 5 🟥 🟥 🟥	🟥 1 🟥 2 🟥 🟥
Ethanol	⬜ ⬜ ⬜ ⬜	🟩 13 🟩 🟧 🟧 23	⬜ ⬜ ⬜ ⬜	🟩 13 🟩 🟩 🟩	⬜ ⬜ ⬜ ⬜	🟩 13 🟩 🟩 🟩	🟩 13 🟩 🟩 🟩	⬜ ⬜ ⬜ ⬜	🟩 13 🟩 🟩 🟩	🟩 13 🟩 🟩 🟩	⬜ ⬜ ⬜ ⬜	🟩 13 🟩 🟩 🟩	🟩 13 🟩 🟩 🟩	⬜ ⬜ ⬜ ⬜	⬜ ⬜ ⬜ ⬜	🟧 🟧 🟧 🟧	🟥 13 🟥 🟥 🟥

🟩	Compatible	🟧	Probably non-compatible
▨	Partially compatible	🟥	Incompatible
🟨	Probably compatible	⬜	No Data

Figure 1.18: Compatibility table for the working fluid, the wick and the structural material [101]

1.2.4.4 Effect of the non-condensable gases

As explained by Ku [35], non-condensable gases (NCGs) can be generated in LHPs for various reasons, according to the manufacturing process (cleaning of the envelope and the wicks, assembling of the LHP elements), the purity of the working fluid and chemical reactions during the operation, due to incompatibility between the fluid and the LHP materials (envelope, wick, transport lines, etc.). The amount of generated gases depends on the working fluid inventory, the surface area of material in contact, the time of exposure and the operating conditions. According to the author, several destinations are possible for the generated NCGs:

- it can accumulate at the compensation chamber where the flow is stagnant.
- it can accumulate in the condenser where the temperature is the lowest.
- it can be absorbed by the working fluid and circulate in the loop.
- it can be adsorbed by the envelope or wick materials.

According to Ku [35], the NCGs affect the LHP performance only if they appear as gas bubbles. In the condenser section, a high solubility likely drives the gas into the solution. Some of the remaining NCGs block part of the condenser while the rest flows to the compensation chamber. The NCGs in the reservoir induce an additional partial pressure and increase the subcooling requirement for the liquid returning from the condenser. As a result, the loop operating temperature is higher.

Nikitkin et al. [103] conducted an experimental study on NCGs effects on the LHP operation, using ammonia as working fluid. Tests are performed by injecting various amounts of hydrogen gas into the loop through the vapour line. In large quantities, NCGs increase the start-up time and the operating temperature. The measured effects are minor because a large amount of gas is absorbed by the working fluid and adsorbed by the envelope and the wick.

Recently, He et al. [104] experimentally investigated the effect of NCGs on the operation of an ammonia-stainless steel loop heat pipe with a nickel wick. The LHP is placed in a thermal-vacuum chamber and all the components are covered with multilayer insulation materials. As a most common composition of NCG, nitrogen does not react chemically with stainless steel nor ammonia and is almost insoluble in liquid ammonia, so it is selected as NCG in this study. Two inventories of nitrogen are injected into the LHP, *i. e.* $2 \cdot 10^{-5}$ mol and $4 \cdot 10^{-5}$ mol. The results show that the NCGs extend considerably the variable conductance mode range and that the temperature rise caused by the NCGs increases with reduced heat load. These effects are amplified when the heat sink temperature decreases. The operating temperature rise may also depend on the heat load cycle. The authors also observe an oscillation phenomenon that could be associated with frequent repeated processes of generation/collapse of bubbles in the evaporator core.

Singh et al. [45] conducted an experimental study on the influence of NCGs on the LHP operation. The miniature loop heat pipe is made of copper and includes a flat disk-shaped evaporator. Water is used as the working fluid. It is shown that the majority of the NCGs are generated in the first few initial runs of the loop and accumulate in the reservoir, due to stagnation conditions. It is estimated that approximately 0.0436 µg of NCG is stored in the compensation chamber in cold state at the end of the test period and results in a 3.73 kPa rise in pressure above the loop saturation pressure at room temperature. The net effect of the NCGs is an increase of the steady-state temperature, particularly at low heat loads (up to 10 °C), and a longer start-up time (Figure 1.19). However, the effects are limited and less pronounced than with conventional heat pipes. An enhancement of the performance could be performed through degassing processes.

Baumann et al. [105] present a theoretical study on LHPs where the effect of NCGs on the loop start-up is investigated. The authors assume a mass of gas trapped in the compensation chamber, that induces an additional partial pressure. The presence of NCGs increases the minimal start-up heat load of the system. Furthermore, the start-up time increases by about 50 %.

1.3 LHP steady-state modelling

In the last decade, with the development of the loop heat pipes and the need of design tools, many efforts have been devoted to propose accurate LHP models, based on a better comprehension of the phenomena occurring in the loops. These models are useful in terms of LHP sizing, optimisation and performance prediction and provide also a better understanding

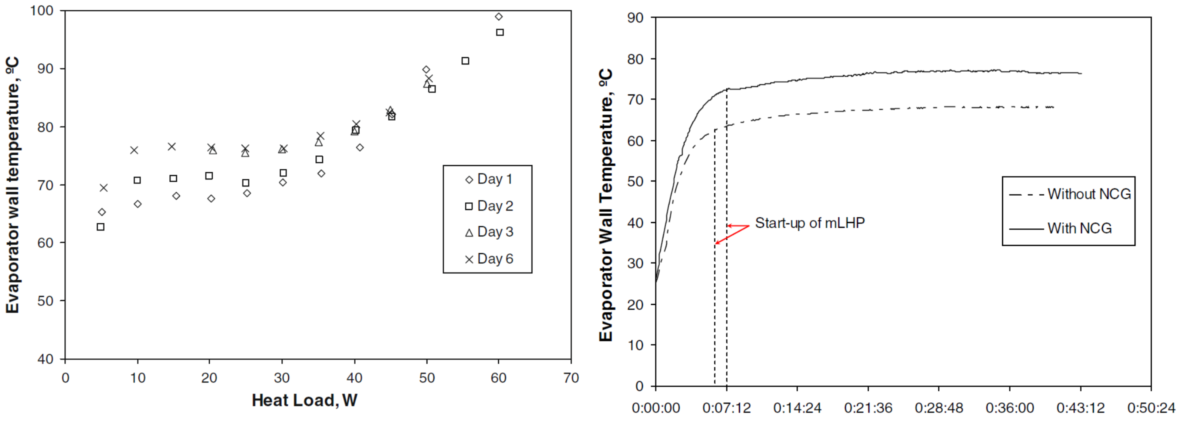

(a) Evaporator temperature trends versus heat load for a number of trial runs over a period of time

(b) Start-up trends with and without NCG

Figure 1.19: Influence of the NCGs on the steady-state and transient operation of the LHP [45]

of the couplings involved in the loop, in particular in the evaporator/reservoir structure. Most of the numerical models can be divided into two categories, corresponding on one hand to complete LHP models and on the other hand to precise evaporator descriptions. Some authors also developed an analytical approach to describe LHPs. This section is limited to steady-state modelling investigations.

1.3.1 Complete numerical LHP models

The majority of complete numerical LHP models are based on a volume element discretisation or on electrical analogies and describe the whole device as a nodal network. The links between the nodes are represented by thermal resistances or conductances and the energy balance equation is applied to each node.

Kaya et al. [106] develop a mathematical model of a loop heat pipe based on the steady-state energy balance equations at each component of the system. A cylindrical evaporator is considered. The following main assumptions are used in the development of the model:

- The heat transfer through the wick is directed only towards the radial direction.
- The compensation chamber and the evaporator core contain both liquid and vapour phases.
- The LHP reaches steady-state for a given loop condition.

The total heat load to be dissipated Q_{in} is equal to the sum of the heat rejected in the two-phase portion of the condenser (latent heat) Q_{c}, the parasitic heat leak Q_{hl} and the heat losses from the vapour line to the ambient $Q_{\text{vl-a}}$:

$$Q_{\text{in}} = Q_{\text{c}} + Q_{\text{hl}} + Q_{\text{vl-a}} \tag{1.17}$$

In the evaporator, the heat leak compensates the subcooling of the returning liquid Q_{sc} and the heat losses from the compensation chamber to the ambient $Q_{\text{cc-a}}$:

$$Q_{\mathrm{hl}} = Q_{\mathrm{sc}} + Q_{\text{cc-a}} \tag{1.18}$$

To calculate the heat leak, the authors only consider conduction through the wick, which can be written as:

$$Q_{\mathrm{hl}} = \frac{2\pi\lambda_{\mathrm{eff}}L_{\mathrm{w}}}{\ln\left(D_{\mathrm{w,o}}/D_{\mathrm{w,i}}\right)}\Delta T_{\mathrm{ac,w}} \tag{1.19}$$

where λ_{eff} is the effective thermal conductivity of the wick, L_{w} its length and $D_{\mathrm{w,i}}$ and $D_{\mathrm{w,o}}$ its inner and outer diameters, respectively. The temperature across the wick $\Delta T_{\mathrm{ac,w}}$ is the difference between the local saturation temperatures caused by the total system pressure drops $\Delta P_{\mathrm{total}}$, excluding the pressure drop in the wick structure ΔP_{w}:

$$\Delta T_{\mathrm{ac,w}} = \left(\frac{\partial T}{\partial P}\right)_{\mathrm{sat}}\left(\Delta P_{\mathrm{total}} - \Delta P_{\mathrm{w}}\right) \tag{1.20}$$

The slope of the vapour-pressure curve $(\partial T/\partial P)_{\mathrm{sat}}$ can be calculated using the Clausius-Clapeyron relation. The total pressure drops in the system consist of the frictional steady-state pressure drops in the vapour line ΔP_{vl}, the liquid line ΔP_{ll}, the condenser ΔP_{c}, a potential subcooler ΔP_{sc}, the bayonet ΔP_{bay}, the porous structure ΔP_{w} and the vapour grooves ΔP_{vgr}. If the LHP is not in horizontal orientation, the pressure difference associated with the gravity effects ΔP_{grav} also needs to be taken into account:

$$\Delta P_{\mathrm{total}} = \Delta P_{\mathrm{vl}} + \Delta P_{\mathrm{ll}} + \Delta P_{\mathrm{c}} + \Delta P_{\mathrm{sc}} + \Delta P_{\mathrm{bay}} + \Delta P_{\mathrm{w}} + \Delta P_{\mathrm{vgr}} + \Delta P_{\mathrm{grav}} \tag{1.21}$$

The authors employ single-phase correlations to calculate all the frictional pressure drops and take into account the flow regime (laminar or turbulent) in the calculation. The relevant properties of the fluid are calculated with respect to the saturation temperature T_{sat}. Two distinct correlations are used to estimate the effective thermal conductivity of the wick. To determine heat losses to the ambient, the authors test either a natural convection hypothesis or a radiative hypothesis.

The two-phase heat removal in the condenser consists of two parts: heat rejection to the sink and heat loss to the ambient (Figure 1.20). The length of the two-phase flow portion in the condenser $L_{\mathrm{c},2\varphi}$ is then given by:

$$L_{\mathrm{c},2\varphi} = Q_{\mathrm{c}}\int_{x_{\mathrm{in}}}^{x_{\mathrm{out}}} \frac{\mathrm{d}x}{(UA/L)_{\mathrm{c},2\phi}\left(T_{\mathrm{sat}} - T_{\mathrm{sink}}\right) + (UA/L)_{\mathrm{c,amb}}\left(T_{\mathrm{sat}} - T_{\mathrm{amb}}\right)} \tag{1.22}$$

where $(UA/L)_{\mathrm{c},2\phi}$ and $(UA/L)_{\mathrm{c,amb}}$ are the thermal conductance per unit length from the surface of the condenser to the heat sink and to the ambient, respectively and x is the thermodynamic quality of the flow: $x_{\mathrm{in}} = 1$ and $x_{\mathrm{out}} = 0$ if the total two-phase region is located in the condenser. The liquid temperature at the exit of the condenser is calculated by integration of the local heat balance on an elementary length of the tube dz:

$$\dot{m}c_{\mathrm{p,l}}\frac{\mathrm{d}T}{\mathrm{d}z} = (UA/L)_{\mathrm{c,amb}}\,(T - T_{\mathrm{amb}}) + (UA/L)_{\mathrm{c,l}}\,(T - T_{\mathrm{sink}}) \tag{1.23}$$

where the mass flow rate $\dot{m}$ is:

$$\dot{m} = \frac{Q_{\mathrm{c}}}{h_{\mathrm{lv}}} \tag{1.24}$$

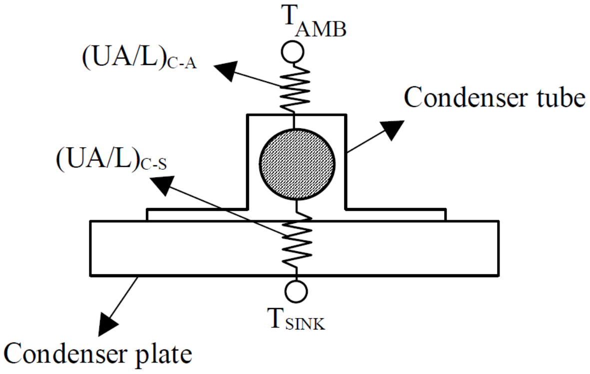

Figure 1.20: Schematic of the condenser thermal resistance network [106]

The same method is applied for the potential subcooler and for the liquid line. The subcooling of the returning liquid is thus given by:

$$Q_{\mathrm{sc}} = \dot{m}c_{\mathrm{p,l}}\,(T_{\mathrm{sat}} - T_{\mathrm{l,out}}) \tag{1.25}$$

where $T_{\mathrm{l,out}}$ is the fluid temperature at the end of the liquid line. The LHP operating temperature T_{sat} is then a function of Q_{in}, T_{sink} and T_{amb}. An iterative procedure is implemented until convergence is reached.

The authors compare their model to experimental data obtained with the GLAS LHP[3] and another loop developed for the Naval Research Laboratory (NRL). The predictions, for two distinct heat sink temperatures, are very close to the experimental results (Figure 1.21). At low powers, some discrepancies exist showing a need of a more precise consideration of the heat losses to the ambient.

The consideration of radial mass flow in the wick was added in a later paper, and new correlations for natural convection were also compared to better take into account heat losses to the ambient [108]. The authors state that the mathematical modelling of the LHP performance characteristics becomes more difficult as the size of the LHP decreases. Indeed, the low mass flow rates associated with the low power levels in small LHPs induce a longer dwelling time for the working fluid in the transport lines, despite smaller tube diameters. Therefore, the heat exchange with the surroundings becomes more important. Additionally, heat and mass transfer in small diameter tubes is less investigated and thus more difficult to predict. According to the authors, the differences between the measured and the calculated

---

[3] GLAS LHP: Geoscience Laser Altimeter System Prototype Loop Heat Pipe, purchased by the NASA in 1997 from Dynatherm Corporation [107]

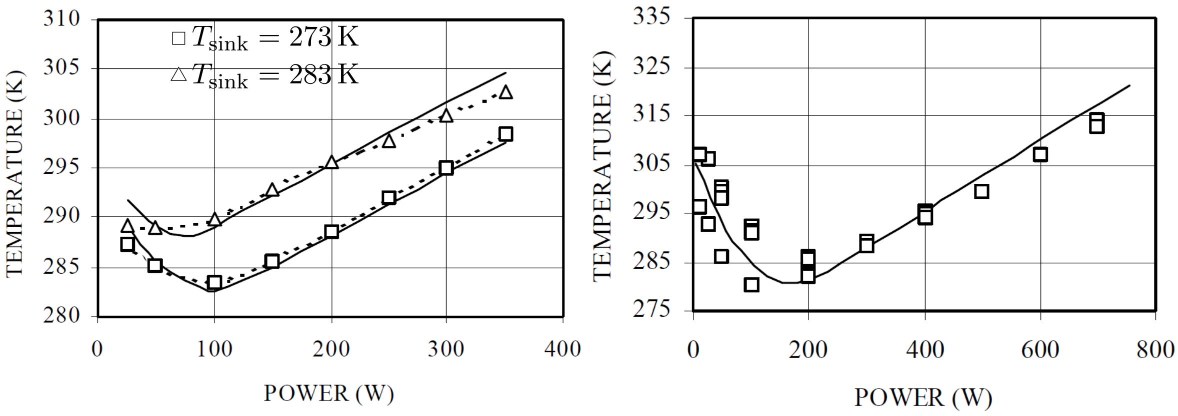

(a) Comparison with the GLAS LHP

(b) Comparison with the NRL LHP

Figure 1.21: Comparison between the mathematical model and experimental results [106]

LHP operating temperatures are mainly attributed to the inability to predict the overall effective thermal conductance across the wick.

The 1-D steady-state model of Chuang [43] is based on the energy balance equation, thermodynamic relationships and detailed heat transfer and pressure drop calculations in the liquid, vapour and condenser lines. The model includes the pressure drops induced by the bends in both the transport lines and the condenser, the convective heat transfer between the fluid and the wall in the vapour groove and both axial and radial heat fluxes in the wick. In a horizontal configuration, pressure drops in the vapour line, in the condenser, and through the wick are found to be in the same order of magnitude, except at low heat loads for which the pressure drops due to the fluid flow in the porous structure are dominant. Moreover, heat transfer in the vapour channels induces a slight superheat (several Kelvins) at the entrance of the vapour line. This study describes extensively the LHP operation in gravity-assisted conditions. When the LHP is operated at a positive elevation (condenser located above the evaporator/reservoir, evaporator/reservoir in horizontal configuration), it can operate in capillary-controlled mode or gravity-controlled mode. When the operation is controlled by the capillary forces, the vapour grooves are only filled with vapour and the total mass flow rate can directly be calculated using the heat flux dissipated by evaporation:

$$\dot{m}_{\text{total}} = \dot{m}_{\text{v}} = \frac{Q_{\text{evap}}}{h_{\text{lv}}} \tag{1.26}$$

In the gravity-controlled mode, the fluid flow in the channel becomes two-phase. The mass flow rate is therefore calculated by:

$$\dot{m}_{\text{total}} = \dot{m}_{\text{v}} + \dot{m}_{\text{l}} = \frac{Q_{\text{evap}}}{h_{\text{lv}}} + \dot{m}_{\text{l}} \tag{1.27}$$

where $\dot{m}_{\text{l}}$ denotes the liquid mass flow rate forced into the vapour groove. Additionally, the pressure gain has to be taken into account in the pressure balance equation. In the gravity-controlled mode, the pressure gain from the liquid head compensates the system total pressure drops. According to the authors' results, when the heat load is low, the LHP operates in gravity-controlled mode and the total mass flow rate in the system does not change much with the heat input. The operation is then similar to that of a thermosyphon. However, for higher heat loads, evaporation across the menisci at the outer surface of the primary wick takes place and provides the additional pressure gain required by the system (capillary-controlled mode). The elevation has a great impact on the LHP operation when the heat load is low and modifies significantly the shape of the characteristic curve. Despite interesting results, heat transfer in the evaporator and the reservoir are not precisely described and the authors stress the need of a better radial heat leak model based on heat load, temperature distribution in the primary wick, orientation, properties of the primary wick and vapour quality in the evaporator core.

Adoni et al. [109] developed a mathematical model to predict thermal and hydraulic performance of an LHP, based on conservation of mass and energy in the system. The presented model is valid for several geometries (cylindrical or flat-plate evaporator, LHP or CPL). The same general method as the one previously described is implemented. Additionally, the pressure drops across the wick are calculated using the Darcyan theory and specific correlations from the works of El Hajal et al. [110] and Thome et al. [111] as well as the Friedel correlation [112] are used to calculate the two-phase heat transfer and pressure drops in the condenser.

Their model includes the consideration of hard-filling, corresponding to a reservoir full of liquid, thus not allowing a two-phase saturation equilibrium in this loop element. In that case, the energy balance equation in the LHP core (Equation (1.18)) is solved simultaneously for the reservoir temperature and the liquid density in the reservoir. Indeed, the reservoir temperature determines both the subcooling of the liquid entering the condenser and the liquid density inside the reservoir. Thus, knowing the exact mass of working fluid in the system, it is possible to determine a reservoir temperature that provides at the same time enough subcooling and a two-phase length that is consistent with a flooded reservoir.

The authors conclude that hard-filling leads to an early fixed conductance mode, an increase of heat leaks and a reduction of the condensation length due to the expansion of the liquid.

A later study adds the consideration of the bayonet and presents the effect of the mass of working fluid on the LHP performance [113]. To take into account the presence of the bayonet, the authors add several nodes to the model (Figure 1.22).

In the evaporator core, there is a heat balance between the radial heat leak Q_{hl}, the heat from the core to the reservoir $Q_{\mathrm{c,r}}$ and the subcooling of the returning liquid:

$$Q_{\mathrm{hl}} = \dot{m} c_{\mathrm{p,54e}} (T_5 - T_{\mathrm{4e}}) + Q_{\mathrm{c,r}} \tag{1.28}$$

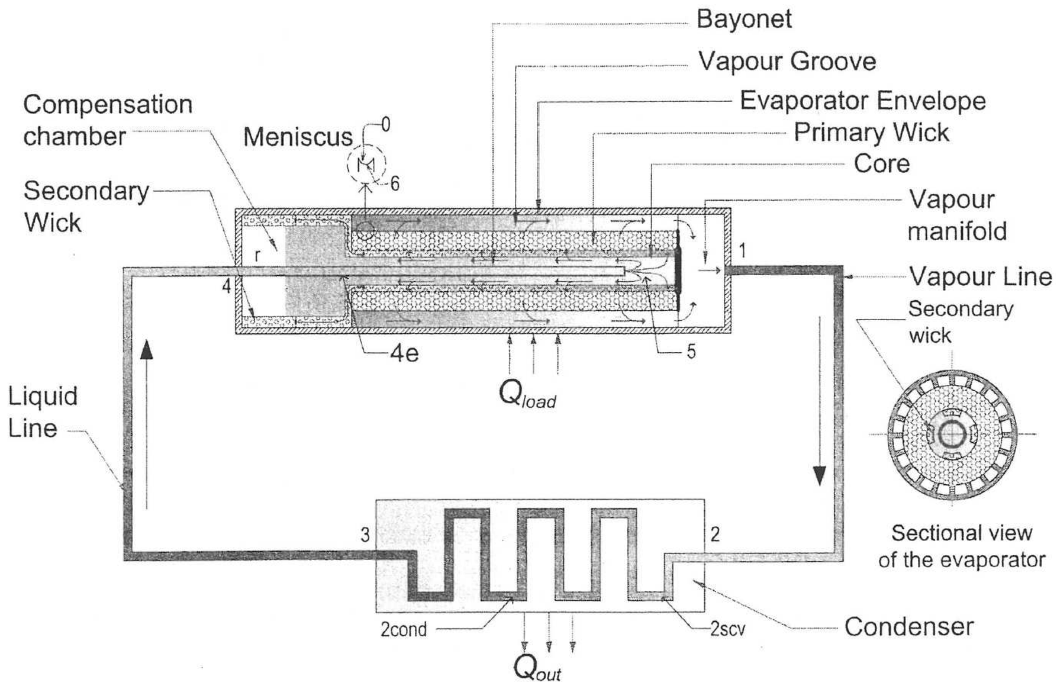

Figure 1.22: Schematic of an LHP with a cylindrical evaporator and a bayonet [113]

where $c_{\mathrm{p,54e}}$ is the mean specific heat of the working fluid between the outlet of the bayonet (5) and the inlet of the core in the bayonet ($4e$). In the reservoir, the energy balance is:

$$Q_{\mathrm{r},\infty} = Q_{\mathrm{b,r}} + Q_{\mathrm{c,r}} + Q_{\mathrm{evap,r}} \tag{1.29}$$

where $Q_{\mathrm{r},\infty}$ is the heat loss to the ambient, $Q_{\mathrm{b,r}}$ is the heat exchange between the fluid and the bayonet in the reservoir and $Q_{\mathrm{evap,r}}$ is the axial parasitic heat flux. The authors describe two distinct states of the reservoir. Indeed, the thermal coupling between the reservoir and the core strongly depends on the volume of working fluid inside the loop. If the height of liquid in the reservoir is such that vapour can exist in the reservoir tube and the core, then the reservoir has a good thermal and hydraulic coupling with the core. Otherwise, a bad thermal link exists. When a bayonet is present in the core, as cold liquid exits from it, the temperature of the reservoir is higher than that of the core which is subcooled. In case of a good thermal link, the vapour generated in the reservoir travels to the colder core where it condenses.

The authors also further studied the hard-filling phenomena and the influence of the bayonet on a hard-filled reservoir [114]. Their results show that the mass of working fluid and the bayonet have a significant influence on the LHP operation (Figure 1.23). With larger masses, the heat load at which hard filling occurs reduces, thus inducing a steep rise in the operating temperature. When a bayonet exists and the ambient temperature is higher than that of the heat sink, the superheat of the reservoir may lead to a deprime of the loop. Indeed, in such a case, the hard-filling leads to a steep rise of the liquid temperature in the reservoir compared to the core temperature. If the superheat is high enough, boiling incipience could occur and induce a major degradation or even the failure of the loop operation.

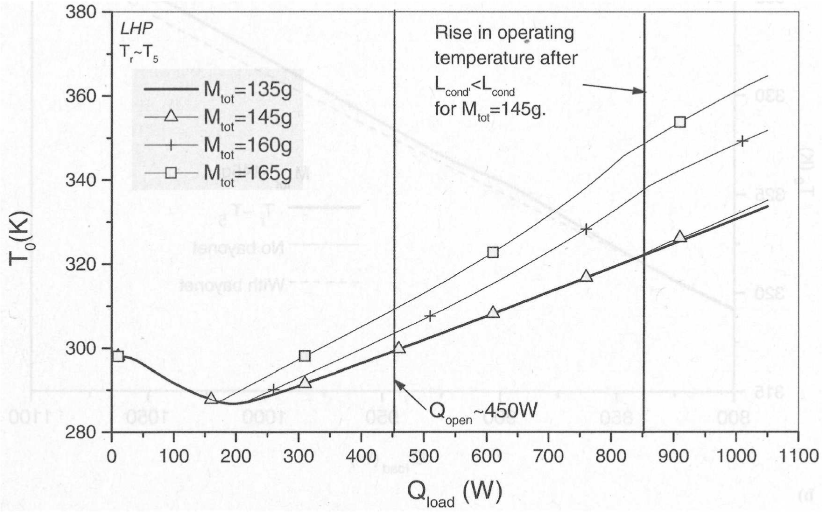

Figure 1.23: Effect of the mass of working fluid on the operating temperature (with hard-filling) [114]

Bai et al. [115] also model an LHP (with cylindrical evaporator) based on energy conservation laws. Their work shows the influence of a two-layer compound wick (Figure 1.24) and takes into consideration the liquid-vapour shear stresses in the condenser, based on an annular flow regime and considering both phases independently. The description of the two-phase region in the condenser (and in the transport lines if the two-phase zone exceeds the condenser boundaries) is obtained by finite difference solutions. The vapour quality and the pressure drops are thus obtained. The transport lines are divided into several nodes, each of which representing a certain control volume, and the calculations are conducted at each node. However, longitudinal conduction in the transport lines is neglected and the thermal conductance between the evaporator wall and the liquid-vapour interface is set in accordance with experimental results. The study also describes the behaviour of a loop with a flooded reservoir (hard-filling). Under this situation, the volume expansion of the working fluid in the reservoir results in the filling of an increasing length of the condenser when the applied heat load and the operating temperature increase. The conclusions are the same as in the work of Adoni et al. [109]. The authors also conducted a parametric analysis of a cryogenic LHP based on the same model, with the addition of secondary condenser, evaporator and compensation chamber [116].

Singh et al. [117] present a steady-state model of an LHP with a flat disk-shaped evaporator on the basis of mass and energy conservation principles for several control volumes. Single-phase flow correlations are used in the condenser and heat losses to the ambient are neglected. A condenser model is developed to take into account the fin-and-tube geometry of the condenser. A global description is presented, defining an overall surface efficiency of the fin array and a log mean temperature difference from the fin surface to the ambient air. The

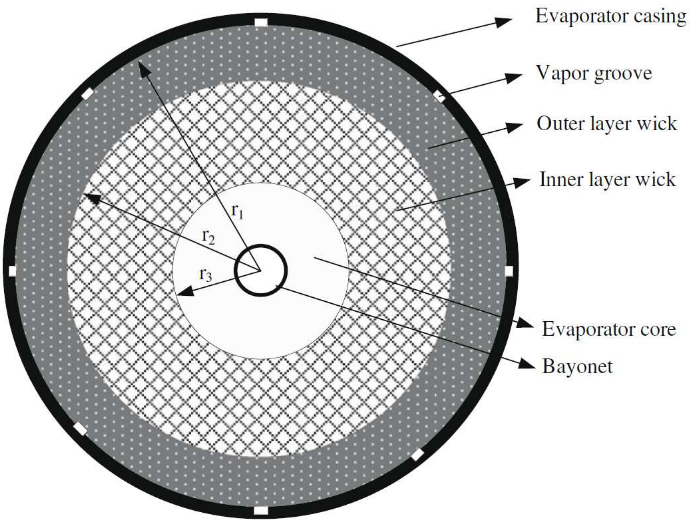

Figure 1.24: Schematic of the cross-section of a two-layer compound wick [115]

surface temperature of the fin array is considered uniform and equal to the temperature of the condenser tube. An acceptable agreement with the experimental data is found with a nickel wick. However, a rather large difference is observed between the calculated performance for a copper wick and the experimental results. According to the authors, this is probably due to the shortcoming of the model to consider accurately the heat and mass transfer inside the evaporation zone.

Rivière et al. [84] present a complete numerical model of LHP in order to study the influence of the fluid mass distribution in a loop with a flat evaporator. The model is based on a classic nodal network for the consideration of heat transfer in the evaporator/reservoir. However, the vapour grooves, the transport lines and the condenser are discretized into small elements and two energy balance equations are applied on each element, one for the solid wall and one for the fluid. Such a distinction between the wall and the fluid temperatures is the main original feature of this model (Figure 1.25). It enables to take into account the temperature variation in the vapour grooves and in the vapour line, as well as the longitudinal conduction through the transport line walls. Furthermore, the possible occurrence of fluid condensation in the vapour line as well as a vapour desuperheating zone in the condenser are considered. The authors show that vapour starts to condensate in the vapour line, due to heat losses to the ambient. They also investigate the influence of the transport line wall thermal conductivity and the fluid mass distribution in the LHP during operation.

Hodot et al. [118] developed a global LHP model, combining a fine three-dimensional description of the evaporator/reservoir and a monodimensional thermo-hydraulic model of the transport lines and the condenser. The 3D heat transfer equation is solved using the *OpenFOAM* software and results are presented for a cylindrical geometry. Convective heat transfer is taken into account inside the reservoir, in the grooves, as well as in the porous medium. The 1D nodal model of the transport lines is based on the work of Rivière et al. [84], enabling the consideration of the longitudinal conduction in the transport lines. The authors

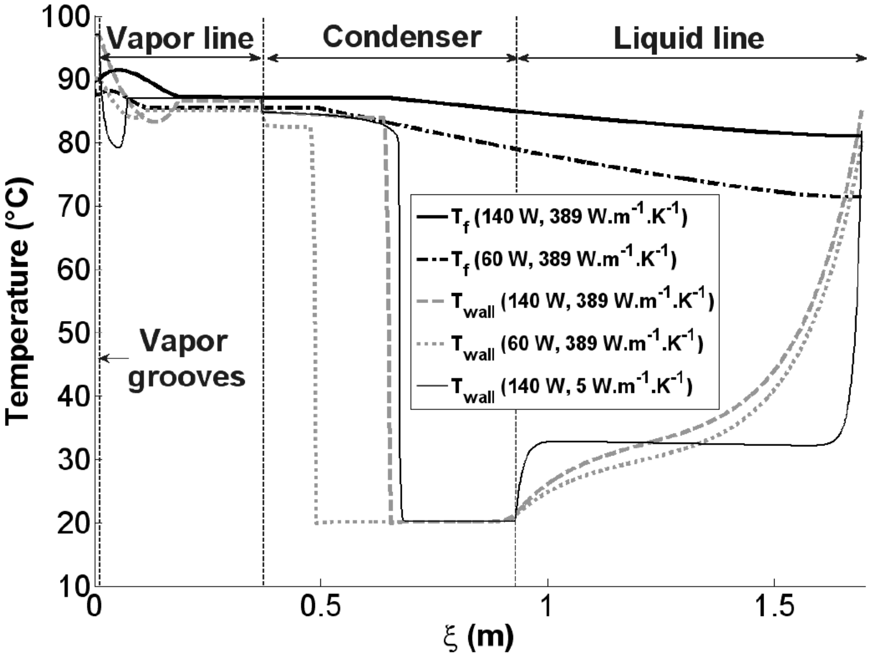

Figure 1.25: Fluid and wall temperatures along the LHP [84]

use the simulations to optimise the saddle shape design (Figure 1.26) and the vapour grooves number and location. Such a complete model associates a thorough modelling of heat and mass transfer in the transport lines and the condenser with a fine 3D thermal description of the evaporator/reservoir, thus enabling an accurate consideration of the parasitic heat losses during operation.

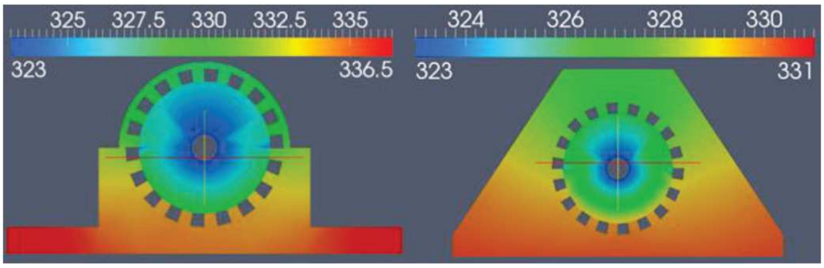

Figure 1.26: Optimisation of the saddle shape [118]

Several other global numerical steady-state models can be found in the literature [25, 27, 119–123]. They are summarised in subsection 1.3.4.

1.3.2 Numerical evaporator models

Many numerical LHP models can be found in the literature and are useful tools for the design and optimization of LHPs as well as for a better understanding of the coupled phenomena involved in the LHP operation. However, these models are limited and their major restriction lies in an inaccurate modelling of the phenomena occurring in the evaporator/reservoir. Indeed, heat transfer inside the evaporator as well as heat losses to the ambient have a decisive influence on the loop operation, particularly at low heat loads. As explained in subsection 1.2.1, heat and mass transfer between the components constituting the evaporator reservoir (the evaporator casing, the wick, the reservoir wall, the liquid pool inside the reservoir and the vapour grooves) must be evaluated accurately. These heat fluxes depend on numerous parameters: groove design, effective thermal conductivity of the wick, evaporation heat transfer, thermal conductivity of the evaporator envelope material, thermohydraulic properties of the fluid, etc. As a consequence, thorough studies have been undertaken to model heat transfer in the evaporating region, in the wick, or in the entire evaporator/reservoir.

Several theoretical analyses specifically investigate the development of a vapour zone inside the porous medium [33, 68, 124–127]. These studies, based on continuum models or pore-network simulations, focus on heat and mass transfer inside the wick in order to evaluate the size and the shape of a potential liquid-vapour interface inside the porous structure. This topic will be further detailed in the next section.

Li and Peterson [128] developed a three-dimensional steady-state model of a square flat evaporator with a fully saturated wick structure. The computational domain includes the liquid bulk of the reservoir, the wick, a groove and a metallic substrate where the heat input is imposed (Figure 1.27). The 3D governing equations for the heat and mass transfer (continuity, Darcy and energy) are developed. A temperature boundary condition is adopted at the liquid-vapour interface, assuming a perfect evaporation rate. Furthermore, no thermal resistance is taken into account for the contact between the envelope and the wick. In order to expedite the convergence of the calculations, a line-by-line iteration and a Tridiagonal Matrix Algorithm along with a Thomas algorithm solver, and successive under-relaxation iterative methods are used to obtained the three-dimensional temperature distribution. The temperature and pressure distributions in the wick are discussed and the velocity field is investigated. The highest heat flux occurs in the wick-fin-groove corner, confirming the results of Demidov and Yatsenko [129]. Furthermore, the results show that the temperature difference is not significant along the axial direction of the groove. Thus, a two-dimensional assumption is acceptable in the modelling of the evaporator.

Zhang et al. [79] also developed a 3D model of a flat evaporator of an LHP. However, in that case, the reservoir is adjacent to the wick (Figure 1.9c). Thus, the liquid flow entering the wick is perpendicular to the heat flux imposed at the evaporator wall. The computational domain is approximately the same as in the work of Li and Peterson [128] (Figure 1.28). The wick is considered to be fully saturated with liquid. The fluid flow in the wick and in the groove are determined based on the equations of continuity, energy, momentum and Darcy. Heat conduction is also computed in the wall region. No heat losses to the ambient nor from the wall to the reservoir are considered. The boundary conditions for the wick region are the reservoir temperature on one side and the saturation temperature of the vapour groove at the liquid-vapour interface. The thermal contact between the wall and the wick is considered perfect. A finite volume method is introduced to solve the problem.

The flow and temperature fields in the wick and the structural optimisation of the evaporator (location and shape of the grooves) are discussed (Figure 1.29). The results show that

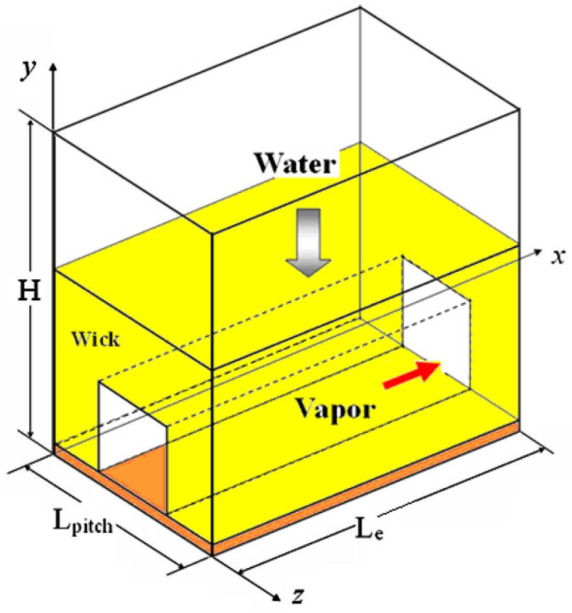

Figure 1.27: View of the computational domain [128]

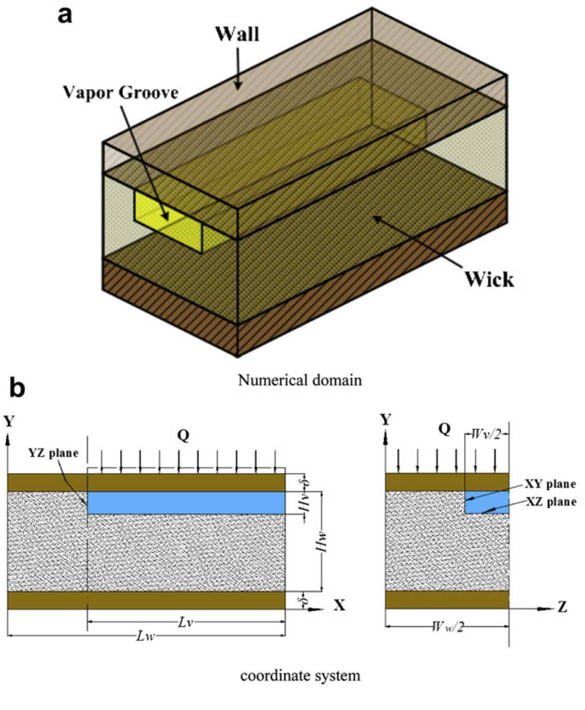

Figure 1.28: Numerical domain and coordinate system [79]

the temperature at the top of the wall increases smoothly in the axial direction of the groove. Due to the effect of evaporation, the temperature is higher in the wick than at the interface between the wick and the vapour groove. The liquid flowing through the wick is superheated before reaching the evaporation zone. The pressure drop induced by the flow in the wick is only of 129 Pa when the heat load is equal to 80 W ($10\,\mathrm{W\cdot cm^{-2}}$). An investigation is also made about the location and the geometrical characteristics of the vapour grooves. Two types of evaporators are compared: one with the vapour grooves machined inside the wick (Figure 1.29b) and another with the grooves inside the wall (Figure 1.29c). When the groove is located inside the wall, the evaporating interface is only located at the bottom of the vapour groove, which results in larger temperature gradients in the wick, a higher superheat of the liquid inside the capillary structure and a higher temperature of the evaporator heating wall. The authors also conclude that the best results are achieved with square grooves (ratio height-width equal to 1) and with a width ratio fin-groove ranging from 0.5 to 1.

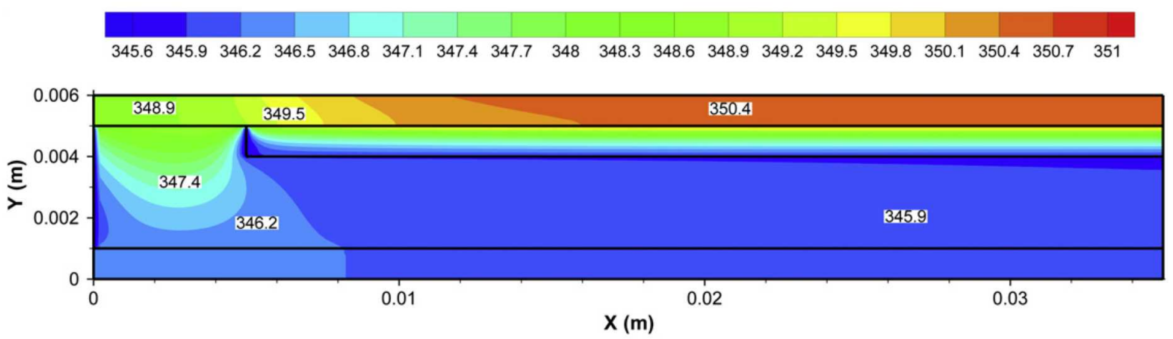

(a) Temperature contours along the axial direction

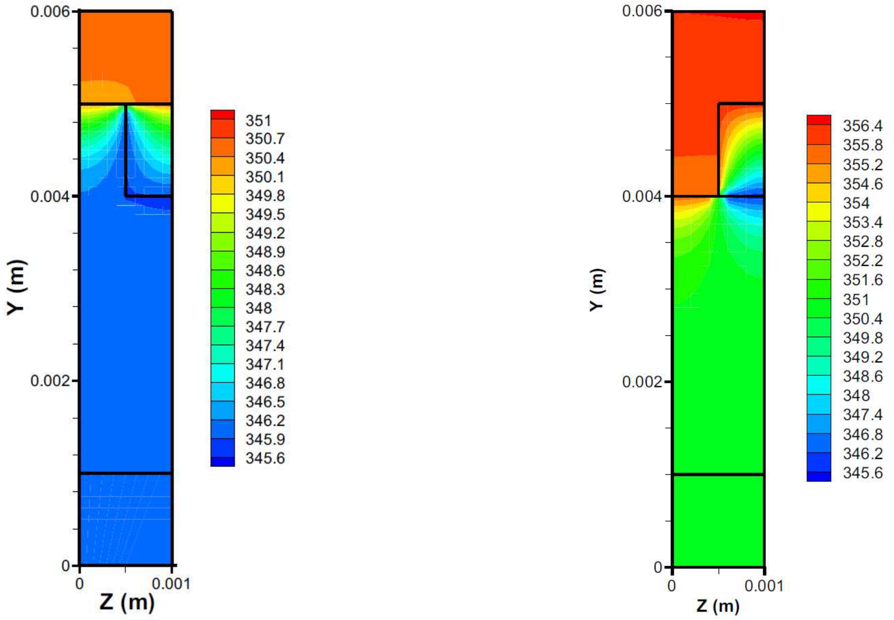

(b) Temperature field with grooves in the wick (c) Temperature field with grooves in the wall

Figure 1.29: Temperature field in the flat evaporator [79]

Chernysheva and Maydanik [130] present a 3D mathematical model of a complete flat LHP evaporator with the reservoir adjacent to the porous structure. All the main structural elements of the evaporator/reservoir are included in the model: body, wick, vapour grooves, barrier layer and compensation chamber (Figure 1.30). The three-dimensional heat equation is solved for the entire evaporator. The authors consider a finite evaporation heat transfer, thermal contact resistance between the wick and the body and the drying of the wick surface, based on the nucleation theory. If the local liquid superheat in the pores is larger than a calculated nucleation superheat, the wick surface is considered dry and no evaporation occurs at this particular spot. Due to the agitation ensured by the liquid that arrives from the liquid line, the fluid inside the compensation chamber is considered at a uniform temperature. A finite difference method is computed to solve numerically the problem. The model adequately describes thermal processes in the evaporator and the specific character of a one-sided heat load supply. The authors obtain the 3D temperature field in the entire evaporator as well as the velocity fields in the grooves (Figure 1.30). The results show a nonuniformity of the evaporation rate in the entire active zone. Indeed, there are low-evaporation zones owing to the insufficient heating of the peripheral sections of the evaporator. The vapour grooves located in the centre of the active zone contribute mainly to the evaporation process. However, at high heat fluxes, large superheats and a potential drying of the wick may lead to a larger activation of the evaporation processes in the peripheral sections. About 90 % of the total heat load is dissipated through evaporation.

Chernysheva and Maydanik [46] further discuss the temperature distribution in the evaporator and different phases of the wick drying process for uniform and concentrated heating, based on the same model. A uniform heating means that the whole active zone is heated whereas in the case of concentrated heating, the heater occupies a small part of the active zone. Another paper presents calculations for the heat and mass transfer in the compensation chamber of the same evaporator and the intensity of internal heat exchange in the reservoir depending on its orientation [131]. The authors model heat and mass transfer processes in the entire evaporator/reservoir using the software *EFD.Lab*[4]. They obtain the temperature field in the evaporator and the velocity field in the compensation chamber. The latter is considered completely filled with liquid. A constant heat transfer coefficient with the ambient is assumed. A constant mass flow rate is taken into account for the entrance into the bayonet as well as for the interface between the wick and the liquid bulk. Furthermore, the surface of the vapour grooves is set at a constant temperature. The results show that the influence of the gravity is significant on the heat and mass transfer in the reservoir. The local heat transfer coefficient in the liquid pool of the reservoir can reach $600\,\mathrm{W \cdot m^{-2} \cdot K^{-1}}$ close to the wick at high heat loads (Figure 1.31). The value of the mean heat exchange coefficient in the compensation chamber is about $140\,\mathrm{W \cdot m^{-2} \cdot K^{-1}}$ at high heat flux ($Q_{\mathrm{in}} = 500\,\mathrm{W}$).

All the previous described numerical analyses give a better understanding of the phenomena involved in the evaporator of a loop heat pipe. Parasitic heat transfer, heat exchange between the evaporator wall and the grooves, heat and mass transfer in the wick, in the vapour grooves and in the compensation chamber as well as the characterisation of the evaporation zone are investigated. These numerical studies show the complexity of heat and mass transfer in a loop evaporator and are a useful tool for improving the design and the manufacturing of LHPs. However, the operating parameters of the model (temperature of the liquid returning to the condenser, pressure difference between the groove and the reservoir)

---

[4] EFD.Lab: a computational fluid dynamics formerly distributed by NIKA GmbH. The latest version, called FloEFD™, is distributed by Mentor Graphics®

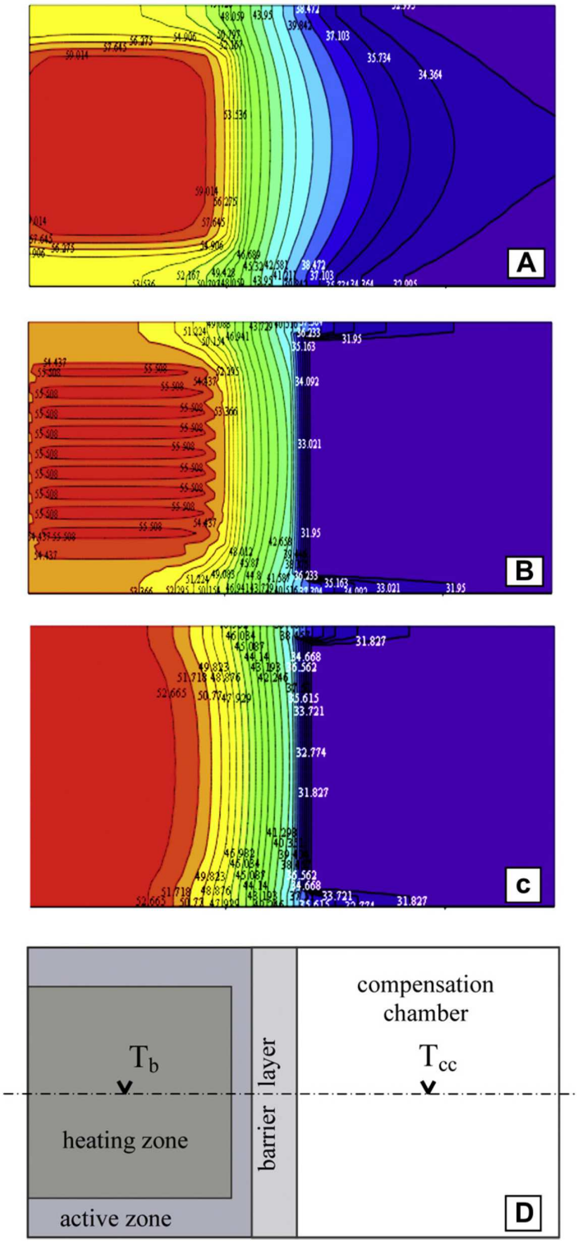

Figure 1.30: Temperature field with $Q_{\text{in}} = 400\,\text{W}$; A - top surface of the body, B - at level of half the groove depth, C - at level of half the evaporator thickness, D - evaporator view from above [130]

are either arbitrarily set or coupled with a very simplified loop model. Therefore, there is a lack of knowledge concerning the influence of the phenomena occurring in the evaporator on the entire system operation.

1.3.3 Analytical studies on LHPs

Following increasing computational resources, the major part of the modelling efforts focus on developing models using various numerical methods. Few research works present analytical

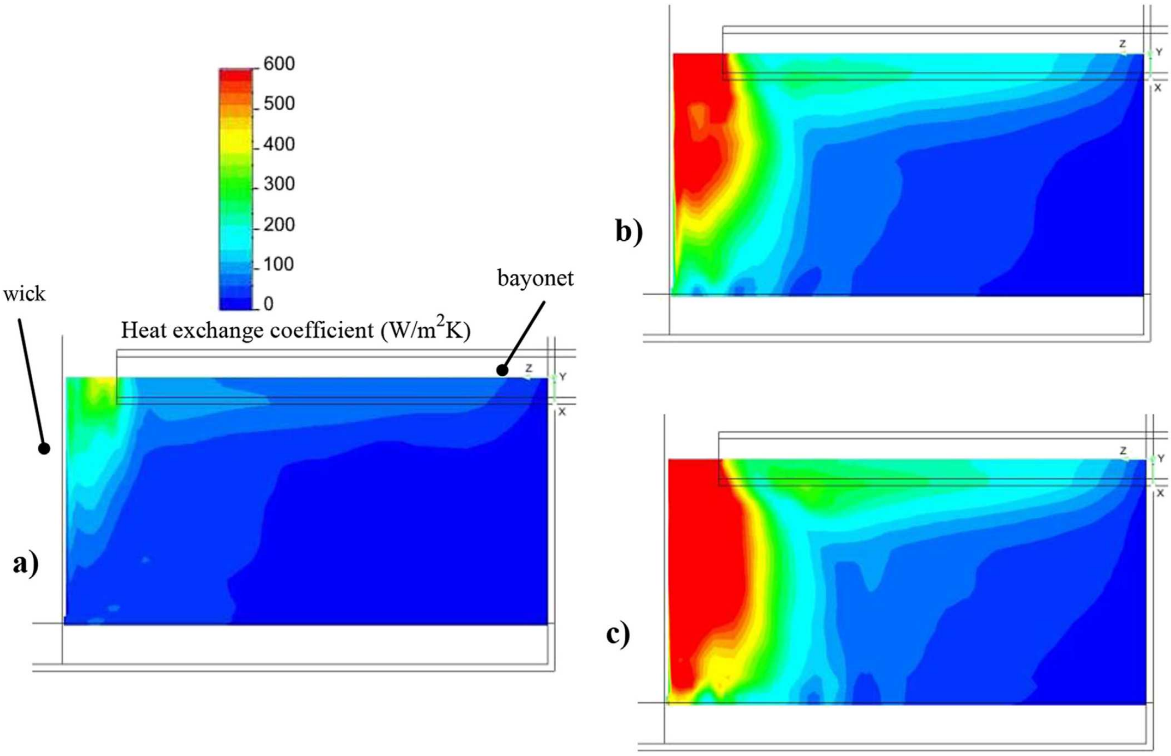

Figure 1.31: Heat transfer coefficient field at different heat loads: a) 100 W, b) 300 W, c) 500 W [131]

models of LHPs, in which the operating parameters (temperature, pressure drops, mass flow rate, etc.) can be explicitly determined, without the need of any numerical scheme. However the analytical approach does not necessitate large numerical resources and can be easily implemented in a simple software. Therefore, it can be a powerful tool for the design and optimisation of loop heat pipes.

According to Launay et al. [6], Maydanik et al. [132] developed an analytical model with a closed-form solution based on an energy balance in the reservoir and the pressure balance in the overall loop. The radial parasitic heat transfer through the cylindrical wick was taken into account, but the axial heat flux and the heat losses to the ambient were neglected. Assuming low heat losses from the liquid line and a heat load equal to the heat dissipated by evaporation, the following simplified expression was given:

$$T_{\mathrm{v}} = T_{\mathrm{c,o}} + (T_{\mathrm{r}} - T_{\mathrm{c,o}}) \left(\frac{D_{\mathrm{w,o}}}{D_{\mathrm{w,i}}}\right)^{\dfrac{Q_{\mathrm{in}} c_{\mathrm{p,l}}}{2\pi \lambda_{\mathrm{eff}} L_{\mathrm{w}} h_{\mathrm{lv}}}} \tag{1.30}$$

where T_{v}, T_{r} and $T_{\mathrm{c,o}}$ are the temperatures in the vapour grooves, in the reservoir and at the end of the condenser, respectively. $D_{\mathrm{w,o}}$ and $D_{\mathrm{w,i}}$ are the outer and inner diameters of the wick, respectively and L_{w} its length. In this closed-form solution, predicting the vapour temperature requires the knowledge of the temperatures at the condenser outlet and in the reservoir. Therefore, this expression cannot be directly used to express the LHP thermal operation based on its geometrical characteristics.

Cao and Faghri [133] present an analytical work for the heat and mass transfer in a rectangular capillary porous structure with partial heating and evaporation on the upper surface (Figure 1.32a). This geometry can be directly related to the evaporator of a CPL or an LHP. Based on symmetry assumptions, the authors use the method of separation of variables to determine solutions in the form of Fourier series. The sides of the computational domain are considered adiabatic, the bottom boundary condition is a set temperature and the upper boundary condition is a heat input on one side and a heat output on the other side. Therefore, analytical solutions for the liquid pressure, velocity and temperature fields in the porous structure are obtained (Figure 1.32).

The results show the maximum temperature at the upper left-hand corner, under the fin. High temperature gradients are expected near the upper limit, whereas the temperature field is more uniform at the bottom. Concerning mass transfer, the liquid flows vertically into the porous structure and remains nearly one-dimensional until reaching the middle section of the wick.

Furukawa [134] present a design-oriented analytical description of an LHP. His approach is very original and aims at optimising the design of the LHP in given operating conditions. The initial hypothesis is the knowledge of a design-specified operating temperature. The author solves the heat and mass transfer equations in the cylindrical evaporator. Pressure losses in the loop and heat transfer in the condenser are calculated as a function of the geometrical properties of the system. Several performance indices are defined (number of transfer units, temperature effectiveness, critical Bond number, pump efficiency) in order to improve the design of the LHP. Based on the operating temperature and on the geometrical and thermo-hydraulic characteristics of the loop, all the design parameters (wick thickness, transport lines diameter, wick pore radius and porosity, reservoir volume, condenser length) are evaluated. The paper presents several charts to optimise the design characteristics of the LHP. This study is a useful tool in the sizing of the LHP components based on temperature constraints. However, in many cases, the operating temperature is not necessarily the operating limit and is, as such, not *a priori* known.

Chernysheva et al. [27] present an analytical investigation of two compensation chamber operating modes, either the hard-filling or the two-phase state. Based on the thermodynamic relationship between the liquid-vapour interfaces in the groove and in the condenser or in the reservoir, the authors develop an analytical expression of the operating temperature T_{ev}. In case of hard-filling, the evaporator temperature is equal to:

$$T_{\mathrm{ev}} = T_{\mathrm{sink}} + \left(\frac{1}{\alpha_{\mathrm{cond,ext}} S_{\mathrm{cond,ext}}} + R_{\mathrm{cond,body}} + \frac{1}{\alpha_{\mathrm{cond,int}} S_{\mathrm{cond,int}}} + \sum_{i} W_{\mathrm{i}} F n_{\mathrm{i}} + \frac{1}{\alpha_{\mathrm{ev}} S_{\mathrm{q}}} \right) Q_{\mathrm{load}} \tag{1.31}$$

where T_{sink} is the heat sink temperature and $\alpha_{\mathrm{cond,ext}}$, $\alpha_{\mathrm{cond,int}}$ and α_{ev} are the heat transfer coefficient at the external side of the condenser, at the internal side of the condenser and

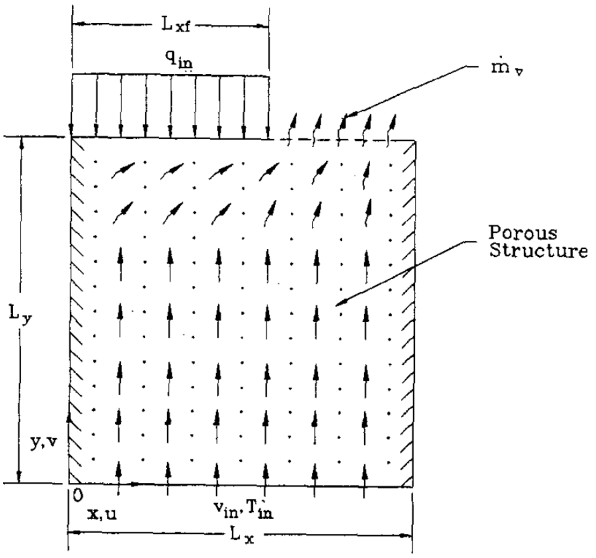

(a) Modelling domain

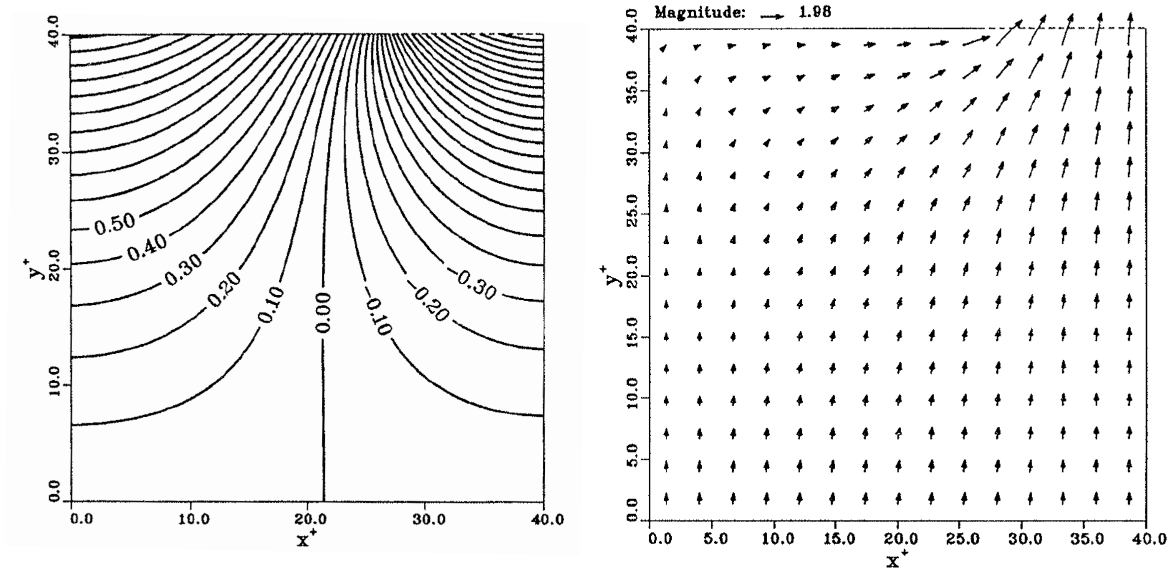

(b) Isotherms in the porous wick

(c) Velocity vectors in the wick

Figure 1.32: Analytical heat and mass transfer in the wick [133]

in the evaporation zone, respectively. $S_{\mathrm{cond,ext}}$ and $S_{\mathrm{cond,int}}$ correspond to the external and internal surface areas of the condenser, respectively and S_{q} is the evaporator surface area where heat is supplied. Q_{load} is the total heat load to be dissipated by the loop, $R_{\mathrm{cond,body}}$ is the thermal resistance of the condenser wall and W_{i} and Fn_{i} are the coefficients taking into account the geometrical and thermophysical parameters in the calculation of pressure drops in the vapour line. In the case of an existing liquid-vapour interface inside the compensation chamber, the equation is modified to:

$$T_{\mathrm{ev}} = T_{\mathrm{cc}} + (\Delta P_{\mathrm{v}} + \Delta P_{\mathrm{l}} + \Delta P_{\mathrm{g}}) \left.\frac{\mathrm{d}T}{\mathrm{d}P}\right|_{T} + \frac{Q_{\mathrm{load}}}{\alpha_{\mathrm{ev}} S_{\mathrm{q}}} \tag{1.32}$$

where T_{cc} is the temperature in the compensation chamber, and ΔP_{v}, ΔP_{l} and ΔP_{g} are the pressure drops in the vapour line, in the liquid line, and due to the gravity, respectively. Despite providing a simple expression of the evaporator temperature, this development shows two main limitations. Firstly, in the case of a saturated reservoir, the operating temperature is a function of the compensation chamber temperature, which is *a priori* not known. Secondly, several major assumptions are made: heat losses to the ambient, parasitic heat transfer, two-phase pressure drops and heat transfer in the transport lines are neglected. Such hypotheses may lead to a large inaccuracy in the operation prediction.

Launay et al. [6] develop closed-form solutions linking the LHP operating temperature to various fluid properties and geometrical parameters. Based on an energy balance on each LHP component and on thermodynamic equations (Figure 1.33), the reservoir temperature T_{r} can be predicted for both the variable and the fixed conductance modes:

$$\text{VCM} \qquad T_{\text{r}} = \frac{T_{\text{sink}} + \dfrac{h_{\text{lv}}}{c_{\text{p,l}}}\left[\dfrac{R_{\text{E}}}{R_{\text{wall}}} + \dfrac{T_{\text{A}}}{R_{\text{A}} Q_{\text{in}}}\right] + (T_{\text{A}} - T_{\text{sink}})\left[1 - \exp\left(-\dfrac{\pi D_{\text{L}} L_{\text{L}} K_{\text{L}} h_{\text{lv}}}{Q_{\text{in}} c_{\text{p,l}}}\right)\right]}{1 - \dfrac{1}{Q_{\text{in}}}\left[\dfrac{1}{\rho_{\text{v}} c_{\text{p,l}}}\left(\dfrac{1}{R_{\text{w}}} + \dfrac{1}{R_{\text{wall}}}\right)(\Delta P_{\text{v}} + \Delta P_{\text{l}} - \Delta P_{\text{g}}) - \dfrac{h_{\text{lv}}}{c_{\text{p,l}} R_{\text{A}}}\right]} \tag{1.33}$$

$$\text{FCM} \qquad T_{\text{r}} = T_{\text{sink}} + \frac{Q_{\text{in}}}{\pi D_{\text{C,i}} L_{\text{C}} K_{\text{C}}} \frac{1 + \dfrac{R_{\text{E}}}{R_{\text{wall}}}\dfrac{K_{\text{C}}}{K_{\text{sub}}}}{1 + \dfrac{R_{\text{E}}}{R_{\text{wall}}}} \tag{1.34}$$

In these expressions, K_{C}, K_{sub} and K_{L} are global conductances defined in Figure 1.33 and R_{E}, R_{w} and R_{wall} are evaporator resistances defined in the same figure. L_{L} and L_{C} are the lengths of the liquid line and of the condenser, respectively, and D_{L} and $D_{\text{C,i}}$ their respective diameters. R_{A} is the thermal resistance that represents heat losses of the reservoir to the ambient at temperature T_{A}. Additionally, simple analytical solutions of the heat load corresponding to the transition between both modes are expressed. The effect of the geometrical parameters and fluid thermophysical properties on the LHP operation are clearly highlighted. However, the identification of the evaporator thermal resistance needs to be adjusted to experimental data or may require an additional evaporator accurate model.

Boo and Jung [135] conduct a theoretical modelling of a loop heat pipe with a flat evaporator. Based on a nodal network of the evaporator and of energy balance at each node of the system, the authors predict the temperatures of each component. The profile and the temperature of the liquid-vapour interface in the pores were expressed using the thin-film theory. The evaporation heat transfer coefficient is then dependent on the accommodation coefficient and on the heat conduction through the liquid film to the vapour. Transversal heat losses are also taken into account and a heat exchanger classical NTU method is used for the modelling of the condenser. However, no closed-form solution of the operating temperature is given in the paper. Furthermore, longitudinal parasitic heat losses are not considered and the reservoir is assumed to be filled with liquid during operation, which does not necessarily

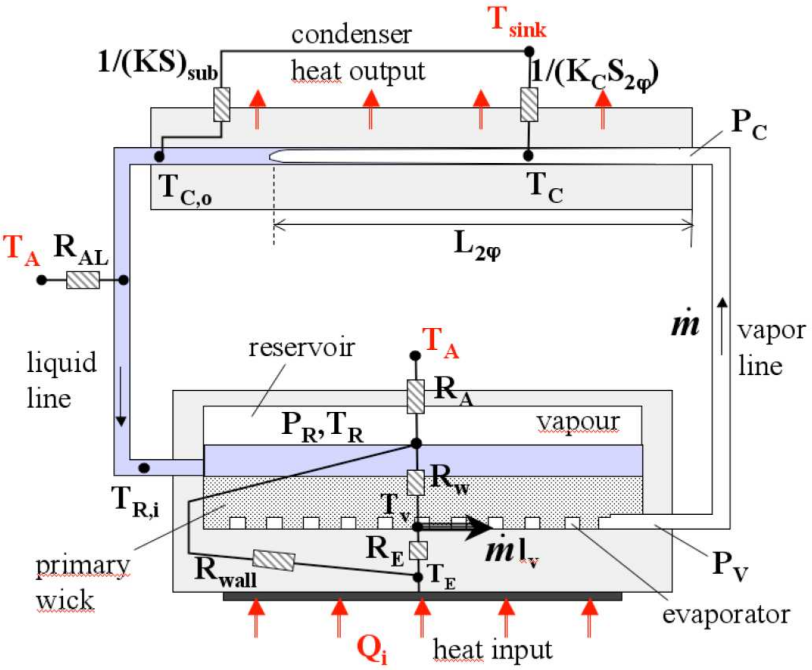

Figure 1.33: LHP thermal resistance network [6]

correspond to an actual LHP operation.

1.3.4 LHP modelling synthesis

Table 1.4 and Table 1.5 summarize the main steady-state modelling works of LHPs published in the past years. This survey considers both the complete models and the partial evaporator models. However, transient analyses were omitted, since they are not in the scope of the present study.

As presented in this section, many theoretical works about LHPs have been undertaken in the past 15 years. Most of them are numerical analyses, based on nodal networks or on finite difference methods, whereas few analytical studies are developed. Specific codes for LHPs have been extensively developed in the past years, including more features and considering more accurately the physical phenomena involved in the loops. However, there are still only few studies that show a complete description of the LHP with a precise consideration of heat and mass transfer in the evaporator/reservoir structure, despite its major significance on the loop operation. This conclusion is a consequence of the complexity of the phenomena occurring in loop heat pipes.

This summary also shows the development of three-dimensional models in the recent years, following the availability of larger computational resources. Flat evaporators have also been more investigated in the last years and show the gain of interest for this geometry of evaporator. The partial drying of the wick and the hard-filling are phenomena that have been seldom considered. However, most of the models investigate intensively heat and mass transfer in the transport lines and the condenser.

Authors	Year	Complete LHP	Partial modelling	3D analysis	2D analysis	1D analysis	Nodal network	Analytical solution	Cylindrical geometry	Flat (reservoir in the thickness)	Flat (reservoir adjacent to the evaporator)	Axial/longitudinal parasitic heat flux	Radial/transversal parasitic heat losses	Contact resistance body-wick	Concentrated heat flux	Convection in the wick	Drying of the wick	Secondary/biporous wick	Bayonet	Heat transfer reservoir-casing	Hard-filling	Finite evaporation coefficient	Infinite evaporation coefficient (set temperature)	Pressure drop in the vapour grooves	Heat transfer in the vapour grooves	Longitudinal conduction in the tubes	Single-phase pressure drops	Two-phase pressure drops	Flow regime	Condensation regime	Homogeneous model	Separated phases model	Condensation in the transport lines	Gravity effects	Non-condensable gases	Evaporator heat losses	Transport lines heat losses	Multiple evaporator/condenser
Kaya et al. [106]	1999	x	-	-	-	-	x	-	x	-	-	-	x	-	-	-	-	-	-	-	-	-	-	x	-	-	x	-	x	-	-	-	x	x	-	x	x	-
Figus et al. [68]	1999	-	x	-	x	-	-	-	x	-	-	-	-	-	-	-	x	-	-	-	-	-	x	-	-	-	-	-	-	-	-	-	-	-	-	-	-	-
Cullimore and Baumann [119]	2000	x	-	-	-	-	x	-	-	-	-	-	x	-	-	x	-	-	-	-	-	-	-	-	-	-	x	x	x	x	x	x	x	x	x	-	x	-
Delil et al. [136]	2002	x	-	-	-	-	x	-	-	-	x	x	x	x	-	-	-	-	-	x	-	-	-	-	-	-	x	x	x	-	x	-	-	x	-	x	x	-
Kim and Golliher [25]	2002	x	-	-	-	-	x	-	-	x	-	-	x	-	-	-	-	-	-	-	-	-	-	-	-	-	x	x	x	x	-	x	-	x	-	x	-	-
Hamdan [44]	2003	-	x	-	-	x	-	-	-	x	-	-	x	-	-	x	-	-	-	-	-	-	x	-	-	-	-	-	-	-	-	-	-	-	-	-	-	-
Chuang [43]	2003	x	-	-	-	x	-	-	x	-	-	x	x	-	-	x	-	-	-	-	-	-	x	-	x	-	x	x	x	x	-	x	-	x	-	x	x	-
Hoang and Ku [137]	2003	x	-	-	-	-	x	x	-	-	-	-	x	-	-	-	-	-	x	x	-	x	-	x	-	-	x	x	x	x	-	-	-	-	-	x	x	-
Hoang et al. [138]	2004	x	-	-	-	-	x	-	x	-	-	-	x	-	-	x	-	-	-	-	-	-	-	-	-	-	x	x	x	x	-	x	-	-	-	x	-	x
Ghajar et al. [121]	2005	x	-	-	x	-	x	-	-	-	x	x	-	-	-	-	-	-	-	-	-	-	-	x	-	-	x	x	-	-	-	-	-	-	-	-	-	-
Kaya and Goldak [33]	2006	-	x	-	x	-	-	-	x	-	-	-	-	-	-	x	x	-	-	-	-	x	-	-	x	-	-	-	-	-	-	-	-	-	-	-	-	-
Furukawa [134]	2006	x	-	-	-	-	-	x	x	-	-	-	x	-	-	x	-	x	x	-	-	-	x	x	-	-	x	x	-	-	-	x	-	-	-	x	-	-
Coquard [124]	2006	-	x	-	x	-	-	-	x	-	-	-	-	-	-	x	x	-	-	-	-	-	x	-	x	-	-	-	-	-	-	-	-	-	-	-	-	-
Atabaki [139]	2006	x	-	-	-	-	x	-	x	x	-	-	x	-	-	-	-	-	-	-	-	-	x	x	x	-	x	x	x	x	-	x	x	x	-	x	x	-
Adoni et al. [109]	2007	x	-	-	-	-	x	-	x	x	-	x	x	-	-	x	-	-	-	-	x	-	-	-	-	-	x	x	x	x	-	x	-	-	-	x	x	-
Chernysheva et al. [27]	2007	x	-	-	-	-	-	x	-	-	-	-	-	-	-	-	-	-	-	-	x	x	-	x	-	-	x	-	-	-	-	-	-	x	-	-	-	-
Launay et al. [6]	2008	x	-	-	-	-	-	x	x	x	-	x	x	-	-	x	-	-	-	-	-	-	-	-	-	-	x	-	x	x	-	-	-	x	-	x	x	-

Table 1.4: Summary of the LHP steady-state models between 1999 and 2008

Authors	Chernysheva and Maydanik [127]	Adoni et al. [113]	Bai et al. [115]	Singh et al. [117]	Hamdan and Elnajjar [123]	Adoni et al. [114]	Rivière et al. [84]	Boo and Jung [135]	Li and Peterson [128]	Jesuthasan [140]	Lin et al. [74]	Zhang et al. [79]	Kuroi and Nagano [83]	Chernysheva and Maydanik [130]	Chernysheva and Maydanik [46]	Hodot et al. [118]	Bai et al. [141]
Year	2009	2009	2009	2009	2009	2010	2010	2010	2011	2011	2011	2012	2012	2012	2012	2013	2014
Complete LHP	-	×	×	×	×	×	×	×	-	×	×	-	×	-	-	×	×
Partial modelling	×	-	-	-	-	-	-	-	×	-	-	×	-	×	×	-	-
3D analysis	-	-	-	-	-	-	-	-	×	-	-	×	-	×	×	×	-
2D analysis	×	-	-	-	-	-	-	-	-	-	-	-	-	-	-	-	-
1D analysis	-	-	-	-	-	-	×	-	-	×	-	-	×	-	-	×	-
Nodal network	-	×	×	×	×	×	×	-	-	×	×	-	×	-	-	-	×
Analytical solution	-	-	-	-	-	-	-	×	-	-	-	-	-	-	-	-	-
Cylindrical geometry	-	×	×	-	-	×	×	-	-	×	×	-	×	-	-	×	×
Flat (reservoir in the thickness)	-	-	-	×	×	×	-	×	×	×	-	-	-	-	-	-	-
Flat (reservoir adjacent to the evaporator)	-	-	-	-	-	-	-	-	-	-	-	×	-	×	×	-	-
Axial/longitudinal parasitic heat flux	-	×	×	-	-	×	×	-	-	-	-	-	×	×	×	×	×
Radial/transversal parasitic heat losses	-	×	×	×	×	×	×	×	-	×	×	×	×	×	×	×	×
Contact resistance body-wick	×	-	-	-	-	-	-	-	-	-	×	-	-	×	×	-	-
Concentrated heat flux	-	-	-	-	-	-	-	-	-	-	-	-	-	-	×	-	-
Convection in the wick	-	×	×	-	×	×	×	×	×	-	-	×	-	×	×	×	-
Drying of the wick	×	-	-	-	-	-	-	-	-	-	×	-	-	×	×	-	-
Secondary/biporous wick	-	-	×	-	-	-	-	-	-	-	×	-	-	-	-	-	-
Bayonet	-	×	-	-	-	×	-	-	-	-	-	-	-	-	-	×	-
Heat transfer reservoir-casing	-	-	×	-	-	-	-	-	-	-	-	-	-	×	×	×	×
Hard-filling	-	-	-	-	-	×	-	×	-	-	-	-	-	-	-	-	×
Finite evaporation coefficient	-	-	-	-	-	-	-	×	-	-	-	-	-	×	×	×	-
Infinite evaporation coefficient (set temperature)	×	-	×	-	-	-	-	-	×	-	-	×	-	-	-	-	×
Pressure drop in the vapour grooves	×	-	×	-	-	-	×	-	×	×	-	×	-	×	×	-	-
Heat transfer in the vapour grooves	-	-	-	-	-	-	×	×	×	×	-	×	×	×	×	×	-
Longitudinal conduction in the tubes	-	-	-	-	-	-	×	-	-	-	-	-	-	-	-	×	-
Single-phase pressure drops	-	×	×	×	×	×	×	-	-	×	×	×	×	-	-	×	×
Two-phase pressure drops	-	×	×	-	-	×	×	-	-	×	×	-	×	-	-	×	×
Flow regime	-	×	×	×	-	×	×	-	-	×	-	-	×	-	-	×	×
Condensation regime	-	×	×	-	-	×	×	-	-	×	-	-	-	-	-	×	×
Homogeneous model	-	-	-	-	-	-	-	-	-	-	-	-	-	-	-	-	-
Separated phases model	-	×	×	-	-	×	×	-	-	×	×	-	×	-	-	×	×
Condensation in the transport lines	-	-	×	-	-	-	×	-	-	×	-	-	-	-	-	×	×
Gravity effects	-	-	-	×	-	-	-	-	-	×	-	-	-	-	-	×	×
Non-condensable gases	-	-	-	-	-	-	-	-	-	-	-	-	-	-	-	-	-
Evaporator heat losses	-	×	×	-	-	×	×	×	-	×	×	-	×	×	×	×	×
Transport lines heat losses	-	×	×	-	-	×	×	×	-	×	-	-	-	-	-	×	×
Multiple evaporator/condenser	-	-	-	-	-	-	-	-	-	-	-	-	-	-	-	-	-

Table 1.5: Summary of the LHP steady-state models between 2009 and 2014

1.4 Location of the liquid-vapour interface

The location of the liquid-vapour interface in the evaporator can have a significant influence on the heat transfer inside the wick and is mostly of interest when investigating the deprime of the loop following the drying out of the porous structure. Indeed, the growth of vapour zones inside the wick leads to a different thermal profile in the wick, to a change of the evaporation interface shape and, in case of a penetration across the entire porous structure, to a failure of the entire loop operation.

A majority of the LHP models from the literature assume a complete liquid saturation of the wick and a static liquid-vapour interface at the surface of the wick in contact with the groove (Table 1.4 and 1.5). In that case, the menisci providing the capillary pressure are all located in the pores at the surface of the porous structure in contact with the grooves and the wick is full of liquid.

Considering heat and mass transfer and evaporation processes in conventional heat pipes, Demidov and Yatsenko [129] theoretically investigate the growth of a vapour zone inside the capillary structure. The authors postulate the existence of a vapour bubble between the wick and the fin, growing in size and eventually communicating with the groove (Figure 1.34).

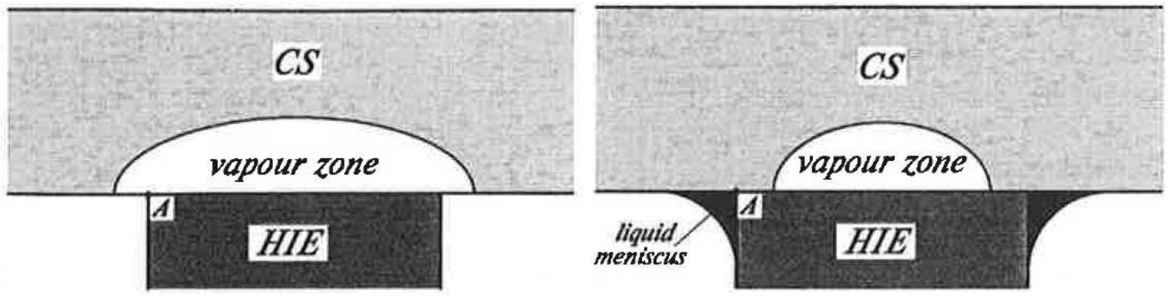

(a) (b)

Figure 1.34: Growth of (a) a "large" vapour zone and (b) a "small" vapour zone inside the capillary structure [129]

This phenomenon is further studied by Figus et al. [68], who also develop a pore network model to consider a pore size distribution inside the porous structure. In this type of model, the pore space is modelled by a network of sites (pores) and bonds (throats), as presented in Figure 1.35. A complementary network is considered to take into account conductive heat transfer.

At the beginning of the numerical procedure, the network is saturated with liquid except the first series of bonds underneath the fin which are saturated with vapour. Mass, momentum and energy balance equations for each element of the networks enable the calculation of the temperature and the pressure fields. If the pressure difference across the liquid-vapour interface is higher than the maximal capillary pressure, the bond associated with that difference is invaded by the vapour. Once the network phase distribution has been updated, the overall procedure is repeated until a stationary solution is found.

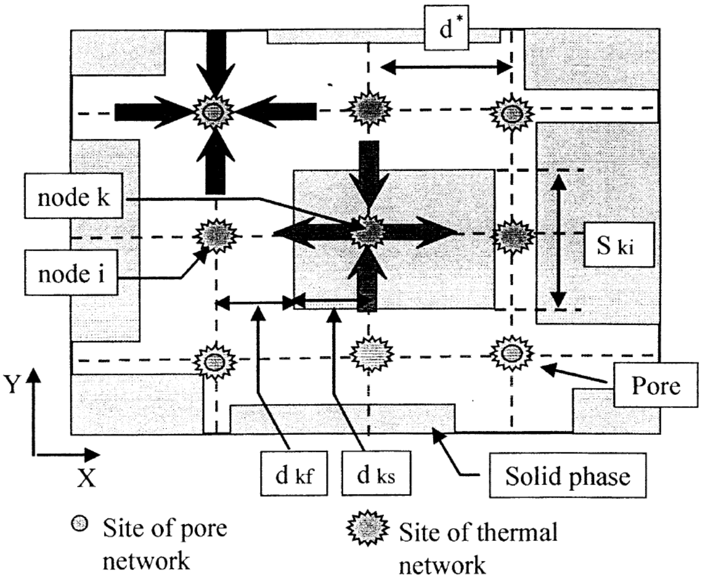

Figure 1.35: Sketch of a pore network model [68]

The authors compare the standard continuum model (based on continuous equations) with the pore network one (Figure 1.36a), for a constant pore size in the entire wick. To locate the liquid-vapour interface inside the wick, the continuum model assumes the wick to be filled with vapour if its temperature is greater than the saturation temperature. Both methods give similar results characterised by a smooth vapour zone under the fin. When the wick does not have a homogeneous porosity, a fractal vapour zone extension is observed (Figure 1.36b). They obtain vapour breakthrough for heat flux equal to about $20\,\mathrm{W \cdot cm^{-2}}$. As in the previously cited work, the authors assume the presence of an initial vapour zone in the wick, initiating the vapour invasion process.

Other modelling works have been more recently published on this topic, further developing a pore network model. Coquard [124] improves the model of Figus et al. [68], considering convection in both the liquid and the vapour phases and taking into account the variation of the vapour density. Heat transfer in the grooves is calculated and the energy balance is also computed in the evaporator wall. Moreover, no symmetry is assumed for the vapour region. The author develops a dual model: the pressure and temperature fields are calculated using homogeneous equations whereas the capillarity and hence the location of the interface are considered using the pore network. To determine the incipience of the vapour development inside the porous structure, the author arbitrarily assumes a nucleation superheat of 3 K. This assumption also implies the existence of vapour or gas embryos under the fin that facilitates the nucleation. According to the author, the presence of the vapour region inside the wick has a major influence on the evaporator operation. It induces an additional thermal resistance, leading to a large superheat of the fin and to an increase of the parasitic heat losses.

The model was further developed by Louriou [125] to take into account transient phenomena. Furthermore, the evaporator model is coupled with a nodal description of a complete LHP and takes into account the imbibition of the pores after vapour invasion (recession of the vapour

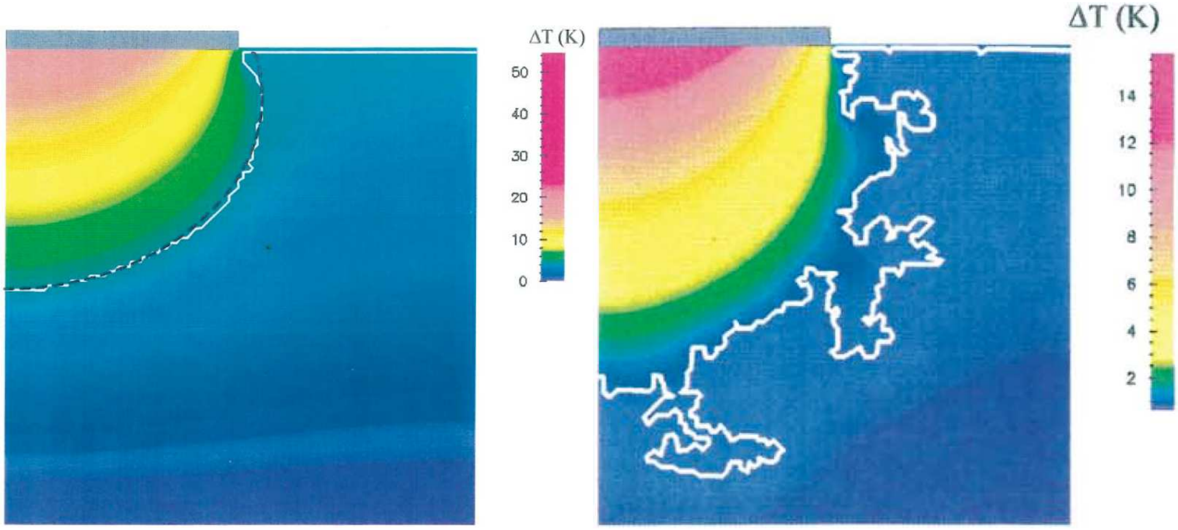

(a) (b)

Figure 1.36: Pore-network simulations of the vapour front inside the porous wick [68]: (a) homogeneous porosity ($\phi = 5\,\mathrm{kW \cdot m^{-2}}$): continuum model (black) and pore-network model (white); (b) inhomogeneous porosity ($\phi = 90\,\mathrm{kW \cdot m^{-2}}$)

region). This imbibition, governed by the capillary forces, enables the vapour-filled pores to be invaded by the liquid if the pressure difference across the meniscus is lower than the maximal capillary pressure generated in the pore. The study shows the various growth modes (driven by the capillary forces alone or by the association of both the capillary and the viscous forces) of the vapour region as a function of the heat load. It also shows that imbibition can induce oscillating phenomena in the porous medium. Despite interesting conclusions, the authors mention the need of further studies concerning the nucleation in porous media and the initiation of the vapour region under the fin. Indeed, like the previous described models, this study assumes an initial vapour nucleus in the wick under the fin.

Kaya and Goldak [33] numerically analyse heat and mass transfer in the porous structure of a loop heat pipe using a finite element method. They study the existence of a vapour region inside the wick to assess the boiling limit of LHPs. The authors expect nucleation to start in the microscopic cavities at the wick-fin interface for small superheat values as a result of trapped gas in these cavities. According to the authors, the boiling incipient superheat value is difficult to predict, since it depends on several parameters in a complex manner. Therefore, they arbitrarily assume the incipience of the vapour zone would occur if a superheat of 4 K of the liquid is reached. However, if the contact between the fin and the wick is improved and the working fluid is purified to the greatest possible extent, thus preventing the presence of vapour embryos trapped at the wick-fin interface, the boiling incipience can be delayed to higher superheats, at the same order of magnitude as that for homogeneous nucleation in a pure liquid. The authors investigate such a scenario, calculating the superheat limit using the cluster nucleation theory. Their experimental results indicate no strong transient effects that could be the expected consequence of an explosive evaporation at the wick-fin interface, even when the applied heat load is higher that the calculated boiling limit. They conclude that a vapour region must exist under the fin and provide an escape path for the bubbles to the groove, thus preventing a flash-like vapour expansion. However, the absence of strong transient effects does not necessarily confirms the partial drying of the capillary structure.

All of these numerical works assume initial clusters of non-condensable gases trapped between the wick and the fin. These clusters would enable the expansion of a vapour zone in the porous structure, requiring only a low superheat. In the case of a good mechanical contact between the wick and the evaporator body and if the purity of the working fluid is high, it can be assumed that no vapour nor gas would initially exist in the porous structure. The conditions of boiling initiation are then given by the homogeneous nucleation theory. In such a case, the boiling condition would be achieved at a very high superheat. As was explained by Mishkinis and Ochterbeck [142] and later confirmed by Kaya and Goldak [33], if the LHP is fabricated and filled with a high degree of carefulness, particularly for the degasing of the liquid and the elimination of non-condensable gases in the system, practically no boiling phenomenon is to be expected during operation.

Owing to the geometrical characteristics of the wick (pore radii in the order of several micrometres, total thickness of several millimetres), its location in the core of the evaporator as well as the use of opaque materials for its structure, a visual investigation of the wetting of the wick during operation proves to be extremely difficult. Therefore, experimental information about the location of the two-phase interface inside the wick is extremely scarce. Some authors experimentally studied two-phase heat transfer inside a porous structure heated on one side in order to reproduce the phenomena involved in a capillary structure of an LHP [124–126].

Zhao and Liao [126] report an experimental study of a capillary porous structure heated with a grooved source at the top. The test section is packed with glass beads, essentially spherical in shape, with an average particle diameter of 1.09 mm. A finned copper block with an embedded heater is placed at the top of the test section and the latter is filled with water. At low to moderate heat fluxes, evaporation takes place uniformly at the heated surface of the porous structure. However, at high heat fluxes, a vapour blanket forms below the heated surface (Figure 1.37).

Coquard [124] investigates the development of a vapour pocket in a heated porous medium. The porous medium consists on stainless steel spherical beads, with a diameter of 1 mm. A brass fin is located at the top and provides heating to the porous medium. Two grooves enable the vapour to escape (Figure 1.38a). The tests are conducted using Fluorinert™ FC-3284 as working fluid. As the brass fin is heated, the author observes the growth of a vapour zone inside the porous structure (Figure 1.38b), eventually leading to a complete breakthrough of the vapour. In all the tests, the grooves are filled with liquid prior to the start-up, which is a potential start-up configuration of an LHP. However, this initial condition does not represent adequately the condition of a vapour groove in a normal steady-state loop heat pipe operation.

Coquard also observes the incipience of the vapour pocket. As shown in Figure 1.39, the boiling first takes place along the groove-fin interface and the small bubbles gather at the

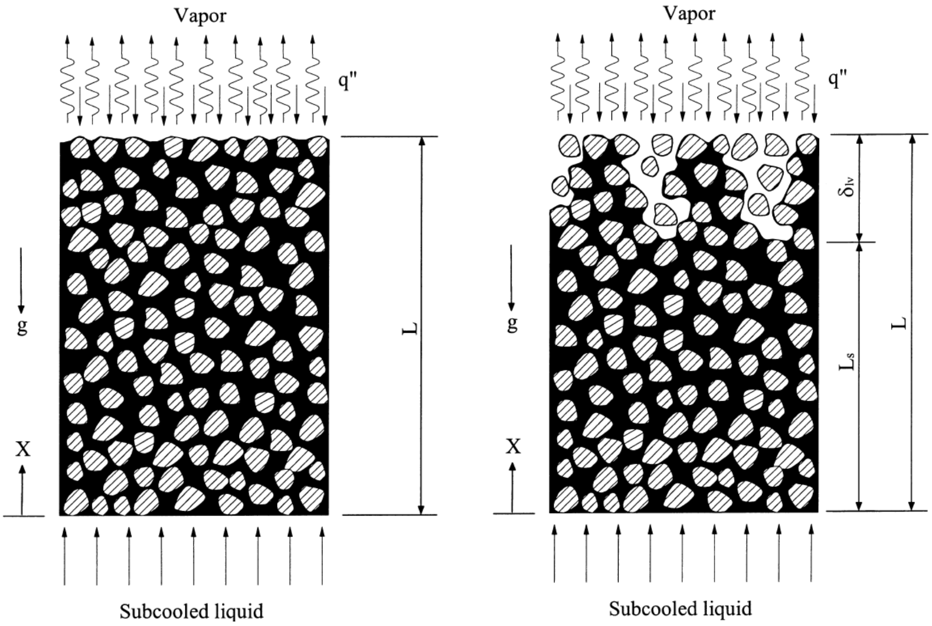

Figure 1.37: Phase-change behaviour at different heat loads [126]: (left) at small and moderate heat fluxes; (right) at high heat fluxes

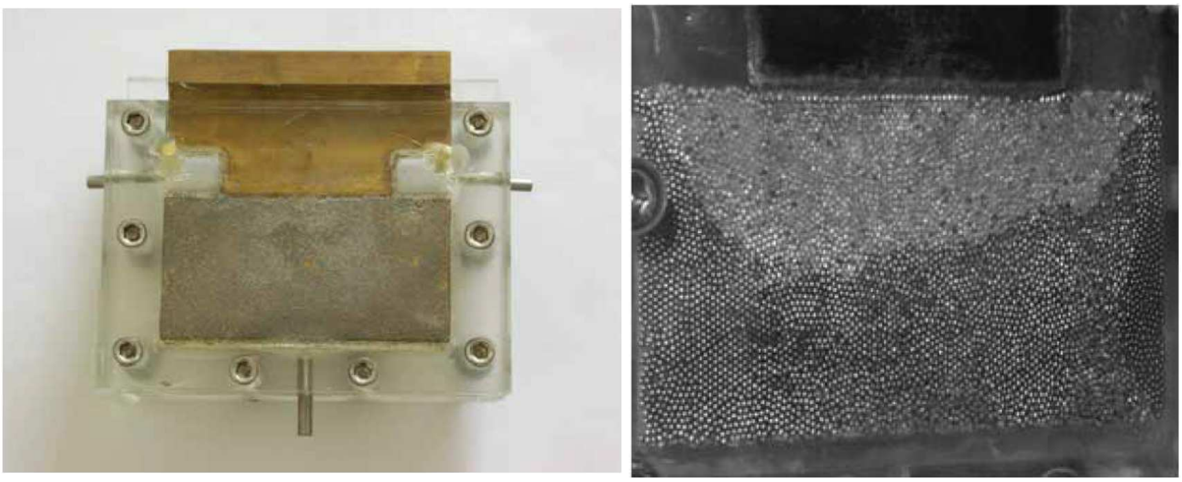

(a) Test sample

(b) Photograph of the vapour region

Figure 1.38: Experimental study of a vapour zone development inside a porous structure [124]

fin-porous structure corner, in the groove filled with liquid. The bubble then grows until complete invasion of the groove and the meniscus at the fin-groove-porous structure interface is broken, letting the vapour enter the porous medium. The vapour then migrates to the centre of the fin. Therefore, it seems that in that case, the incipience of the vapour is located in the groove and not inside the porous medium.

Louriou [125] develop an experimental setup to study the growth of a vapour region inside a porous medium (Figure 1.40). The porous medium consists of machined grooves in an aluminium or in a silicon plate. The porous structure is filled with ethanol and heated

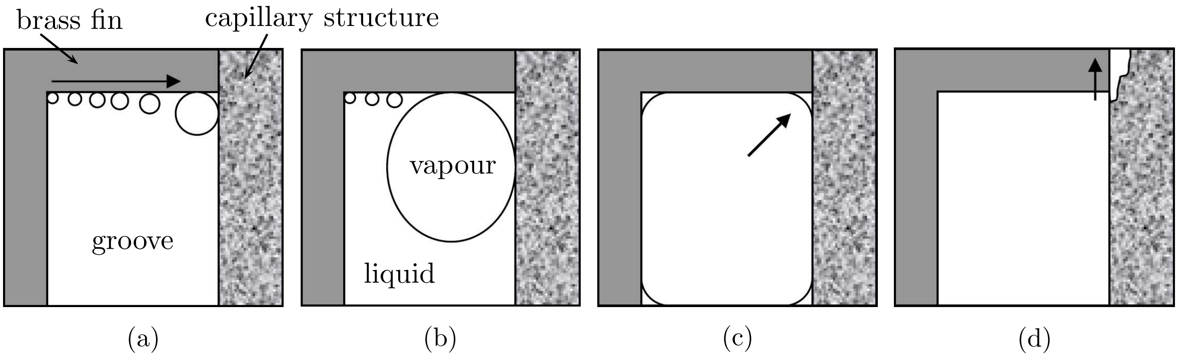

Figure 1.39: Growth of the first vapour zone in the groove [124]

on one side. Despite giving interesting qualitative results concerning the growth pattern of a vapour zone in a porous medium, the experimental setup does not provide any vapour grooves or channels for the evacuation of the vapour and forces therefore the development of a vapour region in the porous medium.

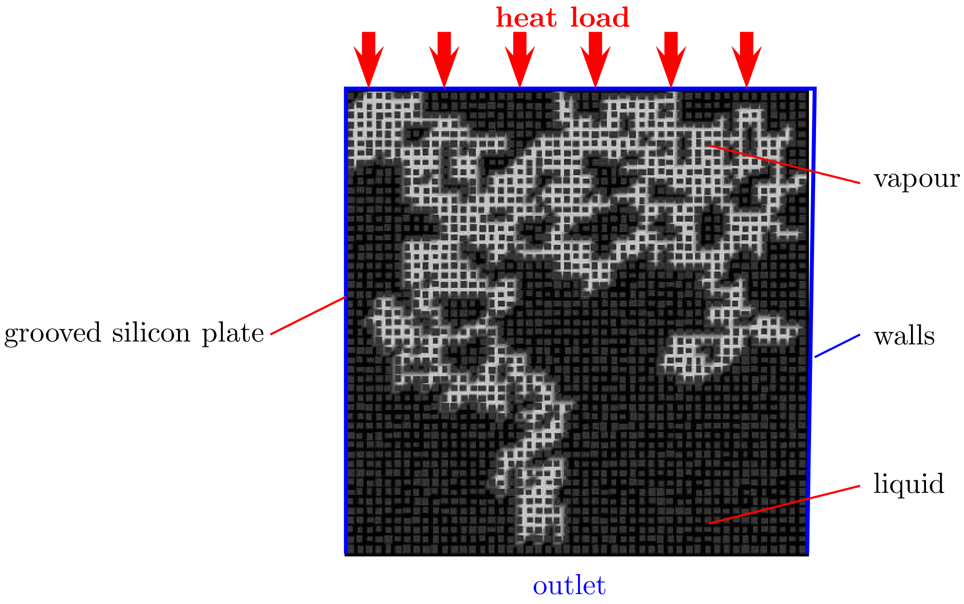

Figure 1.40: Study of the growth of a vapour region inside a porous medium [125]

In all of these investigations, the pore size of the tested capillary material is not of the same order of magnitude as in the capillary wicks used in LHPs. In practice, the diameter of the pores in a wick is equal to several micrometres. This induces a significant capillary pressure at the location of the menisci, particularly when the surface tension of the working fluid is large. It is therefore difficult to assess if the same phenomenon would occur in a practical application of LHP.

Launay and Mekni [143] developed a test bench for the infrared visualization of the liquid-vapour interface in the wick of a complete loop heat pipe experimental setup. As shown in Figure 1.41a, an aluminium heat spreader and a capillary wick (made of 1–2 µm sintered glass powder) are clamped and may be regarded as a slice 3 mm-thick. The aluminium plate with 2 mm-width fins is covered with black paint to increase its emissivity. The capillary wick is plunged into an ethanol reservoir to provide initial saturation of the wick and a heat input is set on the top of the heat spreader. The authors observe the liquid-vapour interface with the IR camera. They report that with the increase of the heat input, the evaporation front slightly moves into the capillary wick, generating a significant increase of the fin temperature (Figure 1.41b). This study tends towards the partial drying of the capillary structure below the fin during LHP operation.

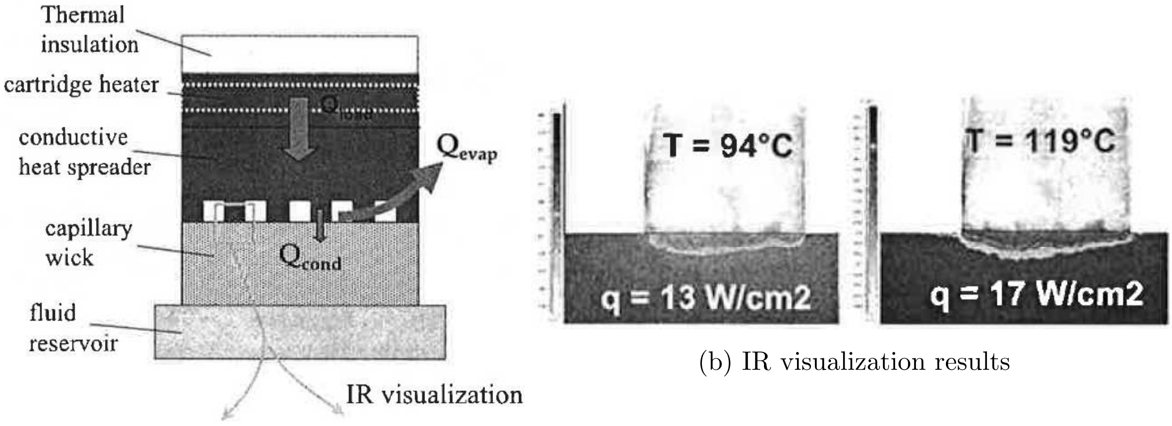

(a) Experimental setup

(b) IR visualization results

Figure 1.41: IR study of a liquid-vapour front in a capillary structure [143]

This literature survey shows the complexity of the potential expansion of a vapour zone in the wick and its influence on the LHP operation. Many theoretical and numerical studies investigate the potential development of such a vapour region and its consequences on the wick behaviour. However, information concerning the effect of this drying on the LHP global operation is very scarce. There exists few experimental works proving the presence of a two-phase interface inside the capillary structure. This phenomenon needs to be further investigated prior to any conclusion, particularly the incipience of the vapour in the wick and the nucleation theory associated to it. Furthermore, the consideration of a partial drying of the wick, particularly in the case of a pore network, in a complete LHP model would induce much additional complexity and the need of larger computational resources. Therefore, the models developed in this thesis assume a careful manufacturing, assembling and filling of the LHP and consider the wick to be completely saturated with liquid.

1.5 Conclusion

As presented in this chapter, loop heat pipes are complex systems involving many coupled phenomena at different scales. The major challenge remains the understanding and the modelling of the evaporator/reservoir, with an accurate consideration of heat and mass transfer in the porous structure, a precise determination of the parasitic heat fluxes and a good characterisation of the evaporation zone. Several thermophysical parameters are difficult to determine accurately because they depend on manufacturing and assembling processes or because they involve complex physical phenomena. This uncertainty concerns particularly the effective thermal conductivity of the wick, the thermal contact between the wick and the evaporator body, heat transfer between the wick and the reservoir, the local evaporation heat transfer in the evaporator and heat transfer and pressure drops in the two-phase flow.

Many theoretical studies have been undertaken to investigate the steady-state operation of LHPs, at a global level, or considering only the evaporator or a part of it. These analyses give a better understanding of the parameters influencing the LHP operating temperature and of the strong thermal couplings between the elements constituting the device.

In order to predict adequately the operation of a complete LHP, a global model that includes all the components is necessary. Therefore, a compromise has to be found in order to model the system globally with an accurate consideration of the heat and mass transfer in the evaporator/reservoir.

Chapter 2

LHP analytical model and parametric study

This chapter presents the development and the results of an analytical model of a complete loop heat pipe with either a flat or cylindrical evaporator. An analytical model provides a solution without excessive computing times and that can be easily implemented for LHP design analysis. The first section presents the equations of the model. Then, a standard LHP is defined in order to conduct a sensitivity analysis to show the influence of the main parameters on the LHP operating principles. Some results are also presented to show the complexity of this system and to help the reader to apprehend the coupled phenomena occurring in an LHP.

2.1 LHP analytical model establishment

The present model is an extension of the analytical study of Launay et al. [6]. However, in order to accurately take into account heat and mass transfer in the evaporator structure, the present study rests upon two analytical solutions describing the temperature field in the wick and the evaporator casing, based on Fourier series expansions. Both solutions enable to determine parasitic heat losses through the wick and the evaporator body, the sensible heat given to the liquid flowing though the porous structure as well as the heat dissipated by evaporation at the wick-groove interface. A similar approach was implemented in the case of conventional heat pipes by Lefèvre and Lallemand [144] and later extended by Lips and Lefèvre [145]. These features, coupled with energy balances and thermodynamic relationships in the rest of the LHP, give a simple solution for the operating temperature.

2.1.1 Energy balance and thermodynamic relationships

The thermal state of the complete LHP can be determined using energy balance equations and thermodynamic relationships. Figure 2.1 presents the operating principle of the LHP and the links between its components.

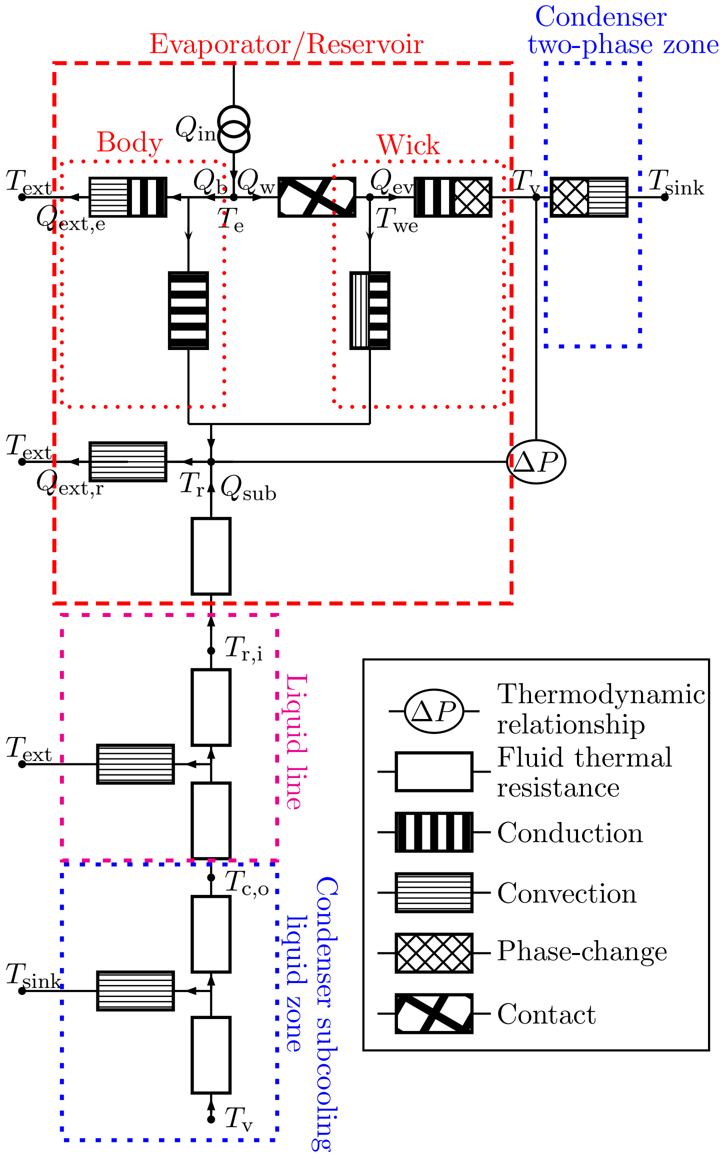

Figure 2.1: LHP schematic nodal network

The total heat load to be dissipated by the evaporator Q_{in} is conducted through the wick or through the evaporator body so that:

$$Q_{\mathrm{in}} = Q_{\mathrm{w}} + Q_{\mathrm{b}} \tag{2.1}$$

The wick is assumed to be fully saturated with liquid. The thermal heat flux Q_{w} is transversally conducted through the evaporator wall, the wall-wick interface and then divides up: a part Q_{ev} is evaporated at the wick-groove interface whereas the rest is dissipated by conduction and convection with the liquid flowing through the porous structure and with the liquid in the reservoir. Q_{b} is conducted longitudinally through the evaporator wall to the reservoir and a part of it, $Q_{\mathrm{ext,e}}$, is given by convection to the ambient. Both the heat flux through the wick Q_{w} and the heat flux conducted through the evaporator casing Q_{b} are functions of the reservoir, the groove, the wick and the evaporator temperatures T_{r}, T_{v}, T_{we} and T_{e}. The same dependence applies for Q_{ev} and $Q_{\mathrm{ext,e}}$:

$$Q_{\mathrm{w}} = f(T_{\mathrm{r}}, T_{\mathrm{v}}, T_{\mathrm{e}}) \tag{2.2}$$

$$Q_{\mathrm{ev}} = \dot{m}_{\mathrm{l}} h_{\mathrm{lv}} = f(T_{\mathrm{r}}, T_{\mathrm{v}}, T_{\mathrm{we}}) \tag{2.3}$$

$$Q_{\mathrm{b}} = f(T_{\mathrm{r}}, T_{\mathrm{e}}) \tag{2.4}$$

$$Q_{\mathrm{ext,e}} = f(T_{\mathrm{r}}, T_{\mathrm{e}}) \tag{2.5}$$

$Q_{\mathrm{ext,e}}$ is also a function of T_{ext}, which is a given data of our model. As a result, the heat load Q_{in} can also be expressed as a function of these four temperatures:

$$Q_{\mathrm{in}} = f(T_{\mathrm{r}}, T_{\mathrm{v}}, T_{\mathrm{we}}, T_{\mathrm{e}}) \tag{2.6}$$

An analytical expression of Q_{in} will be derived in subsection 2.1.2 and 2.1.3. The part of Q_{w} that is not dissipated by evaporation is the transversal parasitic heat flux. Part of this flux is conducted through the wick and released to the reservoir whereas the rest is dissipated by convection due to the liquid flow inside the porous structure. At the interface between the wick and the evaporator envelope, there is a temperature gap T_{e}-T_{we} due to a contact resistance R_{c} defined as:

$$R_{\mathrm{c}} = S_{\mathrm{c}} \frac{T_{\mathrm{e}} - T_{\mathrm{we}}}{Q_{\mathrm{w}}} \tag{2.7}$$

where S_{c} is the contact surface between the wick and the evaporator body and T_{e} and T_{we} are the temperatures on the envelope side and on the wick side, respectively.

A global heat balance on the evaporator/reservoir gives the following equation:

$$Q_{\mathrm{in}} = Q_{\mathrm{ev}} + Q_{\mathrm{sen}} + Q_{\mathrm{sub}} + Q_{\mathrm{ext,e}} + Q_{\mathrm{ext,r}} \tag{2.8}$$

where Q_{sen} is the sensible heat given to the liquid, Q_{sub} is the subcooling due to the liquid entering the reservoir and $Q_{\mathrm{ext,r}}$ is the heat flux dissipated to the ambient by the reservoir. The determination of Q_{sen} and Q_{sub} leads to:

$$Q_{\mathrm{sen}} = \dot{m}_{\mathrm{l}} c_{\mathrm{p,l}} \left(T_{\mathrm{v}} - T_{\mathrm{r}}\right) \tag{2.9}$$

$$Q_{\mathrm{sub}} = \dot{m}_{\mathrm{l}} c_{\mathrm{p,l}} \left(T_{\mathrm{r}} - T_{\mathrm{r,i}}\right) \tag{2.10}$$

where $T_{\mathrm{r,i}}$ is the temperature of the liquid coming from the condenser and flowing back to the reservoir.

To evaluate the heat transfer given by the reservoir to the ambient, it is assumed that its surface is at a uniform temperature equal to T_{r}. Heat transfer with the ambient $Q_{\mathrm{ext,r}}$ is then approximated by:

$$Q_{\mathrm{ext,r}} = h_{\mathrm{ext}} S_{\mathrm{r}} \left(T_{\mathrm{r}} - T_{\mathrm{ext}}\right) \tag{2.11}$$

where S_r is the total external surface of the reservoir. A single expression of Q_in can be derived by combining equations (2.3), (2.5) and (2.7) to (2.11):

$$Q_\mathrm{in} = f(T_\mathrm{r}, T_\mathrm{v}, T_\mathrm{we}, T_\mathrm{e}, \dot{m}_\mathrm{l}, T_\mathrm{r,i}) \tag{2.12}$$

In some cases, the reservoir can be full of liquid. This phenomenon has been extensively studied by Adoni *et al.*[114]. In the present model, the existence of a two-phase equilibrium in the reservoir is assumed. As shown by Launay *et al.* [6], a thermodynamic relationship exists between the saturation temperature inside the grooves and the one at the liquid-vapour interface in the reservoir:

$$\Delta T = T_\mathrm{v} - T_\mathrm{r} = \left(\frac{\partial T}{\partial P}\right)(\Delta P_\mathrm{v} + \Delta P_\mathrm{l} - \rho_\mathrm{l} g \Delta H) \tag{2.13}$$

where ρ_l is the liquid density and ΔH is the elevation of the condenser compared to the evaporator. The slope of the pressure-temperature saturation curve is given by the Clausius-Clapeyron equation:

$$\frac{\partial T}{\partial P} = \frac{T\,(1/\rho_\mathrm{v} - 1/\rho_\mathrm{l})}{h_\mathrm{lv}} \tag{2.14}$$

The model can also cope with non-condensable gases (NCG), which can be generated for various reasons in the LHP and accumulate in the reservoir, as explained by Singh et al. [45]. We assume that in operating conditions, these NCG are drained to the reservoir. In order to take into account the overpressure generated by the NCG P^*_NCG, equation (2.13) is modified:

$$\Delta T = T_\mathrm{v} - T_\mathrm{r} = \left(\frac{\partial T}{\partial P}\right)(\Delta P_\mathrm{v} + \Delta P_\mathrm{l} - \rho_\mathrm{l} g \Delta H + P^*_\mathrm{NCG}) \tag{2.15}$$

The vapour line is considered adiabatic so that the vapour enters the condenser with a temperature equal to T_v. Furthermore, the condensation temperature T_c and the vapour temperature T_v are linked with the thermodynamic relationship (2.14). Since the pressure drops in the vapour line are low and $\rho_\mathrm{l} g \Delta H$ is also small, it is assumed that condensation occurs at temperature T_v ($T_\mathrm{c} \approx T_\mathrm{v}$).

In the part of the condenser where liquid subcooling occurs, heat transfer with the heat sink and with the ambient are calculated considering a convective heat transfer h_sink and h_ext, respectively:

$$\begin{aligned} T_\mathrm{c,o} = {} & T_\mathrm{sink} + (T_\mathrm{v} - T_\mathrm{sink}) \\ & \times \exp\left(\frac{-\pi D_\mathrm{c,i}\,(L_\mathrm{c} - L_{2\varphi})}{\dot{m}_\mathrm{l} c_\mathrm{p,l}\,(1/h_\mathrm{l} + D_\mathrm{c,i}/(h_\mathrm{sink} D_\mathrm{c,o}))}\right) \end{aligned} \tag{2.16}$$

where $T_\mathrm{c,o}$ is the temperature of the liquid at the condenser outlet, L_c and $L_{2\varphi}$ are the lengths of the condenser and of the two-phase region respectively. $D_\mathrm{c,i}$ and $D_\mathrm{c,o}$ are the inner and outer condenser diameters and h_l is the heat transfer coefficient between the liquid flow and the tube wall. In a similar way, the liquid line heat balance is:

$$\begin{aligned} T_{\mathrm{r,i}} = T_{\mathrm{ext}} + \left(T_{\mathrm{c,o}} - T_{\mathrm{ext}}\right) \\ \times \exp\left(\frac{-\pi D_{\mathrm{l,i}} L_{\mathrm{l}}}{\dot{m}_{\mathrm{l}} c_{\mathrm{p,l}} \left(1/h_{\mathrm{l}} + D_{\mathrm{l,i}}/(h_{\mathrm{ext}} D_{\mathrm{l,o}})\right)}\right) \end{aligned} \tag{2.17}$$

where $D_{\mathrm{l,i}}$ and $D_{\mathrm{l,o}}$ are the inner and outer diameters of the liquid line and L_{l} its length. Additionally, in the condenser, the heat exchange with the heat sink in the two-phase zone is equal to the latent heat of the condensing vapour:

$$\dot{m}_{\mathrm{l}} h_{\mathrm{lv}} = \frac{1}{\dfrac{1}{h_{\mathrm{cond}} D_{\mathrm{c,i}}} + \dfrac{1}{h_{\mathrm{sink}} D_{\mathrm{c,o}}}} \pi L_{2\varphi} \left(T_{\mathrm{v}} - T_{\mathrm{sink}}\right) \tag{2.18}$$

with h_{cond} the condensation heat transfer.

Equations (2.3), (2.7), (2.8), (2.12), (2.15) to (2.17) and (2.18) form a set of 8 independent equations with 8 unknowns: T_{we}, T_{e}, T_{r}, $T_{\mathrm{r,i}}$, $T_{\mathrm{c,o}}$, T_{v}, $\dot{m}_{\mathrm{l}}$ and $L_{2\varphi}$. Their solution leads to the determination of the complete thermal state of the LHP. The values of Q_{b}, Q_{w} and Q_{ev} (equations 2.2-2.4) can be calculated using several methods. In the large majority of LHP models from the literature, heat transfer in the evaporator is simply described using equivalent thermal resistances based on the geometrical characteristics, the thermophysical properties of the evaporator and the operating conditions. However, such a method does not take into account adequately the heat flux in the wick and the evaporator body since the determination of the thermal resistances requires a 2D or 3D approach. Thus, in the present study, an accurate thermal analysis of the evaporator has been conducted, based on an analytical approach.

2.1.2 Heat and mass transfer in the wick

The first part of the analytical model of the evaporator deals with heat and mass transfer inside the porous structure. As shown in Figure 2.2, a part of the porous wick is modelled, bordered on one side by the liquid bulk of the reservoir and by half of a fin and half of a groove on the other side.

The 2-D stationary heat equation in the wick without heat source is expressed as:

$$\frac{\partial^2 T_{\mathrm{w}}}{\partial x^2} + \frac{\partial^2 T_{\mathrm{w}}}{\partial y^2} = 0 \tag{2.19}$$

where T_{w} is the temperature of the porous structure and x and y are the axis coordinates (Fig. 2.3). A non-dimensional temperature is defined as:

$$T_{\mathrm{w}}^{*} = \frac{\lambda_{\mathrm{eff}} \left(T_{\mathrm{w}} - T_{\mathrm{r}}\right)}{\varphi_0 b} \tag{2.20}$$

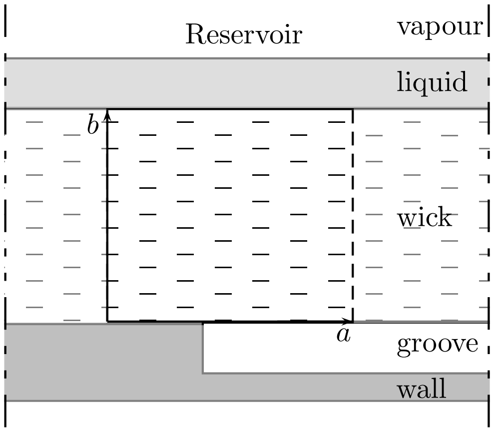

Figure 2.2: Evaporator cross-section

and leads to:

$$\frac{\partial^2 T^*_{\mathrm{w}}}{\partial X^2} + \frac{1}{B^2}\frac{\partial^2 T^*_{\mathrm{w}}}{\partial Y^2} = 0 \tag{2.21}$$

with

$$X = \frac{x}{a}, \qquad Y = \frac{y}{b} \qquad \text{and} \qquad B = \frac{b}{a} \tag{2.22}$$

where a and b are the lengths of the modelled region in the x and y directions respectively, λ_{eff} is the wick effective thermal conductivity and φ_0 is an arbitrary heat flux.

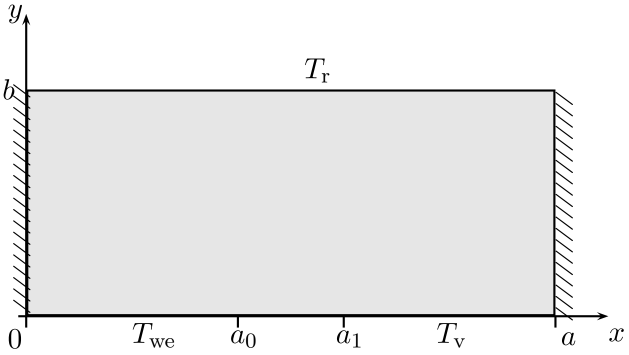

Figure 2.3: Schematic of the wick model

A general expression of the non-dimensional temperature field expanded in 2-D Fourier series is given by:

$$T^*_{\mathrm{w}}(X,Y) = \sum_{m=0}^{\infty} A_{\mathrm{m}}(Y)cos(m\pi X) + B_{\mathrm{m}}(Y)sin(m\pi X) \tag{2.23}$$

For $X = 0$ and $X = 1$, an adiabatic boundary condition is considered based on a symmetry hypothesis:

$$\left.\frac{\partial T^*_{\mathrm{w}}}{\partial X}\right|_{X=0} = \left.\frac{\partial T^*_{\mathrm{w}}}{\partial X}\right|_{X=1} = 0 \tag{2.24}$$

Thus equation (2.23) becomes:

$$T^*_{\mathrm{w}}(X,Y) = \sum_{m=0}^{\infty} A_{\mathrm{m}}(Y) cos(m\pi X) \tag{2.25}$$

Combining equations (2.21) and (2.25) yields:

$$-\left(m\pi B\right)^2 A_{\mathrm{m}}(Y) + \frac{\partial^2 A_{\mathrm{m}}(Y)}{\partial Y^2} = 0 \tag{2.26}$$

Solving the previous differential equation leads to:

$$A_0(Y) = A_{01}Y + A_{02} \qquad \text{if} \quad m = 0 \tag{2.27}$$

$$A_{\mathrm{m}}(Y) = A_{\mathrm{m1}}e^{m\pi BY} + A_{\mathrm{m2}}e^{-m\pi BY} \qquad \text{otherwise} \tag{2.28}$$

The boundary condition for $Y = 0$ is a set temperature profile corresponding to the evaporator temperature T_{we} for one side ($x \leqslant a_0$) and to the groove temperature T_{v} for the other side ($x \geqslant a_1$). At the junction between the wall and the groove, a singularity exists. This particular point corresponds to the microregion where intensive evaporation occurs. This temperature singularity is treated by considering a linear variation of the temperature between two fictive points a_0 and a_1. The slope of the temperature gradient and thus the position of these points depend on the maximum evaporation rate at the liquid-vapour interface that can be calculated using the kinetic gas theory, which gives a heat transfer coefficient h_{ev} [34]:

$$h_{\mathrm{ev}} = \frac{2a_{\mathrm{ev}}}{2-a_{\mathrm{ev}}} \frac{\rho_{\mathrm{v}} h_{\mathrm{lv}}^2}{T_{\mathrm{sat}}} \left(\frac{2\pi \overline{R} T_{\mathrm{sat}}}{\overline{M}}\right)^{-0.5} \left(1 - \frac{P_{\mathrm{sat}}}{2\rho_{\mathrm{v}} h_{\mathrm{lv}}}\right) \tag{2.29}$$

where a_{ev} is the accommodation coefficient, T_{sat} is the saturation temperature of the fluid, $\overline{R}$ is the universal gas constant and $\overline{M}$ is the molar mass of the fluid. In the case of the evaporation of a thin liquid film, the accommodation coefficient is defined as the ratio of the actual evaporation rate to a theoretical maximal phase change rate. A coefficient equal to unity describes perfect evaporation while a lower value represents incomplete evaporation. In the case of water, values varying from 0.01 to 1 are suggested in the literature [146]. We assume the following relationship between h_{ev} and the position of a_0 and a_1:

$$h_{\mathrm{ev}} = \frac{\lambda_{\mathrm{eff}}}{a_1 - a_0} \tag{2.30}$$

The boundary condition for $Y = 0$ is then defined as:

$$T_\mathrm{w}^*(X,0) = \begin{cases} \dfrac{\lambda_\mathrm{eff}\left(T_\mathrm{we} - T_\mathrm{r}\right)}{\varphi_0 b} & \text{if } 0 < X \leqslant \dfrac{a_0}{a} \\ \dfrac{\lambda_\mathrm{eff}}{\varphi_0 b}\left(\left(T_\mathrm{v} - T_\mathrm{r}\right) + \left(T_\mathrm{we} - T_\mathrm{v}\right) \dfrac{a_1 - aX}{a_1 - a_0} \right) & \\ \qquad\qquad \text{if } \dfrac{a_0}{a} < X < \dfrac{a_1}{a} & \\ \dfrac{\lambda_\mathrm{eff}\left(T_\mathrm{v} - T_\mathrm{r}\right)}{\varphi_0 b} & \text{if } \dfrac{a_1}{a} \leqslant X < 1 \end{cases} \tag{2.31}$$

For $Y = 1$, the reservoir temperature is set:

$$T_\mathrm{w}^*(X,1) = 0 \tag{2.32}$$

The non-dimensional temperature field is then:

$$\begin{aligned} T_\mathrm{w}^*(X,Y) = {} & A_{01} Y + A_{02} \\ & + \sum_{m=1}^{\infty} \left(A_\mathrm{m1} e^{m\pi BY} + A_\mathrm{m2} e^{-m\pi BY} \right) \cos(m\pi X) \end{aligned} \tag{2.33}$$

with

$$A_{01} = -\frac{\lambda_\mathrm{eff}}{\varphi_0 b}\left(T_\mathrm{v} - T_\mathrm{r} + \left(T_\mathrm{we} - T_\mathrm{v}\right) \frac{a_0 + a_1}{2a} \right) \tag{2.34}$$

$$A_{02} = \frac{\lambda_\mathrm{eff}}{\varphi_0 b}\left(T_\mathrm{v} - T_\mathrm{r} + \left(T_\mathrm{we} - T_\mathrm{v}\right) \frac{a_0 + a_1}{2a} \right) \tag{2.35}$$

$$A_\mathrm{m1} = 2\frac{\lambda_\mathrm{eff}}{\varphi_0 b} \frac{T_\mathrm{we} - T_\mathrm{v}}{m^2 \pi^2} \frac{a}{a_1 - a_0} \frac{\cos\left(m\pi \frac{a_0}{a}\right) - \cos\left(m\pi \frac{a_1}{a}\right)}{1 - e^{2m\pi B}} \tag{2.36}$$

$$A_\mathrm{m2} = 2\frac{\lambda_\mathrm{eff}}{\varphi_0 b} \frac{T_\mathrm{we} - T_\mathrm{v}}{m^2 \pi^2} \frac{a}{a_1 - a_0} \frac{\cos\left(m\pi \frac{a_0}{a}\right) - \cos\left(m\pi \frac{a_1}{a}\right)}{1 - e^{-2m\pi B}} \tag{2.37}$$

In equation (2.33), the liquid flow inside the porous structure is not taken into account. This flow is two-dimensional. However, in the present study, we assume a 1D flow inside the wick, considering a homogeneous volumetric source inside the wick q defined as:

$$q = -\frac{4\dot{m}_\mathrm{l} c_\mathrm{p,l}\left(T_\mathrm{v} - T_\mathrm{r}\right)}{\pi D_\mathrm{w}^2 b} \tag{2.38}$$

where $\dot{m}_\mathrm{l}$ is the total liquid mass flow rate in the wick, D_w is the diameter of the wick (in the case of a circular wick) and $c_\mathrm{p,l}$ is the specific heat of the liquid. This assumption respects the energy balance and enables to derive an analytical expression for the influence of the liquid flow inside the wick. The superposition principle enables to add a simple model of heat transfer in the wick with a homogeneous source to the previous developed analysis. It has to be noted that a 2D approach of heat and mass transfer in a porous wick was presented by Cao and Faghri [133], but the model is not entirely analytical. The heat equation in the wick is thus:

$$\frac{\partial^2 T_\mathrm{c}}{\partial y^2} = \frac{q}{\lambda_\mathrm{eff}} \tag{2.39}$$

where T_c is the temperature of the wick considering only convection. The boundary conditions are:

$$T_\mathrm{c}(y=0) - T_\mathrm{c}(y=b) = b^2 \frac{q}{\lambda_\mathrm{eff}} \tag{2.40}$$

$$T_\mathrm{c}(y=b) = T_\mathrm{r} \tag{2.41}$$

This leads to the non-dimensional temperature field $T_\mathrm{c}^*(Y)$ induced by the liquid flow inside the wick:

$$T_\mathrm{c}^*(Y) = \frac{qb}{2\varphi_0}\left(Y^2 - 3Y + 2\right) \tag{2.42}$$

This solution is added to the previous one to give a general expression of the non-dimensional temperature field in the wick, with consideration of 1-D convection:

$$T_\mathrm{t}^*(X,Y) = T_\mathrm{w}^*(X,Y) + T_\mathrm{c}^*(Y) \tag{2.43}$$

The previously described model enables to calculate the heat flux through the wick Q_w and the heat dissipated by evaporation Q_ev:

$$\begin{aligned} Q_\mathrm{w} &= \frac{S_\mathrm{w}}{a}\int_0^{\frac{a_0+a_1}{2}} -\lambda_\mathrm{eff}\left.\frac{\partial T_\mathrm{t}}{\partial y}\right|_{y=0} dx \\ &= -S_\mathrm{w}\varphi_0\left[\frac{a_0+a_1}{2a}\left(A_{01} - \frac{3qb}{2\varphi_0}\right)\right. \\ &\quad \left. + \sum_{m=1}^{\infty} B\left(A_\mathrm{m1} - A_\mathrm{m2}\right)\sin\left(m\pi\frac{a_0+a_1}{2a}\right)\right] \end{aligned} \tag{2.44}$$

$$\begin{aligned} Q_\mathrm{ev} &= \frac{S_\mathrm{w}}{a}\int_{\frac{a_0+a_1}{2}}^{a} \lambda_\mathrm{eff}\left.\frac{\partial T_\mathrm{t}}{\partial y}\right|_{y=0} dx \\ &= S_\mathrm{w}\varphi_0\left[\left(1 - \frac{a_0+a_1}{2a}\right)\left(A_{01} - \frac{3qb}{2\varphi_0}\right)\right. \\ &\quad \left. - \sum_{m=1}^{\infty} B\left(A_\mathrm{m1} - A_\mathrm{m2}\right)\sin\left(m\pi\frac{a_0+a_1}{2a}\right)\right] \end{aligned} \tag{2.45}$$

where S_w is the cross-sectional area of the wick.

In practice, heat transfer between the liquid-vapour interface in the reservoir and the wick is not ideal and may not always be accurately modelled by a set temperature boundary condition. In such a case, heat exchange can be modelled using a heat transfer coefficient between the porous structure and the liquid bulk. Such a method is developed in Appendix C.

2.1.3 Heat transfer in the evaporator casing

The model of the wick is sufficient if the heat losses through the evaporator body are negligible. Nevertheless, the body is usually made of a high conductive material. Therefore, it is generally necessary to estimate the heat transferred longitudinally by conduction from the evaporator to the reservoir and to the ambient. A second analytical model is developed to describe the evaporator casing. First, a two-dimensional analysis is conducted for a flat disk-shaped evaporator. Following the same methodology, a 3D model is then developed for a cylindrical evaporator.

2.1.3.1 Disk-shaped evaporator 2D analysis

Figure 2.4 shows a part of the evaporator. Due to the axisymmetry, only a radial section is modelled. The evaporator wall is “unwrapped” and modelled as a rectangular domain. At $x = 0$ and $x = c$, an adiabatic condition is assumed due to the symmetry. At $y = 0$, a convective heat transfer with the ambient is taken into account on the whole external surface, including the heating section ($0 \leqslant x \leqslant c_0$), where a heat flux φ_{in} is also applied. The inner part of the body is highly influenced by the reservoir temperature. The rectangular shape chosen to represents the evaporator body does not consider the effect of the grooves on the distortion of the temperature field between the base plate and the wick. We assume, therefore, a set temperature profile, with the evaporator temperature T_{e} on one side ($0 \leqslant x \leqslant c_0$) and the reservoir temperature T_{r} on the other side ($c_1 \leqslant x \leqslant c$) with a linear profile in-between.

The sum of two solutions T^*_{b1} and T^*_{b2} is necessary to take into account the complete set of boundary conditions. The first one corresponds to a set temperature profile in the inner part of the wall, in contact with the wick and the liquid-vapour bulk in the reservoir. Convective heat losses to the ambient are assumed for the whole external surface of the evaporator/reservoir. This hypothesis considers that the electronic component to cool down dissipates heat to the LHP on one side and to the ambient on the other. The second solution adds the heat input to the evaporator.

Using the same mathematical procedure as previously, the heat equation becomes:

$$\frac{\partial^2 T^*_{\mathrm{b}}}{\partial X^2} + \frac{1}{D^2}\frac{\partial^2 T^*_{\mathrm{b}}}{\partial Y^2} = 0 \tag{2.46}$$

where:

$$X = \frac{x}{c}; \qquad Y = \frac{y}{d}; \qquad D = \frac{d}{c}; \qquad T^*_{\mathrm{b}} = \frac{\lambda_{\mathrm{b}}\left(T_{\mathrm{b}} - T_{\mathrm{r}}\right)}{\varphi_0 d} \tag{2.47}$$

and T^*_{b1} is the non-dimensional temperature in the evaporator body. The boundary conditions

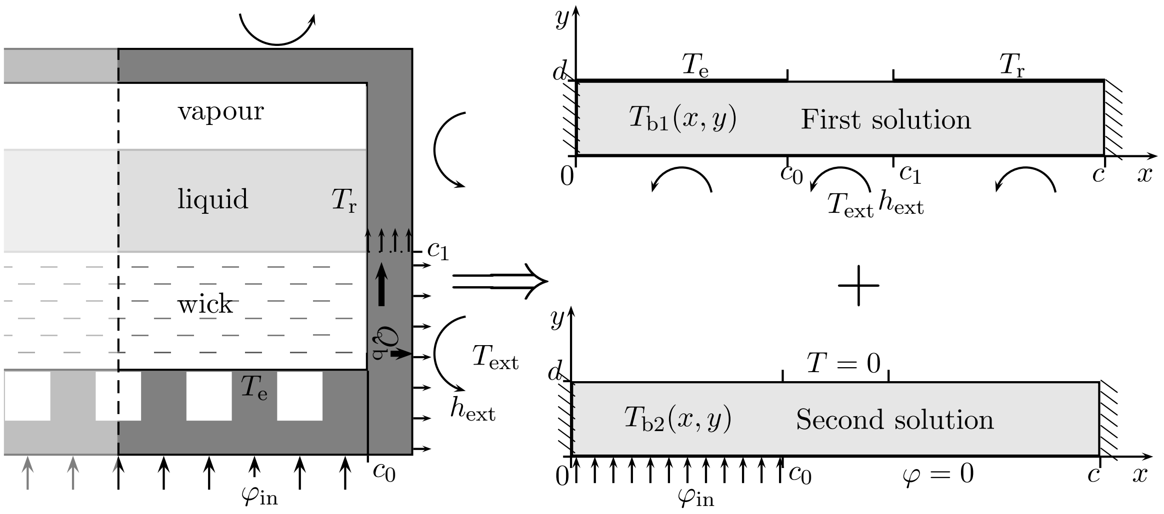

Figure 2.4: Evaporator casing modelling

for the first solution T^*_{b1} are:

$$\left.\frac{\partial T^*_{\mathrm{b1}}}{\partial X}\right|_{X=0} = \left.\frac{\partial T^*_{\mathrm{b1}}}{\partial X}\right|_{X=1} = 0 \qquad \text{(symmetry)} \tag{2.48}$$

$$\begin{gathered}\left.\frac{\partial T^*_{\mathrm{b1}}}{\partial Y}\right|_{Y=0} = Bi_{\mathrm{b}} T^*_{\mathrm{b1}} + \frac{h_{\mathrm{ext}}}{\varphi_0}\left(T_{\mathrm{r}} - T_{\mathrm{ext}}\right) \\ \text{with} \qquad Bi_{\mathrm{b}} = \frac{d h_{\mathrm{ext}}}{\lambda_{\mathrm{b}}} \qquad \text{(Biot number)}\end{gathered} \tag{2.49}$$

$$T^*_{\mathrm{b1}}(X,1) = \begin{cases} \dfrac{\lambda_{\mathrm{b}}\left(T_{\mathrm{e}} - T_{\mathrm{r}}\right)}{\varphi_0 d} & \text{if } 0 < X \leqslant \dfrac{c_0}{c} \\ \dfrac{\lambda_{\mathrm{b}}}{\varphi_0 d}\left(T_{\mathrm{e}} - T_{\mathrm{r}}\right)\dfrac{c_1 - cX}{c_1 - c_0} & \text{if } \dfrac{c_0}{c} \leqslant X < \dfrac{c_1}{c} \\ 0 & \text{if } \dfrac{c_1}{c} < X < 1 \end{cases} \tag{2.50}$$

where λ_{b} is the thermal conductivity of the casing. For the second solution T^*_{b2}:

$$\left.\frac{\partial T^*_{\mathrm{b2}}}{\partial X}\right|_{X=0} = \left.\frac{\partial T^*_{\mathrm{b2}}}{\partial X}\right|_{X=1} = 0 \tag{2.51}$$

$$\left.\frac{\partial T^*_{\mathrm{b2}}}{\partial Y}\right|_{Y=0} = \begin{cases} -\dfrac{\varphi_{\mathrm{in}}}{\varphi_0} & \text{if } 0 < X \leqslant \dfrac{c_0}{c} \\ 0 & \text{if } X > \dfrac{c_0}{c} \end{cases} \tag{2.52}$$

$$T^*_{\mathrm{b2}}(X,1) = 0 \tag{2.53}$$

The combination of equations (2.46) to (2.53) and the addition of both solutions lead to the non-dimensional temperature field in the evaporator body:

$$\begin{aligned} T_{\mathrm{b}}^{*}(X,Y) = {} & C_{01}Y + C_{02} \\ & + \sum_{m=1}^{\infty} \left(C_{\mathrm{m1}} e^{m\pi DY} + C_{\mathrm{m2}} e^{-m\pi DY} \right) cos(m\pi X) \end{aligned} \tag{2.54}$$

with

$$\begin{aligned} C_{01} = {} & \frac{Bi_{\mathrm{b}}}{Bi_{\mathrm{b}}+1} \frac{\lambda_{\mathrm{b}}}{\varphi_0 d} \left(\left(T_{\mathrm{e}} - T_{\mathrm{r}}\right) \frac{c_0 + c_1}{2c} + \left(T_{\mathrm{r}} - T_{\mathrm{ext}}\right) \right) \\ & - \frac{c_0}{c} \frac{\varphi_{\mathrm{in}}}{\varphi_0} \end{aligned} \tag{2.55}$$

$$\begin{aligned} C_{02} = {} & \frac{1}{Bi_{\mathrm{b}}+1} \frac{\lambda_{\mathrm{b}}}{\varphi_0 d} \left(\left(T_{\mathrm{e}} - T_{\mathrm{r}}\right) \frac{c_0 + c_1}{2c} - Bi_{\mathrm{b}} \left(T_{\mathrm{r}} - T_{\mathrm{ext}}\right) \right) \\ & + \frac{c_0}{c} \frac{\varphi_{\mathrm{in}}}{\varphi_0} \end{aligned} \tag{2.56}$$

$$\begin{aligned} C_{\mathrm{m1}} = {} & 2 \frac{\lambda_{\mathrm{b}}}{\varphi_0 d} \frac{T_{\mathrm{e}} - T_{\mathrm{r}}}{m^2\pi^2} \frac{c}{c_1 - c_0} \frac{\cos\left(m\pi \frac{c_0}{c}\right) - \cos\left(m\pi \frac{c_1}{c}\right)}{e^{m\pi D} + \frac{m\pi D + Bi_{\mathrm{b}}}{m\pi D - Bi_{\mathrm{b}}} e^{-m\pi D}} \\ & - 2 \frac{\varphi_{\mathrm{in}}}{\varphi_0} \frac{1}{m^2\pi^2 D} \sin\left(m\pi \frac{c_0}{c}\right) \frac{1}{1 + e^{2m\pi D}} \end{aligned} \tag{2.57}$$

$$\begin{aligned} C_{\mathrm{m2}} = {} & 2 \frac{\lambda_{\mathrm{b}}}{\varphi_0 d} \frac{T_{\mathrm{e}} - T_{\mathrm{r}}}{m^2\pi^2} \frac{c}{c_1 - c_0} \frac{\cos\left(m\pi \frac{c_0}{c}\right) - \cos\left(m\pi \frac{c_1}{c}\right)}{e^{-m\pi D} + \frac{m\pi D - Bi_{\mathrm{b}}}{m\pi D + Bi_{\mathrm{b}}} e^{m\pi D}} \\ & + 2 \frac{\varphi_{\mathrm{in}}}{\varphi_0} \frac{1}{m^2\pi^2 D} \sin\left(m\pi \frac{c_0}{c}\right) \frac{1}{1 + e^{-2m\pi D}} \end{aligned} \tag{2.58}$$

The heat dissipated to the ambient in the evaporator section of the body is:

$$\begin{aligned} Q_{\mathrm{ext,e}} = {} & \int_0^{c_0} h_{\mathrm{ext}} \pi x \left(T_{\mathrm{b}}(x,0) - T_{\mathrm{ext}}\right) dx \\ & + \int_{c_0}^{c_1} h_{\mathrm{ext}} \pi c_0 \left(T_{\mathrm{b}}(x,0) - T_{\mathrm{ext}}\right) dx \\ = {} & h_{\mathrm{ext}} \pi c_0 \left(c_1 - \frac{c_0}{2}\right) \left(T_{\mathrm{r}} - T_{\mathrm{ext}} + \frac{\varphi_0 d}{\lambda_{\mathrm{b}}} C_{02}\right) \\ & + h_{\mathrm{ext}} \pi \frac{\varphi_0 d}{\lambda_{\mathrm{b}}} \sum_{m=1}^{\infty} \left(C_{\mathrm{m1}} + C_{\mathrm{m2}}\right) \frac{c}{m\pi} \\ & \times \left(\frac{c}{m\pi} \left(-1 + \cos\left(\frac{m\pi c_0}{2}\right)\right) + \frac{c_0}{m\pi} \sin\left(m\pi \frac{c_1}{c}\right) \right) \end{aligned} \tag{2.59}$$

The heat transferred by thermal conduction through the evaporator body to the reservoir section is calculated by integrating the Fourier's law at $y = c_1$ (Fig. 2.4). Thus, the total heat losses through the body is:

$$Q_{\mathrm{b}} = Q_{\mathrm{ext,e}} + \int_0^d -\pi c_0 \lambda_{\mathrm{b}} \left.\frac{\partial T_{\mathrm{b}}}{\partial x}\right|_{x=c_1} dy \tag{2.60}$$

$$
\begin{aligned}
&= Q_{\text{ext,e}} + dc_0\varphi_0 \sum_{m=1}^{\infty} \pi \sin\left(m\pi\frac{c_1}{c}\right) \\
&\quad \times \left(C_{\text{m1}}\left(e^{m\pi D}-1\right) - C_{\text{m2}}\left(e^{-m\pi D}-1\right)\right)
\end{aligned}
$$

2.1.3.2 Cylindrical evaporator 3D analysis

A cylindrical evaporator is also modelled using a similar approach but with a 3D analysis. As shown in Figure 2.5, the evaporator is “unwrapped” and only a half of it is modelled because of the symmetry. The half cylinder is approximated by a flat structure to simplify the equations and to obtain Fourier series[1]. Thus, the heat transfer equation is solved in Cartesian coordinates rather than in cylindrical coordinates. With such a hypothesis, the wick (red zone) can be modelled with the method from subsection 2.1.2. However, for the evaporator envelope (blue zone), a 3D approach is chosen to thoroughly take into account heat transfer from the heated zone to the reservoir and heat losses to the ambient. One has to notice that the heated zone does not cover the entire periphery of the cylinder but only one part of it, connected to a flat saddle where an electric component can be fixed.

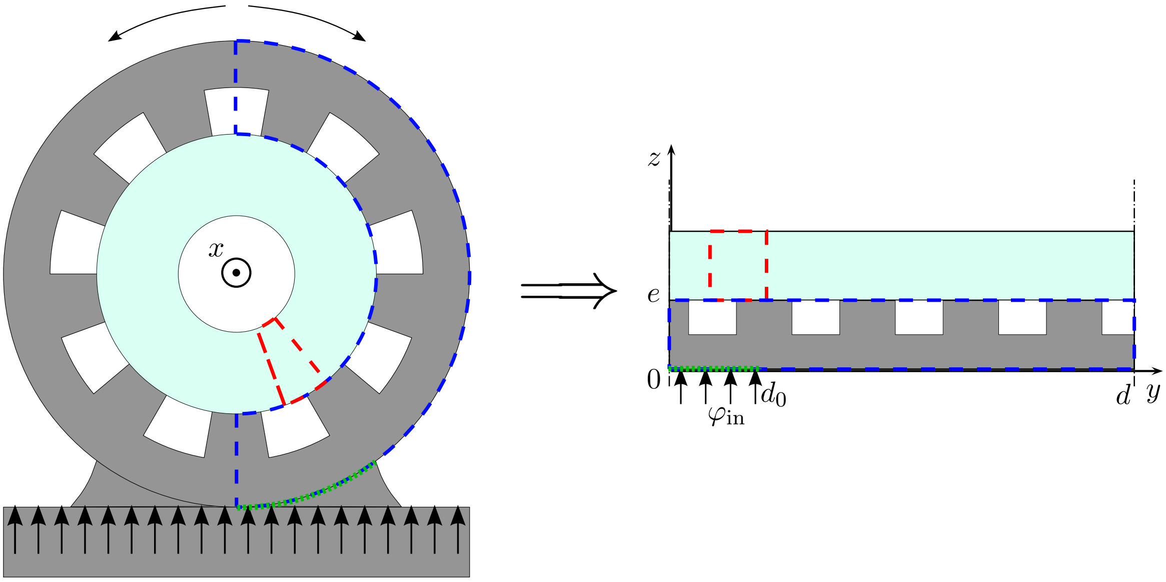

Figure 2.5: Cylindrical evaporator modelling

In the same way as for the two-dimensional model, the sum of two solutions is required to consider all the boundary conditions. As shown in Figure 2.6, the LHP is represented by a basic rectangular parallelepiped. At $y = 0$ and $y = d$, an adiabatic condition is assumed due to the symmetry. An adiabatic condition is also adopted at $x = 0$ and $x = c$, considering no heat losses at both ends of the evaporator body. At $z = 0$, a convective heat transfer with the ambient is taken into account on the entire external surface of the evaporator and an additional heat flux φ_{in} is applied on a part of the surface ($x < c_0$ and $y < d_0$). For the inner

---

[1] A more accurate development could be undertaken with a cylindrical geometry and a Bessel series expansion [147].

part of the body ($z = e$), the reservoir temperature T_r is set for the reservoir side ($x > c_1$) and a temperature profile dependent on y is the condition for the rest.

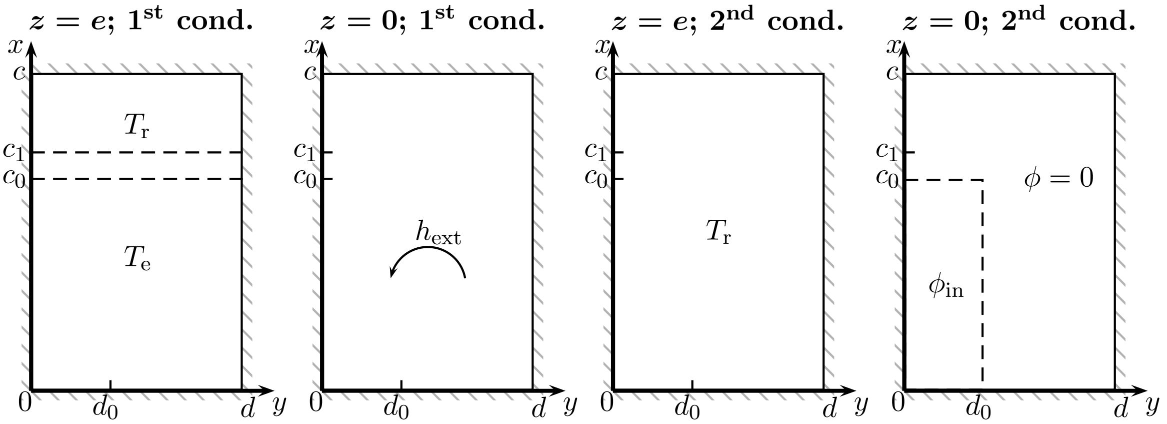

Figure 2.6: Evaporator body boundary conditions

The 3-D stationary heat transfer equation in the evaporator wall is expressed as:

$$\frac{\partial^2 T_\mathrm{b}}{\partial x^2} + \frac{\partial^2 T_\mathrm{b}}{\partial y^2} + \frac{\partial^2 T_\mathrm{b}}{\partial z^2} = 0 \tag{2.61}$$

The non-dimensional temperature T_b^* is defined as:

$$T_\mathrm{b}^* = \frac{\lambda_\mathrm{b}\left(T_\mathrm{b} - T_\mathrm{r}\right)}{\varphi_0 e} \tag{2.62}$$

and leads to:

$$\frac{\partial^2 T_\mathrm{b}^*}{\partial X^2} + \frac{1}{D^2}\frac{\partial^2 T_\mathrm{b}^*}{\partial Y^2} + \frac{1}{E^2}\frac{\partial^2 T_\mathrm{b}^*}{\partial Z^2} = 0 \tag{2.63}$$

with

$$X = \frac{x}{c}, \qquad Y = \frac{y}{d}, \qquad Z = \frac{z}{e}, \qquad D = \frac{d}{c}, \qquad E = \frac{e}{c} \tag{2.64}$$

The 3D Fourier expansion of the temperature field in the body is:

$$\begin{aligned} T_\mathrm{b}^*(X,Y,Z) &= \sum_{m=1}^{\infty}\sum_{n=1}^{\infty} A_\mathrm{mn}(Z) sin(m\pi X) sin(n\pi Y) \\ &+ \sum_{m=1}^{\infty}\sum_{n=0}^{\infty} A'_\mathrm{mn}(Z) sin(m\pi X) cos(n\pi Y) \\ &+ \sum_{m=0}^{\infty}\sum_{n=1}^{\infty} B'_\mathrm{mn}(Z) cos(m\pi X) sin(n\pi Y) \\ &+ \sum_{m=0}^{\infty}\sum_{n=0}^{\infty} B_\mathrm{mn}(Z) cos(m\pi X) cos(n\pi Y) \end{aligned} \tag{2.65}$$

For $X = 0$, $X = 1$, $Y = 0$ and $Y = 1$, an adiabatic boundary condition is considered:

$$\left.\frac{\partial T_{\mathrm{b}}^*}{\partial X}\right|_{X=0} = \left.\frac{\partial T_{\mathrm{b}}^*}{\partial X}\right|_{X=1} = \left.\frac{\partial T_{\mathrm{b}}^*}{\partial Y}\right|_{Y=0} = \left.\frac{\partial T_{\mathrm{b}}^*}{\partial Y}\right|_{Y=1} = 0 \tag{2.66}$$

Eq. (2.65) then becomes:

$$T_{\mathrm{b}}^*(X,Y,Z) = \sum_{m=0}^{\infty}\sum_{n=0}^{\infty} B_{\mathrm{mn}}(Z)cos(m\pi X)cos(m\pi Y) \tag{2.67}$$

Combining Eq. (2.63) and (2.67) yields:

$$\frac{\partial^2 B_{\mathrm{mn}}(Z)}{\partial Z^2} - E^2\pi^2\left(m^2 + \frac{n^2}{D^2}\right)B_{\mathrm{mn}}(Z) = 0 \tag{2.68}$$

Solving the previous differential equation leads to:

$$B_{00}(Z) = B_{001}Z + B_{002} \quad \text{if} \quad m = n = 0 \tag{2.69}$$

$$B_{\mathrm{mn}}(Z) = B_{\mathrm{mn1}}e^{E\pi GZ} + B_{\mathrm{mn2}}e^{-E\pi GZ} \quad \text{else} \tag{2.70}$$

$$\text{with} \quad G = \sqrt{m^2 + \frac{n^2}{D^2}} \tag{2.71}$$

The boundary conditions for the first solution T_{b1}^* are:

$$\begin{aligned} \left.\frac{\partial T_{\mathrm{b1}}^*}{\partial Z}\right|_{Z=0} &= Bi_{\mathrm{b}}T_{\mathrm{b1}}^* + \frac{h_{\mathrm{ext}}}{\varphi_0}\left(T_{\mathrm{r}} - T_{\mathrm{ext}}\right) \\ \text{with} \qquad Bi_{\mathrm{b}} &= \frac{eh_{\mathrm{ext}}}{\lambda_{\mathrm{b}}} \end{aligned} \tag{2.72}$$

$$T_{\mathrm{b1}}^*(X,Y,1) = \begin{cases} \dfrac{\lambda_{\mathrm{b}}}{\varphi_0 e}\left(T_{\mathrm{e}} - T_{\mathrm{r}}\right) & \text{if } 0 < X \leqslant \dfrac{c_0}{c} \\ \dfrac{\lambda_{\mathrm{b}}}{\varphi_0 e}\left(T_{\mathrm{e}} - T_{\mathrm{r}}\right)\dfrac{c_1 - cX}{c_1 - c_0} & \text{if } \dfrac{c_0}{c} < X \leqslant \dfrac{c_1}{c} \\ 0 & \text{if } \dfrac{c_1}{c} < X < 1 \end{cases} \tag{2.73}$$

whereas for the second solution T_{b2}^*:

$$\left.\frac{\partial T_{\mathrm{b2}}^*}{\partial Z}\right|_{Z=0} = \begin{cases} -\dfrac{\varphi_{\mathrm{in}}}{\varphi_0} & \text{if } 0 < X < \dfrac{c_0}{c} \quad \text{and} \quad 0 < Y < \dfrac{d_0}{d} \\ 0 & \text{else} \end{cases} \tag{2.74}$$

$$T_{\mathrm{b2}}^*(X,Y,1) = 0 \tag{2.75}$$

The combination of Eq. (2.63) to (2.75) and the addition of both solutions lead to the non-dimensional temperature field in the evaporator body:

$$\begin{aligned} T^*_{\mathrm{b}}(X,Y,Z) = & B_{001}Z + B_{002} \\ & + \sum_{m=1}^{\infty} \left(B_{\mathrm{m01}} e^{E\pi GZ} + B_{\mathrm{m02}} e^{-E\pi GZ}\right) cos(m\pi X) \\ & + \sum_{n=1}^{\infty} \left(B_{\mathrm{0n1}} e^{E\pi GZ} + B_{\mathrm{0n2}} e^{-E\pi GZ}\right) cos(n\pi Y) \\ & + \sum_{m=1}^{\infty}\sum_{n=1}^{\infty} \left(B_{\mathrm{mn1}} e^{E\pi GZ} + B_{\mathrm{mn2}} e^{-E\pi GZ}\right) cos(m\pi X) cos(n\pi Y) \end{aligned} \tag{2.76}$$

with

$$B_{001} = \frac{Bi_{\mathrm{b}}}{Bi_{\mathrm{b}}+1}\frac{\lambda_{\mathrm{b}}}{\varphi_0 e}\left(\left(T_{\mathrm{e}}-T_{\mathrm{r}}\right)\frac{c_0+c_1}{2c} + \left(T_{\mathrm{r}}-T_{\mathrm{ext}}\right)\right) - \frac{c_0 d_0 \varphi_{\mathrm{in}}}{c d \varphi_0} \tag{2.77}$$

$$B_{002} = \frac{1}{Bi_{\mathrm{b}}+1}\frac{\lambda_{\mathrm{b}}}{\varphi_0 e}\left(\left(T_{\mathrm{e}}-T_{\mathrm{r}}\right)\frac{c_0+c_1}{2c} - Bi_{\mathrm{b}}\left(T_{\mathrm{r}}-T_{\mathrm{ext}}\right)\right) + \frac{c_0 d_0 \varphi_{\mathrm{in}}}{c d \varphi_0} \tag{2.78}$$

$$\begin{aligned} B_{\mathrm{m01}} = & \frac{2}{m^2\pi^2}\frac{c}{c_1-c_0}\frac{\lambda_{\mathrm{b}}}{\varphi_0 e}\left(T_{\mathrm{e}}-T_{\mathrm{r}}\right)\frac{\left(\cos\left(m\pi\frac{c_0}{c}\right)-\cos\left(m\pi\frac{c_1}{c}\right)\right)}{e^{E\pi G} + e^{-E\pi G}\left(\frac{E\pi G - Bi_{\mathrm{b}}}{E\pi G + Bi_{\mathrm{b}}}\right)} \\ & - \frac{2\frac{d_0}{d}\frac{\varphi_{\mathrm{in}}}{\varphi_0}\frac{1}{m\pi}\sin\left(m\pi\frac{c_0}{c}\right)}{E\pi G\left(1+e^{2E\pi G}\right)} \end{aligned} \tag{2.79}$$

$$\begin{aligned} B_{\mathrm{m02}} = & \frac{2}{m^2\pi^2}\frac{c}{c_1-c_0}\frac{\lambda_{\mathrm{b}}}{\varphi_0 e}\left(T_{\mathrm{e}}-T_{\mathrm{r}}\right)\frac{\left(\cos\left(m\pi\frac{c_0}{c}\right)-\cos\left(m\pi\frac{c_1}{c}\right)\right)}{e^{-E\pi G} + e^{E\pi G}\left(\frac{E\pi G + Bi_{\mathrm{b}}}{E\pi G - Bi_{\mathrm{b}}}\right)} \\ & + \frac{2\frac{d_0}{d}\frac{\varphi_{\mathrm{in}}}{\varphi_0}\frac{1}{m\pi}\sin\left(m\pi\frac{c_0}{c}\right)}{E\pi G\left(1+e^{-2E\pi G}\right)} \end{aligned} \tag{2.80}$$

$$B_{\mathrm{0n1}} = -\frac{2\frac{c_0}{c}\frac{\varphi_{\mathrm{in}}}{\varphi_0}\frac{1}{n\pi}\sin\left(n\pi\frac{d_0}{d}\right)}{E\pi G\left(1+e^{2E\pi G}\right)} \tag{2.81}$$

$$B_{\mathrm{0n2}} = +\frac{2\frac{c_0}{c}\frac{\varphi_{\mathrm{in}}}{\varphi_0}\frac{1}{n\pi}\sin\left(n\pi\frac{d_0}{d}\right)}{E\pi G\left(1+e^{-2E\pi G}\right)} \tag{2.82}$$

$$B_{\mathrm{mn1}} = -\frac{4\frac{\varphi_{\mathrm{in}}}{\varphi_0}\frac{1}{mn\pi^2}\sin\left(m\pi\frac{c_0}{c}\right)\sin\left(n\pi\frac{d_0}{d}\right)}{E\pi G\left(1+e^{2E\pi G}\right)} \tag{2.83}$$

$$B_{\mathrm{mn2}} = +\frac{4\frac{\varphi_{\mathrm{in}}}{\varphi_0}\frac{1}{mn\pi^2}\sin\left(m\pi\frac{c_0}{c}\right)\sin\left(n\pi\frac{d_0}{d}\right)}{E\pi G\left(1+e^{-2E\pi G}\right)} \tag{2.84}$$

2.1.4 Complete analytical model solving procedure

The solving procedure is presented in Figure 2.7. The set of equations is not linear. Thus, an iterative procedure is used to solve it. After initialisation of the parameters of the model, the two-phase length in the condenser $L_{2\varphi}$ is set, according to the energy balance for a given heat input Q_{in} (2.18). $L_{2\varphi}$ has a major influence on the determination of the temperature of the liquid entering in the reservoir $T_{\mathrm{r,i}}$ (equations 2.16-2.17). Then, the thermophysical properties are calculated, as well as the pressure drops in the transport lines.

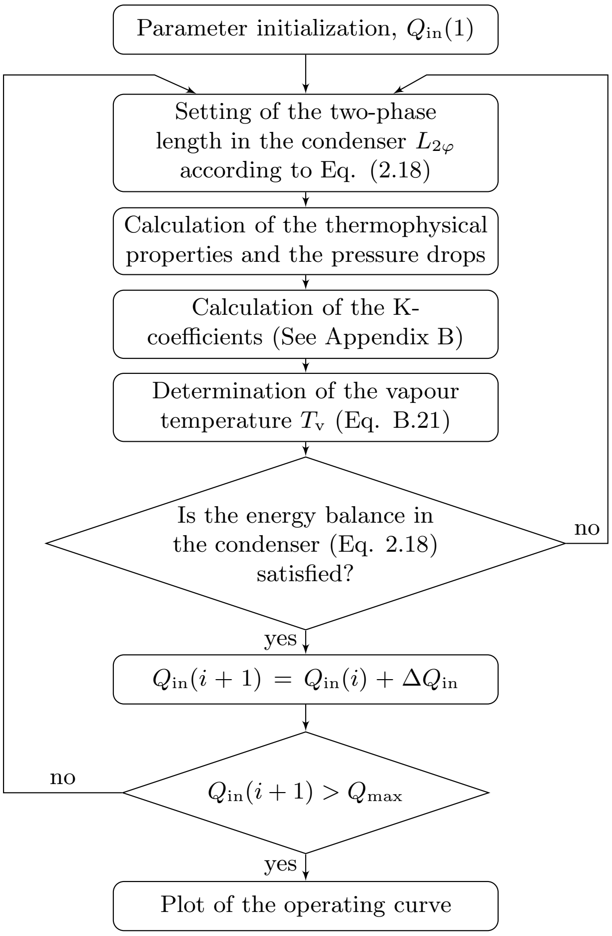

Figure 2.7: Solving algorithm flowchart

K-coefficients can be defined to reformat the expression of Q_{w}, Q_{ev}, Q_{b} and $T_{\mathrm{r,i}}$ as functions of T_{r}, T_{v}, T_{e} and T_{we}:

$$Q_{\mathrm{w}} = K_1 T_{\mathrm{r}} + K_2 T_{\mathrm{v}} + K_3 T_{\mathrm{we}} \quad \text{using (2.34,2.36,2.37,2.44)} \tag{2.85}$$

$$Q_{\mathrm{ev}} = K_4 T_{\mathrm{r}} + K_5 T_{\mathrm{v}} + K_6 T_{\mathrm{we}} \quad \text{using (2.34,2.36,2.37,2.45)} \tag{2.86}$$

$$Q_{\mathrm{ext,e}} = K_{10} T_{\mathrm{r}} + K_{11} T_{\mathrm{e}} + K_{12} \quad \text{using (2.56,2.57,2.58,2.59)} \tag{2.87}$$

$$Q_{\mathrm{b}} = K_7 T_{\mathrm{r}} + K_8 T_{\mathrm{e}} + K_9 \quad \text{using (2.57,2.58,2.60,2.87)} \tag{2.88}$$

$$T_{\mathrm{r,i}} = K_{13} T_{\mathrm{v}} + K_{14} \quad \text{using (2.16,2.17)} \tag{2.89}$$

The detailed expression of these coefficients is presented in Appendix B. Equations (2.1,2.7-2.11, 2.15-2.17,2.85-2.89) are solved and give a second-order expression which enables to calculate the vapour temperature T_v (Appendix B).

This procedure is iterated until the energy balance is satisfied in the condenser (equation 2.18). The same method is computed for each heat input $Q_\mathrm{in}(i)$ of the operating curve. Since the heat transfer coefficient with the heat sink is generally much lower than the condensation heat transfer coefficient, the condensation thermal resistance is neglected to simplify equation (2.18).

Equation (2.15) is a function of the pressure drops ΔP_v and ΔP_l. These parameters, due to the friction forces in the vapour and the liquid lines, depend on the fluid flow regime. They are calculated as follows:

$$\Delta P = \frac{f}{2\rho D}\left(\frac{\dot{m}_\mathrm{f}}{S_\mathrm{tube}}\right)^2 L \tag{2.90}$$

where S_tube is the cross-section area of the tube. For a smooth tube wall of diameter D and length L and a fully-developed flow, the friction factor f is expressed by [148]:

$$f = \begin{cases} 64/Re & \text{if} \quad Re \leq 2000 \\ 0.032 & \text{if} \quad 2000 < Re < 9150 \\ 0.316 Re^{-0.25} & \text{if} \quad 9150 \leq Re < 20000 \\ 0.184 Re^{-0.2} & \text{if} \quad Re \geq 20000 \end{cases} \tag{2.91}$$

where Re is the Reynolds number.

Equation (2.15) also includes the pressure of non-condensable gases P^*_NCG. In order to take into account the NCG, it is necessary to calculate the liquid level in the reservoir that depends on the heat load. We assume that the void fraction of the two-phase flow in the condenser is 0.5 and that the vapour density is negligible compared to the liquid density. The liquid level e_l in the reservoir is therefore expressed as:

$$e_\mathrm{l} = \frac{1}{S_\mathrm{w}}\left(\frac{m_\mathrm{f}}{\rho_\mathrm{l}} - \varepsilon S_\mathrm{w} e_\mathrm{w} - \frac{L_\mathrm{l}\pi D^2_\mathrm{l,i}}{4} - \frac{(L_\mathrm{c} - \frac{1}{2}L_{2\varphi})\pi D^2_\mathrm{c,i}}{4}\right) \tag{2.92}$$

where m_f is the total fluid charge in the system and e_w is the wick thickness. The total volume of NCG and vapour in the reservoir V_v is equal to:

$$V_\mathrm{v} = S_\mathrm{w}\left(e_\mathrm{r} - e_\mathrm{l}\right) \tag{2.93}$$

with e_r the thickness of the reservoir. Considering the non-condensable gases as ideal gases, their partial pressure is calculated by:

$$P^*_\mathrm{NCG} = \frac{m_\mathrm{NCG}\overline{R}T_\mathrm{r}}{\overline{M}_\mathrm{NCG}V_\mathrm{v}} \tag{2.94}$$

where $\overline{R}$ is the ideal gas constant and m_{NCG} and $\overline{M}_{\mathrm{NCG}}$ are the NCG total mass and the molar mass, respectively.

To solve equations (2.16-2.18), the heat sink heat transfer coefficient h_{sink} is determined in accordance with the condenser design, whereas the heat transfer coefficient of the liquid h_{l} is calculated assuming a laminar fully-developed flow and a constant Nusselt number $Nu_{\mathrm{D}} = 4.36$ [148].

Equations (2.11) and (2.17) depend on the heat transfer coefficient with the ambient h_{ext}. It is given by the correlation of Churchill and Chu [148] for free convection on the surface of an isothermal cylinder:

$$h_{\mathrm{ext}} = \frac{\lambda_{\mathrm{air}}}{D}\left[0.60 + \frac{0.387 Ra_{\mathrm{D}}^{\frac{1}{6}}}{\left(1 + (0.559/Pr)^{\frac{9}{16}}\right)^{\frac{8}{27}}}\right]^2 \tag{2.95}$$

where Pr is the Prandtl number. This correlation is valid for Rayleigh numbers Ra_{D} lower than 10^{12}. The determination of the effective thermal conductivity of the porous structure will be discussed in the next section.

2.2 Standard case

The LHP geometry considered for this analysis is similar to standard systems used for electronic cooling applications. Its geometrical characteristics are based on the experiments of Singh et al. [42] and Choi et al. [61]. The properties of this “ standard” LHP, having a flat disk-shaped evaporator, is defined in Table 2.1. The bold lines correspond to the variable parameters of the sensitivity analysis of the next section. The system is supposed to be in horizontal orientation. The wick is made of nickel and the working fluid is water. The main parameters for the wick are the effective thermal conductivity, the accommodation and the contact thermal resistance between the wick and the casing.

As explained in subsection 1.2.1.2, extensive studies have been undertaken to develop models able to predict accurately the effective thermal conductivity of a porous structure. Thus, many different correlations can be found in the literature to determine the effective thermal conductivity of a porous material (Appendix A). Table 2.2 presents the results obtained for a nickel wick of 75 % porosity saturated with water, using various correlations. For the standard case, an effective thermal conductivity equal to $5\,\mathrm{W \cdot m^{-1} \cdot K^{-1}}$ is chosen, which corresponds to the wick properties of Singh et al. [42].

Based on the work of Choi et al. [61], a constant contact resistance of $10^{-4}\,\mathrm{m^2 \cdot K \cdot W^{-1}}$ is chosen for the standard case.

Although the accommodation coefficient is a key parameter in the determination of the LHP temperature, its value is very difficult to predict. In the literature, several studies are dedicated to the determination of this parameter for various fluids [146]. However, the scattering of the results confirms the difficulty of describing the evaporation accurately. For water,

Evaporator design	Flat disk-shaped
Wick diameter	40 mm
Wick thickness	3 mm
Wick effective thermal conductivity	**$5\,\mathrm{W\cdot m^{-1}\cdot K^{-1}}$**
Vapour groove width	1 mm
Wick-wall contact resistance	**$10^{-4}\,\mathrm{K\cdot m^{2}\cdot W^{-1}}$**
Accommodation coefficient	**0.1**
Reservoir depth	10 mm
Evaporator diameter	41 mm
Evaporator wall material	Stainless steel
Working fluid	Water
Fluid charge	7 g
Condenser and transport lines i/o diameters	2/2.4 mm
Transport lines length	200 mm
Condenser length	100 mm
Heat sink temperature	22 °C
Heat transfer coefficient with the heat sink	**$2000\,\mathrm{W\cdot m^{-2}\cdot K^{-1}}$**
Ambient temperature	22 °C
Heat transfer coefficient with the ambient	**$5\,\mathrm{W\cdot m^{-2}\cdot K^{-1}}$**

Table 2.1: Definition of the standard LHP for the sensitivity analysis

Correlation	**λ_{eff} ($\mathrm{W\cdot m^{-1}\cdot K^{-1}}$)**
Alexander	5.82
Chaudhary-Bandhari	4.06
Maxwell	16.96
Parallel scheme	23
Zehner-Schlunder	1.75

Table 2.2: Effective thermal conductivity calculation with a water-saturated nickel wick, 75% porosity

values ranging from 0.01 to 1 have been found. Therefore, an accommodation coefficient equal to 0.1 is chosen for the standard case.

The temperatures at different locations in the LHP are plotted in Figure 2.8 for heat inputs ranging between 10 W and 110 W. A temperature difference of several degrees between T_{e} and T_{we} shows the impact of the thermal contact resistance between the wick and the casing, particularly at high heat inputs. Since the mass flow rates in the transport lines and the condenser are moderate due to the high latent heat of vaporization of water, pressure drops in the loop are not significant. Therefore, the saturation temperatures in the reservoir and in the grooves, T_{r} and T_{v}, are almost equal. The values of $T_{\mathrm{c,o}}$ and $T_{\mathrm{r,i}}$ are also very similar because the heat transfer between the liquid line and the ambient is limited.

A clear transition between the variable conductance mode and the fixed conductance mode is observed around 60 W. For lower heat inputs, the temperature of the liquid exiting the condenser is constant and equal to the heat sink temperature. Above this point, $T_{\mathrm{c,o}}$

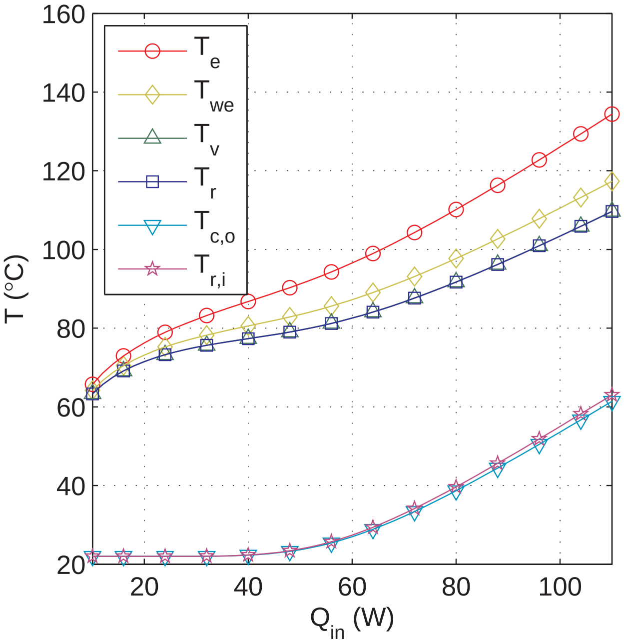

Figure 2.8: Temperature of the LHP in the standard case

starts to increase and the shape of all the temperature curves in the LHP is quasi-linear.

Figure 2.9 presents the distribution of heat transfer in the loop. The largest part (97 %) of the heat input enters the wick whereas the rest is thermally conducted through the evaporator body. Between 87 % and 90 % of the heat load is dissipated by evaporation. The rest is given to the ambient (2 %–8 %) or compensated by the subcooling of the liquid entering the reservoir (6 %–9 %). The sensible heat due to the heating of the liquid between the reservoir and the groove is insignificant since the difference between T_r and T_v is minor. When the heat input Q_in increases, the part of heat that is transferred through the evaporator body and to the ambient decreases. This leads to an increase of both the ratio of heat that enters the wick and the part of heat that is dissipated by evaporation.

Figure 2.10 shows the temperature in the porous structure in the standard case, for a total heat load Q_in of 50 W. For $y = 0\,\mathrm{mm}$, the temperature profile shows a sharp discontinuity at the transition between the groove and the fin. The intense evaporation occurring at $x = 0.5\,\mathrm{mm}$ causes the convergence of the heatlines toward this point and a sharp distortion of the lines in its neighbourhood. As y increases, the temperature profile flattens and the heat flux becomes one-dimensional in the y-direction for $y > 2\,\mathrm{mm}$. Then, the alternation between the fin and the groove does not have any influence and the temperature field in the wick in contact with the liquid bulk of the reservoir is uniform.

As defined in Equation (2.13), the difference between the groove temperature and the reservoir temperature is set only by the pressure losses in the transport lines, the hydrostatic pressure difference and the non-condensable gases partial pressure. Smooth tubes with a relatively large diameter lead to reduced pressure losses. Therefore, the LHP operates with a groove temperature and a reservoir temperature almost equal. As a consequence, the

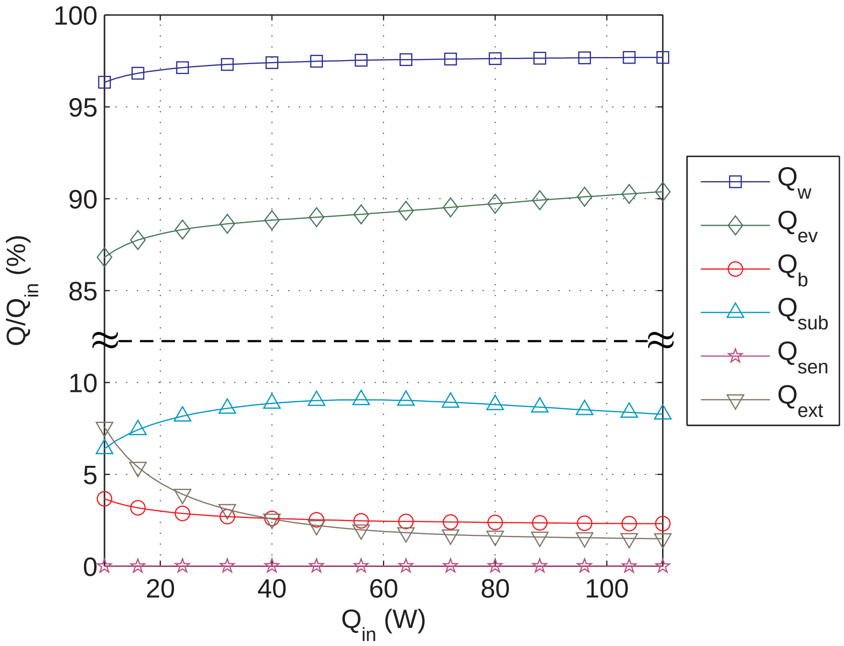

Figure 2.9: Distribution of heat transfer in the LHP

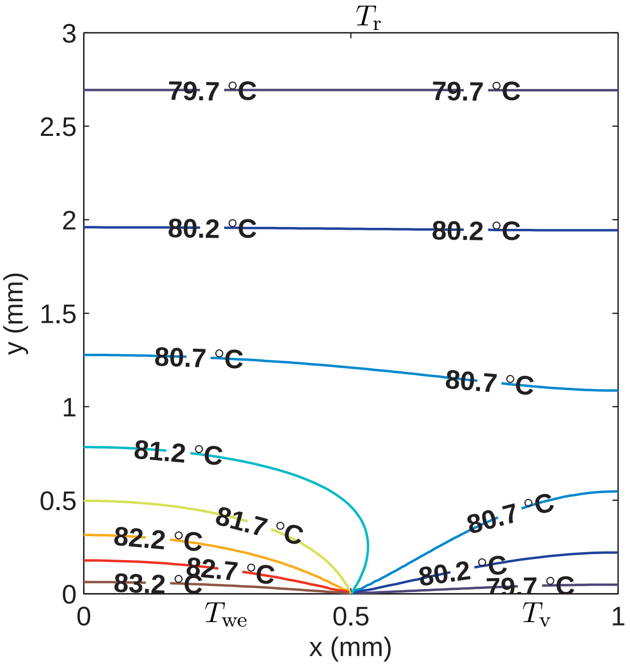

Figure 2.10: 2D temperature field in the wick – $Q_{\text{in}} = 50\,\text{W}$

convective cooling due to the liquid flow in the wick is extremely low and heat transfer in the porous structure is mainly controlled by heat conduction.

2.3 Sensitivity analysis

The LHP operation depends on many distinct parameters: the geometrical design (size, shape) of the system, the thermophysical properties of the working fluid and of the materials of the loop elements, the heat transfer characteristics inside and outside the LHP and the pressure losses in the system. Most of these parameters are easy to determine if the LHP geometry and the working fluid properties are known. However, some parameters are very difficult to determine precisely theoretically as it has been explained in the previous section: the effective thermal conductivity of the wick λ_{eff}, the contact resistance between the wick and the evaporator envelope R_{c} and the accommodation coefficient a_{ev}. Furthermore, the heat sink heat transfer coefficient h_{sink} and the heat transfer coefficient with the ambient h_{ext} are also calculated using correlations being inherently inaccurate. Thus, in the present section, a sensitivity analysis is conducted on these parameters to see their influence on the model.

The sensitivity coefficient S_{i} of the function $T = f(x_{\mathrm{i}}, x_{\mathrm{j}}, x_{\mathrm{k}}, ...)$ in relation to the parameter x_{i} is defined as:

$$S_{\mathrm{i}} = \left.\frac{\partial T}{\partial x_{\mathrm{i}}}\right|_{x_{\mathrm{j}}, x_{\mathrm{k}}, ...} \tag{2.96}$$

In order to compare several parameter sensitivities, it is convenient to define relative sensitivities S_{i}^{*}:

$$S_{\mathrm{i}}^{*} = x_{\mathrm{i}} S_{\mathrm{i}} = x_{\mathrm{i}} \left.\frac{\partial T}{\partial x_{\mathrm{i}}}\right|_{x_{\mathrm{j}}, x_{\mathrm{k}}, ...} \tag{2.97}$$

This coefficient enables to quantify the variation ΔT caused by a relative variation $\Delta x_{\mathrm{i}}/x_{\mathrm{i}}$ of the parameter x_{i}. A greater absolute value of the coefficient means that the function is more sensitive to the parameter.

Unless otherwise mentioned, the sensitivity analysis is conducted with the standard LHP defined in Table 2.1. A slight variation (5 %) of each studied parameter is applied, the value of the other parameters being constant. This effect on the temperatures at different locations of the LHP is predicted by the model.

Figure 2.11 presents the relative sensitivity of T_{e}, T_{v}, $T_{\mathrm{r,i}}$ and $T_{\mathrm{c,o}}$ to the heat transfer coefficient with the ambient. Sensitivities of T_{e} and T_{v} are significant for low heat inputs and decrease with the heat load. Heat transfer with the ambient cools the loop down and leads to a lower operational temperature. The heat flux ratio transferred to the ambient is larger at low heat loads, leading to a higher sensitivity. As expected, h_{ext} does not have any influence on $T_{\mathrm{r,i}}$ and $T_{\mathrm{c,o}}$ in variable conductance mode because their value is only set by the heat sink. For higher heat loads, the increase of the heat losses to the ambient leads to a lower operational temperature. As a consequence, a larger part of the condenser is used to condensate the vapour, the subcooling length in the condenser is smaller and $T_{\mathrm{c,o}}$ increases, inducing an increase of its sensitivity to h_{ext}. The same effect is observed on $T_{\mathrm{r,i}}$, but partially offset by the heat losses from the liquid line to the ambient.

In many experimental configurations, an adequate thermal insulation of the entire LHP

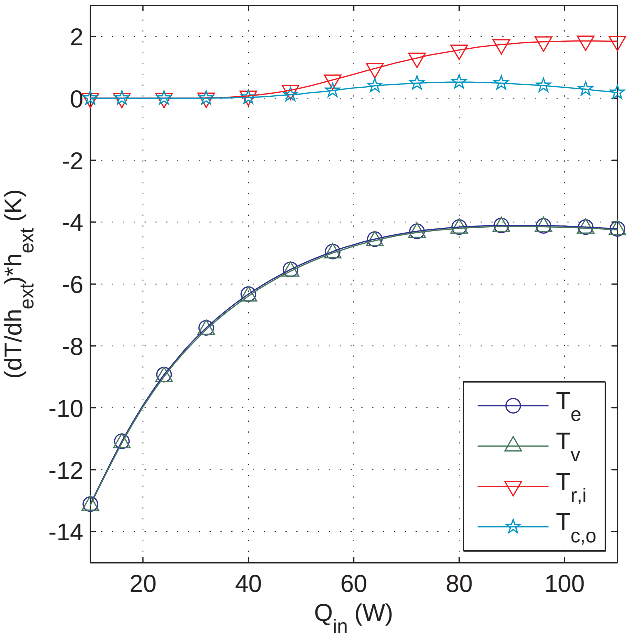

Figure 2.11: Relative sensitivity of the LHP temperatures to h_{ext}

enables to reduce considerably the heat losses to the ambient. In the following, the parameter h_{ext} is set to zero in order to better highlight the effect of the other parameters on the LHP.

The relative sensitivity of the vapour temperature to the other parameters is shown in Figure 2.12. It is clear that heat transfer inside the evaporator (function of the parameters λ_{eff}, R_{c} and a_{ev}) governs the operation in variable conductance mode whereas at high heat loads, h_{sink} becomes the dominant parameter. Indeed, at low heat loads, $T_{\text{c,o}}$ equals T_{sink} so the heat transfer coefficient with the heat sink has no influence on the subcooling of the liquid and on the LHP operation in general. In fixed conductance mode, heat transfer in the condenser sets the LHP operational temperature and the sensitivity of T_{v} to h_{sink} is linear. The parameters a_{ev}, λ_{eff} and R_{c} have a moderate influence on the vapour temperature and this influence decreases as the heat load increases.

The relative sensitivity of T_{e} to the same parameters is shown in Figure 2.13. The influence of the accommodation coefficient and of the heat transfer with the heat sink is almost the same as for T_{v}. However, the sensitivities to R_{c} and λ_{eff} have a different behaviour. While the contact resistance has a limited effect on T_{v}, its influence on T_{e} is large and increases with the heat input. Indeed, the difference between T_{e} and T_{we} is proportional to the heat transfer rate Q_{w} and to R_{c}. As the heat input Q_{in} increases, Q_{w} increases almost linearly and leads to a higher sensitivity of T_{e} to the contact resistance.

The particular shape of the relative sensitivity of T_{e} to λ_{eff} is discussed in the following; it requires a more detailed analysis on the effect of λ_{eff} on the LHP thermal behaviour.

Figure 2.14 shows the variation of the vapour temperature with the effective thermal conductivity of the wick for several heat loads. An optimal value of λ_{eff} is found between 1 and $2\,\mathrm{W\cdot m^{-1}\cdot K^{-1}}$ whatever the heat input. This minimum value of T_{v} is a consequence of

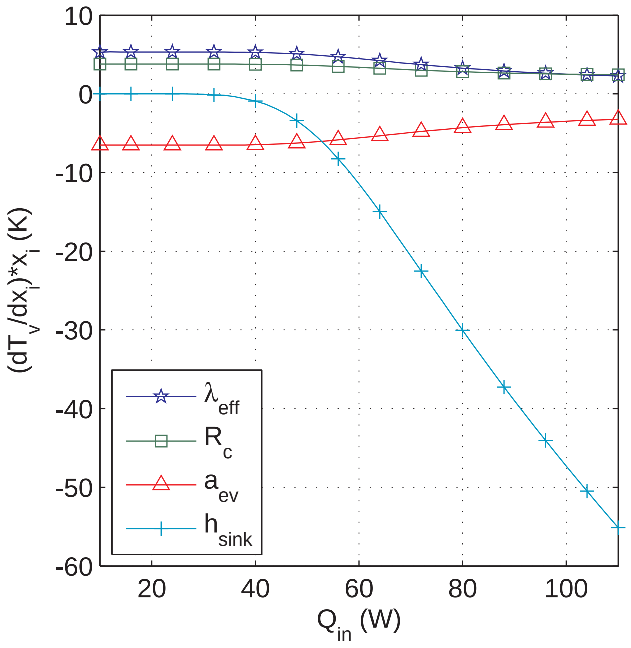

Figure 2.12: Relative sensitivity of T_v to various parameters

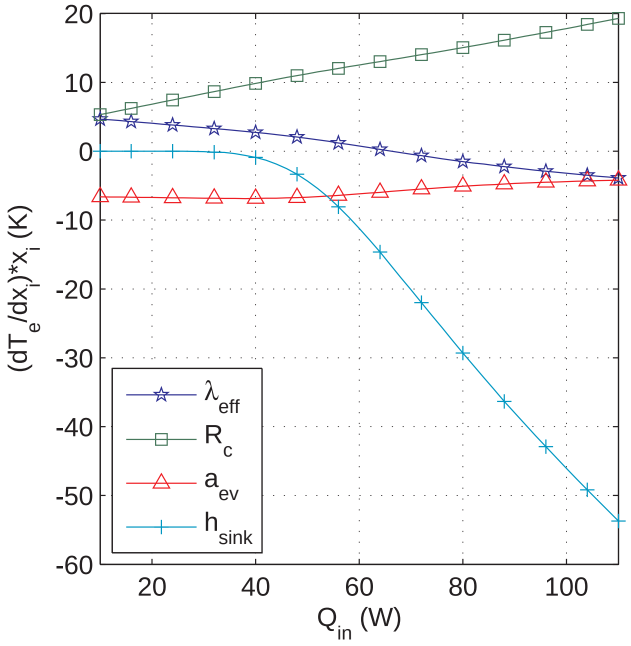

Figure 2.13: Relative sensitivity of T_e to various parameters

the evolution of the heat transferred from the casing to the evaporation zone. As the thermal conductivity of the wick increases, the heat entering the wick becomes larger at the expense of the longitudinal parasitic heat flux. Figure 2.15 shows the distribution of heat transfer in the evaporator. The largest part of the heat load Q_in enters the wick (Q_w), whereas the rest is thermally conducted through the evaporator body (Q_b). When the value of λ_eff is very low, increasing the conductivity enhances both the evaporation (Q_{ev}) and the transversal parasitic heat flux ($Q_{\mathrm{w}} - Q_{\mathrm{ev}}$). When λ_{eff} exceeds $1\,\mathrm{W \cdot m^{-1} \cdot K^{-1}}$, the increase of the heat flux entering the wick Q_{w} is smaller, leading to an increase of the transversal parasitic heat flux at the expense of Q_{ev}, that decreases as λ_{eff} becomes larger. The maximum evaporation heat flux leads to a minimum vapour temperature (Figure 2.14).

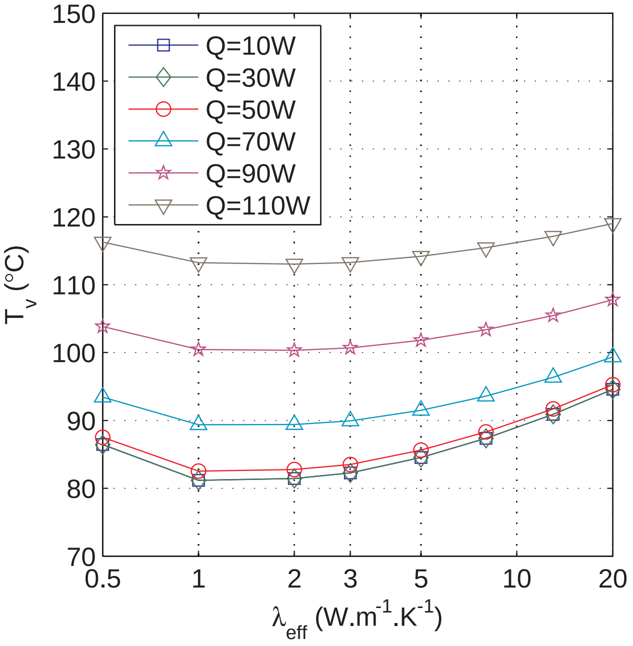

Figure 2.14: Influence of λ_{eff} on T_{v}

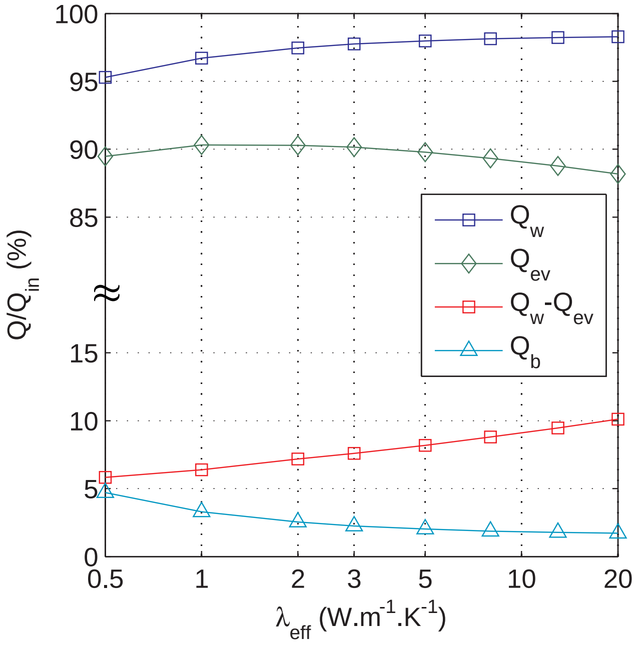

Figure 2.15: Influence of λ_{eff} on Q_{w} and Q_{ev} ($Q_{\mathrm{in}} = 50\,\mathrm{W}$)

The evolution of the temperature difference $T_e - T_v$ with λ_{eff} for several heat inputs is given in Figure 2.16. As expected, this difference decreases when the thermal conductivity of the wick increases. Indeed, a higher value of λ_{eff} leads to lower thermal resistances in the evaporator (Figure 2.1). Figure 2.17 presents the evolution of T_e with λ_{eff}, which is a consequence of the results obtained in figures 2.14 and 2.16. An optimal effective thermal conductivity exists, for which T_e is minimal. However, its value is also dependent on the heat input Q_{in}, contrary to the temperature of the vapour (Figure 2.14). The optimal value of λ_{eff} (obtained for the minimum value of T_e) increases from $2\,\mathrm{W \cdot m^{-1} \cdot K^{-1}}$ to $10\,\mathrm{W \cdot m^{-1} \cdot K^{-1}}$ with the increase of the heat input from 10 W to 110 W. Therefore, there is not an optimal value of the thermal conductivity of the wick but a range of optimal values depending on the heat load.

Figure 2.17 shows that at a given λ_{eff} (for example $5\,\mathrm{W \cdot m^{-1} \cdot K^{-1}}$ in the standard case), the sign of the slope of the temperature curve changes as the heat flux increases. As a consequence, the sign of the sensitivity of T_e to λ_{eff} changes when increasing the heat load, as it is shown in Figure 2.13. This is not the case for T_v, since the minimum of the curves $T_v(\lambda_{\text{eff}})$ does not depend on the heat flux (Figure 2.14).

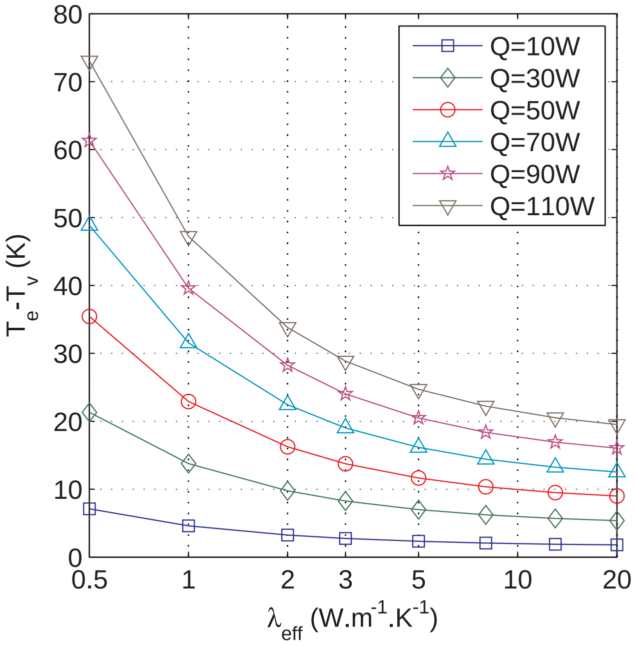

Figure 2.16: Influence of λ_{eff} on $T_e - T_v$

This sensitivity analysis shows that the main parameters of the model are independent from each other. Therefore, their influence can be differentiated from each other. Thus, the availability of precise experimental data of several representative temperatures of the LHP for various heat inputs may theoretically lead to a precise determination of these parameters and provide the model with adequate input parameters. This sensitivity analysis also shows the large influence of the tested parameters on the LHP operation. Their inaccurate determination can lead to a major error on the LHP operation prediction.

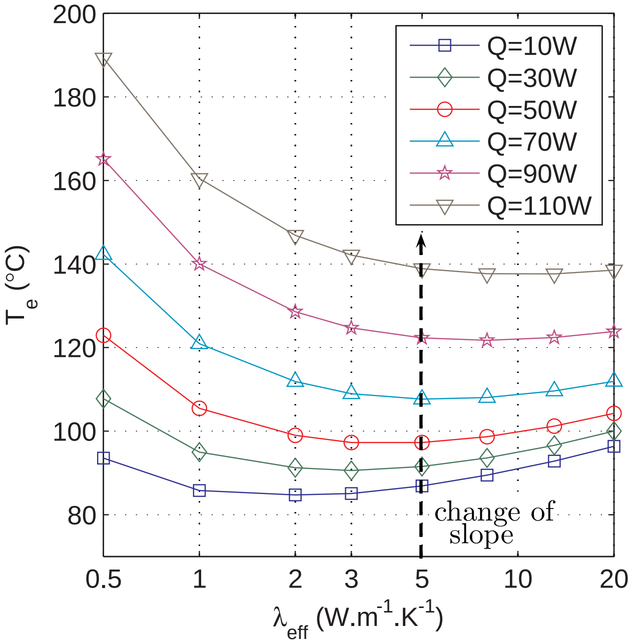

Figure 2.17: Influence of λ_{eff} on T_{e}

2.4 Analytical model validation

The present analytical model is compared to an experimental data set from Singh et al. [42] for a validation purpose. These authors studied the operational characteristics of a flat disk-shaped evaporator LHP, 30 mm in diameter, using water as working fluid. The 3 mm thick porous wick is made of sintered nickel and its thermal effective conductivity is considered equal to about $5.87\,\mathrm{W}\cdot\mathrm{m}^{-1}\cdot\mathrm{K}^{-1}$ using Alexander's formula and based on Singh et al.'s study [48]:

$$\lambda_{\text{eff}} = \lambda_{\text{l}} \left(\frac{\lambda_{\text{l}}}{\lambda_{\text{wm}}}\right)^{-(1-\varepsilon)^{0.59}} \tag{2.98}$$

where λ_{l} and λ_{wm} are the thermal conductivities of the liquid and of the wick material respectively and ε is the porosity, equal to 75 %. The wick is embedded in a copper evaporator. The vapour and liquid lines, of internal diameter 2 mm, are 150 mm and 290 mm long respectively. A fin-and-tube condenser, 50 mm long, dissipates heat by forced convection of air at ambient temperature (*i.e.* 22 °C). No parasitic heat transfer through the evaporator body is taken into account, since an O-ring seal prevents heat conduction to the reservoir. Figure 2.18 shows the comparison between the experimental results and the calculated temperatures of the evaporator wall and of the vapour in the grooves. A good agreement is found between the experimental data and the model.

Several unknown parameters were identified by comparison of the predicted values with the experimental data of Singh et al.: the heat transfer coefficient between the condenser wall and the heat sink, the thickness of the evaporator body, the contact resistance and the accommodation coefficient. As a result, a straight-tube equivalent condenser is simulated with

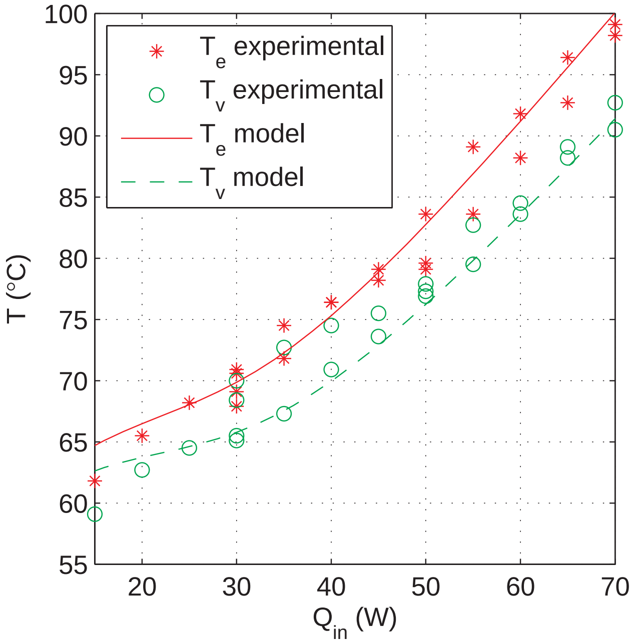

Figure 2.18: Comparison between the model and data from Singh *et al.* [42]

a heat transfer coefficient h_{sink} fixed to $3.2\,\text{kW}\cdot\text{m}^{-2}\cdot\text{K}^{-1}$, considering an outside diameter of 2.4 mm for the tubes. The accommodation coefficient is equal to 0.4. The value of R_c is set to $10^{-5}\,\text{K}\cdot\text{m}^2\cdot\text{W}^{-1}$. The value of R_c that enables to fit at best the results is very small, but it has to be noted that T_v is not really the experimental measurement of the vapour temperature, but the temperature of the tube at the exit of the evaporator. Therefore, these experimental results are not sufficient to estimate accurately the parameters. Nevertheless, the order of magnitude of the parameters are close to the one defined for the standard case. This shows that the model could be used to estimate adequately and independently the parameters of the LHP with accurate temperature measurements.

2.5 Parametric study

A parametric study is presented in this section, based on the analytical model previously described. In practice, many parameters are dependent from each other and the variation of one of them influences the other. For instance, the choice of the working fluid determines also the accommodation coefficient, the wick effective thermal conductivity, the influence of NCGs and may also induce a change of casing and wick materials for compatibility reasons. However, this analysis is conducted for the standard case and only one parameter varies at once in an effort to understand the particular effect of each of the parameters on the evaporator temperature separately.

2.5.1 Influence of the accommodation coefficient

Figure 2.19 shows the variation of T_e with the heat load for various values of the accommodation coefficient ranging from 0.01 to 1. As explained before, a lower value of a_{ev} induces a lower evaporation rate in the evaporator. As a consequence, parasitic heat fluxes increase and the loop operates at a higher temperature. The difference can be of more than 30 K and is larger in variable conductance mode, for which the LHP is particularly controlled by heat transfer in the evaporator/reservoir structure. However, the general shape of the operating curve remains the same.

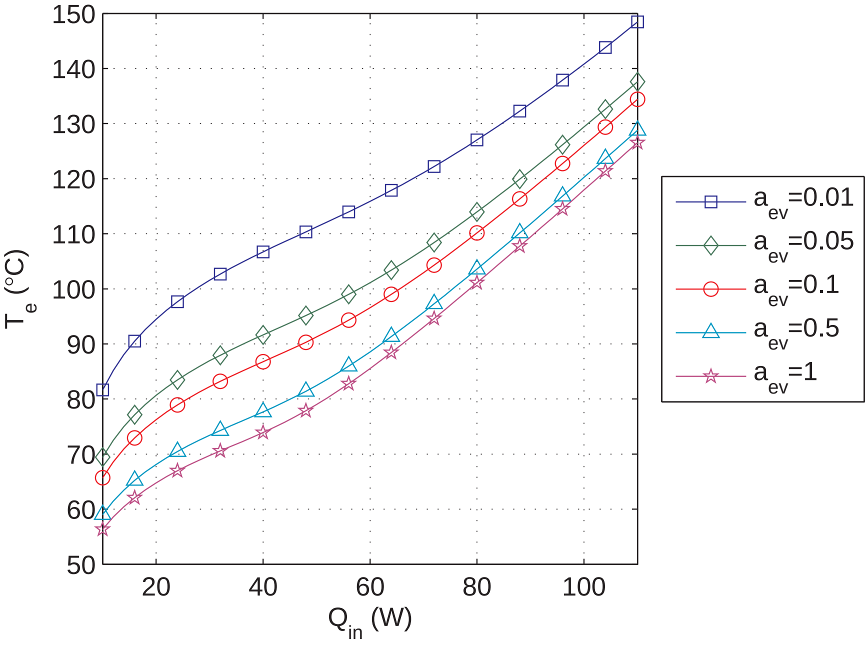

Figure 2.19: Influence of the accommodation coefficient on the evaporator temperature

2.5.2 Influence of the wick effective thermal conductivity

The influence of the wick effective thermal conductivity on the evaporator temperature is shown in Figure 2.20. As explained in subsection 1.2.1.2, theoretical expressions developed in the literature fail to accurately determine the effective thermal conductivity of a porous material saturated with liquid. The figure shows an optimal value of λ_{eff}, as it was previously discussed in section 2.3. A low thermal conductivity, for instance for polymer wicks, leads to a higher evaporator temperature for almost the entire heat input range. The effect is more pronounced for high heat loads. An increase of the wick conductivity enables a better evaporation rate and thus a lower operational temperature. However, at low heat input, the transversal parasitic heat flux is larger and may reduce the performance of the LHP.

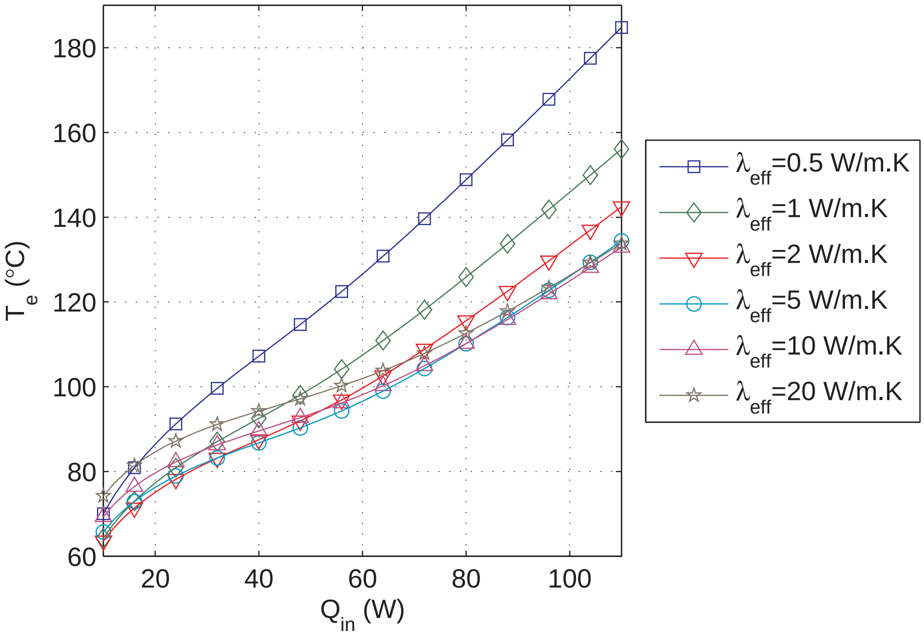

Figure 2.20: Influence of the wick effective thermal conductivity on the evaporator temperature

2.5.3 Influence of the evaporator casing thermal conductivity

The influence of the evaporator casing thermal conductivity is presented in Figure 2.21. This parameter affects the longitudinal parasitic heat transfer as well as the heat losses of the evaporator to the ambient whatever the heat load. A high thermal conductive material increases both heat fluxes. Hence, the ratio of the heat load that is actually dissipated by evaporation is lower and the LHP operational temperature increases. Low thermal conductivity materials should be preferred for the casing to prevent the increase of the longitudinal parasitic heat fluxes.

2.5.4 Influence of the contact resistance

Figure 2.22 shows the influence of R_c on the evaporator temperature. The thermal contact between the porous structure and the evaporator casing strongly affects the part of the heat load that actually enters the wick and the one that is thermally conducted through the evaporator casing. Furthermore, a higher value of R_c increases the temperature difference between the evaporator body and the grooves/reservoir. As a consequence, the thermal contact resistance increases T_e whatever the heat load. As shown in the figure, as long as the thermal contact is lower than $10^{-4}\,\mathrm{K \cdot m^2 \cdot W^{-1}}$, the effect is limited. For higher values, this parameter has a major influence on the LHP operation, particularly at high heat inputs. Therefore, a particular care is required in the manufacturing and mounting processes of the LHP in order to ensure a proper mechanical and thermal contact between the wick and the evaporator body, and this whatever the heat load and the thermal expansion effects that can

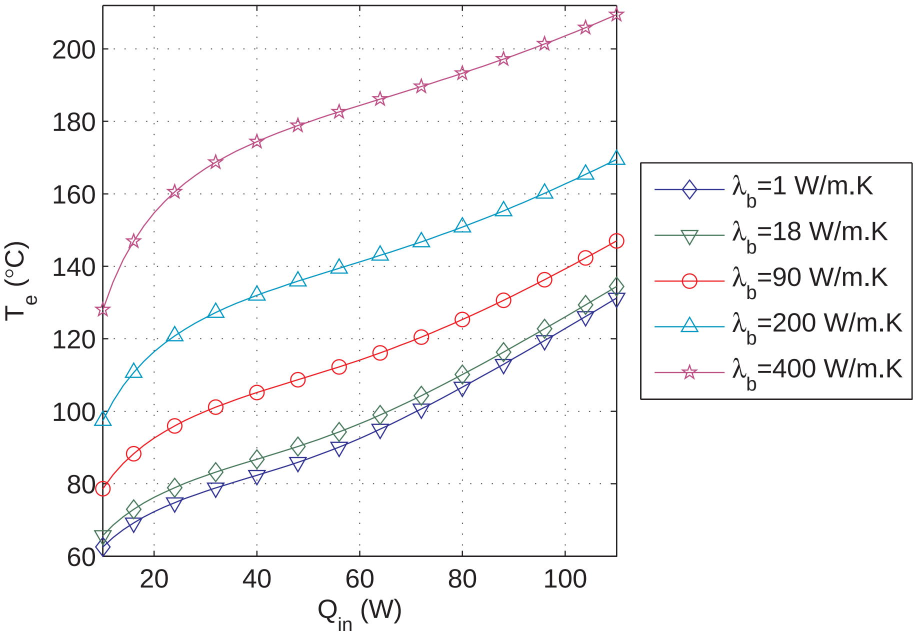

Figure 2.21: Influence of the casing thermal conductivity on the evaporator temperature

occur during operation.

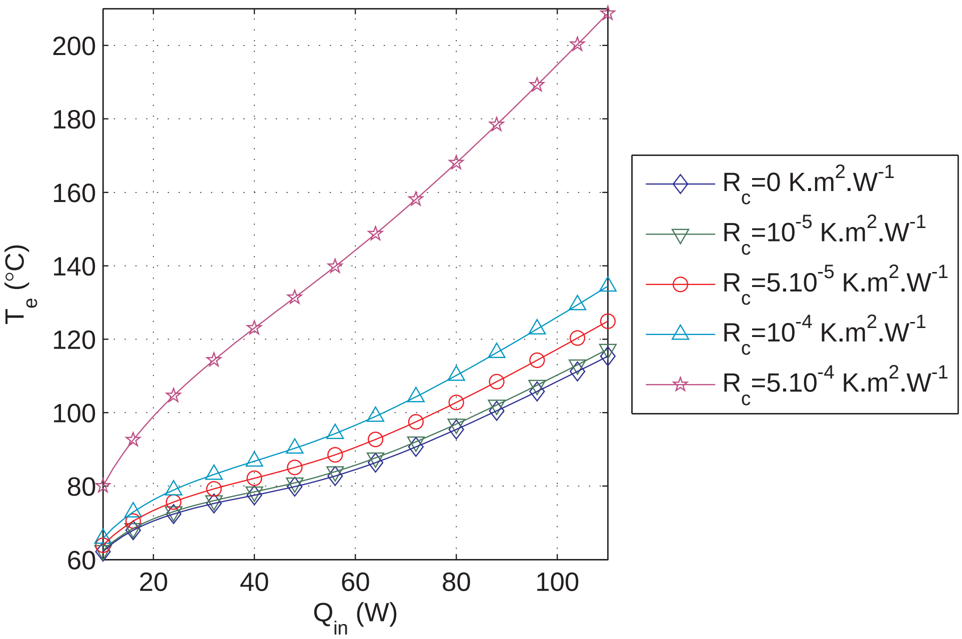

Figure 2.22: Influence of the contact resistance on the evaporator temperature

2.5.5 Influence of the ambient temperature

Figure 2.23 presents the influence of the ambient temperature on the LHP operation, with a constant heat sink temperature of 22 °C. As expected, heat losses to the ambient are mainly of interest at low heat loads, whereas their influence on the evaporator temperature is minor in fixed conductance mode. The global shape of the characteristic curve changes from a constantly increasing temperature with the heat flux to a flattened shape or even a V-shaped curve when the ambient temperature is much higher than the heat sink temperature. When the heat flux is low, the liquid mass flow rate is low too, leading to a larger residence time in the liquid line. Therefore, the reservoir inlet temperature is much more influenced by the ambient.

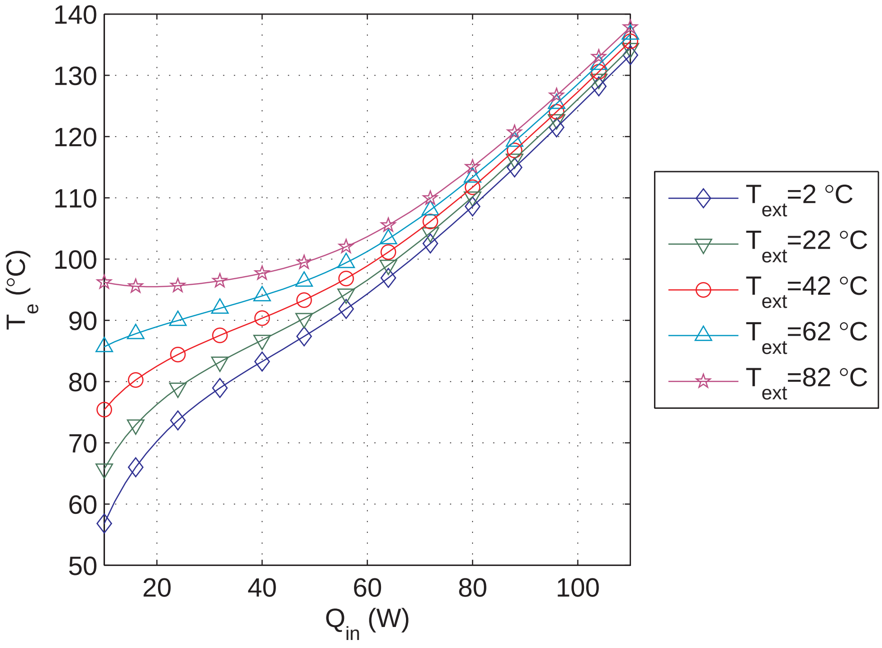

Figure 2.23: Influence of the ambient temperature on the evaporator temperature

2.5.6 Influence of the heat transfer at the condenser

The influence of the heat transfer coefficient with the heat sink on T_e is shown in Figure 2.24. In variable conductance mode, the liquid exits the condenser at the heat sink temperature whatever the heat transfer with the heat sink. Therefore, h_sink does not affect the LHP operation. However, the transition between both operating modes as well as the variation of the evaporator temperature with the heat input in fixed conductance mode is primarily controlled by the heat transfer coefficient between the LHP and the heat sink. A lower value of h_sink leads thus to a sharper and earlier increase of the operational temperature of the LHP.

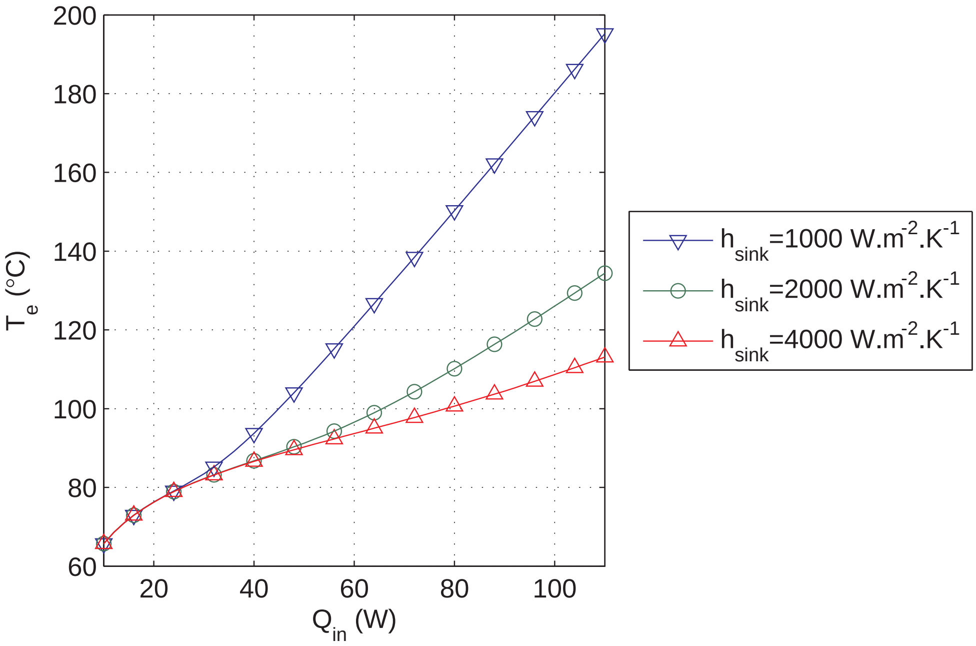

Figure 2.24: Influence of the heat transfer coefficient with the heat sink on the evaporator temperature

2.5.7 Influence of the working fluid

Several usual working fluids are compared in Figure 2.25. This analysis is limited to the thermal performance of each fluid. In practice, a complete comparative study would require to consider other parameters, such as the chemical compatibility of the fluid with the materials of the loop, the working pressure and the mechanical stress associated to it, the toxicity of the fluid, etc. From the figure, ammonia proves to be a very good fluid for the entire simulated heat input range, enabling the lowest operating temperature. Acetone enables low operating temperatures only for very low heat loads. For higher heat inputs, a sharp increase of the evaporator temperature is observed due to its low heat of vaporization. Both ethanol and methanol share analogous performance since their thermophysical properties are very similar. The behaviour of the LHP with water is quite different. Indeed, the heat of vaporization of water is extremely large and leads to a transition between both operating modes at high heat loads. Hence, the performance of the water-filled LHP is limited for low heat inputs. However, for high heat loads, water proves to be the best working fluid. These results are in accordance with the results of Launay et al. [149] who compared the influence of various working fluids on the reservoir temperature.

2.5.8 Influence of non-condensable gases

Figure 2.26 shows the effect of non-condensable gases on the evaporator temperature. Various quantities of air ranging between 1 µg and 200 µg are simulated in the reservoir. For an NCG mass below 10 µg, corresponding to a partial pressure P^*_{NCG} equal to about 400 Pa, NCGs do

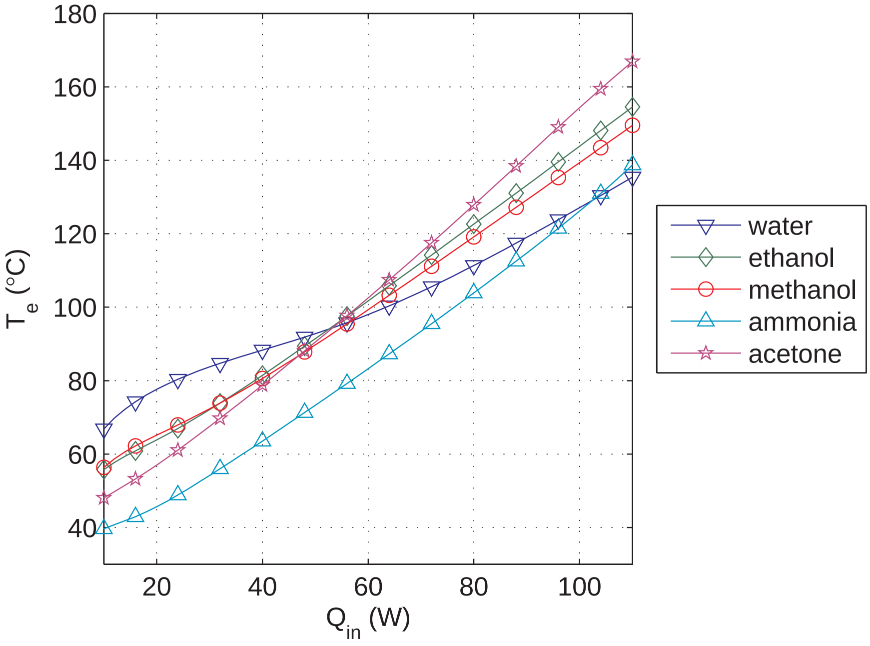

Figure 2.25: Influence of the working fluid on the evaporator temperature

not have a determinant influence on the evaporator temperature. However, when the mass of NCGs in the LHP is larger, its partial pressure becomes greater than pressure drops in the transport lines and the condenser. The ratio P^*_{NCG} to the sum of pressure drops increases as the heat load decreases. The influence of NCGs becomes then important at low heat input, leading to a significant increase of the evaporator temperature. As a consequence, the shape of the characteristic curve of the LHP is flattened.

These results are in accordance with Singh et al.'s experimental study [45]. Their work shows that the net effect of the generated NCG in the LHP is to produce an overall rise of the steady-state operating temperature. Besides, it is observed that the performance degrading effect of the NCG is more pronounced at low heat loads.

2.6 Results with a cylindrical evaporator

The model with the 3D analysis of a cylindrical evaporator is compared to experimental data from the study of Chuang et al. [150]. The authors investigated the steady-state operation of a loop heat pipe with a cylindrical evaporator and ammonia as working fluid. A schematic of the LHP is presented in Figure 2.27 and the specifications of the tested device are given in Table 2.3.

The evaporator, vapour line and reservoir were insulated with fibreglass during the experimental operation. Therefore, an equivalent convective heat transfer coefficient equal to $1\,\mathrm{W}\cdot\mathrm{m}^{-2}\cdot\mathrm{K}^{-1}$ is taken into account in the model, to cope with this insulation material. Concerning the liquid line, its exact external surface area is not known because of the presence of the flexible tube (unknown diameter) and of various connectors. Therefore, the value

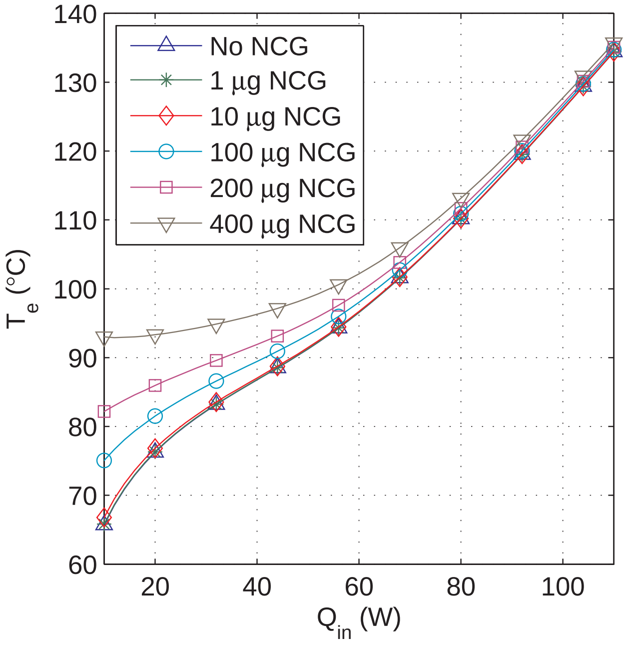

Figure 2.26: Influence of the NCGs on the evaporator temperature

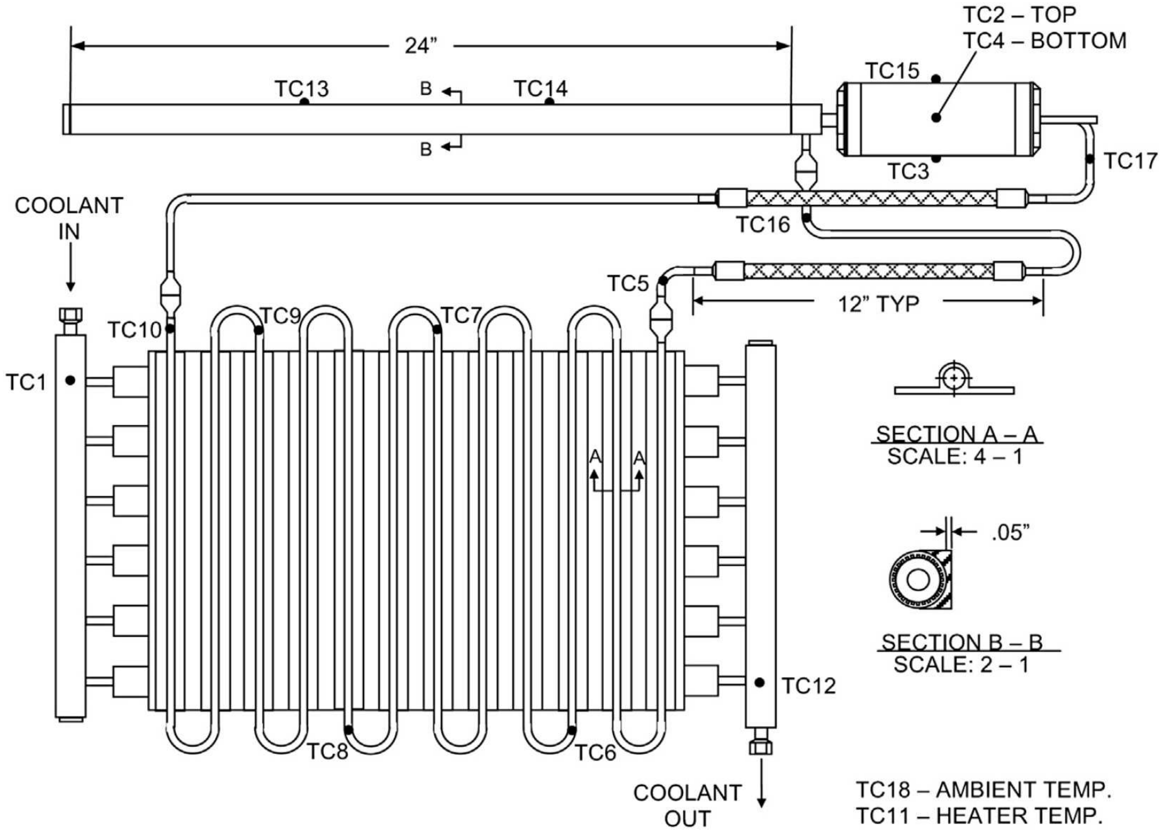

Figure 2.27: Schematic of the tested LHP [150]

Working fluid	Ammonia
Evaporator	Axially grooved aluminium extrusion
Active length	610 mm
Cylinder outer diameter	24.1 mm
Number of grooves	43
Primary wick	Sintered powder nickel
Outer diameter	19.1 mm
Inner diameter	9.5 mm
Effective pore radius	1.6 µm
Permeability	$2 \cdot 10^{-14}\,\mathrm{m}^2$
Reservoir	Stainless steel
Cylinder outer diameter	69.9 mm
Cylinder inner diameter	68.3 mm
Cylinder length	158 mm
Transport line	Stainless steel
Outer diameter	6.4 mm
Inner diameter	5.3 mm
Length of the vapour line	740 mm (including 300 mm flex line)
Length of the liquid line	970 mm (including 300 mm flex line)
Condenser ammonia-side	Aluminium
Outer diameter	6.4 mm
Inner diameter	5.3 mm
Active length	3.66 m
Total length	4.65 m
Condenser coolant-side	Water
Plate length	460 mm
Plate width	300 mm
Plate thickness	6.4 mm
Number of parallel lines	6
Bayonet	Aluminium
Outer diameter	4.8 mm
Inner diameter	3.3 mm
Length	1.71 m

Table 2.3: Specifications of the experimental setup [150]

of the external heat transfer coefficient for the model is arbitrarily set to $30\,\mathrm{W} \cdot \mathrm{m}^{-2} \cdot \mathrm{K}^{-1}$, assuming a constant outer diameter of 6.4 mm. This is equivalent to a heat transfer coefficient equal to $10\,\mathrm{W} \cdot \mathrm{m}^{-2} \cdot \mathrm{K}^{-1}$ if the actual surface area is three times larger than the modelled one. This value is consistent with the experimental measurements.

The tests are conducted with a positive elevation (condenser above the evaporator) equal to 25.4 mm. Based on a previous work of one of the authors [43], the diameter of the grooves is taken equal to 1 mm and a porosity of 60 % is considered for the porous structure. As for the LHP of Singh et al. [42] , the effective thermal conductivity of the wick is calculated with the correlation of Alexander. The ambient temperature is constant and equal to 18.5 °C. Despite a value of 5 °C given in the paper, the heat sink temperature is considered equal to 7 °C because this value seems more consistent with the experimental data. In addition, the thermal contact resistance R_c is equal to $8 \cdot 10^{-5}\,\mathrm{K \cdot m^2 \cdot W^{-1}}$, the accommodation coefficient is equal to 0.1 and the value of the heat transfer coefficient with the heat sink is $500\,\mathrm{W \cdot m^{-2} \cdot K^{-1}}$, in order to fit with the experimental data. Given the geometry of the evaporator/reservoir and according to the experimental results, a heat transfer coefficient equal to $700\,\mathrm{W \cdot m^{-2} \cdot K^{-1}}$ is considered for the heat transfer between the wick and the liquid in the reservoir (see Appendix C).

The analytical simulation is compared with four distinct experimental temperature results: the evaporator temperature T_e, the reservoir temperature T_r, the temperature at the exit of the condenser $T_{c,o}$ and the temperature of the liquid at the end of the liquid line $T_{r,i}$. As shown in Figure 2.28, a very good accordance is found for almost the entire tested range. However, at very low heat load, there are some discrepancies concerning T_e and T_r. According to the parametric study, these differences can be due to an inaccurate consideration of the heat losses to the ambient at very low heat fluxes or to the presence of NCGs.

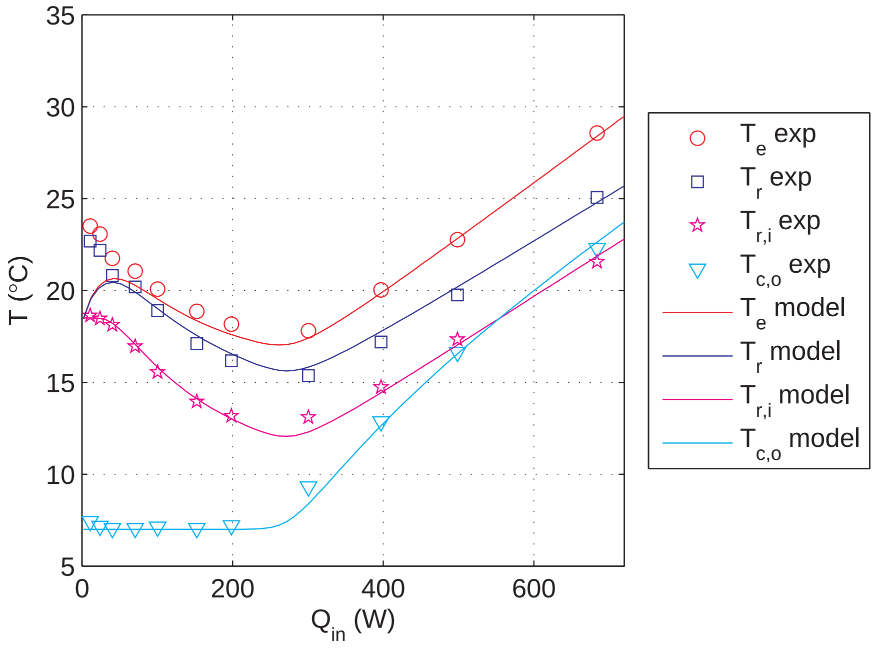

Figure 2.28: Comparison between theoretical and experimental results

The temperature field in the evaporator/casing is presented in Figure 2.29. The input parameters are the one presented previously for a heat load of 500 W. The figure shows a slight temperature gradient in the active zone of the evaporator (upper-right side) where the heat input is applied. This gradient, due to the thermal conduction in the evaporator casing, is not present in the opposite side of the evaporator (lower-right side). Far from the saddle, the temperature is lower and the temperature field is more homogeneous than close to the saddle. As the heat transfer coefficient with the ambient is very low, heat losses have no impact on the temperature field.

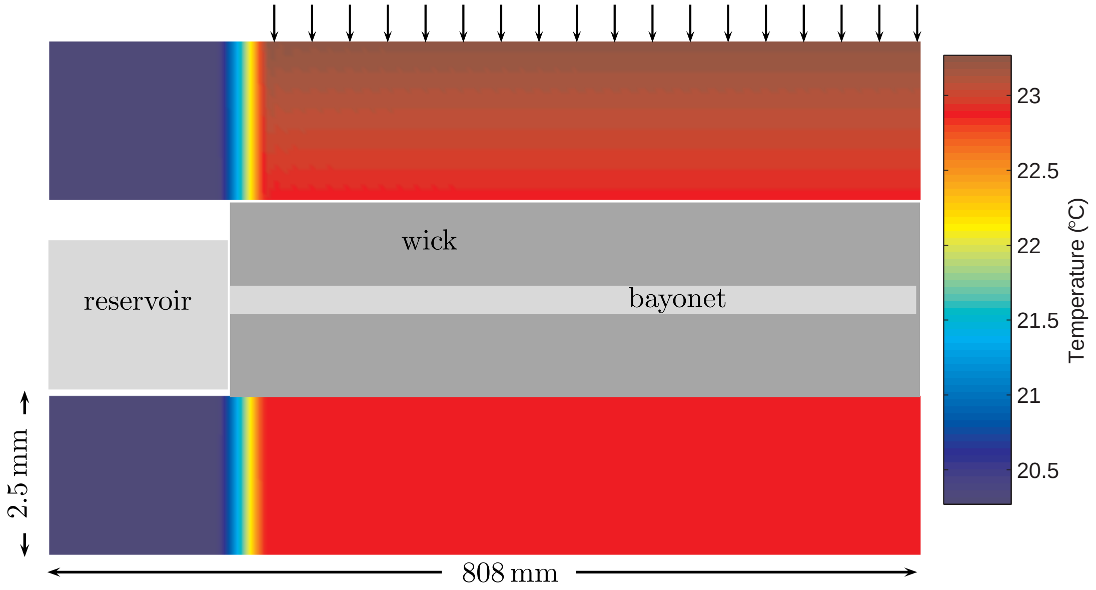

Figure 2.29: Temperature field in the cylindrical wall of the evaporator/reservoir, $Q_{\text{in}} = 500\,\text{W}$

2.7 Conclusion

An analytical model of an LHP with either a flat or a cylindrical evaporator has been developed. This design tool, validated in several experimental configurations, highlights the parameters of influence of LHPs (wick effective thermal conductivity, contact resistance, accommodation coefficient and heat transfer coefficients with the heat sink and the ambient, respectively) and their impact on the system operation. The results show the great complexity of such a system in which these parameters are intimately linked one to the other. However, the sensitivity analysis shows that a distinction between these parameters is possible based on an experimental setup with wisely chosen temperature measurements.

Chapter 3

Experimental study

This chapter introduces an experimental investigation of the design, the manufacturing and the test of a loop heat pipe. A research-oriented apparatus is developed to provide key elements on the understanding of the thermal and hydraulic phenomena occurring in LHPs. This system is also instrumented to provide experimental data necessary to validate the models developed in the laboratory. The first results obtained with this LHP are presented in this chapter. First, the various components of the experimental setup are presented with the different sensors and techniques used to characterise the system. Then, a power cycle of the LHP is studied through an analysis of the main temperatures inside the system. A further investigation is conducted to evaluate the characteristics of the LHP in steady-state and in transient operations. A visual study is then undertaken to understand the condensation phenomena inside the condenser and the transport lines and to evaluate their consequences on the thermal operation of the system.

One has to note that the device was operational only three months before this manuscript was written. Therefore, the results presented in this chapter are preliminary results showing the capability of the system.

The results presented here are all obtained using water as working fluid. The main drawback is that the system is not perfectly tight at the moment. This does not prevent the operation of the device but decreases its performance.

3.1 Experimental setup and procedures

This section presents an experimental facility to analyse the physical mechanisms responsible for the operation of the loop heat pipe. The setup has been designed to be as modular as possible: the various components (transport lines, porous structure, copper block, etc.) are interchangeable in order to perform experimental parameter analyses with various fluids. Several components of the device are transparent to enable a better understanding of the phenomena involved in the loop. This apparatus is designed for a research purpose and does not necessarily aims at obtaining outstanding performance. This is particularly true for the transparent condenser made of glass that leads to poor thermal performance.

3.1.1 Experimental apparatus

The experimental apparatus consists of the main standard elements of an LHP (Figure 3.1): a disk-shaped evaporator/reservoir structure with embedded porous structure (similar to the system tested by Singh et al. [42]), vapour and liquid transport lines and a parallel-flow straight condenser. In addition, a secondary reservoir controlling the liquid filling ratio is connected to the liquid line and a facility for the working fluid filling is also mounted. A window on the reservoir and transparent transport lines and condenser enable visual monitoring of the loop operation. Figure 3.2 presents a global view of the experimental apparatus.

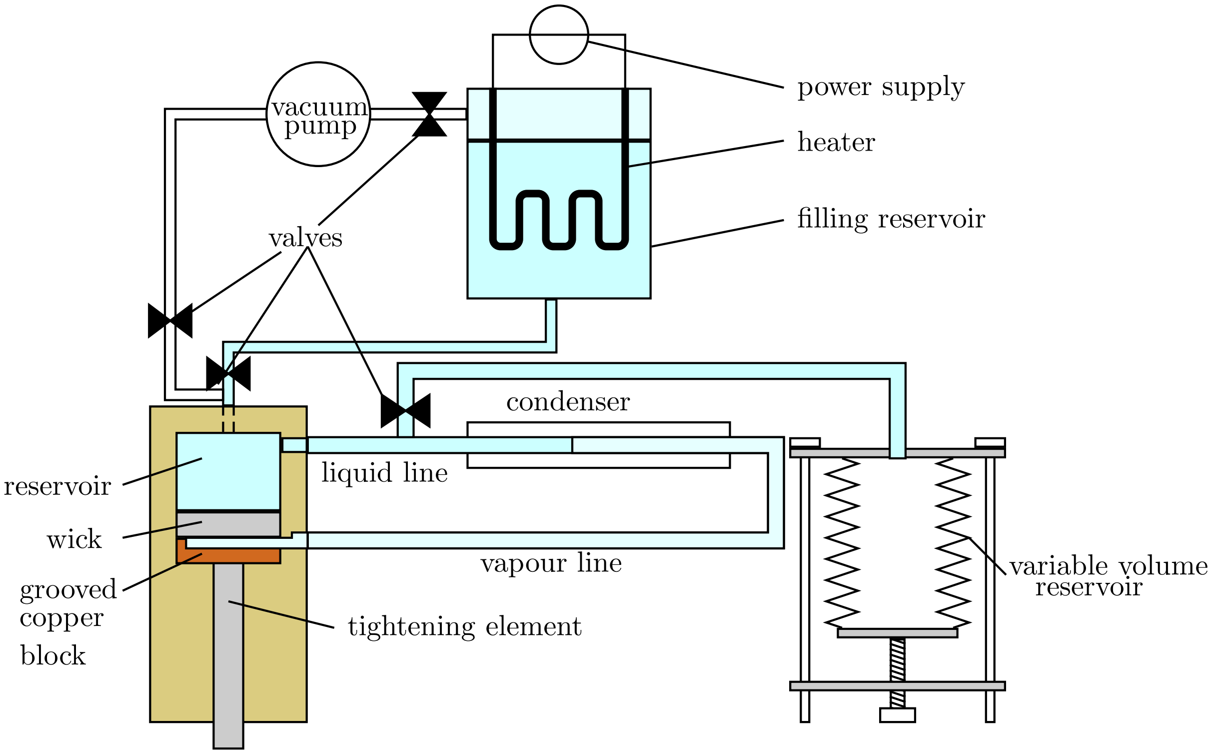

Figure 3.1: Schematic of the experimental apparatus

In the next section, a detailed description of every component constituting the system is presented.

3.1.1.1 Evaporator/reservoir

The evaporator/reservoir structure, shown schematically in Figure 3.3, is a stack of disk-shaped elements. Its casing is made of polyether ether ketone (PEEK), an organic polymer with a thermal conductivity approximately equal to $0.25\,\mathrm{W \cdot m^{-1} \cdot K^{-1}}$. Such a material prevents the longitudinal parasitic heat losses through the casing while maintaining a good mechanical integrity for the entire operating temperature range, *i.e.* 20–100 °C. The reservoir, with a diameter of 38 mm and a height equal to 30 mm is located in the upper part. The entry of the liquid flowing from the condenser, of inner diameter 8 mm, is situated on its side.

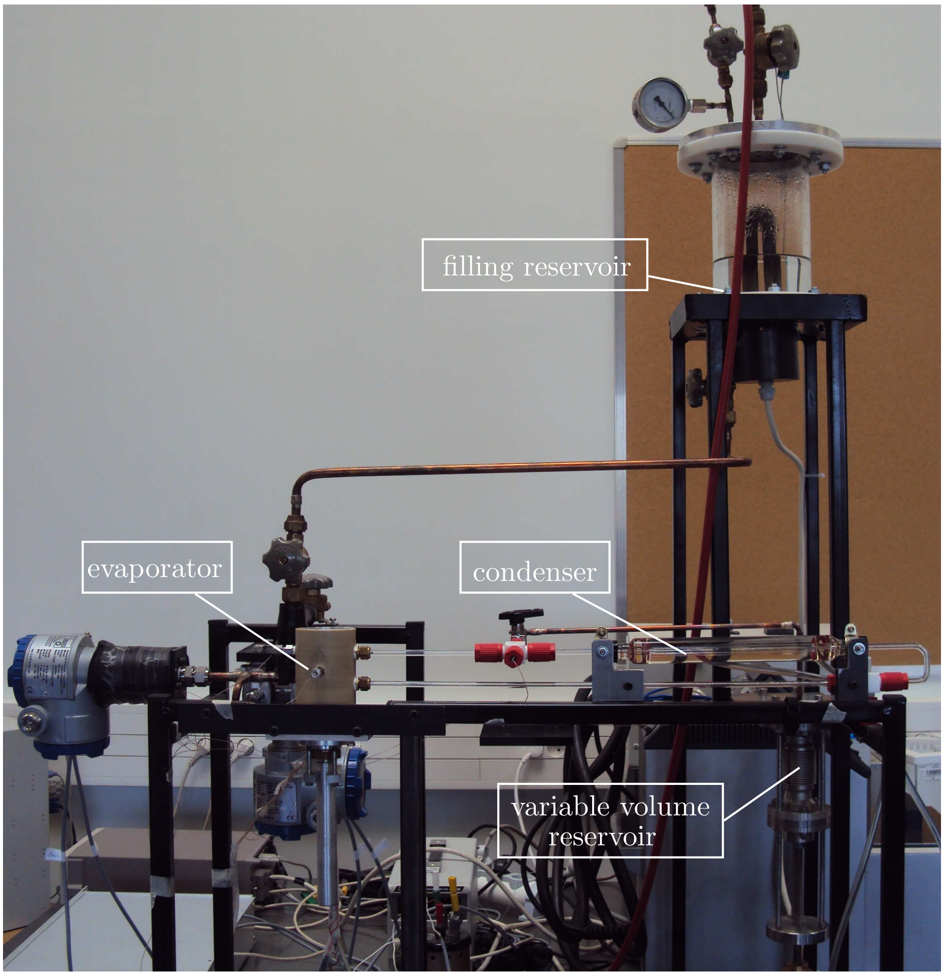

(a) Global view

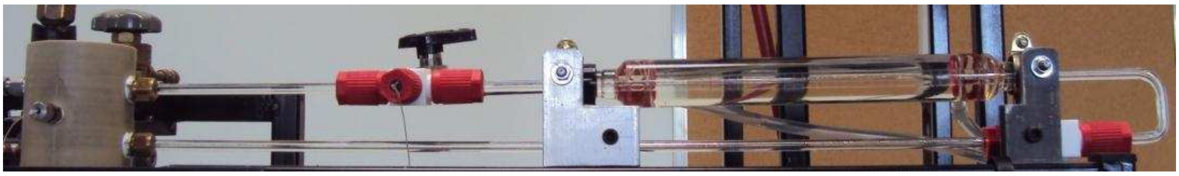

(b) Magnified view of the LHP main components

Figure 3.2: View of the experimental apparatus

A borosilicate glass window is mounted at the top for a direct view of the reservoir inner part.

A porous wick is in contact with the reservoir and drains the liquid to the evaporation zone. The vapour grooves are engraved in a 8 mm thick copper block which provides a uniform heat distribution to the wick. A vapour channel of inner diameter 8 mm enables the exit of the vapour on the side of the evaporator.

Several tightening elements provide the mechanical integrity of the device, an adequate mechanical and thermal contact between the various components and the sealing between the reservoir and the evaporator parts, respectively. The plug shown in the figure is designed to

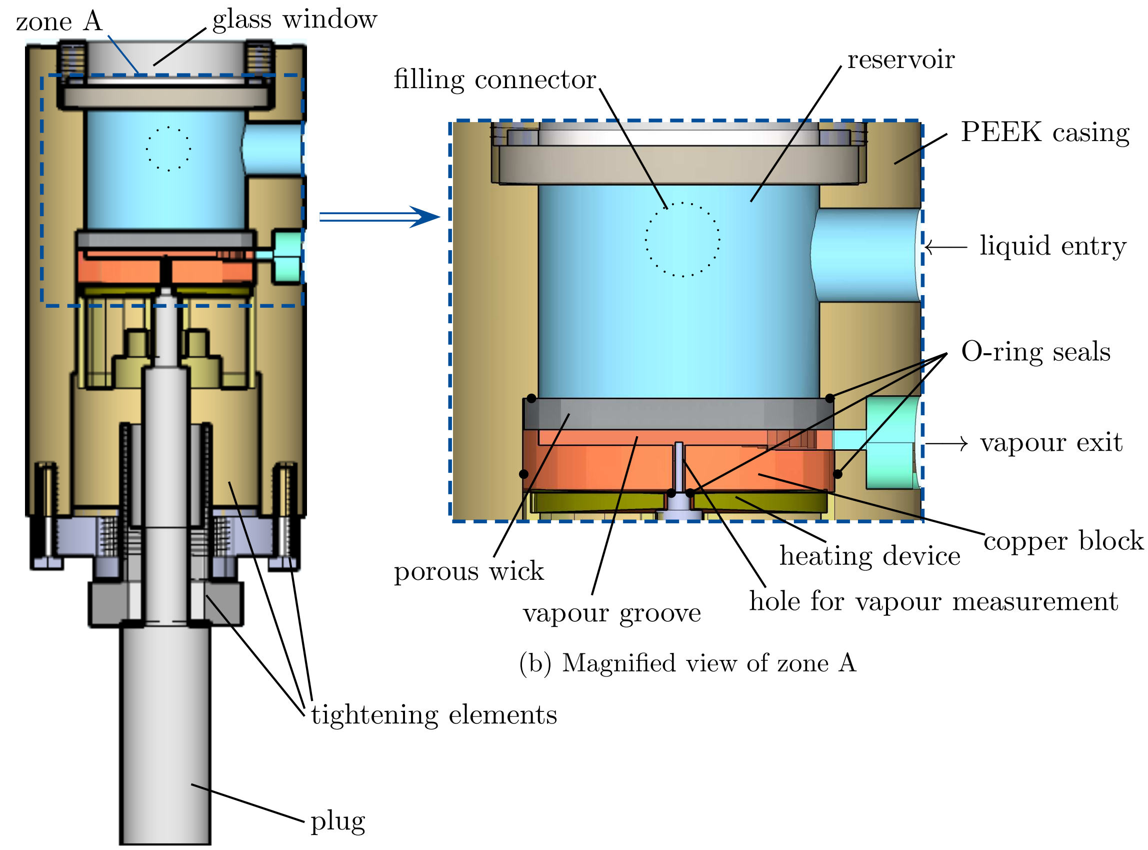

(a) Cross section of the evaporator/reservoir

(b) Magnified view of zone A

Figure 3.3: The evaporator/reservoir structure

enable temperature or optical measurements inside the vapour grooves using a thermocouple or an endoscope, respectively, with a hole of inner diameter of 800 µm. This system is not used in the present work but it will be useful in the future to understand the physical mechanisms inside the vapour space, especially during the start-up of the device.

3.1.1.2 Vapour groove design

The vapour groove design is shown in Figure 3.4. The diameter of the copper block is equal to 40 mm. The nine grooves are 2 mm wide and 1.5 mm deep each. The fins between the grooves are 1.5 mm wide. Since the vapour mass flow rate is coming from the side vapour channels to the central grooves, the cross-section area of the vapour collector increases to prevent large variations of the flow velocity and thus restrict pressure losses. The grooved copper block is interchangeable to enable the test of other geometries (concentric grooves for instance). A small hole is machined at the centre of the copper block for the insertion of a thermocouple or an endoscope, as discussed previously.

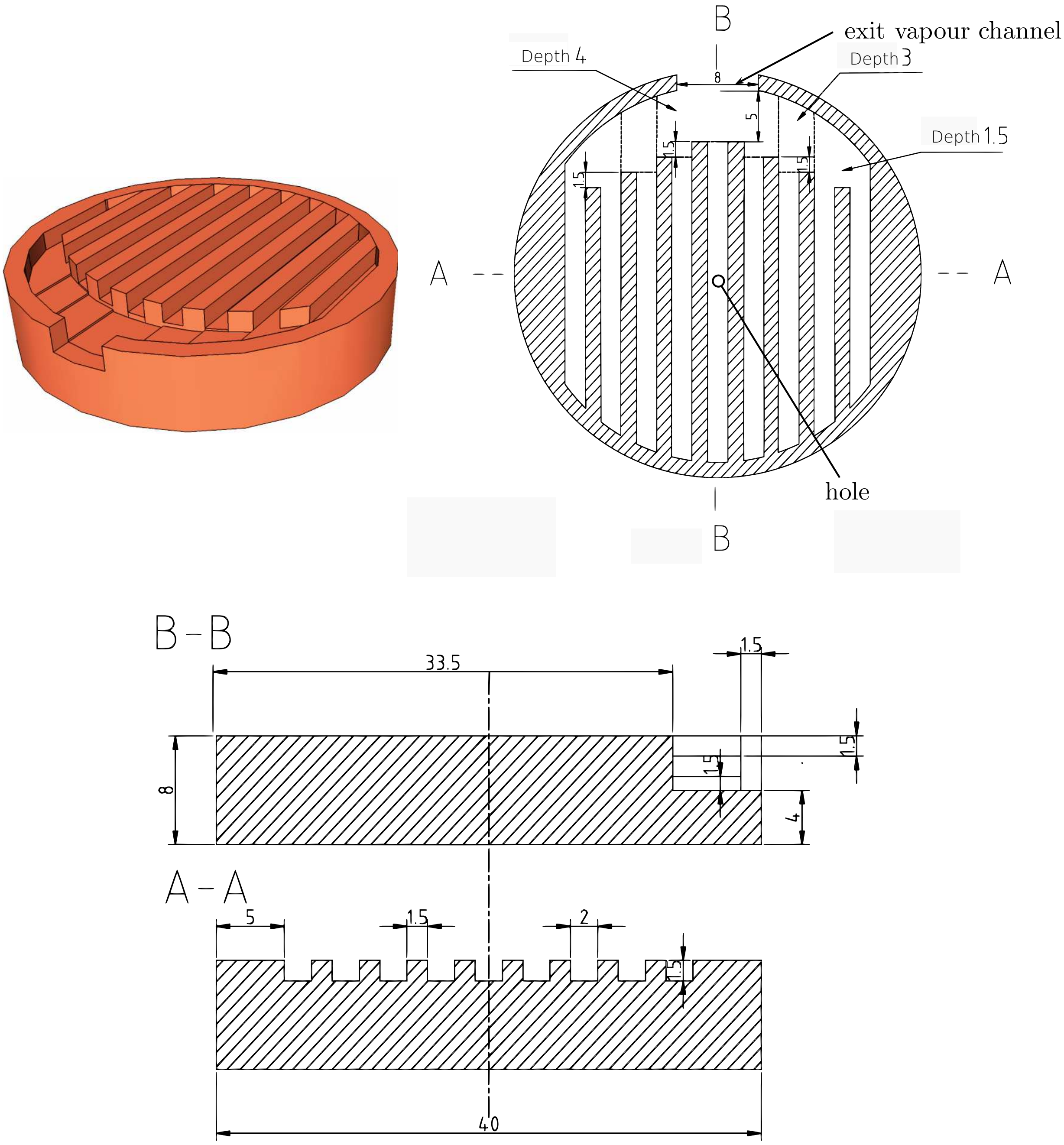

Figure 3.4: Groove design

3.1.1.3 Porous wick

A sintered porous metal disk manufactured by *Mott Corporation*[1], a provider of porous metal, is inserted between the copper block and the reservoir. The wick diameter D_{w} is equal to 40 mm (±0.2 mm) and its thickness e_{w} is equal to 6 mm (±0.2 mm). The material is an austenitic chromium-nickel alloy type 316L. This material is a common stainless steel well-known for its high resistance to corrosion. The mass of the wick m_{w} has been determined

---

[1] www.mottcorp.com

using a high-precision weighting scale and is equal to 40.04 g. Its porosity is then evaluated:

$$\varepsilon = 1 - \frac{4m_{\mathrm{w}}}{\pi D_{\mathrm{w}}^2 e_{\mathrm{w}} \rho_{316\mathrm{L}}} = 1 - \frac{4 \times 40.04 \cdot 10^{-3}}{\pi \times 0.04^2 \times 0.006 \times 8000} = 33.6\,\% \tag{3.1}$$

where $\rho_{316\mathrm{L}}$ is the density of stainless steel 316L. This porosity is lower than the porosity of wicks usually used in LHPs. Indeed, the manufacturer is specialised in filtering products that do not correspond to the present application. Nevertheless, this porous structure is used for the first tests, but wicks with other characteristics (material, pore size, porosity, etc.) will be developed and tested with the same setup in the future.

The manufacturer does not provide any accurate information regarding the pore size. However, a media grade equal to 10 is indicated, meaning that the porous structure would stop 90 % of the 10 µm OD particles in a liquid stream and 99.9 % of the 10 µm OD particles in a gas stream. The other properties of the porous wick (permeability, effective thermal conductivity, pore size distribution) are not known. The laboratory is currently designing an experimental setup to measure adequately the thermal conductivity and the permeability of a porous structure. Such characterisations are necessary to better understand the influence of these parameters on the LHP operation as well as to reduce the bias regarding the input parameters of the modelling analyses.

To provide an adequate mechanical contact between the wick and the evaporator body, an O-ring seal is used (Figure 3.3). It prevents vapour from flowing from the evaporation zone to the reservoir.

3.1.1.4 Transport lines and condenser

The condenser and the vapour and liquid lines are glass tubes with an internal diameter of 2 mm and a wall thickness of 2 mm. The vapour line is 685 mm long whereas the liquid line length is equal to 245 mm. The condenser is a 250 mm long parallel-flow tube-in-tube heat exchanger, with an external diameter equal to 26 mm. It has been pre-designed to enable the test of the LHP in various operating modes (variable and fixed conductance) for heat loads up to at least 30 W (Appendix D). The heat sink temperature is thermoregulated using a thermostatic bath. Two PTFE connectors (T-shaped and cross-shaped) enable the insertion of two thermocouples as well as the connection with the secondary reservoir (Figure 3.5).

Glass offers two main advantages over copper for the present study. First, the low thermal conductivity of glass, about $1\,\mathrm{W} \cdot \mathrm{m}^{-1} \cdot \mathrm{K}^{-1}$, prevents longitudinal transport of heat along the lines as well as heat losses to the ambient. Consequently, the transport lines are not thermally influenced neither by the evaporator nor the condenser. Such a feature is of great importance when comparing experimental data to simulations, because heat losses is a parameter that is difficult to estimate accurately and the consideration of thermal conduction through the tube walls makes the modelling more complex. Secondly, glass enables a direct observation of the fluid flow inside the transport lines and the condenser. Thus, the vapour and liquid zones, the presence of vapour bubbles or liquid slugs, the flow pattern and the two-phase length in the

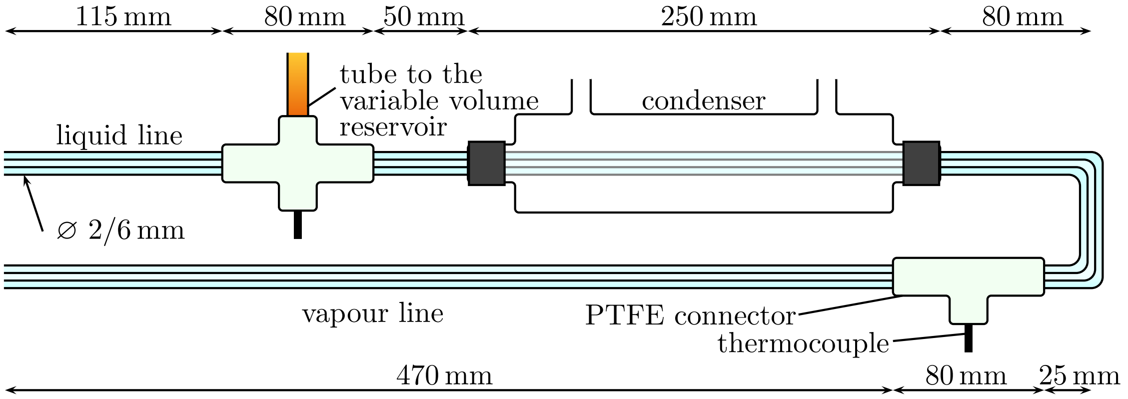

Figure 3.5: Liquid and vapour lines and condenser

condenser can all be characterised accurately. Such measurements are useful to understand the phenomena occurring during the LHP operation as well as to compare theoretical and experimental results.

The internal diameter of the tubes (2 mm) is selected in accordance with experiments from the literature concerning electronic thermal management. Furthermore, such a diameter provides large capillary effects, ensuring capillary-driven flow regimes in the transport lines and the condenser. The Bond number, representing the ratio between gravitational forces and surface tension forces, is defined by:

$$Bo^2 = \frac{D_{\mathrm{i}}^2 g \left(\rho_{\mathrm{l}} - \rho_{\mathrm{v}}\right)}{\sigma} \tag{3.2}$$

where σ is the surface tension of the fluid. In the case of water which is the fluid used in the results presented in this chapter, it ranges between 0.53 and 0.64 for T_{sat} varying from 20 °C to 100 °C, showing a major contribution of the capillary forces.

Despite enabling a direct observation of the condensation regimes, a glass condenser provides a lower performance than a metallic one. Indeed, the large thickness of the tubes associated with the low thermal conductivity of glass reduces drastically the heat transfer with the heat sink. Thanks to the modularity of the experimental setup, other types of transport lines and condenser can be tested in the future.

3.1.1.5 Filling device and filling ratio variation device

A secondary reservoir made of wrinkled stainless steel is connected to the liquid line (Figure 3.1). Its volume can be manually varied. Such a feature enables the management of the liquid filling ratio inside the LHP through a variation of its total volume, prior to start-up.

A filling apparatus has been designed to provide a correct degassing and filling of the loop heat pipe (Figure 3.1). It consists of a reservoir including a heating device, which is connected to the compensation chamber. Thus, the fluid can be heated and degassed several times prior to the filling of the loop. Large dead volumes exist in the loop, due to the numerous connecting tubes. Therefore, an accurate determination of the mass of fluid that is inserted into the system is not possible. However, the filling ratio can be approximately monitored and repeated, knowing the state (vapour or liquid) of the fluid inside the transport lines and the liquid level inside the reservoir. The latter can be estimated by direct viewing through the window glass that closes the reservoir.

During operation, the secondary reservoir and the filling apparatus are disconnected from the rest of the loop by closing valves to prevent any disturbance of the system.

3.1.1.6 Heat source

The heat input is produced by a flat circular Kapton® (polyimide) heater (38.1 mm diameter, 50 µm thick) manufactured by *Minco*. It is in contact with the copper block of the evaporator (Figure 3.6). Thermal grease increases the thermal contact between both components. The heater resistance is equal to 7.2 Ω. According to the manufacturer, at 110 °C, the maximum allowable power is equal to 57.6 W, corresponding to a heat density of $5.6\,\mathrm{W \cdot cm^{-2}}$. This maximum heat density decreases as the temperature increases ($4.3\,\mathrm{W \cdot cm^{-2}}$ at 130 °C). To ensure the integrity of the heater, a temperature controller shuts the power off when reaching 110 °C. A 0–36 V / 0–10 A power supply manufactured by *Française d'Instrumentation* enables to set the heat input.

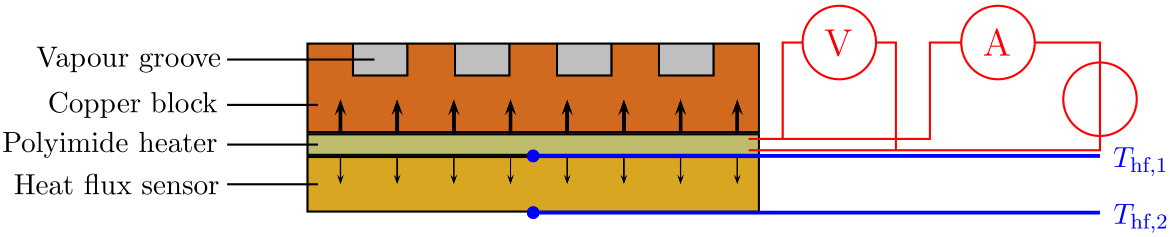

Figure 3.6: Heat input measurement

3.1.1.7 Heat sink

The heat sink is provided by a *Huber* cooling circulator. It operates from −40 °C to 200 °C and its cooling capacity is equal to 420 W at 20 °C. The suction pump enables a maximal mass flow rate of $27\,\mathrm{L \cdot min^{-1}}$. Given the dimensions of the condenser, the maximal expected flow velocity of the cooling fluid inside the condenser is about $0.8\,\mathrm{m \cdot s^{-1}}$ (Appendix D). PVC flexible pipes connect the cooling circulator to the condenser.

3.1.2 Measurement techniques

A pressure gauge enables the measurement of the absolute pressure in the reservoir and K-type thermocouples monitor the temperature in various locations of the LHP during its operation. Furthermore, the heat load is accurately measured and a camera enables high-speed optical measurements of the fluid flow inside the condenser and the transport lines.

3.1.2.1 Temperature measurements

Several K-Type thermocouples (80 µm in diameter) are inserted inside the experimental setup to provide information on the thermal state of the device. All the thermocouples have been calibrated between 0 °C and 100 °C. The uncertainty of each temperature measurement itself, after calibration, is estimated to ±0.2 K. However, the measured temperature is not necessarily representative of the parameter one intends to evaluate, as it will be discussed further. The location and the name of the thermocouples are as follows (Figure 3.7):

- $\boldsymbol{T}_{\mathrm{e}}$ is the most interesting temperature from a designer point of view because it is the highest temperature of the device and determines as such the operating limit of the LHP. This thermocouple is inserted in a small groove machined near the centre of the copper block in the evaporator, close to the heater. Conductive silver lacquer is used to improve the thermal contact of T_{e} to the copper block. The thermocouple is inserted in a groove. The size and shape of the copper block ensure a good thermal homogeneity. Therefore, T_{e} can be considered as the mean temperature of the copper block close to the heater.

- $\boldsymbol{T}_{\mathrm{r}}$ is the temperature of the liquid bulk in the reservoir. It is located at approximately 5 mm of the porous wick and 10 mm of the reservoir internal wall. A significant difference can exist between T_{r} and the temperature at the liquid-vapour interface. The reliability of this measurement is further discussed in section 3.2.

- $\boldsymbol{T}_{\mathrm{ext}}$ is the ambient temperature. At the moment, it is measured by a PT100 sensor located in the cold-junction box of the thermocouples. Its thermal inertia is larger than the inertia of the thermocouples. Therefore, a delay can be expected when measuring the variation of the ambient temperature. A better measurement with a judiciously located thermocouple is planned for future experiments. Nevertheless, as it has been discussed in the previous section, T_{ext} has not a strong influence on the system because most of the elements are made of low conductive material.

- $\boldsymbol{T}_{\mathrm{hf,1}}$ and $\boldsymbol{T}_{\mathrm{hf,2}}$ are the temperatures on both sides of the heat flux sensor that serves to estimate heat losses inside the evaporator (Figure 3.6).

- $\boldsymbol{T}_{\mathrm{v}}$ is the temperature of the vapour. The thermocouple is inserted inside the vapour line at 175 mm of the condenser and 510 mm of the evaporator, using a PTFE coupling.

- $\boldsymbol{T}_{\mathrm{c,o}}$ is the temperature of the liquid exiting the condenser. The thermocouple is inserted in the liquid line at about 90 mm of the condenser, using a PTFE coupling.

- $\boldsymbol{T}_{\mathrm{r,i}}$ is the temperature of the liquid entering the reservoir. The thermocouple is inserted through the reservoir (from its opposite side) and in the liquid line at 10 mm of the end of the liquid line.

The evaluation of the measurements of T_{v}, $T_{\mathrm{c,o}}$ and $T_{\mathrm{r,i}}$ is the most difficult. In many experimental studies of the literature, the fluid temperature in the transport lines is measured using a thermocouple on the external surface of the tube, the latter being made of a conductive material such as copper. However, a large temperature difference may exist between the tube wall and the fluid, particularly in the vapour line [84]. Such a method is anyhow not applicable in the present study, since thick glass tubes are used. Therefore, in the present study, the thermocouples are inserted directly inside the tubes. Despite additional pressure drops (presence of the PTFE coupling, invasive presence of the thermocouple inside the liquid flow), such a method provides a much accurate temperature measurement. However, the measurement may still be influenced by the surroundings.

In addition, the heat sink temperature $\boldsymbol{T}_{\mathrm{sink}}$ is given by the thermoregulation unit. Nevertheless, heat losses to the ambient may change the temperature that is actually flowing through the condenser. In the future, temperature sensors at the entry and at the exit of the condenser will be installed to provide a precise determination of the heat sink temperature. The temperature difference between the entry and the exit of the condenser is negligible (for the maximal flow rate delivered by the thermostatic bath, equal to $27\,\mathrm{L}\cdot\mathrm{min}^{-1}$, a temperature of 20 °C and a heat load equal to 50 W, the increase of the fluid temperature is theoretically lower than 0.1 K, neglecting the heat losses to the ambient). For the calculation of the thermal resistances, the uncertainty of T_{sink} is considered equal to ±0.5 K.

All data are recorded using a *Keithley* acquisition system, connected to a *LabVIEW* program.

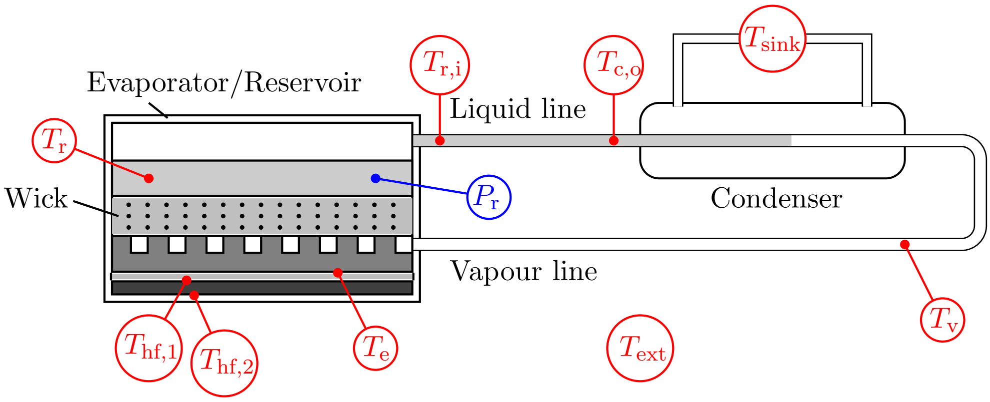

Figure 3.7: Location of the thermocouples and of the pressure sensor

3.1.2.2 Pressure measurement

A *Kobold* absolute pressure sensor (range 0–2.5 bar, accuracy ±0.075 % of the range, *i. e.* ±187 Pa) is mounted on the experimental setup (Figure 3.7). The current output signal (4–20 mA) is converted to a voltage output using a 50 Ω (±0.1 %) resistor. The pressure in the reservoir can be compared to the saturation pressure corresponding to the reservoir temperature to estimate the amount of non-condensable gases in the loop.

3.1.2.3 Heat input measurement

A four-wire circuit is used to measure accurately the heat dissipated by the heater Q_{heater} (Figure 3.6). The intensity is determined using a high-precision *AOIP* Manganin® shunt ($R = 0.01\,\Omega$ at 20 °C). The largest part of this heat, Q_{in} is conducted through the copper block and dissipated by the LHP. The remainder part Q_{hf} is conducted through the casing, then lost to the ambient and does not participate in the loop operation.

In order to evaluate these heat losses, a heat flux sensor is located next to the polyimide heater. The sensor consists of two thin copper disks separated by an insulating material. At each side of this sensor, two thermocouples, $T_{\mathrm{hf,1}}$ and $T_{\mathrm{hf,2}}$ are inserted in small grooves. Conductive silver lacquer ensures a good thermal contact between the thermocouples and the copper. After calibration, the temperature difference between both sides of the sensor gives the heat flux that is actually thermally conducted through it. The calibration curve is presented in Figure 3.8. Q_{hf} is calculated by:

$$Q_{\mathrm{hf}} = 0.1826\,(T_{\mathrm{hf,1}} - T_{\mathrm{hf,2}}) - 0.0206 \tag{3.3}$$

This linear equation fits the experimental data with an accuracy of ±0.03 W. The uncertainty associated with the measurement of Q_{heater} is considered negligible compared to the uncertainty of Q_{hf}. Furthermore, since the thickness of the heater is extremely small compared to its diameter (ratio of 760), the radial heat losses can be neglected. Therefore, the heat load dissipated by the LHP is determined:

$$Q_{\mathrm{in}} = Q_{\mathrm{heater}} - Q_{\mathrm{hf}} \tag{3.4}$$

with an accuracy of ±0.03 W.

3.1.2.4 Optical measurements

The choice of glass as material for the transport lines and for the condenser enables the direct visualisation of the fluid flow inside the tubes. To provide an accurate slow motion analysis of these phenomena, a high-speed digital camera is used. The camera is a monochrome *Photron Fastcam SA3*. For the present investigation, the acquisition frequency ranges from 50 fps to 500 fps, depending of the mechanisms that are studied, with a resolution of 1024 by 1024 pixels. A white LED *Phlox*® square light, 100 × 100 mm^2 in size, provides the proper lighting.

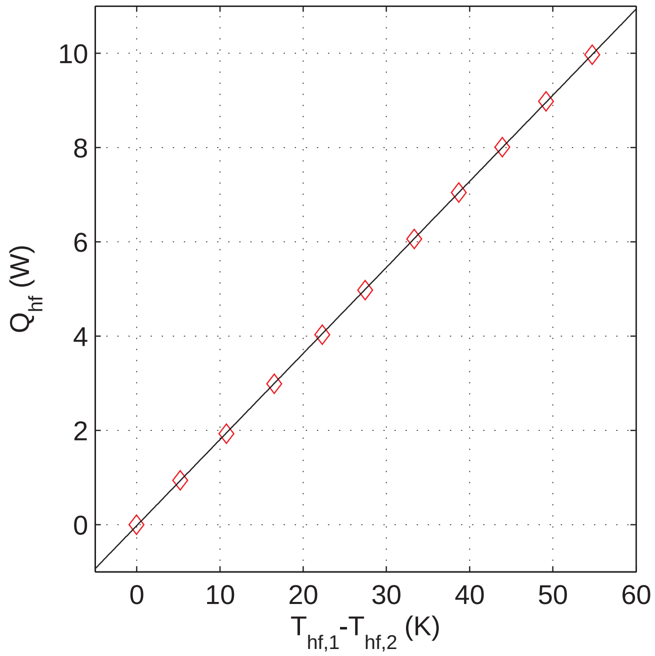

Figure 3.8: Calibration of the heat flux sensor

When necessary, image post-processing is implemented with *Matlab*® to improve the image contrast and gamma correction (Figure 3.9).

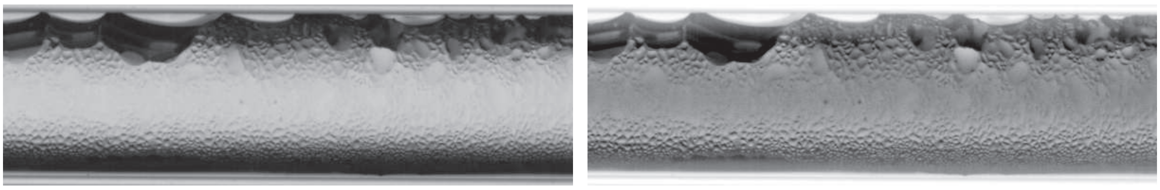

Figure 3.9: Example of image post-processing

3.2 Reliability of the experimental results

The LHP operation does not only depend on the invariable geometrical and thermophysical characteristics of the system. Several other parameters influence the steady-state and the transient behaviour of the LHP: the amount of non-condensable gases in the system and their location, the variation of the ambient temperature and the amount of working fluid in the LHP. Therefore, it is necessary to control or monitor these parameters and to assess their significance on the LHP operation.

3.2.1 Filling of the system / Mass of working fluid and NCGs

A proper care is taken to fill the loop adequately in order to prevent any non-condensable gases from entering the loop and to ensure a high purity of the working fluid. The filling reservoir is evacuated using a vacuum pump (Figure 3.1) before filling with the working fluid. The system is heated for several hours and periodically degassed using the vacuum pump. The entire loop heat pipe is also evacuated. The valve between the loop and the filling apparatus is then opened and the filling of the LHP with liquid is ensured using gravity forces. During this procedure, the filling ratio of the reservoir is monitored by a direct observation through the glass window. The liquid filling ratio can also be controlled using the secondary reservoir with variable volume. The amount of NCGs in the LHP can be estimated by comparing the pressure in the reservoir with the saturation pressure associated with the reservoir temperature.

At the moment, the tightness of the apparatus is not entirely ensured. Indeed, minor leaks still exist and induce a pressure increase equal to about 1000 Pa per day. This value is small enough to provide a relative stability of the partial pressure of NCGs in the system throughout a single test, since the maximal testing time in one day is about 13 hours. However, such a leak prevents the realisation of many consecutive tests without partially emptying the setup and degassing. Indeed, at such low working pressures, even a small amount of NCGs can have a significant influence on the LHP operation. For instance, an increase of 1000 Pa at 30 °C corresponds to an increase of the saturation temperature equal to 3.8 K. Besides, the amount of NCGs in the reservoir can only be approximately estimated, considering on one hand the accuracy of the pressure sensor and on the other hand the presence of liquid between the upper part of the reservoir and the pressure sensor than induces an additional hydrostatic pressure.

The mass of working fluid in the system is not controlled during the filling of the LHP. However, the presence of liquid or vapour inside the transport lines and the condenser, as well as the height of liquid in the reservoir are visually monitored. Therefore, despite some inaccuracy, the tests are conducted with approximately the same amount of working fluid (unless specifically mentioned), corresponding to a height of liquid inside the reservoir equal to about 20 mm. Besides, due to the large size of the reservoir compared to the transport lines and the condenser, the height of the liquid bulk in the reservoir does not vary much during operation (the total volume of the transport lines and the condenser correspond to a height of 3 mm in the reservoir). The influence of the mass of working fluid is not discussed in the present study, but may be investigated in the future.

3.2.2 Analysis of two independent similar tests

Figure 3.10 presents two similar tests, conducted independently to show the behaviour of the system. The ambient temperature is similar for both tests and a degassing prior to start-up ensures a minimal amount of NCGs inside the system. The heat sink temperature is set to 20 °C. At low heat loads, a minor temperature difference is observed between the tests, the evaporator temperature of the second test being slightly larger than the first one. At high heat loads however, the behaviour of the LHP is very different from one test to another. Boiling occurs in the reservoir at 35 W in the first case, inducing a major increase of T_{e}.

For the second test, the onset of boiling occurs only at 40 W. As a consequence, a major difference is observed between both tests, particularly for the evaporator temperature. This phenomenon is further discussed in subsection 3.4.3.

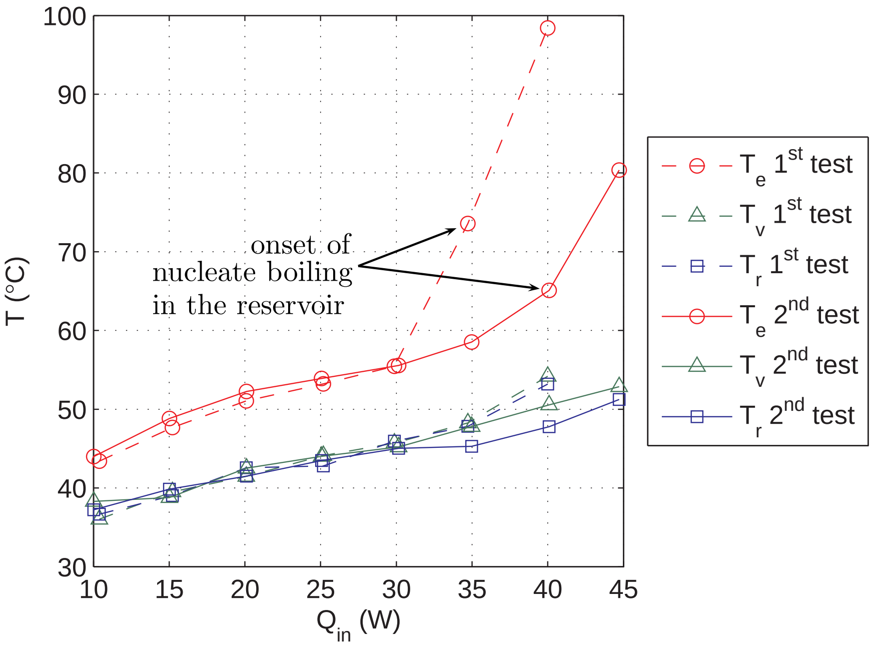

Figure 3.10: Reproducibility of the results – $T_{\text{sink}} = 20\,°\text{C}$

One can also observe that below 30 W, the difference between T_{v} and T_{r} is insignificant, and the temperature measured in the reservoir is sometimes even higher than the one measured in the vapour line. This minor difference can be explained by small pressure drops inside the transport lines but also by the reliability of the temperature measurements. Indeed, as previously explained, the thermocouple T_{r} is located inside the liquid bulk, at several millimetres of the wick (Figure 3.11). Therefore, the measured temperature can exceed the saturation temperature of the reservoir. Thermal inhomogeneity exists in the reservoir induced by the heat losses to the ambient, the liquid returning from the condenser and the parasitic heat transfer from the wick, particularly in the liquid bulk. Indeed, the reservoir is large. That may lead to large gradients between the bottom and the free surface. Furthermore, the flow rate inside the reservoir remains quite small and does not initiate a strong homogenisation of the liquid phase. For the future experiments, a major improvement of the bench will be to measure the temperature of the reservoir inside the vapour phase rather than in the liquid phase. Finally, the measurement of the vapour temperature may be influenced by the surroundings (presence of the PTFE connector, heat losses to the ambient, stagnancy of condensate in the PTFE connector), inducing an underestimation of T_{v}.

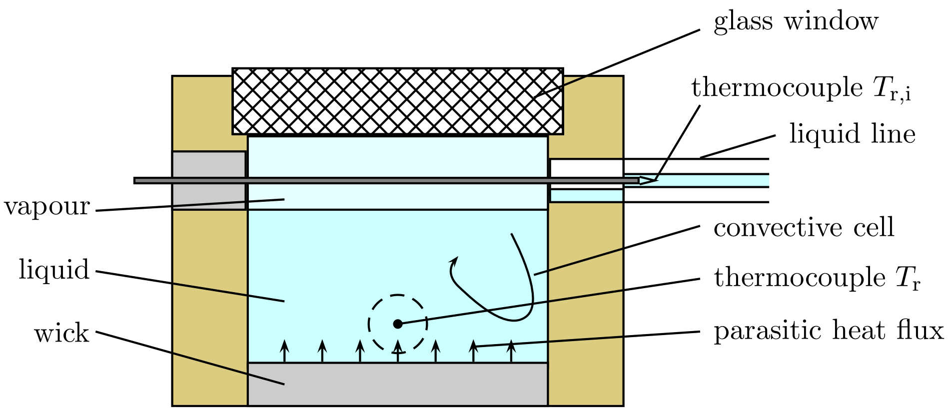

Figure 3.11: Reliability of the measurement of the reservoir temperature

3.2.3 Analysis of two consecutive tests

Figure 3.12 presents two consecutive increase-decrease tests conducted on the same day, without shutdown of the system. The power cycle is set as follows: 10 W-20 W-30 W-35 W-25 W-15 W-5 W-10 W-20 W-30 W-25 W-15 W-5 W. The heat sink temperature is constant and equal to 20 °C throughout the entire experiment. At very low heat loads (5 W), the mass flow rate inside the LHP is extremely small. As a consequence, the meniscus recedes in the vapour line and the thermocouple inserted inside the vapour line measures the temperature of the subcooled liquid at the end of the vapour line rather than the saturation temperature. Thus, no reliable measurement of the vapour temperature is available.

At low heat loads, a moderate difference is observed between both tests, which may be partly explained by an increase of the ambient temperature during the test. An increase of the amount of NCGs throughout the test (desorption, leak, chemical incompatibility) could also influence the LHP operation. However, the measured pressure during the test shows no significant increase compared to the saturation pressure corresponding to T_{r}.

At higher heat loads, boiling occurs in the reservoir and induces a major difference between both tests regarding the evaporator temperature. This confirms the non-reproducible characteristic of the boiling phenomenon in the reservoir and its major influence on the LHP operation which will be further developed.

3.2.4 Conclusion

This analysis shows that a satisfactory reproducibility can be ensured at low to moderate heat loads. At higher heat loads, the onset of nucleate boiling in the reservoir is a non-predictable phenomenon that may significantly change the LHP operation. Furthermore, the amount of NCGs and the variation of the ambient temperature may also influence the operation of the system. However, all these parameters can be either partially controlled by an appropriate procedure or monitored by temperature and pressure measurement as well as direct observation. The present reliability is considered good enough for the first

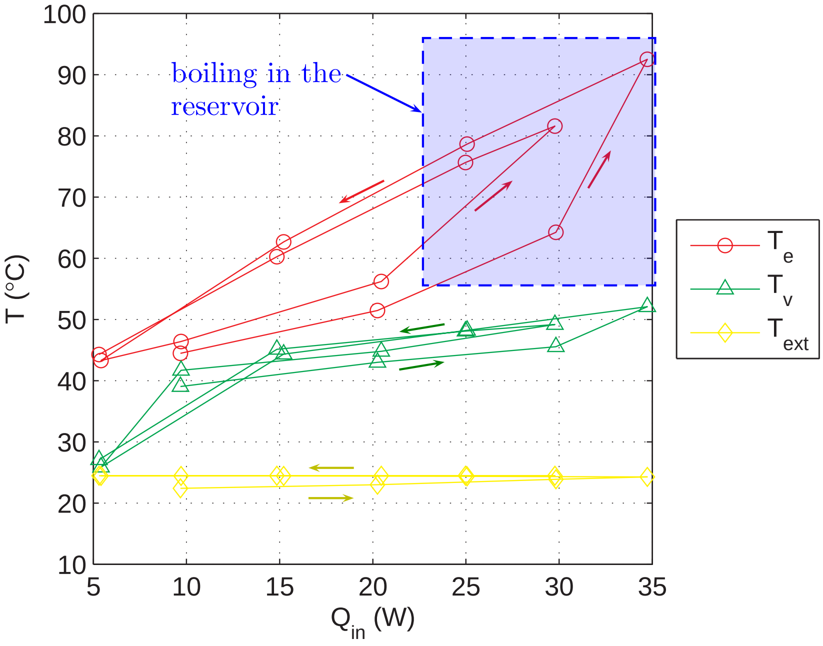

Figure 3.12: Consecutive tests – $T_{\mathrm{sink}} = 20\,°\mathrm{C}$ (in blue: boiling in the reservoir)

experimental results of this setup, presented in this thesis. In future studies, it is imperative to better control the tightness of the entire system, as well as to provide a more accurate measurement of the reservoir temperature, by the insertion of a thermocouple in the vapour zone of the reservoir.

3.3 Behaviour of the LHP during a power cycle

In order to observe the global behaviour of the LHP, a power cycle (increase-decrease) is applied to the evaporator.

The main temperatures (left-sided y-axis) and the heat load (right-sided y-axis) are plotted versus the time of the experiment. The heat load steps are approximately the following: 0 W–10 W–20 W–30 W–40 W–50 W–45 W–35 W–25 W–15 W–5 W–0 W. These values are approximate because the voltage at the terminals of the heater is manually set and its resistance slightly varies with the temperature. Therefore, a difference of ±1 W may exist between these expected values and the measured heat loads. The maximum heat load has been set in order to maintain the maximal measured temperature (hot side of the heat flux sensor $T_{\mathrm{hf},1}$) below 100 °C to ensure the integrity of the heater in the evaporator.

The heat sink temperature is set to 20 °C during the entire test and the ambient temperature varies between 20.5 °C and 23.3 °C, as shown in Figure 3.13.

As observed in the figure, the thermal inertia of the system is large and the stabilisation time for each heat load ranges from about 2200 s to 5900 s. This is a consequence of the large amount of liquid in the reservoir, the size of the evaporator/reservoir and the use of a low conductive polymer for the casing. With such a test duration, a slight change of the experimental conditions is unavoidable during the test. This change has to be considered, particularly when heat losses have a major influence on the LHP behaviour, *i.e.* at low heat loads.

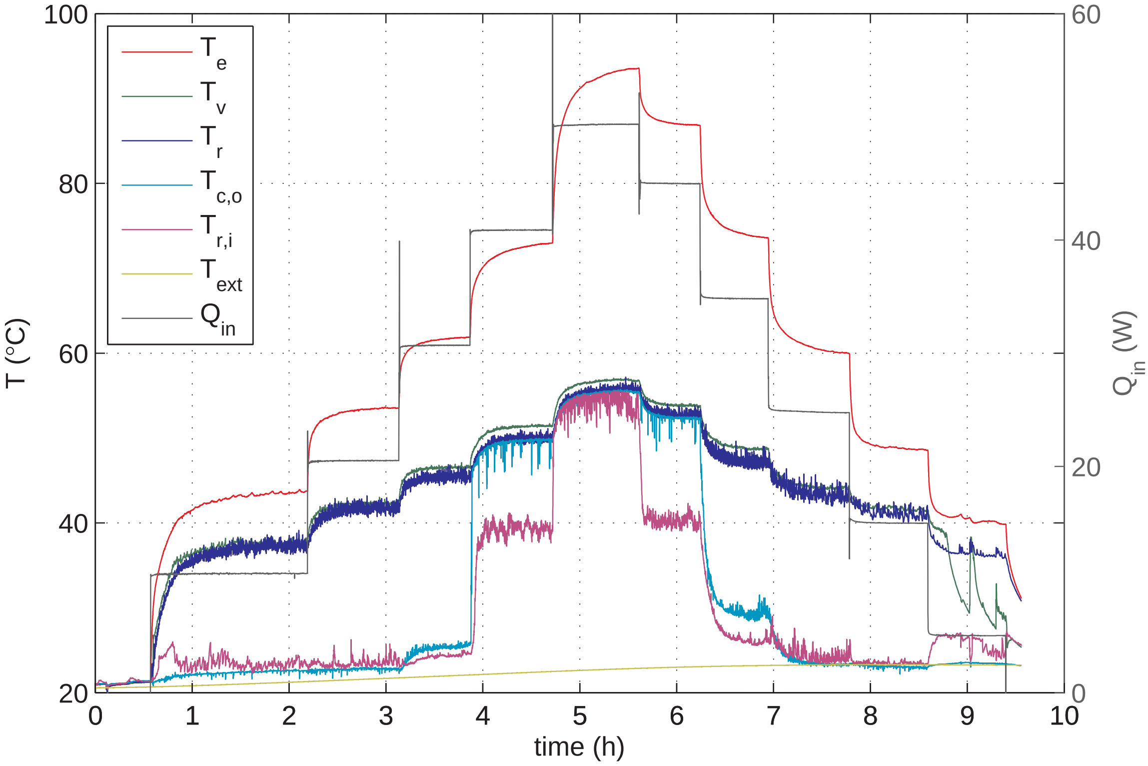

Figure 3.13: Power cycle of the LHP – $T_{\text{sink}} = 20\,°\text{C}$

Before the start-up, the vapour line is filled with liquid while the liquid line is filled with vapour. The state of the fluid in the vapour line (liquid or vapour) prior to start-up is further discussed in subsection 3.5.1. When the heat load is applied, the evaporator temperature starts to increase sharply, as shown in Figure 3.14 which a magnified view of Figure 3.13. Heat is also conducted to the reservoir (parasitic heat fluxes), mainly by conduction through the wick. The longitudinal parasitic heat losses are small because the thermal conductivity of the casing is extremely low ($\lambda_{\text{wall}} = 0.25\,\text{W}\cdot\text{m}^{-1}\cdot\text{K}^{-1}$). As a consequence, T_{r} increases also, at a lower rate than T_{e}. After 80 s, boiling occurs in the vapour grooves and vapour starts to flow through the vapour line, thus pushing the liquid present inside the tube. After 90 s, the vapour reaches the thermocouple T_{v}, inducing a sudden increase of the measured temperature. From that moment on, T_{v} is close to the saturation temperature inside the vapour line, slightly above the reservoir temperature.

As expected, the difference between T_{r} and T_{v} is very low. This difference is only due to pressure drops along the transport lines and the condenser and to the partial pressure of the NCGs in the reservoir (Equation (2.15)). NCGs may be produced inside the LHP for various reasons (subsubsection 1.2.4.4) or enter inside the system as a consequence of an insufficient airtightness. Comparing the pressure measured in the reservoir and the saturation pressure corresponding to T_r, the partial pressure of the NCGs trapped in the reservoir is estimated to 750 Pa (At $T_r = 20.8\,°\mathrm{C}$, $P_\mathrm{sat} = 2450\,\mathrm{Pa}$ and $P_\mathrm{r} = 3200\,\mathrm{Pa}$).

The figure shows many oscillations for the measurement of the reservoir temperature. This phenomenon is believed to be induced by the location of the thermocouple, at it was explained in section 3.2. At steady-state, the minimal value of T_r is assumed to be the closest to the liquid-vapour interface temperature and is, as such, used in the steady-state analysis.

Since vapour is present inside the liquid line initially, the temperature at the end of the tube $T_\mathrm{r,i}$ is function of the reservoir temperature. As a consequence, $T_\mathrm{r,i}$ increases. After 900 s, the subcooled liquid reaches the end of the transport lines and $T_\mathrm{r,i}$ slightly decreases.

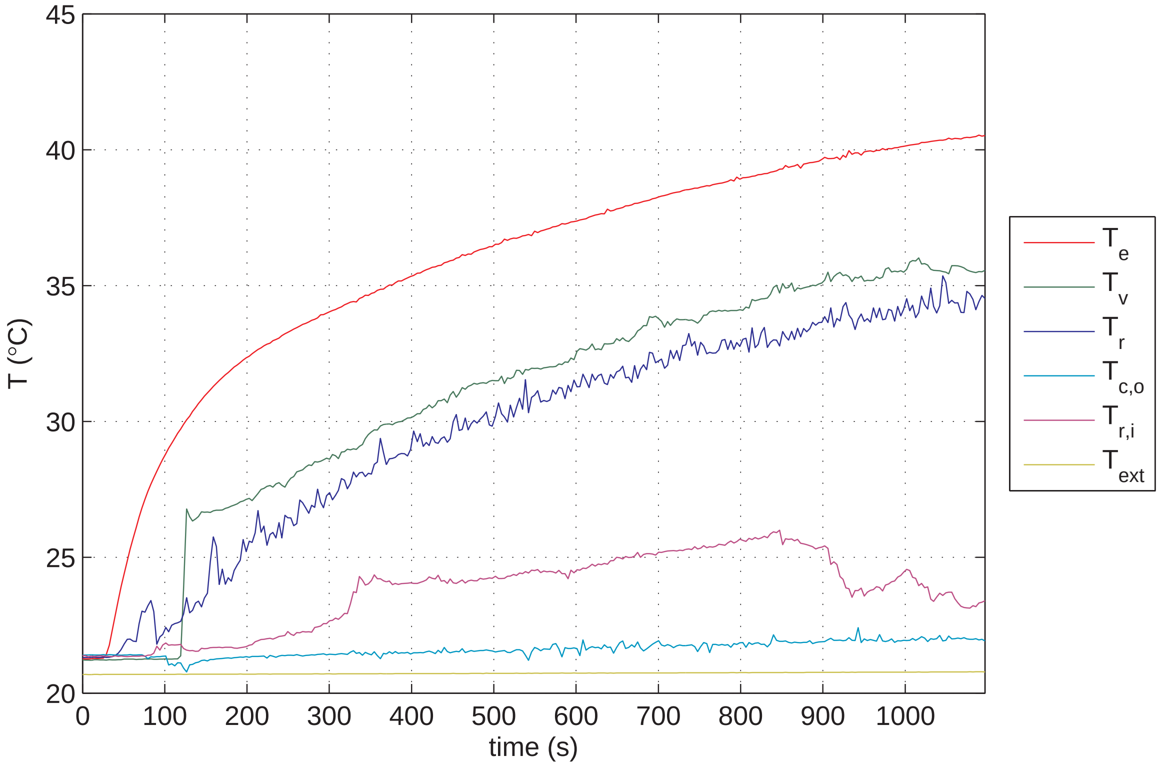

Figure 3.14: start-up of the LHP – $Q_\mathrm{in} = 10\,\mathrm{W}$

When the heat load increases to 20 W, T_e, T_v and T_r increase. However, since the meniscus is far from the end of the condenser, the LHP operates in variable conductance mode and $T_\mathrm{c,o}$ remains constant, nearly equal to T_sink.

At $Q_\mathrm{in} = 30\,\mathrm{W}$, the liquid-vapour interface almost reaches the exit of the condenser. Thus, the length of liquid subcooling inside the condenser is smaller and $T_\mathrm{c,o}$ starts to increase. The transition to the fixed conductance mode occurs.

At $Q_\mathrm{in} = 40\,\mathrm{W}$, the condenser is completely filled with vapour and the meniscus is located at the middle of the liquid line. As a consequence, $T_\mathrm{c,o}$ is equal to the saturation temperature. In the vapour line and the condenser, a thin liquid film of condensation is observed and flows downstream at a velocity lower than the vapour velocity. Besides, a liquid slug intermittently flows inside the transport lines and the condenser. The flow inside the tubes is further investigated in section 3.6. The length of the liquid zone in the liquid line being reduced, the subcooling of the liquid caused by heat losses to the ambient is limited and the liquid enters into the reservoir at a higher temperature $T_{\mathrm{r,i}}$. The location of the meniscus oscillates in the first half of the liquid line, inducing large variations of $T_{\mathrm{c,o}}$ and $T_{\mathrm{r,i}}$.

At $Q_{\mathrm{in}} = 50\,\mathrm{W}$, the vapour fills the vapour line, the condenser and almost the entire liquid line. The liquid exits the liquid line at a temperature close to the saturation temperature. The two-phase interface moves inside the second half of the line, resulting in variations of $T_{\mathrm{r,i}}$ of several kelvins.

When the heat load decreases from 50 W to 15 W, the observed phenomena are the same as for the increasing heat load. However, the temperature measurements show significant hysteresis effects (Figure 3.13). These phenomena are further discussed in the next section. At decreasing heat flux, the LHP operates at a very low heat load ($Q_{\mathrm{in}} = 5\,\mathrm{W}$). In that case, the operation is slightly different than at 10 W (Figure 3.15). At such a low heat load, the mass flow rate inside the tubes is extremely low ($< 2 \cdot 10^{-3}\,\mathrm{g \cdot s^{-1}}$). The liquid line and the condenser are both filled with liquid. The two-phase interface recedes progressively inside the vapour line until reaching the thermocouple T_{v}. As it oscillates inside the vapour line, T_{v} varies strongly between the vapour temperature and the liquid temperature.

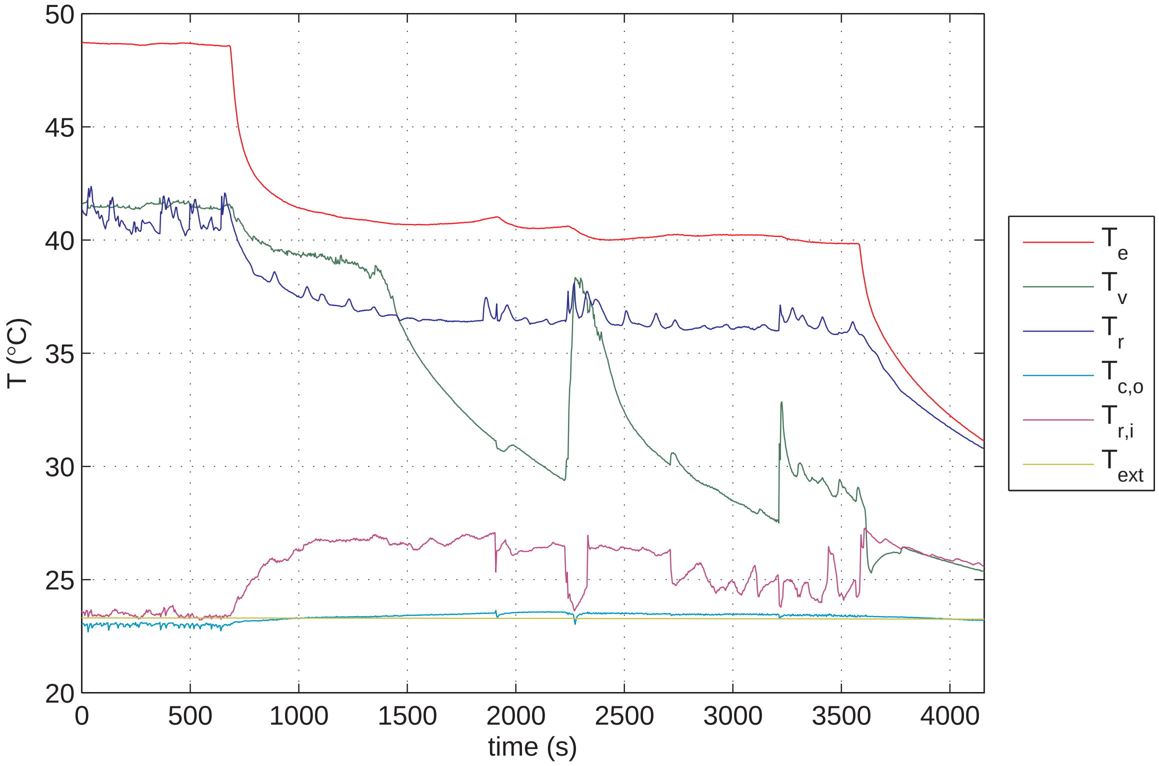

Figure 3.15: Operation at very low heat load – $Q_{\mathrm{in}} = 5\,\mathrm{W}$

3.4 Steady-state operation

In this section, various tests are conducted in order to assess the thermal steady-state performance of the LHP as well as to study the influence of several parameters (NCGs, heat sink temperature, boiling in the reservoir) on the steady-state operation of the LHP and on the hysteresis that is observed.

3.4.1 LHP thermal performance

Figure 3.16 presents the main temperatures as a function of the heat load in steady-state operation. The LHP operates with $T_{\mathrm{sink}} = 20\,°\mathrm{C}$ and a significant amount of NCGs ($P^{*}_{\mathrm{NCG}} \approx 1500\,\mathrm{Pa}$). The temperatures are measured with an increasing heat load. The transition between the variable conductance mode and the constant conductance mode ranges between 40 W and 45 W. Boiling in the reservoir is not observed during this test. The large amount of NCGs induces a higher operational temperature than in the test presented in section 3.3, leading to better heat transfer in the condenser and therefore, the transition between the two modes occurs at a higher heat load. The difference between T_{e} and T_{r} increases with the heat load for the entire tested range, but particularly at very low heat loads and in constant conductance mode. This difference is mainly due to the thermal contact resistance between the evaporator copper block and the porous wick.

The difference between the vapour temperature and the temperature inside the reservoir is exclusively dependent on the pressure losses inside the transport lines and the NCGs in the reservoir. In the present case, the partial pressure of NCGs induces a rather significant difference between T_{v} and T_{r}, as shown in Figure 3.16.

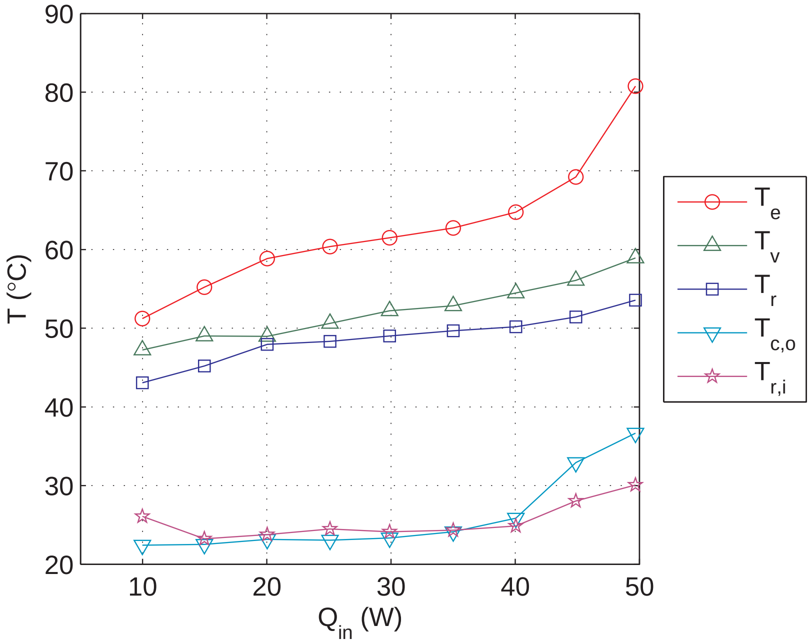

Figure 3.16: Characteristic curve

The performance of the LHP can also be assessed by the thermal resistance of the system. In the present study, the LHP thermal resistance R_{LHP}, the evaporator resistance R_{e} and the condenser resistance R_{c} are calculated as follows (subsection 1.1.3):

$$R_{\mathrm{LHP}} = \frac{T_{\mathrm{e}} - T_{\mathrm{sink}}}{Q_{\mathrm{in}}} \tag{3.5}$$

$$R_{\mathrm{e}} = \frac{T_{\mathrm{e}} - T_{\mathrm{v}}}{Q_{\mathrm{in}}} \tag{3.6}$$

$$R_{\mathrm{c}} = \frac{T_{\mathrm{v}} - T_{\mathrm{sink}}}{Q_{\mathrm{in}}} \tag{3.7}$$

The different thermal resistances are shown in Figure 3.17. The total resistance ranges from $1.1\,\mathrm{K}\cdot\mathrm{W}^{-1}$ at high heat loads to more than $3\,\mathrm{K}\cdot\mathrm{W}^{-1}$ at 10 W. The variation of the LHP resistance with the heat load follows a standard shape that can be found in classical experimental analyses [31, 40, 42]. The resistance is high for low heat loads for which the part of heat that is actually dissipated by evaporation is low and heat losses to the ambient have a major effect on the operation. The total resistance decreases sharply as the heat load increases in variable conductance mode. In constant conductance mode, the thermal resistance of the LHP is almost constant whatever the heat input. The heat load is limited to 50 W because the maximal temperature of the heater which is 100 °C is reached for higher heat inputs.

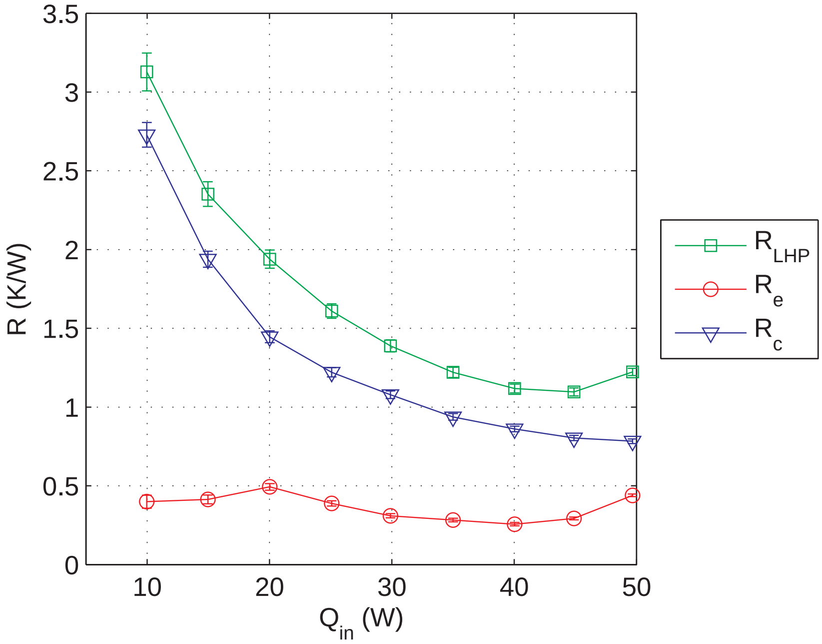

Figure 3.17: Thermal resistances of the LHP

One can also observe that the major LHP thermal resistance is due to the condenser and not to the evaporator. This contribution is particularly pronounced at low heat loads. R_{c} decreases when the heat flux increases, whereas R_{e} is almost constant for the entire range. Such a resistance at the condenser was expected with a glass condenser. Indeed, the thickness of the tube (2 mm) and the low thermal conductivity of glass ($1\,\mathrm{W \cdot m^{-1} \cdot K^{-1}}$) reduce drastically heat transfer between the working fluid and the heat sink.

The uncertainties plotted in Figure 3.17 are calculated with the values given in subsection 3.1.2 regarding the measurement of both the temperatures and the heat load. However, the accuracy of R_c and R_e is much lower if one considers the representativeness of the measurements. Indeed, T_v may underestimate the actual temperature of the vapour flowing in the transport line, thus inducing a much larger uncertainty on the thermal resistances. Therefore, the values of both the thermal resistances should be considered with caution and a slight change as the one observed at 20 W for R_e does not necessarily have a physical meaning.

3.4.2 Hysteresis phenomena

Hysteresis phenomena during LHP operation have already been investigated in the literature. Wolf and Bienert [21] report a vapour temperature hysteresis at low power, and with a large positive elevation (evaporator above the condenser). However, the authors do not provide any explanation regarding this phenomenon. Low power hysteresis effects have also been observed by Cheung et al. [151]. The authors hypothesise that the loop steady state temperatures can be shifted due to two-phase dynamics in the evaporator core that influence the parasitic heat fluxes. Indeed, a steep power decrease leads to a sudden recession of the meniscus in the condenser and change the distribution of liquid and vapour inside the evaporator core and the bayonet. Ku [35] also describes another hysteresis phenomenon, which occurs between two consecutive tests. If the vapour partially invades the wick during the first test, there might be entrapment of vapour zones inside the capillary structure. During the second test, the LHP then operates at a higher temperature.

Vershinin and Maydanik [152] conduct an extensive analysis of hysteresis phenomena in LHPs. They report three types of hysteresis effects, all of them being connected to the redistribution of liquid between the compensation chamber and the condenser in case of change of heat load. The first type is induced by a capillary hysteresis. The evaporation front may change and moves into the wick at very low heat loads or at high heat loads, inducing heat-exchange and temperature hystereses. The second type is connected to the change between a partially filled and a hard-filled reservoir, while the third one is a consequence of the initial distribution of liquid in the LHP.

Major hysteresis phenomena have been observed in the present study, as shown for instance in Figure 3.18 for a power cycle with a heat sink temperature of 20 °C, an ambient temperature ranging from 21.6 °C to 23.9 °C and a partial pressure of NCGs equal to about 1500 Pa. A significant difference is observed between operating curves at increasing and decreasing heat fluxes. Data is not available for T_v at very low heat loads because the thermocouple is in contact with subcooled liquid due to the recession of the meniscus inside the vapour line.

The observed hysteresis cannot be explained by the presence of NCGs. Indeed, the des-

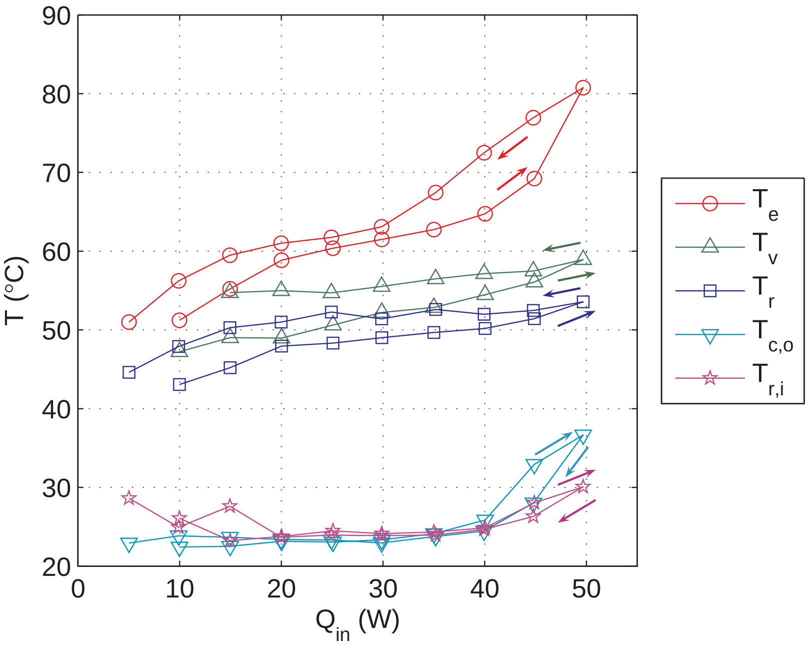

Figure 3.18: Temperature hysteresis

orption of NCGs trapped in the system and heat leaks would lead to a higher operating temperature. However, in this test, no significant increase of NCGs has been observed neither on the pressure measurement nor on the difference between T_v and T_r (Figure 3.18).

The location of the liquid inside the system does also not explain this hysteresis. Indeed, no significant change of the filling level of the reservoir is reported and the initial state of the LHP prior to start-up cannot be the source of the hysteresis. Therefore, we assume that the hysteresis could be due to the evaporation zone and may correspond to the capillary hysteresis observed by Vershinin and Maydanik [152]. Indeed, at high loads, the wick may partially be dried. The displacement of the liquid-vapour front inside the porous structure may increase the transversal parasitic heat flux, thus leading to an increase of the operating temperature. The development of a vapour region inside the capillary structure and its recession when decreasing the heat load (imbibition) may lead to a significant hysteresis, as it was presented in the numerical investigation of Louriou [125].

3.4.3 Boiling in the reservoir

Boiling is observed in the reservoir in particular operating conditions. It occurs at moderate to high heat loads and this phenomenon is delayed when the amount of NCGs increases. In the example presented in Figure 3.19, when the heat load increases from 10 W to 30 W, heat transfer between the wick and the liquid bulk in the reservoir is mainly convective. When the heat load reaches 35 W, boiling incipience occurs at the surface of the capillary structure and leads to larger heat exchange inside the reservoir. Such an enhanced heat transfer at the surface of the wick increases the parasitic heat flux. As a consequence, T_r

and T_v slightly increase. The major change, however, is observed for T_e. The evaporator temperature increases abruptly after the boiling incipience.

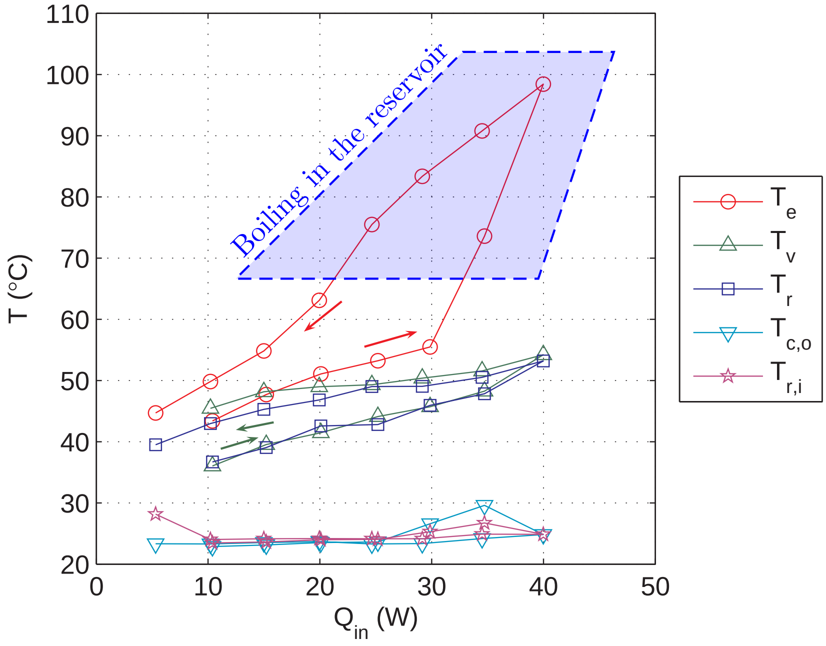

Figure 3.19: Consequences of the boiling phenomena in the reservoir on the temperatures of the LHP

When the heat load decreases, boiling remains inside the reservoir until $Q_\mathrm{in} = 20\,\mathrm{W}$. This is the well-known boiling hysteresis: a superheat is necessary to initiate the nucleation process at the surface of the wick, but this superheat is not necessary to keep the nucleation sites active. This boiling hysteresis effect accentuates the capillary hysteresis that have been previously observed.

The prediction and the prevention of boiling incipience in the reservoir is of major interest, given the consequences on the evaporator temperature. However, the nucleation depends on many parameters and an accurate prediction of the phenomenon is, as such, not available. The following parameters may have a significant influence on the nucleation:

- The nucleation superheat is inversely proportional to the radius of the nucleation site. Therefore, smaller pores in the capillary structure lead to a higher superheat for boiling at the surface of the wick. Likewise, a clean reservoir without impurities and smooth contacts between the wick, the evaporator envelope and eventual seal also prevent the nucleation.
- The nucleation is also dependant on the surface tension, the density and the latent heat of vaporisation of the fluid. Thus, the nature of the working fluid and the operating temperature have a significant influence on the boiling incipience.
- Heat that is dissipated at the wick surface in the reservoir corresponds to the transversal parasitic heat flux which depends on the geometrical and thermophysical properties of

the wick, as it has been explained in chapter 2. Therefore, nucleation can be avoided by optimising the properties of the wick.

- The level of liquid in the reservoir may change the homogeneity of the liquid bulk and the devlopment of convective cells in it. Therefore, the amount of working fluid in the system can also modify the boiling incipience.
- The presence of NCGs may strongly modify the occurrence of boiling in the reservoir. This is further detailed in the next subsection.

3.4.4 Influence of the NCGs on the steady-state behaviour

Figure 3.20 shows the comparison of the LHP temperatures with and without degassing of the reservoir prior to start-up. The objective of this comparison is to evaluate the influence of the amount of NCGs on the LHP operating temperature and on the onset of nucleate boiling inside the reservoir.

As explained before, when NCGs are present inside the reservoir, the partial pressure they induce leads to a higher temperature difference between T_v and T_r. As a consequence, the parasitic heat transfer through the wick is larger and the operating temperature is higher. As the operating temperature increases, P^*_NCG remains almost constant ($P^*_\mathrm{NCG} \approx 3000\,\mathrm{Pa}$) because the gas density does not vary much and the volume occupied in the reservoir is almost constant. However, the pressure inside the system increases significantly with the increase of the operating temperature, inducing a lower influence of the NCGs.

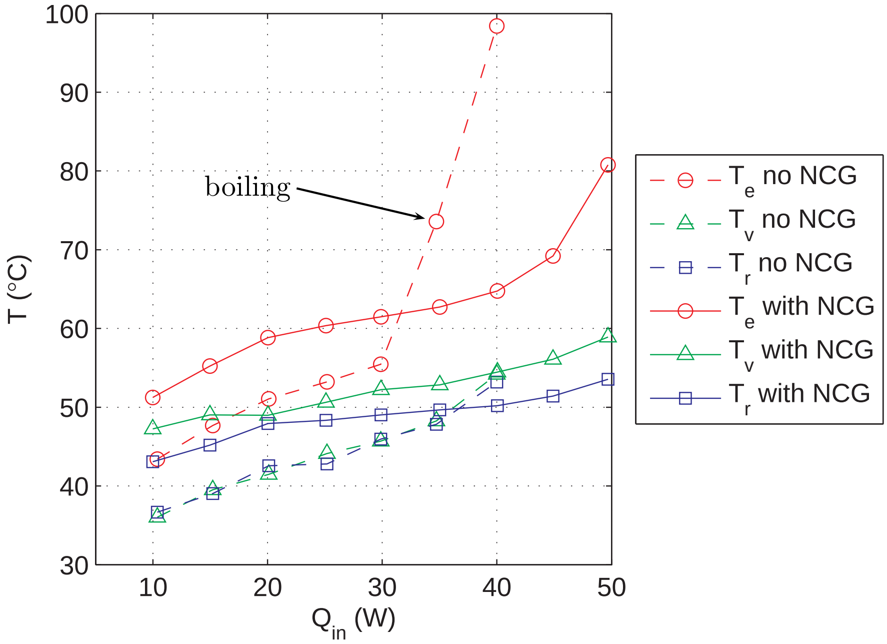

Figure 3.20: Influence of the NCGs on the LHP temperatures – increasing heat load

When the heat load exceeds 30 W, a major difference is observed between both configurations. As explained before, the evaporator temperature of the LHP without NCGs sharply increases due to boiling occurrence in the reservoir. When NCGs are present in the reservoir, the nucleation temperature in the reservoir is higher and boiling is not observed. The LHP can thus operate at higher heat loads and reaches the variable conductance mode at $Q_{\text{in}} \approx 45\,\text{W}$.

In case of pool boiling, the temperature required to initiate the nucleation T_{nuc} is equal to:

$$T_{\text{nuc}} = T_{\text{sat}}(P|_{\text{at the boiling surface}}) + \Delta T_{\text{nuc}} \tag{3.8}$$

where ΔT_{nuc} is the nucleation superheat, depending on the operating conditions, the nature of the fluid and the material as well as the topology of the surface. Without NCGs, the pressure at the boiling surface is equal to:

$$P|_{\text{at the boiling surface}} = P_{\text{sat}}|_{\text{at the interface}} + \Delta P_{\text{static}} \tag{3.9}$$

where ΔP_{static} is the hydrostatic pressure induces by the height of liquid above the surface. In theory, various effects on the nucleate boiling can be attributed to NCGs:

- NCGs in the reservoir lead to a larger pressure difference between the vapour in the grooves and the reservoir. Consequently, the temperature difference also increases and larger parasitic heat fluxes are expected towards the reservoir, which may increase the probability of boiling incipience.

- Gas dissolved in the fluid as well as gas entrapment at the surface of the porous structure tend to increase the boiling phenomena [153]. As explained by Carey [34], both entrapped gas in surface cavities and dissolved gas facilitate the initial nucleation process, lowering the superheat required to initiate the nucleation. The entrapment of gas in the wick depends on the history of the LHP operation. Therefore, the presence of preferential nucleation sites at the surface of the capillary structure may vary for several consecutive tests. An extensive discussion regarding heterogeneous nucleation can be found in Carey [34].

- An opposite effect on the nucleation process may also be attributed to NCGs. The gas present above the free surface inside the reservoir induces a partial pressure P^*_{NCG}. The pressure at the surface of nucleation is then equal to:

  $$P|_{\text{at the boiling surface}} = P_{\text{sat}}|_{\text{at the interface}} + \Delta P_{\text{static}} + P^*_{\text{NCG}} \tag{3.10}$$

  and the nucleation temperature becomes:

  $$T_{\text{nuc}} = T_{\text{sat}}(P_{\text{sat}}|_{\text{at the interface}} + \Delta P_{\text{static}}) + \Delta T_{\text{nuc}} + \frac{\partial T_{\text{sat}}}{\partial P_{\text{sat}}} P^*_{\text{sat}} \tag{3.11}$$

  The last term depends on both the amount of NCGs, the nature of the fluid and the experimental conditions. In the case of water at low temperature, $\frac{\partial T_{\text{sat}}}{\partial P_{\text{sat}}}$ is significant and induces a large effect of the partial pressure of NCGs. For instance, if the saturation temperature is equal to 45 °C, a partial pressure of 3000 Pa leads to an additional superheat of 5.4 K. The nucleation phenomenon can therefore be delayed due to the NCGs. This effect was experimentally observed in loop thermosyphons by He et al. [154].

According to the experimental results, the third mentioned effect has the largest influence on the LHP behaviour in the present case. Although NCGs induce a higher operating temperature, particularly at low heat loads, they prevent the LHP from a degraded operation mode due to boiling in the reservoir. Therefore, the system performance is maintained at high heat loads and the maximal heat load that can be reached by the LHP increases.

3.4.5 Influence of the heat sink temperature

Figure 3.21 shows the influence of the heat sink temperature on T_e and T_v. At very low heat loads, T_sink has no significant influence. Indeed, in that case, the LHP operation is governed by the evaporator/reservoir structure and heat losses to the ambient rather than by the condenser. Since the mass flow rate is extremely low, the temperature of the liquid at the end of the liquid line is almost constant and equal to the ambient temperature, whatever the heat sink temperature.

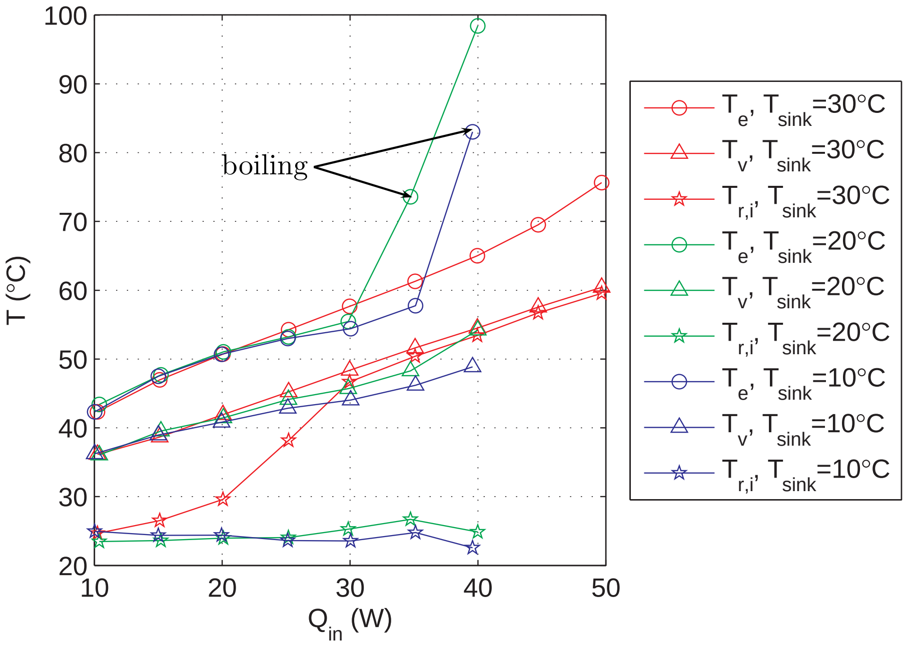

Figure 3.21: Influence of the heat sink temperature on the evaporator and vapour temperatures

For moderate heat loads (20 W to 30 W), a lower heat sink temperature enables a lower operating temperature, as expected. T_sink has an influence on the subcooling of the fluid entering in the reservoir, and thus on the vapour and the evaporator temperatures.

At higher heat loads, T_{e} and T_{v} are more influenced by the boiling in the reservoir than by T_{sink}. In this experiment, boiling occurs at 40 W for $T_{\text{sink}} = 10\,°\text{C}$, at 35 W for $T_{\text{sink}} = 20\,°\text{C}$ and above 50 W for $T_{\text{sink}} = 30\,°\text{C}$ (not represented). As previously discussed, the nucleation process cannot be predicted accurately because it depends on many parameters. A small amount of NCGs in the reservoir can have a significant effect on the boiling incipience. Furthermore, when the heat sink temperature is equal to 30 °C, the intermittent vapour-liquid flow entering in the reservoir provides larger flow perturbation in the liquid bulk that may lead to a better temperature homogeneity and prevent the nucleation.

The evaporator and condenser thermal resistances are presented in Figure 3.22. As expected, the heat sink temperature has no significant effect on the evaporator resistance. An increase of T_{sink} induces a large decrease of the condenser thermal resistance. Indeed, because of its poor thermal performance, the condenser does not govern the behaviour of the LHP and a change of the heat sink temperature does not have a significant influence on the LHP operation. The sharp discontinuity at high heat loads at 10 °C and 20 °C is simply due to the boiling phenomena in the reservoir.

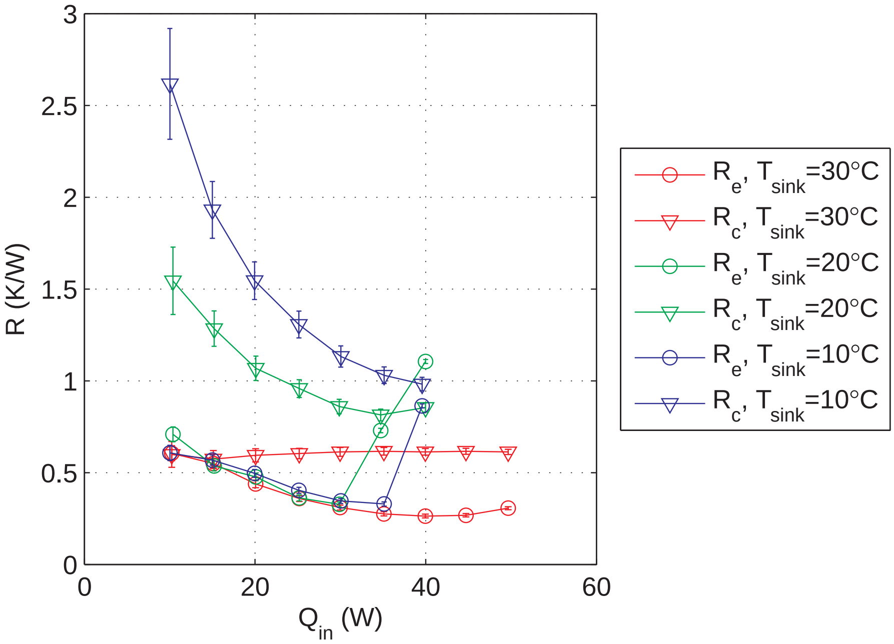

Figure 3.22: Influence of the heat sink temperature on the thermal resistance

Figure 3.23 presents the two-phase length inside the condenser and the liquid line as a function of the heat load for three distinct heat sink temperatures. When the heat sink temperature decreases, heat transfer is enhanced in the condenser and the LHP operates with a shorter two-phase region. For $T_{\text{sink}} = 10\,°\text{C}$ and $T_{\text{sink}} = 20\,°\text{C}$, the meniscus is located inside the condenser, and the two-phase length increases with the heat load in normal operation. When boiling occurs, parasitic heat fluxes sharply increase. To compensate this phenomenon, the meniscus recedes inside the condenser to provide a large subcooling.

The operation with $T_{\text{sink}} = 30\,°\text{C}$ is singular. At $Q_{\text{in}} = 10\,\text{W}$, the condenser is almost

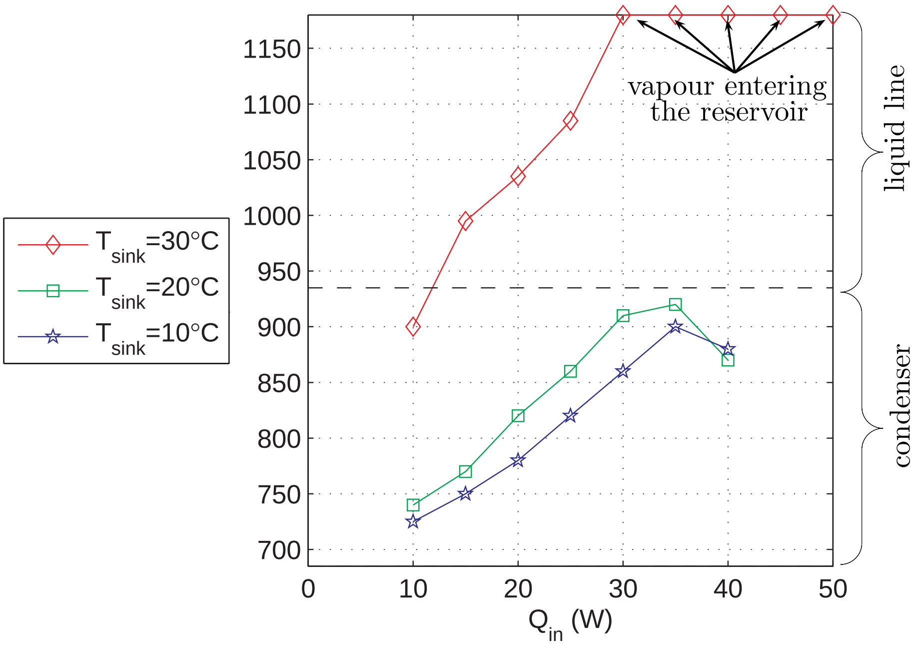

Figure 3.23: Influence of the heat sink temperature on the two-phase length

already filled with vapour. For $10\,\mathrm{W} < Q_{\mathrm{in}} < 30\,\mathrm{W}$, vapour is located inside the liquid line. Above 30 W, vapour occupies the entire liquid line and enters in the reservoir, while liquid slugs intermittently circulates in the lines and reaches the reservoir. Therefore, the vapour also condenses inside the reservoir. Such a steady-state operation is not usual and is due to the poor performance of the condenser. In the present investigation, the reservoir is very large and provides significant heat losses to the ambient. Therefore, if the LHP operates at a sufficiently high temperature, heat losses can be larger than parasitic heat fluxes, thus inducing a steady-state operation where both vapour and liquid enter the reservoir.

3.5 Transient analysis

This section discusses the transient behaviour of the LHP, in particular the operation of the system during start-up, in the case of power steps and the oscillating phenomena observed at very low and high heat loads, respectively.

3.5.1 Start-up behaviour

3.5.1.1 Effect of the heat load on the start-up

Figure 3.24 presents the evaporator temperature during the start-up of the LHP for various heat inputs ranging from 10 W to 30 W. As shown in Figure 3.24b, the start-up has an influence on the time required for the circulation of the fluid inside the loop. Vapour is generated more rapidly in the case of high heat loads. The larger mass rate of evaporation also leads to a smaller time needed for the vapour to invade the vapour line and to enter the condenser. However, this start-up time is much lower than the time required for the LHP temperature to reach a steady-state (Figure 3.24a). Furthermore, no temperature overshoot is observed, unlike some experiments from the literature [35, 39, 155].

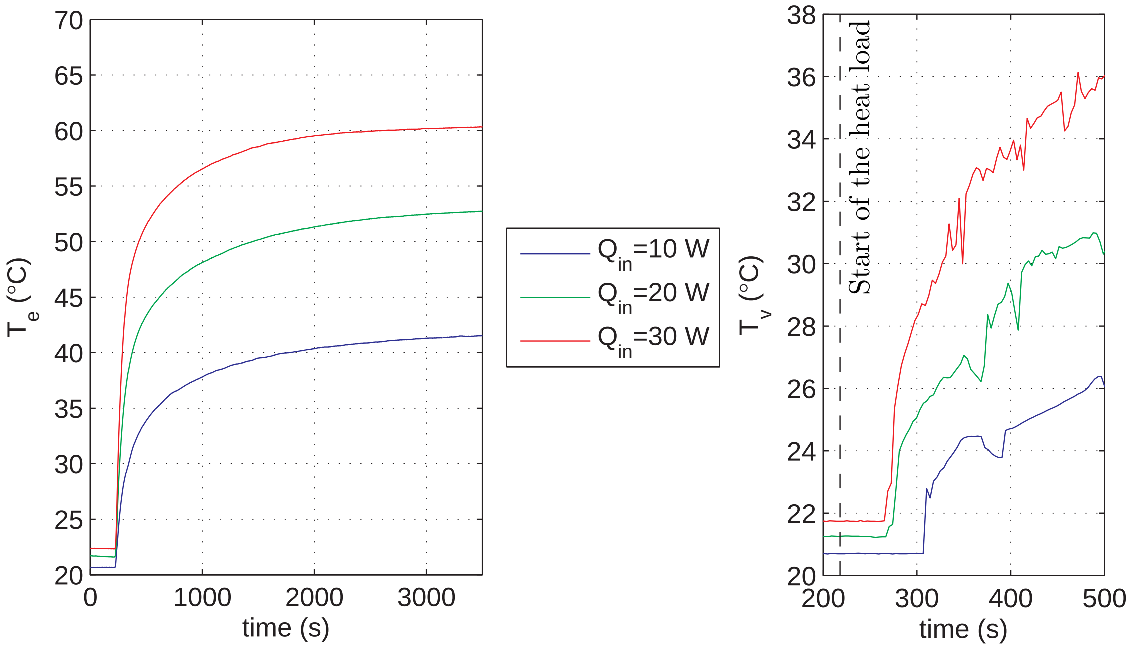

(a) Evaporator temperature

(b) Vapour temperature

Figure 3.24: Influence of the heat load on the start-up – $T_{\text{sink}} = 20\,°\text{C}$

3.5.1.2 Effect of the state of the fluid in the vapour line prior to start-up

Figure 3.25 shows the temperature profile in the LHP for two start-ups, one with the vapour line filled with liquid prior to the start-up and one with the vapour line filled with vapour. For both tests, T_{sink} is set to 20 °C and the heat load is equal to about 31.5 W. Experimental results for both conditions are similar and no influence on the start-up time can be attributed to the filling of the vapour line prior to the start-up. The temperatures of the LHP flooded with liquid are slightly above those reached when the line is filled with vapour. This small difference can be explained by different applied heat loads for both tests (31.2 W and 31.7 W), respectively. The increase of T_{v} and $T_{\text{c,o}}$ occurs with a small delay for a flooded vapour line. In that case, the time for the fluid to flow through the transport lines in the first minutes of the start-up is slightly longer.

3.5.1.3 Effect of non-condensable gases

Figure 3.26 presents the influence of the NCGs on the LHP start-up. For the test without NCGs, the LHP was degassed prior to start-up, whereas for the test with NCGs, the

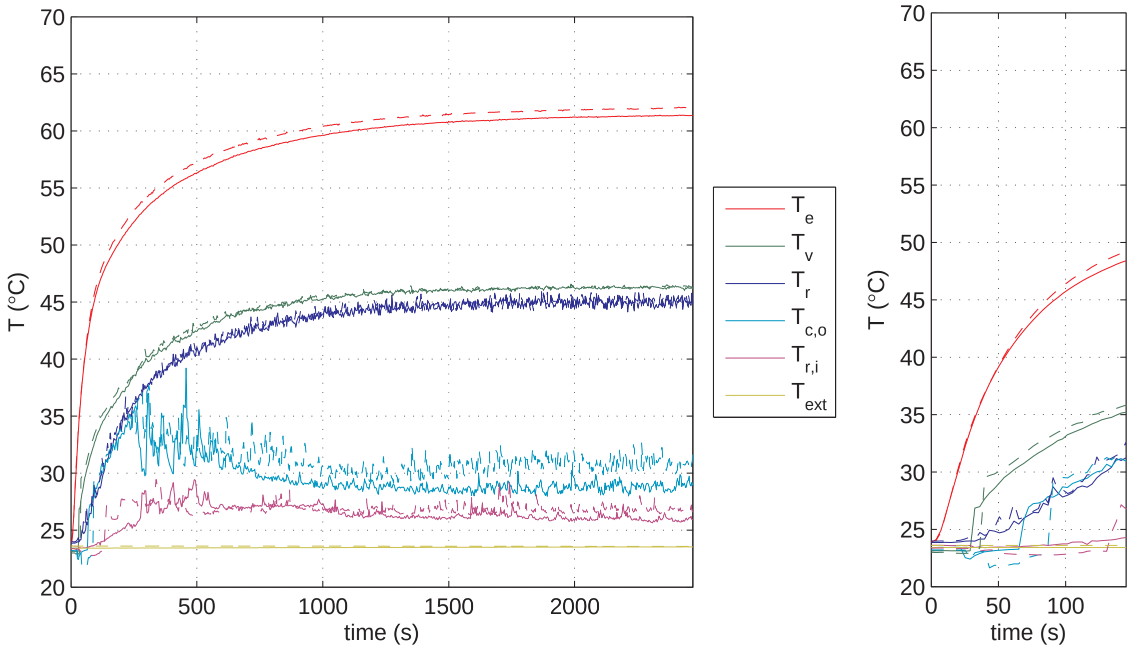

(a) (b)

Figure 3.25: Influence of the vapour line state prior to start-up – flooded with liquid (dashed lines) and filled with vapour (solid lines)

partial pressure of NCGs is estimated to 3000 Pa. As explained before, the presence of non-condensable gases in the reservoir induces a higher operating temperature in steady-state. NCGs have also a significant influence on the stabilisation time after start-up. As it is observed in the figure, a sharp increase of T_v occurs 95 s after the heat load is applied without NCGs while it requires 120 s when NCGs are present. This delay shows that the start-up time is significantly increased by the presence of NCGs in the reservoir, which confirms the conclusions of Singh et al. [45].

3.5.2 Power steps

The response of the LHP to several power steps is presented in Figure 3.27. The following heat load cycle is applied: 0 W–30 W–10 W–30 W–10 W–40 W–30 W-10 W–30 W–0 W. Due to the size of the system and its thermal inertia, the time required for the LHP temperature to reach steady-state ranges between 30 and 60 minutes.

This test enables to evaluate the influence of the thermal history of the LHP on its behaviour. The behaviour of the LHP during a decreasing step from 30 W to 10 W is almost the same along the test. A slight increase (+2 K) of the operating temperature is observed which can be attributed to the increase of the ambient temperature, to a potential increase of the amount of NCGs in the reservoir and to hysteresis phenomena. When the heat load increases from 0 W to 30 W or from 10 W to 30 W, the LHP always operates at the same temperature. However, during operation at 40 W, boiling occurs in the reservoir, resulting in

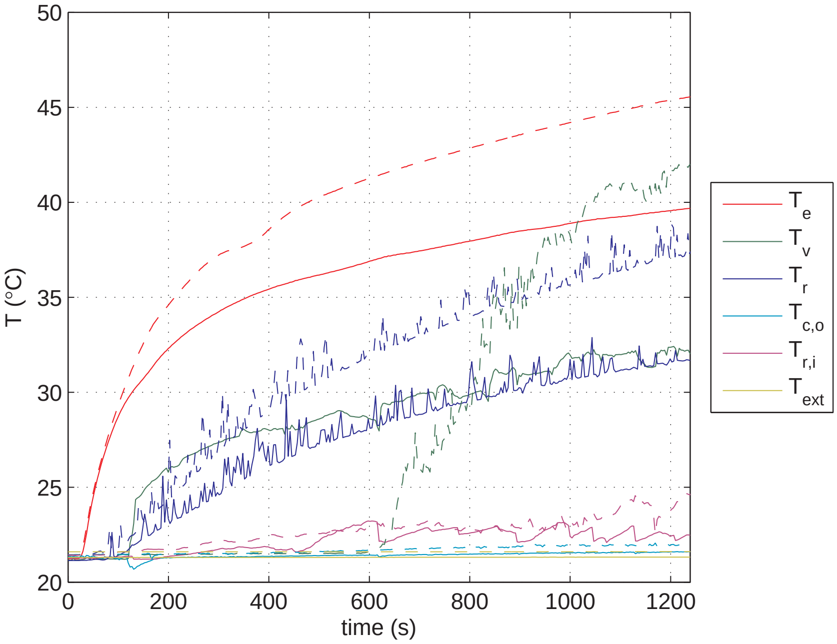

Figure 3.26: Influence of the NCGs on the start-up – with NCG (dashed lines) and without NCG (solid lines)

a sharp increase of the evaporator temperature and in a large hysteresis (11 K) of T_e when decreasing the heat load to 30 W. This increase is small for the other temperatures of the system.

The behaviour of the LHP for similar increasing or decreasing power steps is quite reproducible during operation. However, the operating temperature of the system cannot be predicted considering only the applied heat load at a given time. The history of the LHP needs to be taken into account because of the hysteresis that was already described in subsection 3.4.2.

3.5.3 Oscillating phenomena

Temperature oscillations are observed during a start-up with a heat load equal to 5 W and a heat sink temperature of 20 °C (Figure 3.28). The start-up has not reached a steady-state operation yet. Thus, T_r continuously increases.

Three types of oscillations are observed:

- high amplitude and low frequency oscillations for T_v (6 K) and $T_\mathrm{r,i}$ (2.5 K).
- low amplitude and low frequency oscillations for T_e and $T_\mathrm{c,o}$ (< 1 K).
- high frequency and low amplitude oscillations for T_r (< 1 K).

The two first mentioned oscillations are a consequence of the condensation regime in the vapour line and the intermittent flow of liquid in it. For T_e, a damping effect due to the large

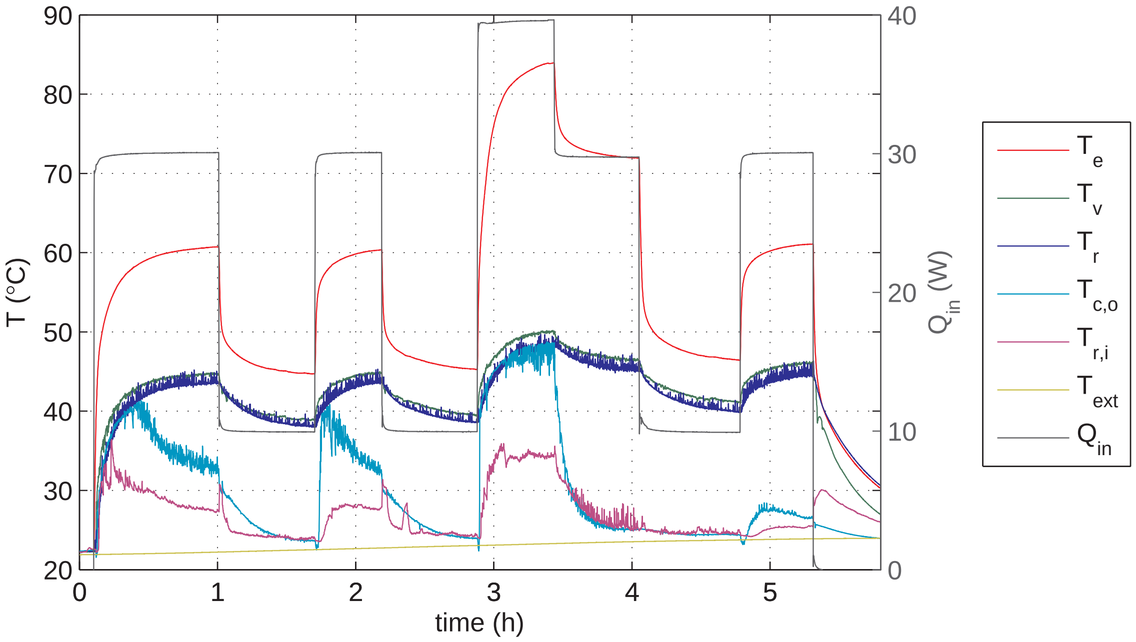

Figure 3.27: Power steps – $T_{\text{sink}} = 20\,°\text{C}$

thermal inertia of the copper block explains a lower amplitude of the oscillations. The third oscillation mentioned is due to the location of the thermocouple inside the reservoir, close to the wick. Temperature gradients as well as convection phenomena exist in the liquid bulk, resulting in variations of the measured temperature as it was previously explained.

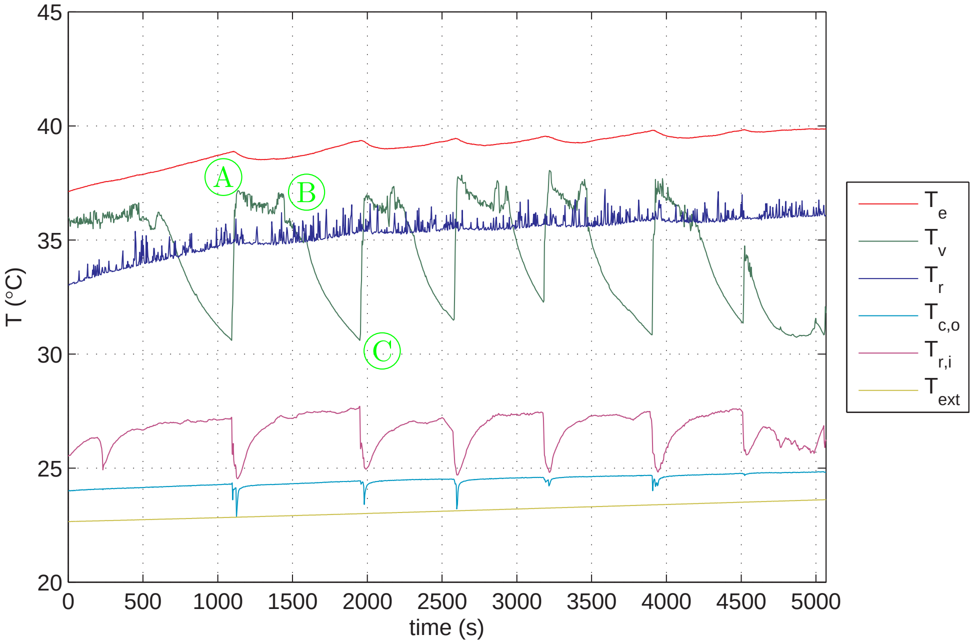

Figure 3.28: Oscillations during a start-up at 5 W – $T_{\text{sink}} = 20\,°\text{C}$

The observations through the transparent vapour line enable to relate the temperature oscillations to the hydrodynamic mechanisms in the tube. At such a very low heat load, the vapour condenses completely in the vapour line. At the point A, the meniscus is located downstream of the thermocouple measuring T_v. The thermocouple then measures the temperature of the vapour coming from the evaporator, close to the saturation temperature. From the point A to the point C, the meniscus slowly moves upstream. The mass flow rate inside the tubes being very low, the influence of the reservoir temperature on $T_\mathrm{r,i}$ is large and a continuous increase of $T_\mathrm{r,i}$ is observed. Between A and C, T_v is first approximately constant until the meniscus reaches the thermocouple (point B) and recedes upstream of T_v. Then, the thermocouple measures the temperature of subcooled liquid, so T_v gradually decreases. Simultaneously, condensation occurs inside the vapour line as a consequence of heat losses to the ambient. Droplets grow on the internal wall of the vapour line while vapour still flows in the central part of the tube. As their size increases, the droplets coalesce. At the point C, the coalescence of large droplets leads to the formation of a liquid slug. This slug is then pushed downstream by the vapour, dragging along the liquid attached on the internal wall. As a consequence, the meniscus moves downstream of the thermocouple, T_v suddenly increases and the temporary increase of the mass flow rate brings subcooled liquid to the liquid line, thus inducing a sharp decrease of $T_\mathrm{c,o}$ and $T_\mathrm{r,i}$.

As shown in Figure 3.29, some oscillating phenomena have also been observed at higher heat loads, with a sink temperature higher than the ambient temperature ($T_\mathrm{sink} = 30\,°\mathrm{C}$, $T_\mathrm{ext} = 23\,°\mathrm{C}$). In such conditions, the meniscus is located in the last part of the liquid line and oscillates significantly. As a result, the thermocouple $T_\mathrm{r,i}$ measures alternatively vapour and liquid and the temperature of the fluid entering in the reservoir varies substantially, with an amplitude equal to about 3 K and a time period of approximately 60 s. The influence on the LHP global behaviour is, however, not important.

3.6 Observations through the transparent lines

3.6.1 Condensation in the condenser

Figure 3.30 shows the flow regimes that can be seen inside the condenser. As presented in the figure, several zones can be determined. Upstream, a long annular zone is observed, governed by capillary forces. A slight asymmetry due to the gravity is seen, with a thicker liquid film on the bottom of the tube than in the upper part. An almost hemispherical meniscus is present at the end of the annular region, followed by a train of bubbles. Further downstream, several uncondensed isolated bubbles are observed.

A similar flow structure has already been reported in the literature in the case of condensation in minichannels [156–158]. Médéric et al. [156] compared the flow characteristics of n-pentane condensing in straight smooth tubes with 3 distinct internal diameters: 10 mm, 1.1 mm and 0.56 mm. For the tube of 1.1 mm inner diameter the hydraulic diameter was close

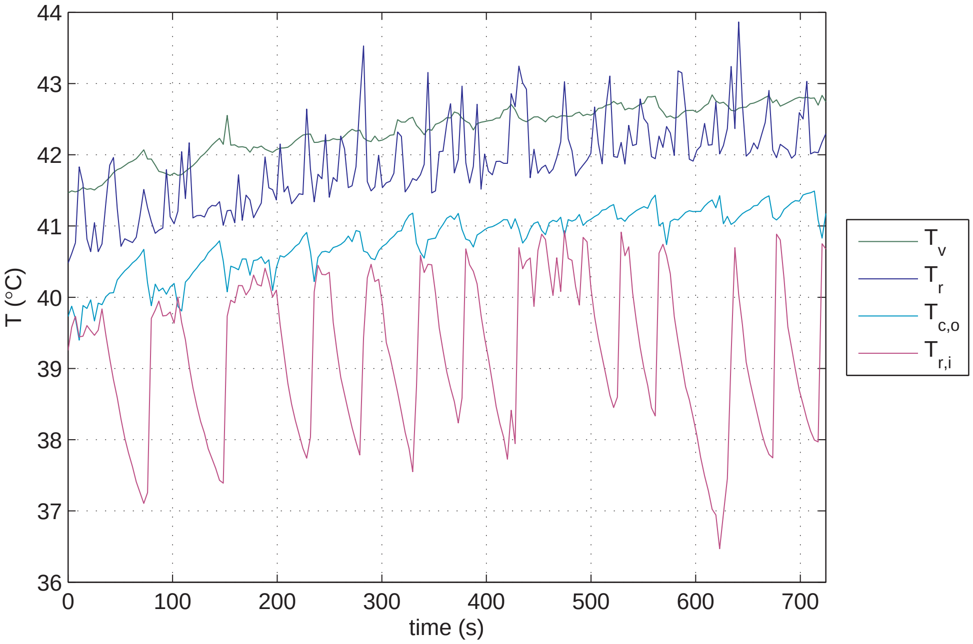

Figure 3.29: Oscillations at the end of the liquid line – $Q_{\text{in}} = 20.2\,\text{W}$, $T_{\text{sink}} = 20\,°\text{C}$

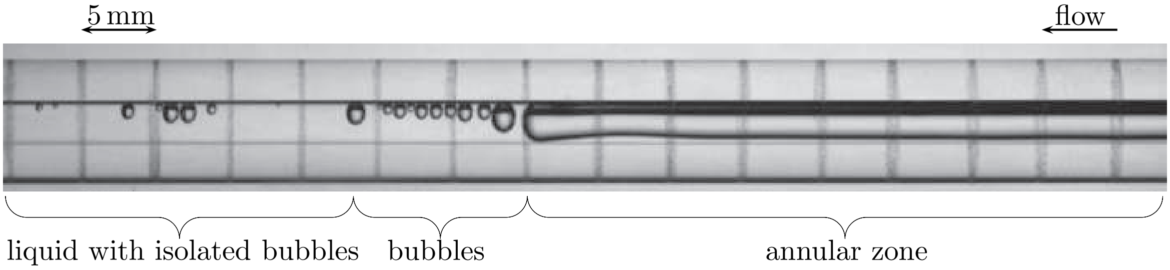

Figure 3.30: Condensation regimes in the condenser – $Q_{\text{in}} = 24\,\text{W}$, $T_{\text{sink}} = 10\,°\text{C}$

to the capillary length defined as:

$$L_{\text{cap}} = \left(\frac{\sigma}{(\rho_{\text{l}} - \rho_{\text{v}})\, g} \right)^{\frac{1}{2}} \tag{3.12}$$

where σ is the surface tension of the working fluid. In that case, gravity and capillary forces are in competition and the stratification phenomenon is weak. The authors observed interfacial instabilities due to the difference of velocity between the vapour and the liquid phases. The increase of the amplitude of these waves lead to the formation of a liquid slug and to the release of a Taylor bubble. The elongated bubble formed was quickly transformed into a spherical one.

In the present study, the same phenomena are observed, as shown in Figure 3.31. The capillary length of water between 0 °C and 100 °C ranges from 2.4 mm to 2.8 mm. The internal diameter of the tubes is slightly lower than this value, leading to a major contribution of the capillary forces on the equilibrium between both phases.

The figure shows the minor stratification of the annular upstream flow regime. On the bottom of the tube, the liquid-vapour interface is wavy. The quasi-hemispherical meniscus moves forward, leading to the potential coalescence of isolated bubbles, as seen at $t = 234\,\mathrm{ms}$, or to the coalescence of an isolated bubble with the annular wavy region ($T = 390\,\mathrm{ms}$). At $t = 460\,\mathrm{ms}$, the amplitude of the wave increases substantially. At $t = 480\,\mathrm{ms}$, the upper part of the interface is also deformed, leading to an eventual detachment of an elongated bubble at $t = 484\,\mathrm{ms}$. This liquid slug, formed between the two vapour regions, moves rapidly downstream while the newly detached elongated bubble condenses. This fast phenomenon induces a large deformation of the bubble and of the meniscus at the end of the annular zone. At $t = 532\,\mathrm{ms}$, the bubble is almost spherical and located in the upper part of the tube, due to the buoyancy.

Figure 3.32 shows the movement of the hemispherical meniscus inside the condenser during a period of 4.8 s. The location of the meniscus varies of about 15 mm between $t = 0.8\,\mathrm{s}$ and $t = 4\,\mathrm{s}$. This back and forth movement inside the condenser and the presence of isolated bubbles downstream show the difficulty to determine a clear two-phase length inside the condenser. According to El Achkar et al. [93], the latent heat dissipated in the isolated bubbles zone is negligible in comparison to the annular and the intermittent zone. Furthermore, these authors state that 80 % to 90 % of the heat transfer in the isolated bubble zone is attributed to sensible heat. This is confirmed by the present observations. Indeed, Figure 3.32 presents no significant variation of the volume of the isolated bubbles. This shows that phase-change is not a major heat transfer mechanism in the isolated bubbles region. Therefore, in a modelling stage of the heat transfer inside the condensation zone, this region can be considered as single-phase with an acceptable approximation. Thus, the two-phase length inside the condenser must correspond to the average location of the meniscus at the end of the annular zone.

3.6.2 Condensation in the liquid line

In constant conductance mode, the end of the vapour region is located inside the liquid line. Figure 3.33 shows the last section of the liquid line, close to the reservoir, during 16 s. As it was seen inside the condenser, a slightly stratified annular zone is followed by isolated vapour bubbles. However, in the liquid line, the annular region releases both vapour slugs and quasi-spherical bubbles. As presented in the figure, the location of the meniscus at the end of the annular zone varies significantly during operation. A change of 100 mm in 14 s is recorded. These hydraulic variations induce thermal oscillations of the measured temperature of the fluid returning to the reservoir, as it was previously discussed in subsection 3.5.3. Moreover, a precise value of the two-phase length is not available in such a case, since the system operation is not completely stable.

Figure 3.34 shows the detachment of a bubble in the liquid line. The phenomenon is similar to the one observed inside the condenser. However, in the liquid line, the instability

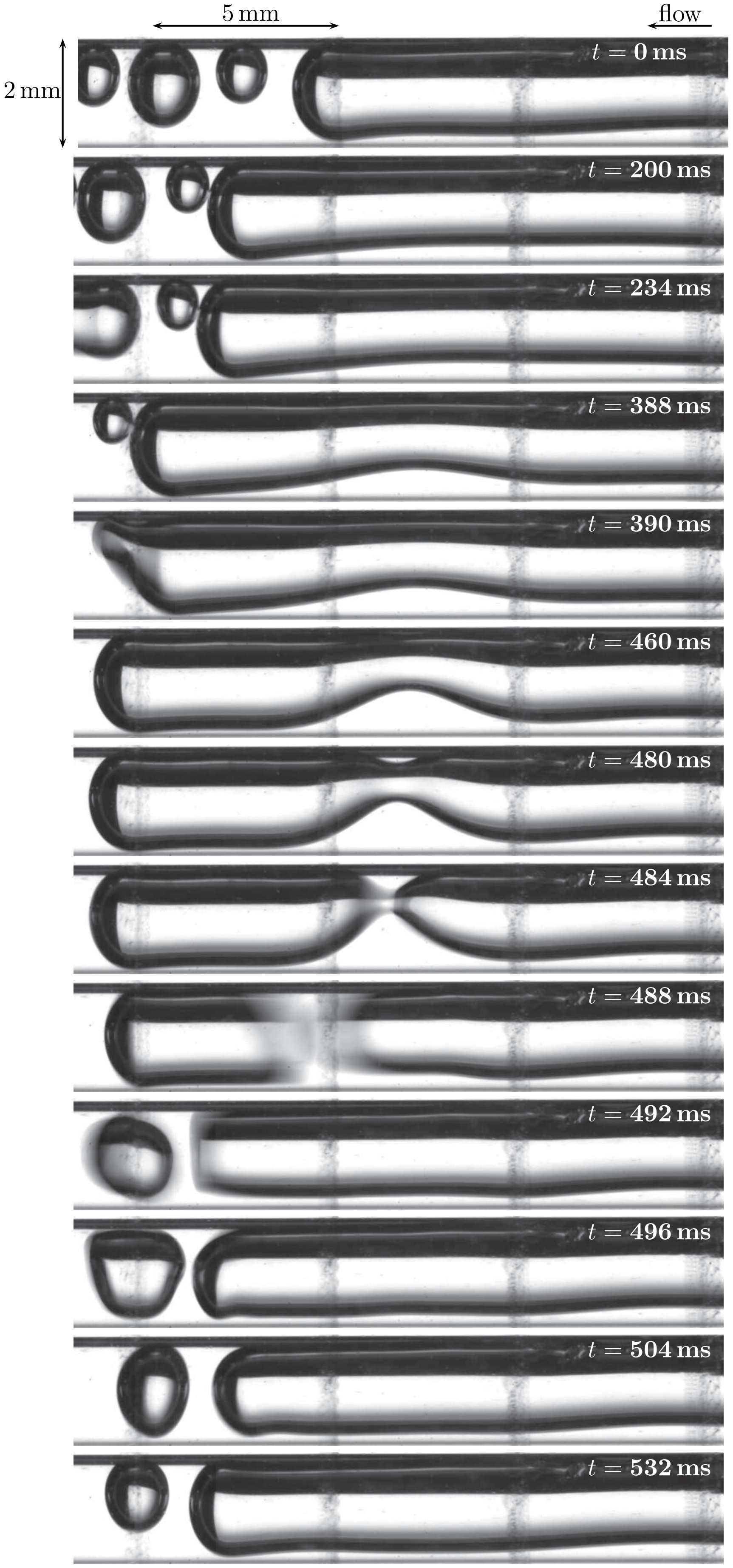

Figure 3.31: Bubble detachment in the condenser – $Q_{\mathrm{in}} = 27\,\mathrm{W}$, $T_{\mathrm{sink}} = 10\,°\mathrm{C}$

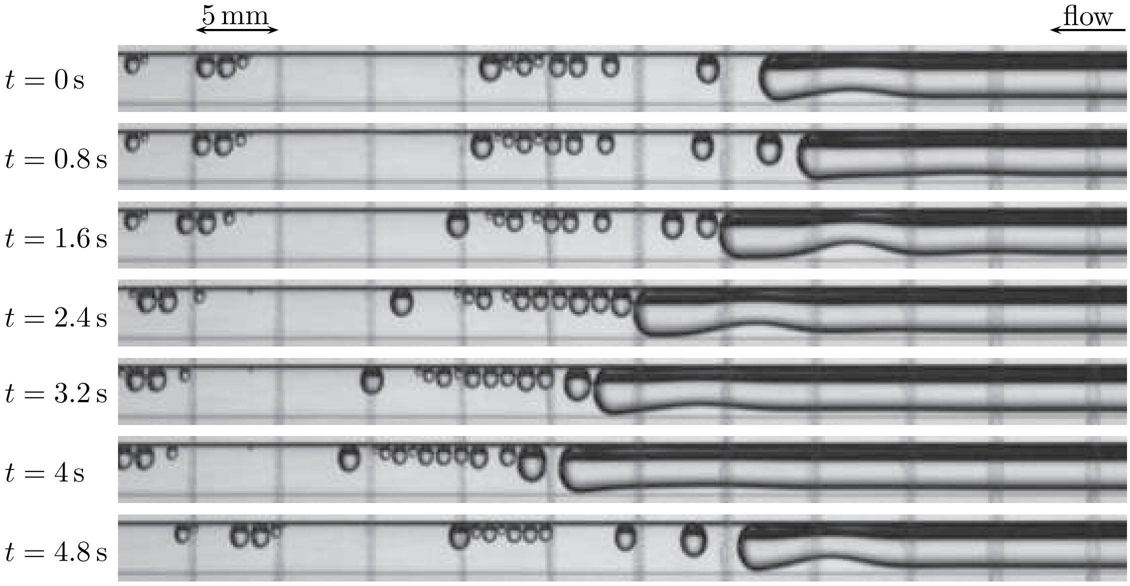

Figure 3.32: Location of the meniscus in the condenser, $Q_{\mathrm{in}} = 24\,\mathrm{W}$, $T_{\mathrm{sink}} = 10\,°\mathrm{C}$

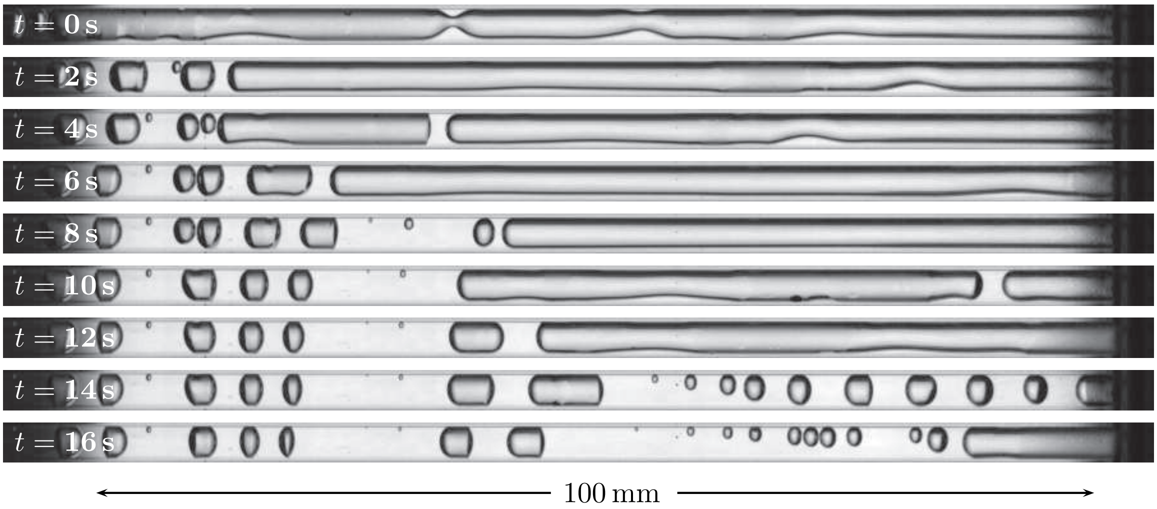

Figure 3.33: Movement of the meniscus in the liquid line – $Q_{\mathrm{in}} = 24.8\,\mathrm{W}$, $T_{\mathrm{sink}} = 30\,°\mathrm{C}$

of the liquid film and thus the location of the detachment is much further away from the meniscus at the end of the annular region. Indeed, for the case presented in the figure, a liquid slug forms and releases a vapour slug about 65 mm long. This vapour slug quickly condenses and its length is divided by a factor 20 in 160 ms.

3.6.3 Drop-wise condensation in the vapour line

Figure 3.35 presents a view of the vapour line during operation at $Q_{\mathrm{in}} = 27\,\mathrm{W}$. Despite the thickness (2 mm) of the tube and the low thermal conductivity of glass ($1\,\mathrm{W \cdot m^{-1} \cdot K^{-1}}$), heat losses to the ambient lead to the condensation of the vapour flowing through the transport

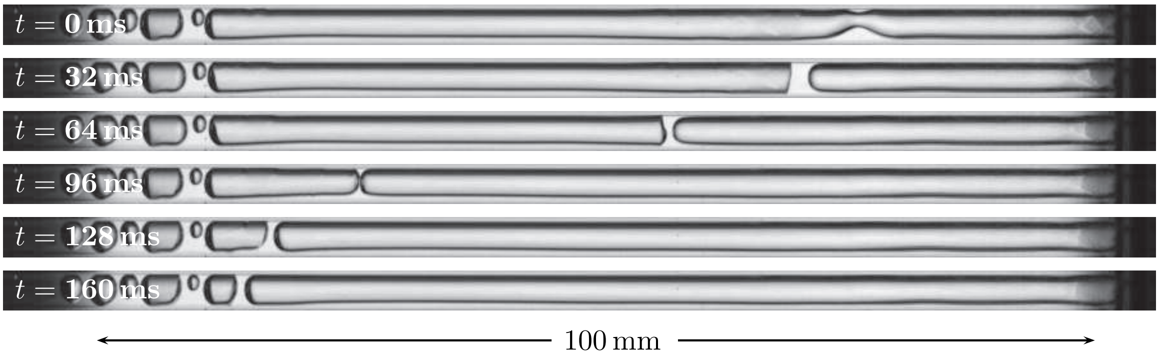

Figure 3.34: Condensation in the liquid line – $Q_{\text{in}} = 24.8\,\text{W}$, $T_{\text{sink}} = 30\,^{\circ}\text{C}$

line. This phenomenon is observed in the entire length of the vapour line, whatever the heat load.

As presented in the figure, drop-wise condensation occurs in the vapour line. When condensation occurs on a surface, the form of condensation, film-wise or drop-wise, is dependant of the wettability of the surface [87]. In the present case, water is the working fluid, and the internal surface of the tube is smooth glass. Such a configuration corresponds to a mildly hydrophobic condition [159] that enables drop-wise phase change. In other experimental conditions, the mode of condensation could differ, depending on the working fluid, the material, the surface roughness and the operating temperature. For example, the contact angle of water on a polished surface of copper at low pressure is low [160] and could lead to film-wise condensation.

In the present investigation, droplets start to form on the internal surface of the tube. As condensation continues, the droplets grow and coalesce to form larger drops. This mechanism is quite slow because heat transfer to the ambient is moderate. When the coalescence of the drops leads to the formation of a liquid slug, vapour cannot circulate in the central part of the tube and pushes the liquid slug downstream, thus carrying away the condensed liquid on the internal surface ($t = 25.4\,\text{s}$). In the upper side of the tube, several larger drops remain unchanged during the entire process and are not necessarily disturbed by the sudden liquid flow.

The drop-wise condensation and the intermittent liquid flow associated to it are the source of temperature oscillations in the vapour line and in the rest of the system at low heat loads, as it was further discussed in subsection 3.5.3.

3.7 Conclusion

A complete experimental setup has been designed, assembled and instrumented. Its features enable to monitor the pressure inside the reservoir, the applied heat load and the temperatures at key locations inside the system. Furthermore, a glass window and transparent tubes make possible a direct observation of the fluid flow inside the transport lines, the condenser and the reservoir. The steady-state and the transient behaviour of the experimental apparatus are

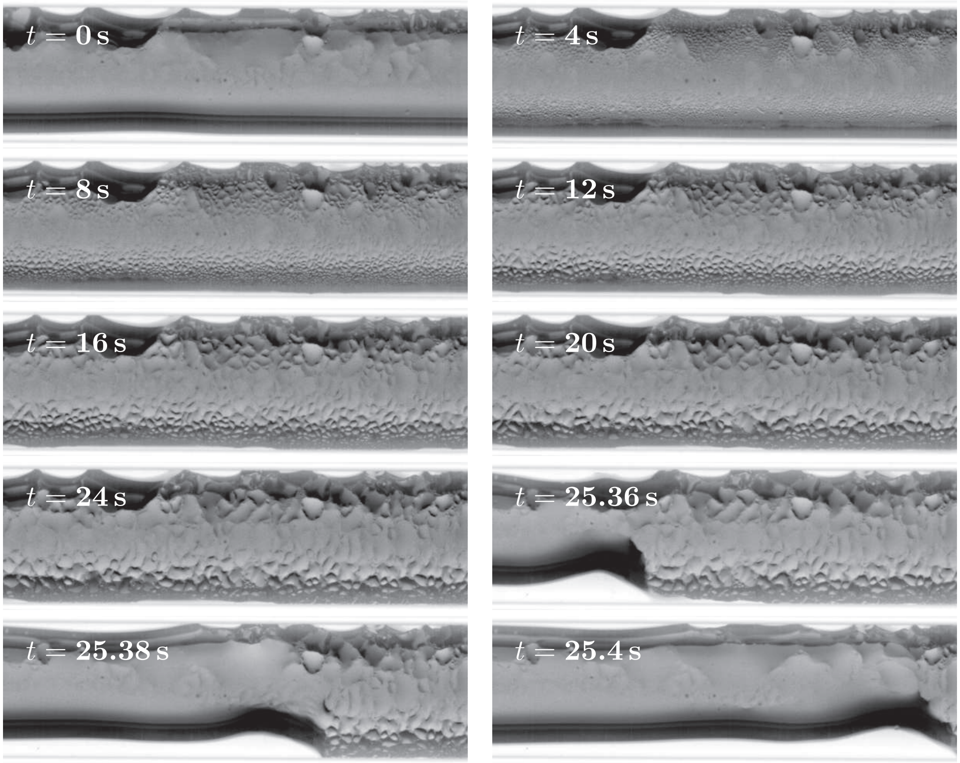

Figure 3.35: Drop-wise condensation in the vapour line – $Q_{\text{in}} = 27\,\text{W}$, $T_{\text{sink}} = 10\,°\text{C}$

investigated and show the influential parameters of the system. The influence of the nucleate boiling in the reservoir on the LHP operation, as well as the effect of the non-condensable gases are assessed. The link between temperature oscillations and the hydrodynamic behaviour of the LHP are highlighted. Finally, observations through the transparent lines confirm the occurrence of the condensation phenomena in the condenser and in the transport lines that were already observed by other authors.

Chapter 4

Numerical model of the experimental LHP

A numerical model is developed in order to further investigate the experimental results obtained in chapter 3, particularly the heat transfer in the evaporator and the condensation in the transport lines. This model is more accurate and detailed than the analytical approach presented in chapter 2 for designing purposes. The different characteristics of the experimental setup are taken into account: conduction heat transfer in the liquid and vapour lines, condensation and pressure drops in the vapour lines, two different materials of the evaporator casing, etc. After the introduction of the main hypotheses, the model is developed. A comparison between the numerical results and the experimental data is presented. Then, heat and mass transfer inside the evaporator, as well as in the transport lines are discussed. The influence of several parameters (material of the body, longitudinal thermal conduction in the transport lines) is investigated.

4.1 Numerical model development

This section introduces the development of a numerical model of an LHP. This numerical model provides an accurate consideration of heat transfer in the evaporator and in the transport lines. This work has already been published in Siedel et al. [85].

4.1.1 Model main assumptions

The steady-state model presented here is based on momentum, mass and energy conservation equations and on thermodynamic relationships. The major assumptions are:

a) The loop operates at steady-state.

b) The wick is fully saturated of liquid and evaporation takes place at the liquid-vapour interface in the vapour grooves.

c) The fluid is considered incompressible because its velocity is much lower than the sound speed in the same medium in a typical LHP operation.

d) The temperature difference between the inner and the outer surfaces of the tubes is neglected.

e) The heat sink temperature and the external heat transfer coefficient are considered uniform along the condenser.

4.1.2 Vapour line, liquid line and condenser

The condenser and the transport lines are discretized into small elements of volume as shown in Figure 4.1.

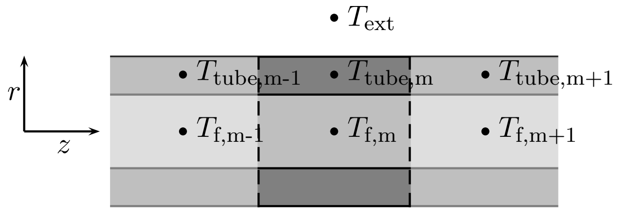

Figure 4.1: Transport lines discretization

To determine the tube wall temperature T_{tube}, the energy balance equation is written, neglecting the radial conduction in the wall:

$$\begin{aligned}\lambda_{\mathrm{tube}} S_{\mathrm{tube}} \frac{\mathrm{d}^2 T_{\mathrm{tube}}}{\mathrm{d}z^2} &= h_{\mathrm{ext}} p_{\mathrm{o}} \left(T_{\mathrm{tube}} - T_{\mathrm{ext}}\right) \\ &+ h_{\mathrm{i}} p_{\mathrm{i}} \left(T_{\mathrm{tube}} - T_{\mathrm{f}}\right)\end{aligned} \tag{4.1}$$

where T_{ext} is the ambient temperature, h_{ext} and h_{i} are the heat transfer coefficients outside and inside the tube respectively, p is the perimeter and S_{tube} the cross-sectional area of the tube. When considering the condenser, T_{sink} and h_{sink} are used instead of T_{ext} and h_{ext}, respectively.

In single-phase flow, the fluid temperature T_{f} is given by:

$$\frac{\mathrm{d}T_{\mathrm{f}}}{\mathrm{d}z} = \frac{h_{\mathrm{i}} p_{\mathrm{i}} \left(T_{\mathrm{tube}} - T_{\mathrm{f}}\right)}{\dot{m}_{\mathrm{f}} c_{\mathrm{p,f}}} \tag{4.2}$$

In two-phase flow, the fluid is at saturation temperature T_{sat} and the variation of the liquid mass flow rate is expressed by:

$$\frac{\mathrm{d}\dot{m}_{\mathrm{l}}}{\mathrm{d}z} = \frac{h_{\mathrm{i}} p_{\mathrm{i}} \left(T_{\mathrm{tube}} - T_{\mathrm{f}}\right)}{h_{\mathrm{lv}}} \tag{4.3}$$

The saturation temperature is determined using the Clausius-Clapeyron relation:

$$\frac{\partial T}{\partial P} = \frac{T\left(1/\rho_{\mathrm{v}} - 1/\rho_{\mathrm{l}}\right)}{h_{\mathrm{lv}}} \tag{4.4}$$

Knowing the phase change mass flow rate along the tubes, it is possible to determine the vapour quality for each element:

$$x = \frac{\dot{m}_{\mathrm{v}}}{\dot{m}_{\mathrm{l}} + \dot{m}_{\mathrm{v}}} \tag{4.5}$$

Pressure drops are calculated assuming smooth tubes with:

$$\left(\frac{\mathrm{d}P}{\mathrm{d}z}\right)_{\mathrm{tot}} = \left(\frac{\mathrm{d}P}{\mathrm{d}z}\right)_{\mathrm{fric}} + \left(\frac{\mathrm{d}P}{\mathrm{d}z}\right)_{\mathrm{static}} + \left(\frac{\mathrm{d}P}{\mathrm{d}z}\right)_{\mathrm{mom}} \tag{4.6}$$

Unlike the analytical model, the present work considers the pressure drops induced by the liquid and vapour phases. As suggested by Thome [88], the two-phase flow is characterized considering a homogeneous pseudo-fluid that obeys the conventional equations for single-phase fluids and which properties correspond to the averaged properties of both the liquid and vapour phase. The frictional pressure drop is:

$$\Delta P_{\mathrm{fric}} = \frac{2 f_{2\varphi} \Delta z \dot{m}_{\mathrm{f}}^{2}}{S_{\mathrm{i}}^{2} D_{\mathrm{i}} \rho_{\mathrm{h}}} \tag{4.7}$$

where S_{i} is the cross-sectional area of the flow. The friction factor $f_{2\varphi}$ is expressed by the Blasius equation, valid for smooth tubes:

$$f_{2\varphi} = \frac{0.079}{Re^{0.25}} \tag{4.8}$$

with Re the Reynolds number. Assuming the vapour and liquid velocities are equal, the void fraction is given by:

$$\varepsilon = \left[1 + \frac{1-x}{x}\left(\frac{\rho_{\mathrm{v}}}{\rho_{\mathrm{l}}}\right)\right]^{-1} \tag{4.9}$$

The homogeneous fluid density is defined as:

$$\rho_{\mathrm{h}} = \rho_{\mathrm{l}}\left(1 - \varepsilon\right) + \rho_{\mathrm{v}}\varepsilon \tag{4.10}$$

The momentum pressure gradient per unit length is then:

$$\left(\frac{\mathrm{d}P}{\mathrm{d}z}\right)_{\mathrm{mom}} = \frac{\dot{m}_{\mathrm{f}}}{S_{\mathrm{i}}} \frac{\mathrm{d}}{\mathrm{d}z}\left(\frac{\dot{m}_{\mathrm{f}}}{\rho_{\mathrm{h}} S S_{\mathrm{i}}}\right) \tag{4.11}$$

whereas the hydrostatic term is defined by:

$$\left(\frac{\mathrm{d}P}{\mathrm{d}z}\right)_{\mathrm{static}} = \rho_{\mathrm{h}} g \frac{\mathrm{d}H}{\mathrm{d}z} \tag{4.12}$$

where H is the altitude of the considered element.

The heat transfer coefficient with the ambient is given by Churchill and Chu [161] for free convection on the surface of an isothermal cylinder:

$$h_{\mathrm{ext}} = \frac{\lambda_{\mathrm{air}}}{D_{\mathrm{o}}} \left[0.60 + \frac{0.387 Ra_{\mathrm{D}}^{\frac{1}{6}}}{\left(1 + (0.559/Pr)^{\frac{9}{16}}\right)^{\frac{8}{27}}} \right]^2 \tag{4.13}$$

This correlation is valid for Rayleigh numbers Ra_{D} lower than 10^{12}.

Inside the tube, in the case of single-phase laminar flow ($Re_{\mathrm{D}} < 2300$), the fully-developed state is described by $Gz_{\mathrm{D}} \leqslant 20$, where the Graetz number is:

$$Gz_{\mathrm{D}} = \frac{D}{z} Re_{\mathrm{D}} Pr \tag{4.14}$$

The heat transfer between the fluid and the tube wall is then given by [148]:

$$Gz_{\mathrm{D}} \leqslant 20 \qquad h_{\mathrm{i}} = 4.36 \frac{\lambda_{\mathrm{l}}}{D_{\mathrm{i}}} \tag{4.15}$$

$$Gz_{\mathrm{D}} > 20 \qquad h_{\mathrm{i}} = 1.86 \left(\frac{Re_{\mathrm{D}} Pr}{L/D}\right)^{\frac{1}{3}} \left(\frac{\mu_{\mathrm{f,T=T_f}}}{\mu_{\mathrm{f,T=T_{wall}}}}\right)^{0.14} \frac{\lambda_{\mathrm{l}}}{D_{\mathrm{i}}} \tag{4.16}$$

For a turbulent flow, the entrance length is much smaller and fully developed conditions are assumed:

$$h_{\mathrm{i}} = 0.023 \frac{\lambda_{\mathrm{f}}}{D_{\mathrm{i}}} Re_{\mathrm{D}}^{\frac{4}{5}} Pr^{\frac{1}{3}} \tag{4.17}$$

In the case of two-phase flow, a fine modelling of the heat transfer associated with condensation can be found in the work of Miscevic et al. [92]. This model takes into account the transient behaviour of the meniscus shape inside the tube due to the capillary effects. However, such an approach is difficult to introduce in a complete steady-state model of a LHP. Thus, another approach is followed: the Soliman's modified Froude number determines the flow regime as a function of the dimensionless liquid Reynolds and Galileo numbers [162]:

$$\text{if } Re_{\mathrm{l}} < 1250 \qquad Fr = 0.025 \frac{Re_{\mathrm{l}}^{1.59}}{Ga^{0.5}} \left(\frac{1 + 1.09 \chi_{\mathrm{tt}}^{0.039}}{\chi_{\mathrm{tt}}}\right)^{1.5} \tag{4.18}$$

$$\text{if } Re_{\mathrm{l}} > 1250 \qquad Fr = 1.26 \frac{Re_{\mathrm{l}}^{1.04}}{Ga^{0.5}} \left(\frac{1 + 1.09 \chi_{\mathrm{tt}}^{0.039}}{\chi_{\mathrm{tt}}}\right)^{1.5} \tag{4.19}$$

$$\text{with } Ga = \frac{g D_{\mathrm{i}}^3 \rho_{\mathrm{l}}^2}{\mu_{\mathrm{l}}^2} \text{ and } Re_{\mathrm{l}} = \frac{4 \dot{m}_{\mathrm{f}} (1 - x)}{\pi D \mu_{\mathrm{l}}} \tag{4.20}$$

and where χ_{tt} is the Martinelli parameter defined as [87]:

$$\chi_{\mathrm{tt}} = \sqrt{\frac{(\mathrm{d}P/\mathrm{d}z)_{\mathrm{l}}}{(\mathrm{d}P/\mathrm{d}z)_{\mathrm{v}}}} \approx \left(\frac{1-x}{x}\right)^{0.9} \left(\frac{\rho_{\mathrm{v}}}{\rho_{\mathrm{l}}}\right)^{0.5} \left(\frac{\mu_{\mathrm{l}}}{\mu_{\mathrm{v}}}\right)^{0.1} \tag{4.21}$$

For Froude numbers lower than 10, the flow is assumed stratified and the correlation of Jaster and Kosky [89] is used to determine the heat transfer coefficient:

$$h_\mathrm{i} = 0.728\varepsilon^{\frac{3}{4}} \left(\frac{g h_\mathrm{lv} \lambda_\mathrm{l}^3 \left(\rho_\mathrm{l} - \rho_\mathrm{v}\right) \rho_\mathrm{l}}{D_\mathrm{i} \mu_\mathrm{l} \left(T_\mathrm{f} - T_\mathrm{tube}\right)} \right)^{0.25} \tag{4.22}$$

The flow is assumed annular otherwise and the correlation given by Akers et al. [90] is used:

$$\text{if } Re \leq 5 \cdot 10^5 \qquad h_\mathrm{i} = 5.03 \frac{\lambda_\mathrm{f}}{D_\mathrm{i}} Re_\mathrm{eq}^{\frac{1}{3}} Pr^{\frac{1}{3}} \tag{4.23}$$

$$\text{if } Re > 5 \cdot 10^5 \qquad h_\mathrm{i} = 0.0265 \frac{\lambda_\mathrm{f}}{D_\mathrm{i}} Re_\mathrm{eq}^{\frac{4}{5}} Pr^{\frac{1}{3}} \tag{4.24}$$

where the equivalent Reynolds number for two-phase flow Re_eq is determined from an equivalent mass flow rate:

$$\dot{m}_\mathrm{eq} = \dot{m}_\mathrm{f} \left[(1-x) + x \left(\frac{\rho_\mathrm{l}}{\rho_\mathrm{v}} \right)^{1/2} \right] \tag{4.25}$$

4.1.3 Determination of the mass flow rate

In a first approach, the heat losses to the ambient, the heat transferred by conduction through the transport lines as well as the sidewall parasitic heat losses are not taken into account. A simplified global energy balance of the evaporator gives then the following equation:

$$Q_\mathrm{in} = Q_\mathrm{ev} + Q_\mathrm{sen} + Q_\mathrm{sub} \tag{4.26}$$

where Q_in is the heat dissipated by the device that has to be cooled by the LHP. The terms on the right-hand side of the equation correspond to the latent heat of vaporization of the fluid at the wick surface, the sensible heat provided to the liquid in the wick, and the subcooling due to the return of liquid from the condenser. Considering the relationships between these heat transfer rates and the mass flow rate inside the LHP:

$$Q_\mathrm{ev} = \dot{m}_\mathrm{f} h_\mathrm{lv} \tag{4.27}$$

$$Q_\mathrm{sen} = \dot{m}_\mathrm{f} c_\mathrm{p,l} \left(T_\mathrm{v} - T_\mathrm{r}\right) \tag{4.28}$$

$$Q_\mathrm{sub} = \dot{m}_\mathrm{f} c_\mathrm{p,l} \left(T_\mathrm{r} - T_\mathrm{r,i}\right) \tag{4.29}$$

with T_v, T_r and $T_\mathrm{r,i}$ the temperatures of the fluid inside the grooves, in the reservoir and entering the reservoir, respectively. The pressure in the reservoir P_r is calculated by the transport lines model and sets the saturation temperature of the reservoir T_r. $T_\mathrm{r,i}$ is also determined using the transport lines model while the value of T_v is solved using a 2-D model described in the next section. The mass flow rate is then calculated by combining Equations (4.26) to (4.29):

$$\dot{m}_\mathrm{f} = \frac{Q_\mathrm{in}}{h_\mathrm{lv} + c_\mathrm{p,l} \left(T_\mathrm{v} - T_\mathrm{r,i}\right)} \tag{4.30}$$

4.1.4 Heat and mass transfer in the wick

In the literature, LHP models usually consider heat transfer through the wick as a uniform 1-D conductive-convective transfer, assuming an equivalent thermal conductivity of the wick. In order to determine accurately heat and mass transfer in the porous media, a 2-D finite difference description of the wick is undertaken in this model. As shown in Figure 4.2, a small element of the evaporator has been chosen for this study, located between the centre of the vapour groove and the centre of the nearby fin, between the liquid-vapour interface in the reservoir and the upper surface of the evaporator wall. The following assumptions are made:

a) Heat and mass transfer are two-dimensional.

b) Evaporation only occurs at the surface of the porous structure nearby the vapour groove.

c) Local liquid and wick temperatures are considered equal.

d) Gravitational effects are neglected.

e) Heat losses to the ambient, through the transport lines and parasitic heat flux through the evaporator casing are neglected.

f) The reservoir contains a two-phase fluid. As it is located above the evaporator, a height of liquid H_l sits on the top of the wick structure.

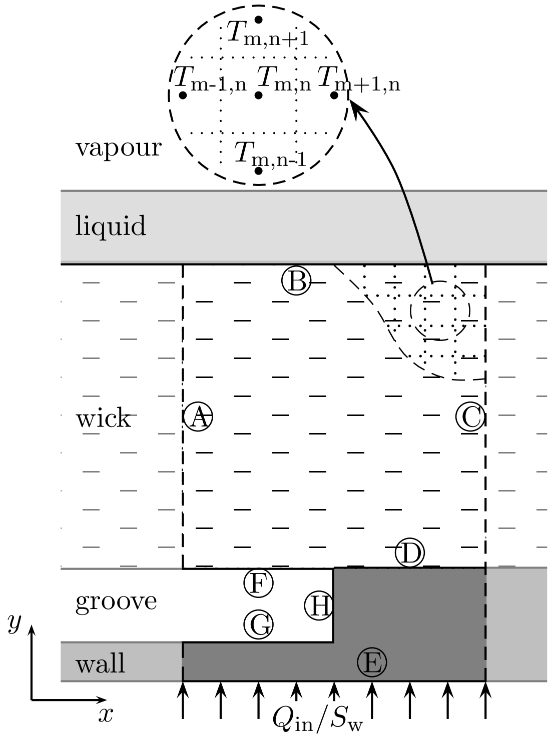

Figure 4.2: Heat and mass transfer in the wick

Based on the total fluid inventory of the LHP, assuming the wick is fully saturated of liquid and calculating the void fraction along the transport lines and the condenser, it is possible to determine the height of liquid H_l in the reservoir.

To describe the liquid flow inside the porous structure, Darcy's law is considered:

$$u = -\frac{K}{\mu_\mathrm{l}} \nabla P \tag{4.31}$$

where u is the liquid velocity and K is the wick permeability, expressed by the Carman-Koseny relationship for a sintered structure [163]:

$$K = \frac{r_\mathrm{p}^2 \varepsilon^3}{37.5\,(1-\varepsilon)^2} \tag{4.32}$$

where r_p is the pore radius and ε is the porosity of the wick. Considering the continuity equation and Equation (4.31), the pressure field in the wick can be written:

$$\nabla^2 P = 0 \tag{4.33}$$

The following boundary conditions are considered at the boundaries A to F:

$$\text{A and C:} \qquad \frac{\partial P}{\partial x} = 0 \tag{4.34}$$

$$\text{B:} \qquad P = P_\mathrm{r} \tag{4.35}$$

$$\text{D:} \qquad \frac{\partial P}{\partial y} = 0 \tag{4.36}$$

$$\text{F:} \qquad P = P_\mathrm{v} \tag{4.37}$$

As frontiers A and C are symmetry axes, the liquid velocities have no x-component. At the boundary D, the impermeability condition is applied. The pressure in the groove is set by the thermodynamic state of the latter $P_\mathrm{v} = P_\mathrm{sat}(T_\mathrm{v})$.

In order to calculate the temperature field, conduction in the porous structure and convective heating of the liquid flowing through the wick are considered, leading to the following energy equation:

$$\lambda_\mathrm{eff} \nabla^2 T = \rho_\mathrm{l} c_\mathrm{p,l} \nabla\,(uT) \tag{4.38}$$

Several models can be found in the literature to estimate the effective thermal conductivity λ_eff of a sintered porous structure filled with liquid (Appendix A). Based on the work of Singh et al. [48] who compared their experimental results for monoporous copper with several correlations, a relationship based on Alexander's work is used in the present study:

$$\lambda_\mathrm{eff} = \lambda_\mathrm{l} \left(\frac{\lambda_\mathrm{l}}{\lambda_\mathrm{wm}}\right)^{-(1-\varepsilon)^{0.59}} \tag{4.39}$$

The boundary conditions are as follows:

$$\text{A and C:} \qquad \frac{\partial T}{\partial x} = 0 \tag{4.40}$$

$$\text{B:} \qquad -\lambda_{\mathrm{eff}} \frac{\partial T}{\partial y} = \frac{\lambda_{\mathrm{l}}}{H_{\mathrm{l}}} \left(T - T_{\mathrm{r}}\right) \tag{4.41}$$

$$\text{E:} \qquad -\lambda_{\mathrm{b}} \frac{\partial T}{\partial y} = \frac{Q_{\mathrm{in}}}{S_{\mathrm{w}}} \tag{4.42}$$

$$\text{F:} \qquad h_{\mathrm{ev}} \left(T - T_{\mathrm{v}}\right) = -h_{\mathrm{lv}} u_{\mathrm{y}} \rho_{\mathrm{l}} \tag{4.43}$$

$$\text{G:} \qquad -\lambda_{\mathrm{b}} \frac{\partial T}{\partial y} = h_{\mathrm{v}} \left(T - T_{\mathrm{v}}\right) \tag{4.44}$$

$$\text{H:} \qquad \lambda_{\mathrm{b}} \frac{\partial T}{\partial x} = h_{\mathrm{v}} \left(T - T_{\mathrm{v}}\right) \tag{4.45}$$

The sides of the considered region (dashed lines) are assumed adiabatic because of the symmetry. The thickness of the liquid layer in the reservoir is supposed to be small enough to neglect the convective heat transfer. Thus a Fourier boundary condition is applied with a heat transfer coefficient defined by the 1-D heat conduction in the liquid. The convective heat transfer coefficient in the groove h_{gr} is set to a constant value considering natural convection. At the outer wall surface, a fixed heat flux $Q_{\mathrm{in}}/A_{\mathrm{w}}$ is applied, where A_{w} is the cross-sectional area of the wick. Additionally, a thermal contact resistance between the porous structure and the evaporator wall is considered.

4.1.5 Solving procedure

For a given heat flux, the thermal and hydraulic states are initialized using the analytical model presented in chapter 2.

The complete solving procedure is presented in Figure 4.3. First, the transport lines and the condenser are computed. The input parameters are the groove temperature T_{v}, the maximum wall temperature in the evaporator T_{e}, the reservoir temperature T_{r} and the mass flow rate $\dot{m}_{\mathrm{f}}$. The pressure at the entrance of the vapour line is the saturation pressure corresponding to the vapour temperature in the groove T_{v}. The tube wall temperatures are determined solving Equation (4.1) with the Thomas algorithm (also known as Tridiagonal Matrix Algorithm), using T_{e} and T_{r} at each end of the transport lines as boundary conditions. Then the fluid pressures P_{f}, the mass vapour qualities x, the inner heat transfer coefficients h_{i} as well as the fluid temperatures T_{f} are computed step by step with an iterative method, using the approach presented in subsection 4.1.2, until each calculated parameter has converged. The energy balance at the evaporator enables to recalculate the mass flow rate $\dot{m}_{\mathrm{f}}$ using Equation (4.30).

The model describing heat and mass transfer in the evaporator is then computed. The input parameters are the mass flow rate $\dot{m}_{\mathrm{f}}$, the reservoir pressure P_{r} and its corresponding saturation temperature T_{r} as well as the temperature of the liquid entering the reservoir $T_{\mathrm{r,i}}$. First, the pressure field and then the temperature field in the porous structure are calculated,

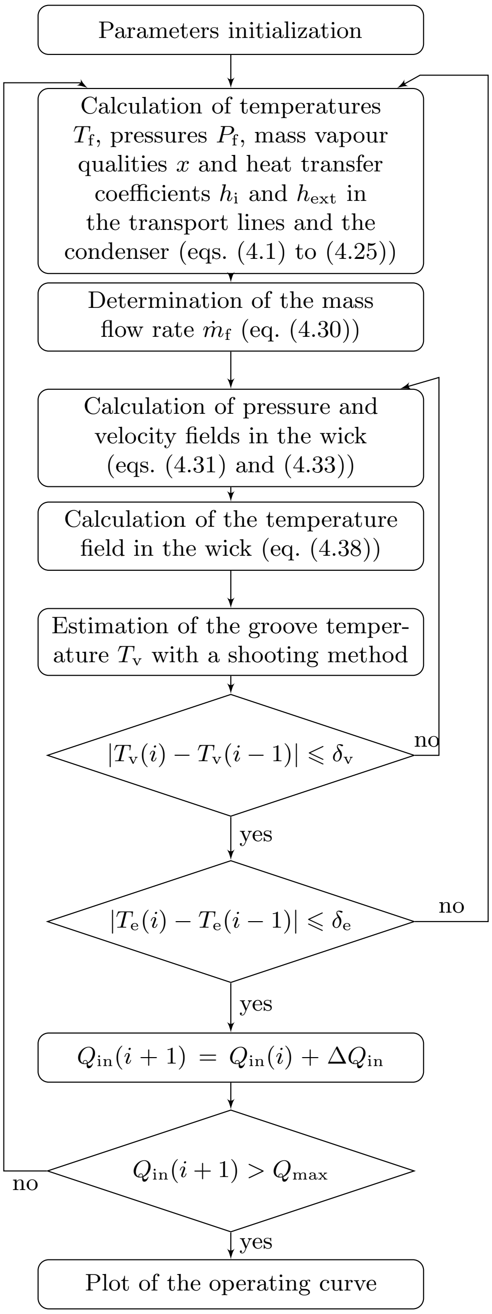

Figure 4.3: Solving algorithm flowchart

using the Thomas algorithm alternatively in both directions. The groove temperature T_v is estimated with a shooting method. T_v is iteratively modified until the heat flux in the evaporation zone is equal to $\dot{m}_\mathrm{f} h_\mathrm{lv}$. When the errors on T_v and T_e are negligible, the complete thermo-hydraulic state of the LHP is determined and another input heat flux is computed, until the complete characteristic curve is calculated.

4.1.6 Heat transfer through the casing

The model presented in subsection 4.1.4 does not take into account the heat losses from the evaporator to the ambient nor the thermal conduction through the evaporator casing to the reservoir and to the transport lines. In order to introduce these parameters, Equations (4.26), (4.30) and (4.42) become respectively:

$$Q_{\mathrm{in}} = Q_{\mathrm{tube,v}} + Q_{\mathrm{tube,l}} + Q_{\mathrm{ev}} + Q_{\mathrm{sen}} + Q_{\mathrm{sub}} + Q_{\mathrm{ext}} \tag{4.46}$$

$$\dot{m}_{\mathrm{f}} = \frac{Q_{\mathrm{in}} - Q_{\mathrm{tube,v}} - Q_{\mathrm{tube,l}} - Q_{\mathrm{ext}}}{h_{\mathrm{lv}} + c_{\mathrm{p,l}}\left(T_{\mathrm{v}} - T_{\mathrm{r,i}}\right)} \tag{4.47}$$

$$-\lambda_{\mathrm{b}} \frac{\partial T}{\partial y} = \left(Q_{\mathrm{in}} - Q_{\mathrm{tube,v}} - Q_{\mathrm{b}}\right) \frac{1}{S_{\mathrm{w}}} \tag{4.48}$$

where $Q_{\mathrm{tube,v}}$ and $Q_{\mathrm{tube,l}}$ are the parts of heat flux transferred by conduction to the vapour line from the evaporator and to the liquid line from the reservoir, respectively. They are determined with the transport lines model considering the temperature gradient of the tube walls at the entrance of the vapour line and at the exit of the liquid line. A 2-D model of the casing cannot precisely consider $Q_{\mathrm{tube,v}}$ because a 3D is necessary to take into account the connection of the tube adequately. Therefore, the heat transfer through the tube is subtracted directly from the total heat load Q_{in} in Equation (4.48) and the model assumes that $Q_{\mathrm{tube,v}}$ never enters into the casing. Q_{ext} is equal to the heat losses to the ambient. Q_{b} is the part of the heat transferred through the evaporator sidewall that is not given back to the wick due to convective heat transfer between the liquid in the porous media and the sidewall. Q_{b} is referred to as the longitudinal heat losses in the following. A part of Q_{b} is then dissipated to the ambient while the rest is given to the reservoir. To take into account heat losses, the 2-D model presented in Figure 4.2 is computed using Equations (4.46) to (4.48).

The estimation of both Q_{ext} and Q_{b} requires an additional model. Obviously, a 3D description of the entire evaporator would give the most accurate results. Such a development is for instance used by Hodot et al. [118], who present a complete 3D model of an LHP with cylindrical evaporator. However, in order to reduce the computational time, a 2D approach has been chosen in this study (Figure 4.4). The number of grooves to be modelled is determined so that edge effects are negligible at the centre of the groove located at the opposite side of the sidewall. The dashed line is thus assumed to be an adiabatic boundary. The vapour zone in the reservoir is considered at a homogeneous temperature T_{r}. Contrarily to the model presented in Figure 4.2, the 2D heat conduction equation is solved in the liquid to take into account the heat transfer with the casing. We assume that the liquid thickness H_{l} in the reservoir is small enough to neglect convection phenomena inside the liquid. The temperature of the liquid-vapour interface I is set to T_{r}. A perfect contact is assumed between the body of the evaporator and the wick.

At the contact surface between the evaporator casing and the vapour, two distinct situations may occur: if the vapour is colder than the wall, the liquid evaporates in the reservoir whereas condensation of the vapour occurs otherwise. In the case of evaporation in the reservoir, heat transfer is greatly enhanced at the triple line, at the contact between the wall and the liquid-vapour interface. The heat transfer can be determined using an evaporation heat transfer coefficient calculated with an accommodation coefficient. In this situation, the convective heat transfer between the wall and the vapour is negligible as compared to the previous one and an adiabatic boundary is assumed. The heat dissipated from the reservoir top surface to the ambient $Q_{\mathrm{ext,top}}$ as well as the heat losses through the liquid line are also due to the heat conduction in the casing. Thus, the boundary condition J is:

$$-\lambda_{\mathrm{b}}\frac{\partial T}{\partial y}=\frac{4\left(Q_{\mathrm{ext,top}}+Q_{\mathrm{tube,l}}\right)}{\pi\left(D_{\mathrm{b}}^{2}-D_{\mathrm{w}}^{2}\right)} \tag{4.49}$$

In the event of condensation of the vapour on the reservoir wall corresponding to a vapour temperature higher than the wall one, the heat transfer along the wall is fixed to $10^4\ \mathrm{W\cdot m^{-2}\cdot K^{-1}}$, based on Nusselt's filmwise condensation theory [148]. With such a high heat transfer coefficient, the heat dissipated from the reservoir top surface and through the liquid line is coming from the reservoir and not from the casing, as in the previous case. Therefore, the boundary J is considered adiabatic in that case.

The boundary conditions in eqs. (4.34) to (4.37) and eqs. (4.43) to (4.45) are similar to those of the model presented in Figure 4.2. On the evaporator bottom surface, a constant heat flux is set:

$$-\lambda_{\mathrm{b}}\frac{\partial T}{\partial y}=\frac{Q_{\mathrm{in}}-Q_{\mathrm{tube,v}}}{S_{\mathrm{w}}} \tag{4.50}$$

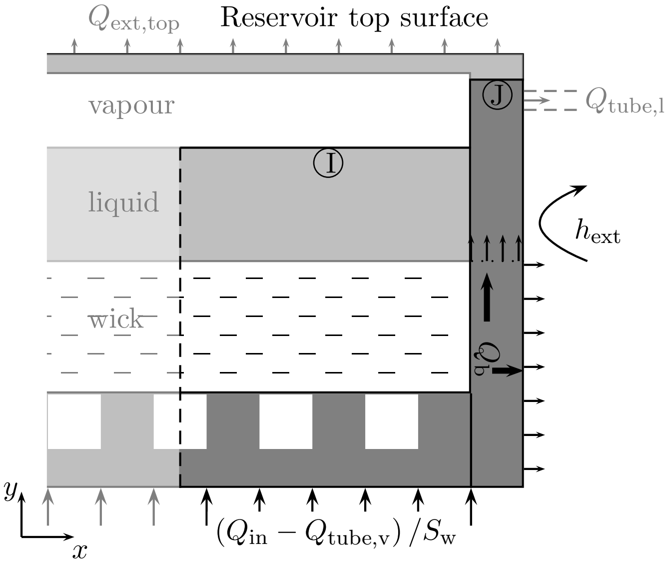

Figure 4.4: Heat transfer to the ambient and through the body

As shown in Figure 4.4, a part of the heat conducted through the evaporator body Q_{b} is dissipated to the ambient while the rest is transported to the reservoir and through the boundary J. Q_{ext} is calculated considering free convection and radiation around the evaporator body, knowing the temperature profile on the side of the evaporator and assuming a reservoir top surface temperature equal to T_{r}. The model presented in Figure 4.2 does not take into account that the temperature at the centre of the evaporator is higher than at its side. Therefore, it gives the mean temperature of the evaporator T_{e}. The maximum temperature $T_{\mathrm{e,max}}$ located in the centre of the evaporator can be obtained by the model presented in Figure 4.4.

4.2 Numerical results in the conditions of the experiment

This section presents numerical results in conditions similar to the experimental conditions of chapter 3. However, as it was already explained in the previous chapter, the actual experimental data does not enable a complete and thorough comparison with the theory. Indeed, the leaks, the hysteresis and the boiling incipience in the reservoir induce a scattering of the experimental data and reduce drastically the repeatability of the experiments. These parameters must be better controlled before performing a more extensive analysis of the numerical model. Anyway, the comparison with the model provides some useful information to explain the experimental results and increase the accuracy of the modelling.

4.2.1 Comparison with the experimental data

The numerical model is initialised with the analytical model and the parameters are then adjusted to fit the experimental data. Figure 4.5 shows the comparison between the simulation results and the experimental data presented in section 3.3. The geometrical parameters are set in accordance with the experimental facility. The heat transfer coefficient in the condenser is set to $280\,\mathrm{W\cdot m^{-2}\cdot K^{-1}}$ which is consistent with the pre-design presented in Appendix D. No partial pressure of NCGs is taken into account. A heat transfer coefficient of $260\,\mathrm{W\cdot m^{-2}\cdot K^{-1}}$ is taken into account between the wick and the reservoir. The contact resistance is adjusted to $R_{\mathrm{c}} = 2.5\cdot 10^{-4}\,\mathrm{K\cdot m^{2}\cdot W^{-1}}$, the heat transfer coefficient with the ambient to $h_{\mathrm{ext}} = 10\,\mathrm{W\cdot m^{-2}\cdot K^{-1}}$, and the accommodation coefficient to $a_{\mathrm{ev}} = 0.6$ so that the simulation results best fit the experimental data. This value of R_{c} is in agreement with the results from the literature, as discussed in subsection 1.2.1.2. The value of a_{ev} seems particularly high compared to usual values of the accommodation coefficient. This can be explained by a potential underestimation of the effective thermal conductivity of the wick (Appendix A), which is calculated using Alexander's formula ($\lambda_{\mathrm{eff}} = 8.7\,\mathrm{W\cdot m^{-1}\cdot K^{-1}}$).

We observe an acceptable agreement between the numerical simulation and the experimental results. However, several discrepancies are observed. At very low heat load ($Q_{\mathrm{in}} = 5\,\mathrm{W}$), the model fails to predict accurately the operating temperature of the system and underestimate the evaporator temperature as well as the saturation temperature of the fluid. Some differences are also observed above 40 W for $T_{\mathrm{r,i}}$ and $T_{\mathrm{c,o}}$. However, this difference does not have any significant influence on the determination of the other temperatures.

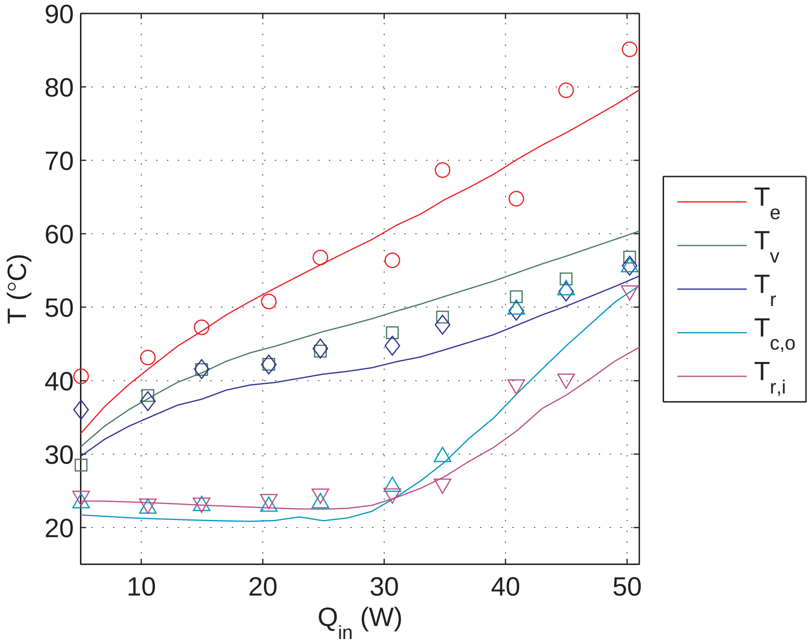

Figure 4.5: Comparison between the numerical simulation and the experimental data: characteristic curve

The largest discrepancy between the theoretical and the experimental results is the difference between T_{v} and T_{r}. The model gives a much larger temperature difference than what is actually measured. This observation may be induced by two combined sources of error. The first source of error is experimental. Indeed, the measured temperature difference may underestimate the actual difference that exists between both saturation states, in the vapour line and in the reservoir, respectively. As explained in subsection 3.2.2, the thermocouple T_{r} is located close to the porous structure and may measure the temperature of superheated liquid, thus overestimating the saturation temperature of the reservoir. Moreover, the measurement of the temperature inside the vapour line may be influenced by the surroundings. The thermal conduction in the sealing feedthrough, the presence of the PTFE connector and the presence of condensate between the thermocouple and the tube in the connector can induce an error on the estimation determination of T_{v}. The ambient temperature being at all times lower than the operating temperature, this would lead to an underestimation of the vapour temperature, and consequently to an underestimation of the actual temperature difference between the condensing vapour inside the vapour line and the liquid-vapour interface in the reservoir.

The second source of error is linked to the hypotheses of the model. The correlation used to calculate the pressure drops – therefore the change of the saturation temperature inside the transport lines and the condenser – are probably not suitable in the case of this experiment. Significant pressure losses are calculated inside the vapour line and in the two-phase region of the condenser as a result of the rather high velocity of the vapour flow. As pointed out by Miscevic et al. [164], information in the literature regarding pressure drops in capillary tubes with low mass fluxes is very scarce. Indeed, the correlations, either for the homogeneous fluid or the separated-phase models, are valid in configurations with larger tube diameters and high mass fluxes. Therefore, these relationships may not be applicable in the present conditions and induce an overestimation of the pressure drops and thus the difference between T_v and T_r.

Figure 4.6 shows the comparison between the simulation and the experimental results regarding the two-phase length. The figure confirms that the model fails to describe accurately heat and mass transfer in the transport lines and the condenser. A rather large discrepancy is observed between both sets of data. According to the model, the end of the two-phase zone is located at all times inside the condenser. However, the experimental results show that it is not the case at very low heat load or at high heat loads, with a meniscus receding in the vapour line or moving inside the liquid line, respectively. At the moment, the accuracy and the repeatability of the experimental setup does not enable to explain the reasons of this difference. Further investigations must be undertaken in the future to better compare and explain the difference between the model and the experimental results.

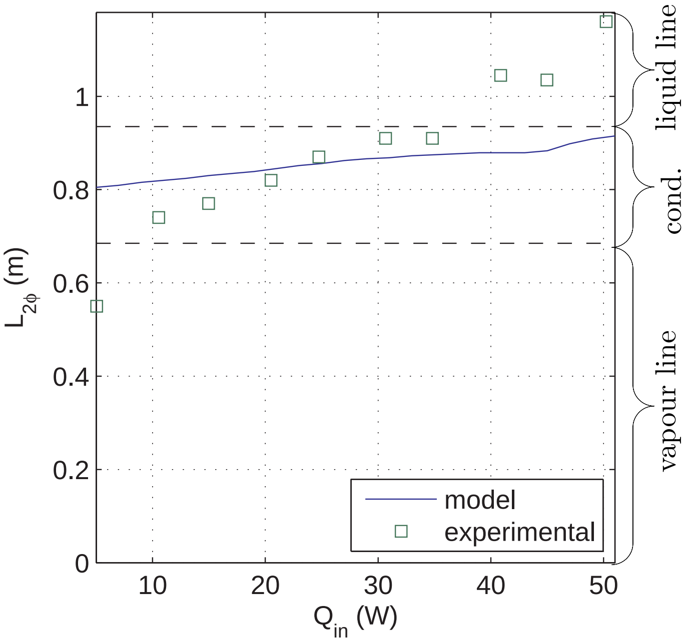

Figure 4.6: Comparison between the numerical simulation and the experimental data: two-phase length

4.2.2 Influence of the heat sink temperature

Simulations with three distinct heat sink temperatures are conducted in conditions similar to subsection 3.4.5. The results are presented in Figure 4.7. The fitting parameters of the previous section remain unchanged, even if the experimental conditions may have slightly changed and the repeatability of the experimental results is still challenging with the actual experimental setup. As expected, a higher heat sink temperature leads to a higher operating temperature. A major difference between the three simulations is observed regarding $T_{\mathrm{r,i}}$ and $T_{\mathrm{c,o}}$. Indeed, heat transfer with the condenser is lower when the heat sink temperature increases, which leads to an early transition to the constant conductance mode and a displacement of the meniscus inside the liquid line. This is in accordance with the experimental observations presented in subsection 3.4.5.

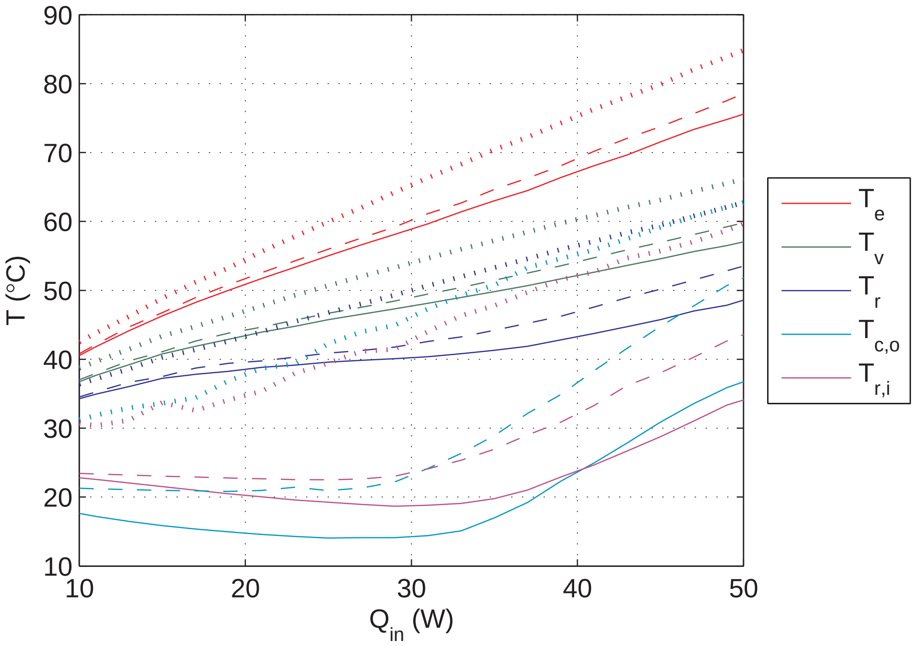

Figure 4.7: Influence of the heat sink temperature on the numerical results: $T_{\mathrm{sink}} = 10\,°\mathrm{C}$, solid lines; $T_{\mathrm{sink}} = 20\,°\mathrm{C}$, dashed lines; $T_{\mathrm{sink}} = 30\,°\mathrm{C}$, dash-dot lines

A comparison between the experimental measurements and the numerical results is shown in Figure 4.8. Only T_{e}, T_{v} and $T_{\mathrm{r,i}}$ are presented. The other temperatures do not give any useful information: T_{r} depends on T_{v} and the pressure drops, $T_{\mathrm{c,o}}$ depends on $T_{\mathrm{r,i}}$ and the heat losses to the ambient. Even if the general behaviour agrees between the results, a large discrepancy is observed for T_{e} and T_{v}. The simulation overestimates both the temperatures and the influence of the heat sink temperature. The difference between the simulation and the experimental data at high heat loads for $T_{\mathrm{sink}} = 10\,°\mathrm{C}$ and $T_{\mathrm{sink}} = 20\,°\mathrm{C}$ is induced by the boiling incipience in the reservoir. However, the comparison of the experimental data and the simulation results regarding $T_{\mathrm{r,i}}$ shows a good agreement. The temperature of the liquid entering the condenser is well predicted, particularly the significant increase of $T_{\mathrm{r,i}}$ with the heat load when the heat sink temperature is equal to 30 °C. These differences between the numerical results and the experimental data should be further studied. They can be induced by unsuitable fitting parameters, as well as by inaccuracies regarding the consideration of heat losses to the ambient, the pressure drops and the measurement of T_{v} and T_{r}.

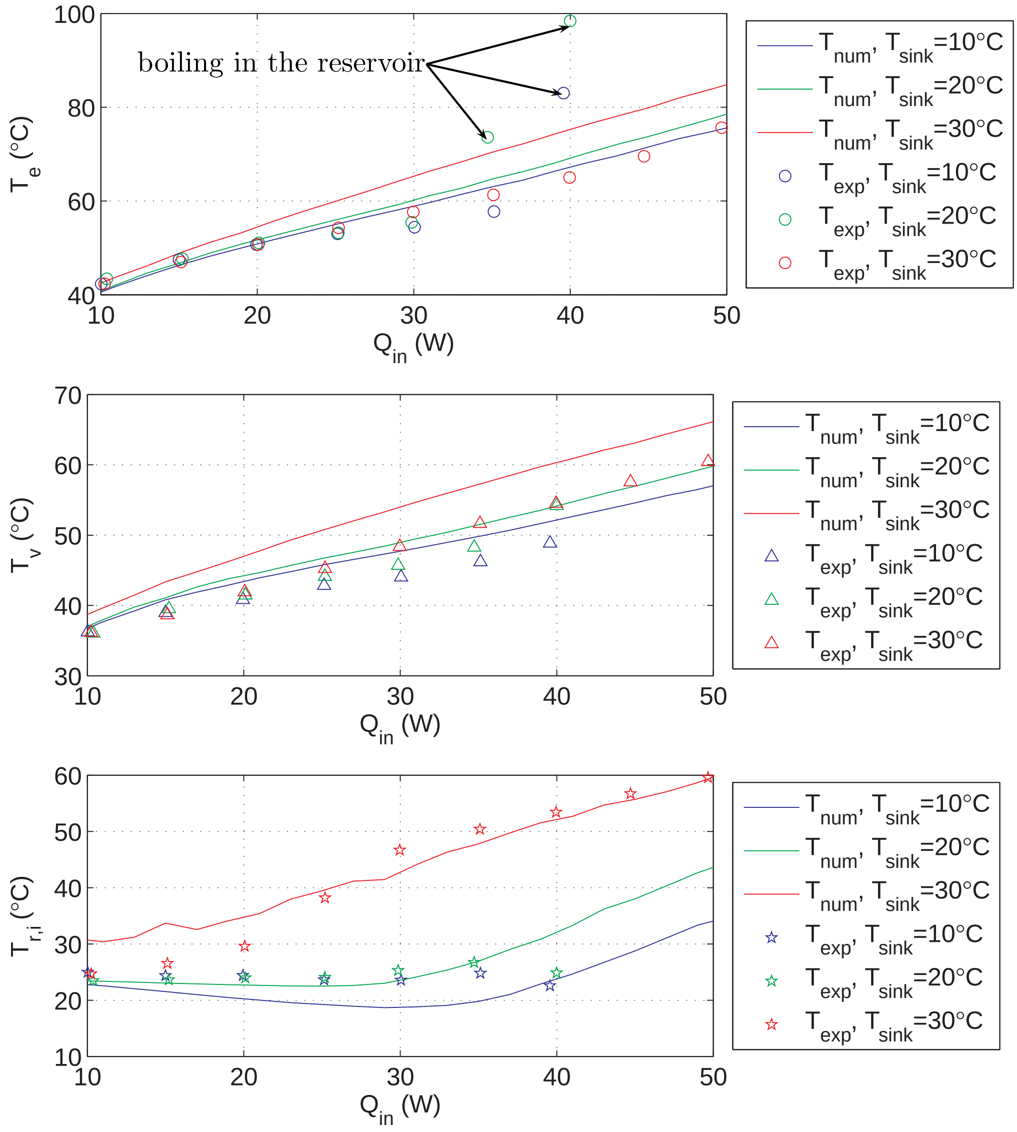

Figure 4.8: Influence of the heat sink temperature: comparison between the experimental data and the numerical results

4.2.3 Temperature field in the evaporator

Figure 4.9 presents the temperature field in the evaporator casing and the wick (Figure 4.4). The reservoir temperature is equal to 38.3 °C and $T_\mathrm{v} = 45.3\,$°C. As expected, the temperature of the copper block is almost homogeneous due to its high thermal conductivity. A temperature step between the copper fins and the wick is induced by the contact resistance. Temperature gradients are much larger in the evaporator casing. Indeed, the thermal conductivity of the PEEK body ($\lambda_\mathrm{b} = 0.25\,\mathrm{W \cdot m^{-1} \cdot K^{-1}}$) is low and prevents the heat from being conducted from the copper block to the ambient and to the reservoir. Far from the copper block, the temperature gradient is almost exclusively oriented in the x-direction in the casing. In that zone, the influence of the copper block is not significant and the casing temperature is much influenced by the reservoir temperature, as a consequence of the condensation phenomena inside the casing. The temperature field in the wick is slightly distorted at the side due to the radial heat transfer with the evaporator casing. In the reservoir, the temperature gradient in the axial direction corresponds to the thermal conduction in the liquid bulk. The temperature of the vapour is uniformly set to T_r.

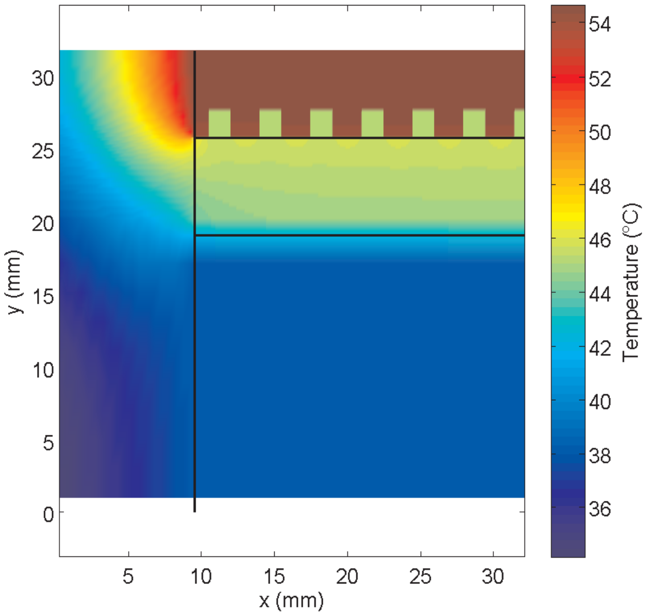

Figure 4.9: Temperature field in the evaporator – $Q_\mathrm{in} = 25\,\mathrm{W}$

The heat conducted through the wick leads to a temperature above the saturation temperature of the fluid. This induces a superheating of the liquid flowing through the wick and may lead to potential nucleate boiling inside the capillary structure.

Figure 4.10 presents the comparison between the numerical simulation and the analytical results. The modelled domain is a part of the wick at the centre of the evaporator. The boundary conditions of the analytical model of the wick are set in accordance with the numerical model: the heat transfer coefficient with the reservoir is equal to $260\,\mathrm{W \cdot m^{-2} \cdot K^{-1}}$ at $y = 0$; at $y = 6\,\mathrm{mm}$, T_v is set on one side, whereas for the other side, the temperature is set to the mean temperature of the wick just below the fin. The boundary conditions for both models are summarised in Table 4.1.

The comparison between the numerical study (Figure 4.10a) and the analytical model (Figure 4.10b) shows similar results. A slight difference is observed near the fin and the groove. The temperature gradually increases in the x-direction in the numerical simulation, whereas there is a sharp step in the temperature profile for the analytical results. This is explained by the boundary conditions at $y = 6\,\mathrm{mm}$, which are a heat flux continuity between the porous media and the fin in the numerical model and an imposed temperature in the analytical model. The global shape of the temperature field is, however, similar for both models.

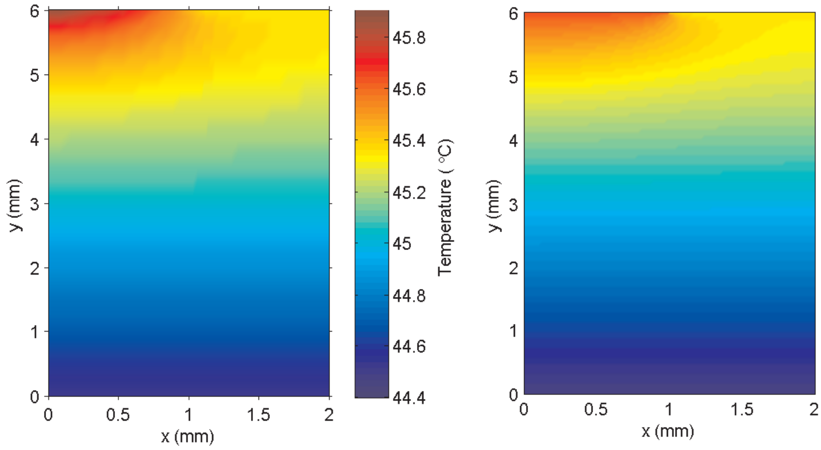

(a) Numerical simulation (b) Analytical simulation

Figure 4.10: Temperature field in the wick – $Q_{\text{in}} = 25\,\text{W}$

type of model	**numerical**	**analytical**
wick sides $(x = 0;\ x = 2\,\text{mm})$	adiabatic	adiabatic
reservoir $(y = 0)$	$T_{\text{r}} = 38.3\,°\text{C}$; $h_{\text{r}} = 260\,\text{W}\cdot\text{m}^{-2}\cdot\text{K}^{-1}$	$T_{\text{r}} = 38.3\,°\text{C}$; $h_{\text{r}} = 260\,\text{W}\cdot\text{m}^{-2}\cdot\text{K}^{-1}$
fin $(y = 6\,\text{mm};$ $0 < x < 1\,\text{mm})$	set heat flux (at the other side of the copper block)	$T = mean(T_{\text{num}}\|_{y=6\,\text{mm},0<x<1\,\text{mm}})$ $= 45.6\,°\text{C}$
groove $(y = 6\,\text{mm};$ $1\,\text{mm} < x < 2\,\text{mm})$	$T_{\text{v}} = 45.3\,°\text{C}$; $h_{\text{ev}} = 2\cdot 10^{7}\,\text{W}\cdot\text{m}^{-2}\cdot\text{K}^{-1}$	$T = T_{\text{v}} = 45.3\,°\text{C}$
evaporation	$a_{\text{ev}} = 0.6$	$a_1 - a_0 = 5\,\mu\text{m}$

Table 4.1: Wick modelling: summary of the boundary conditions

4.2.4 Influence of the casing thermal conductivity

In order to observe the influence of the casing thermal conductivity, a simulation is run with $\lambda_{\text{b}} = 2\,\text{W}\cdot\text{m}^{-1}\cdot\text{K}^{-1}$, a thermal conductivity 8 times higher than the one of PEEK. The results are presented in Figure 4.11. The temperatures are much higher than with a PEEK casing (Figure 4.9). Indeed, a larger part of the heat load is transferred from the copper block to the evaporator casing. This heat flux is then either dissipated to the ambient or given to the reservoir (longitudinal parasitic heat flux). As a result, both the copper block and the casing are at a higher temperature. The casing temperature is much higher than the ambient temperature, even at $y = 0$, inducing major heat losses to the ambient. This configuration also reduces the part of the heat load that is actually dissipated by evaporation (82 %) compared to the polymer casing (91 %).

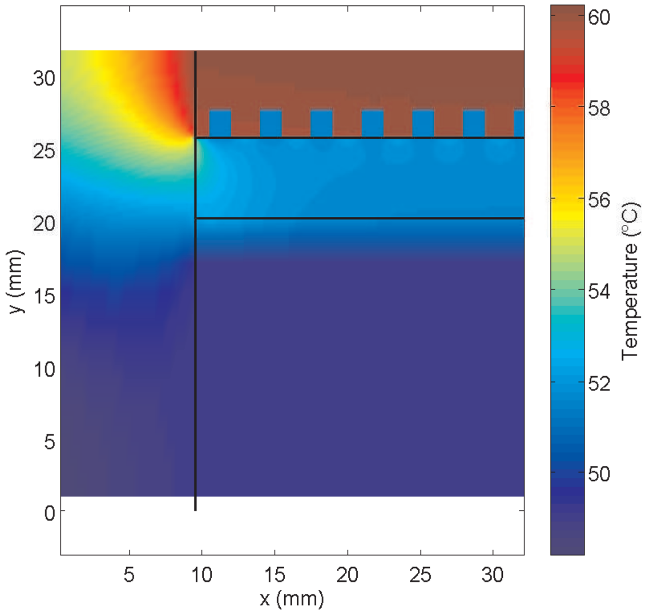

Figure 4.11: Temperature field in the evaporator with a conductive casing – $Q_{\text{in}} = 25\,\text{W}$

In usual application, the evaporator casing is often made of metal. It is therefore essential to reduce drastically the longitudinal parasitic heat transfer to enhance the thermal performance of the evaporator. In that effort, the following parameters should be paid attention to:

- The thickness of the casing should be reduced to prevent thermal conduction. However, this geometrical parameter is also dependent on the material used, the manufacturing and assembling process and the mechanical constraints.
- A low conductive material, such as stainless steel, can also help to reduce parasitic heat fluxes. However, if the entire evaporator is made of a low conductive material, the thermal conduction from the heat source to the wick is also lower and can decrease the global performance of the evaporator.
- The thermal contact between the fins and the wick should be enhanced to provide a good heat transfer to the evaporation zone.
- A seal could also prevent heat from being conducted to the reservoir. Such a configuration is for example used by Singh et al. [42]. However, it is hardly possible in case of a commercial application.

4.2.5 Influence of the boiling incipience inside the reservoir

In order to numerically study the influence of a major change of heat transfer inside the reservoir that occurs in case of boiling, the thermal conductivity of the liquid bulk inside the reservoir is artificially increased by a factor 100 therefore leading to heat transfer coefficient close to that encountered during nucleate boiling. In that case, the heat flux between the porous structure and the reservoir significantly increases. The comparison between both cases is presented in Table 4.2.

parameter	**without boiling**	**with boiling**
heat load	40 W=100 %	40 W=100 %
heat dissipated by evaporation	37 W=92.5 %	34.5 W=86.4 %
heat conducted through the casing	0.31 W=0.8 %	0.36 W=0.9 %
transversal parasitic heat transfer	2.7 W=6.7 %	5.1 W=12.7 %
T_{e}	69.4 °C	75.2 °C
T_{v}	54.3 °C	60.3 °C
T_{r}	47.2 °C	57.4 °C
$T_{\mathrm{r,i}}$	44 °C	22.9 °C
$T_{\mathrm{c,o}}$	46 °C	21.1 °C

Table 4.2: Influence of boiling on the LHP operation

As expected, the evaporation rate in the grooves decreases when boiling occurs, whereas the transversal parasitic heat transfer significantly increases. As a result, the LHP operates at a higher temperature and the two-phase length is reduced. This provides a sufficient subcooling of the liquid entering the reservoir to compensate for the increasing parasitic heat flux. These simulation results are in accordance with the experimental measurements discussed in subsection 3.4.3.

The temperature profile inside the wick is presented in Figure 4.12. Heat transfer with the reservoir increases, inducing a larger temperature difference between both sides of the wick. Furthermore, the temperature gradients are oriented in the y-direction as a result of the parasitic heat flux.

4.2.6 Temperature profile along the transport lines

Figure 4.13 presents the vapour quality in the transport lines and in the condenser and various temperatures, for a heat load equal to 25 W: the temperature of the tube T_{tube}, the fluid temperature T_{f}, the saturation temperature T_{sat} and the external temperature of the tube T_{ext} or T_{sink} for the transport lines and the condenser, respectively. Several distinct zones are observed:

- $z < 0.03\,\mathrm{m}$ corresponds to the first part of the vapour line. Superheated vapour exits the evaporator and enters the vapour line at $z = 0\,\mathrm{m}$. The tube wall temperature rapidly decreases due to heat losses to the ambient, inducing a decrease of the vapour temperature.

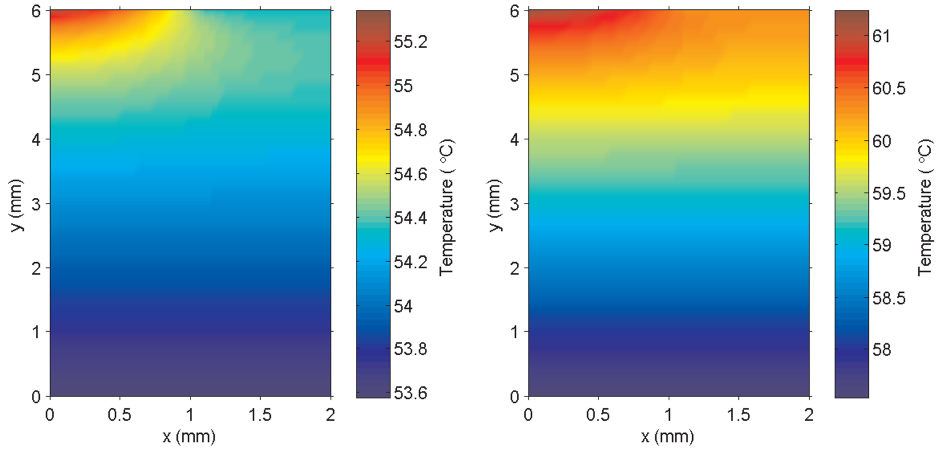

(a) without boiling

(b) with boiling

Figure 4.12: Temperature field in the wick – $Q_{\text{in}} = 40\,\text{W}$

At $z = 0.03\,\text{m}$, T_{f} reaches the saturation temperature. Since T_{tube} is slightly lower than T_{sat}, condensation begins. As a result, the vapour quality starts decreasing and heat transfer between the fluid and the wall significantly increases. This is consistent with the observations presented in the previous chapter. Indeed, condensation does not only occurs inside the condenser but also in the vapour line, due to the heat losses to the ambient.

- At $0.03\,\text{m} < z < 0.685\,\text{m}$, the two-phase fluid flows through the vapour line. The large condensation heat transfer coefficient induces a small temperature difference between T_{f} and T_{tube}. These temperatures continuously decrease ($-4.5\,\text{K}$) due to the pressure drops. The condensation rate is limited by the convective heat transfer with the ambient, thus the vapour quality does not decrease significantly inside the vapour line.

- At $0.685\,\text{m} < z < 0.87\,\text{m}$, the fluid further condenses inside the condenser. However, the phase-change rate is much larger than in the vapour line, as shown by the change of slope of the vapour quality. The external temperature is equal to T_{sink}. Since the condensation heat transfer coefficient is much larger than the external convective heat transfer coefficient of the condenser, the tube wall temperature is almost equal to T_{sat}. The difference between T_{f} and T_{tube} is larger than in the two-phase region of the vapour line because in the condenser, the heat transfer outside the tube is much larger than outside the transport line. The saturation temperature continues to decrease, but at a lower rate. Indeed, the vapour quality decreases, resulting in a lower fluid velocity. Therefore, the frictional pressure drops decrease and are partially compensated by the deceleration (variation of the momentum).

- The region where $0.87\,\text{m} < z < 0.935\,\text{m}$ corresponds to the subcooling part of the condenser. The vapour quality is equal to 0, *i. e.* only liquid flows inside the tube. Therefore, the fluid velocity is much lower and pressure drops are not significant, resulting in a quasi-constant saturation temperature. Both T_f and T_tube sharply decrease and the liquid is subcooled at a temperature close to T_sink at the end of the condenser.

- At $z > 0.935\,\mathrm{m}$, the fluid is in the liquid line. The saturation temperature is still quasi-constant. Both the temperature of the fluid and of the wall slightly decrease because of heat losses to the ambient. At the very end of the liquid line, a small increase of T_tube is observed, corresponding to the longitudinal thermal conduction from the evaporator/reservoir. These effects (longitudinal conduction and heat losses) are not significant because glass has a very low thermal conductivity ($\lambda_\mathrm{tube} = 1\,\mathrm{W \cdot m^{-1} \cdot K^{-1}}$). Therefore, both radial and longitudinal thermal conductions through the tube wall are minor. T_f remains almost equal to T_tube because its variation is not significant and the heat transfer coefficient inside the liquid line ($h_\mathrm{i} \approx 1300\,\mathrm{W \cdot m^{-2} \cdot K^{-1}}$) is much larger than with the ambient.

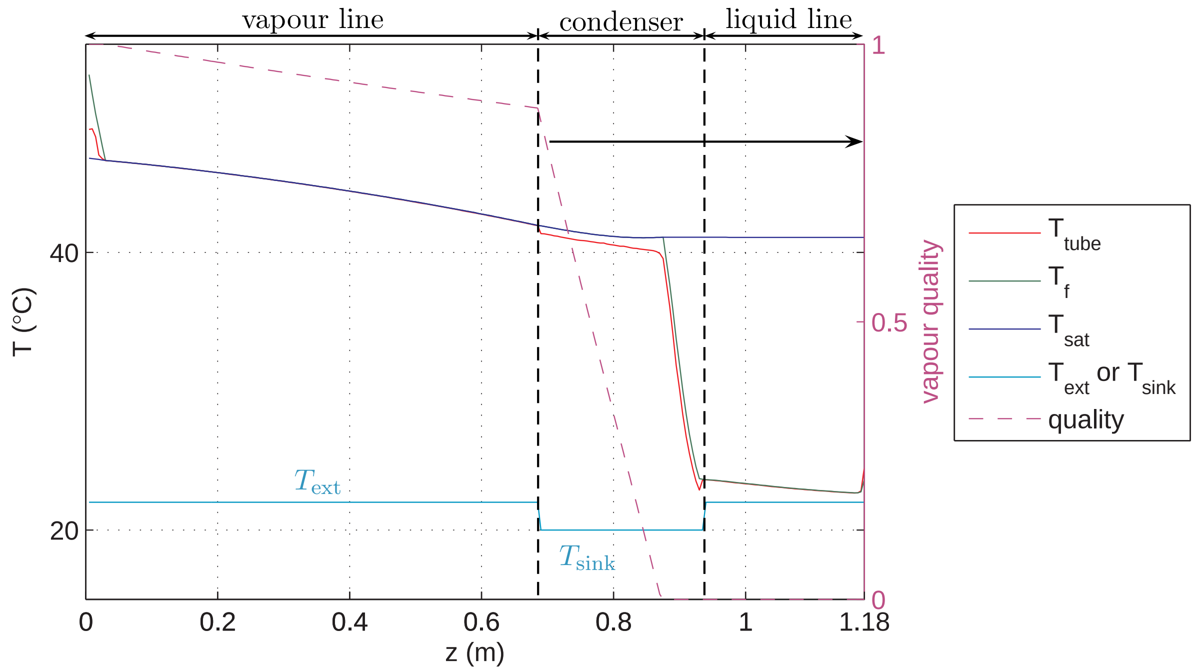

Figure 4.13: Temperature profile and vapour quality along the glass transport lines – $Q_\mathrm{in} = 25\,\mathrm{W}$

4.2.7 Influence of the thermal conductivity of the tubes

A simulation is conducted with the same parameters as previously, except that the thermal conductivity of the vapour and liquid lines corresponds to copper ($\lambda_\mathrm{tube} = 398\,\mathrm{W \cdot m^{-1} \cdot K^{-1}}$) and the outer diameter of the tubes is set to 2.4 mm because the wall of a copper capillary tube is usually much thinner than a glass tube. The wall temperature at the beginning of the vapour line is set to T_e, whereas it is equal to T_r at the end of the liquid line. This hypothesis may overestimate the effect of copper tubes in the case of this study. Indeed, the

PEEK casing would lead to a lower temperature at the boundary conditions, as explained in subsection 4.2.3. However, for smaller reservoirs made of high conductive materials which correspond to the majority of the LHP presented in the literature, such boundary conditions are consistent with the temperature field in the evaporator. The results with copper tubes at 25 W is presented in Figure 4.14. The general behaviour of the temperatures is similar as for glass tubes. However, some differences are observed at the beginning of the vapour line and at the end of the liquid line, as shown in the magnified view presented in Figure 4.15. As expected, in the case of copper, longitudinal thermal conduction inside the tube wall induces a larger influence of the evaporator/reservoir on the tube wall temperature. In the vapour line, the wall is at a higher temperature. Therefore, T_f decreases at a lower rate along the vapour line and the saturation temperature is reached at a longer distance of the evaporator. At the end of the liquid line also, thermal conduction leads to a significant increase of both the wall and the fluid temperatures. Therefore, the material of the transport lines has a direct consequence on both the heat losses to the ambient and the subcooling of the liquid entering the reservoir. The slight changes of slope observed in Figure 4.15a in the case of copper tubes are a consequence of the numerical adjustment of the beginning of the condensation and the use of under-relaxation factors for the heat transfer coefficient inside the tubes.

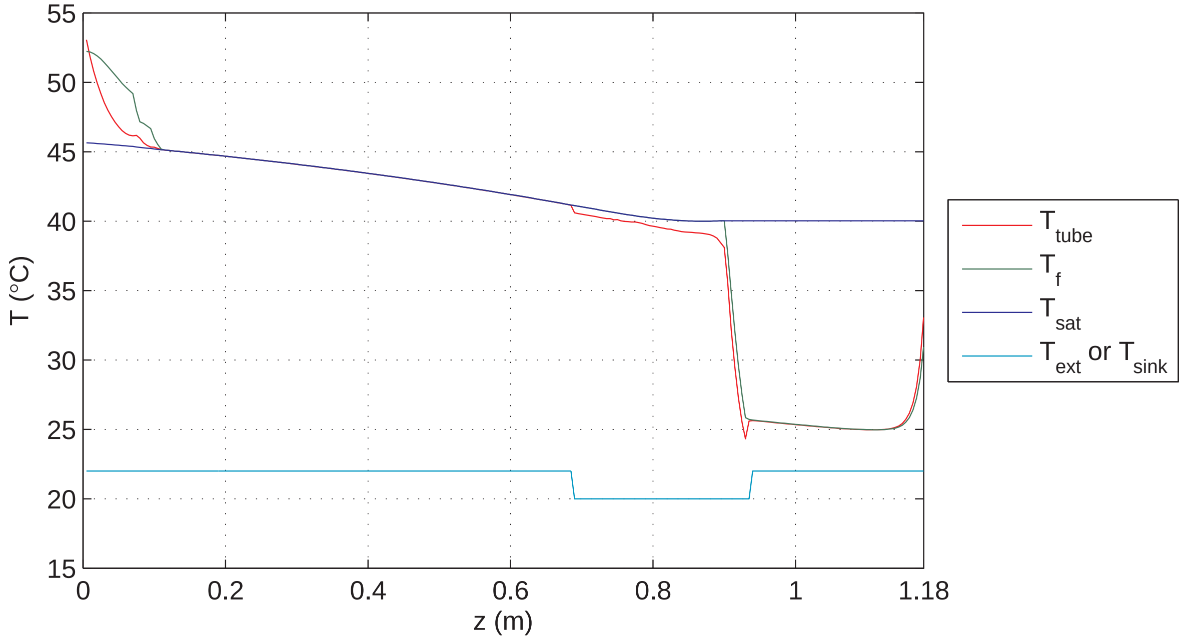

Figure 4.14: Temperature profile and vapour quality along the copper transport lines – $Q_\mathrm{in} = 25\,\mathrm{W}$

The influence of copper tubes is confirmed in Figure 4.16, where the operating curve of both configurations is compared. At low heat loads, the LHP with copper tubes operates at a slightly lower temperature. Indeed, the transport lines act as fins for the evaporator/reservoir and induce therefore larger heat losses to the ambient. As previously explained, the subcooling is affected by the longitudinal thermal conduction and $T_\mathrm{r,i}$ is significantly higher (+5 K)

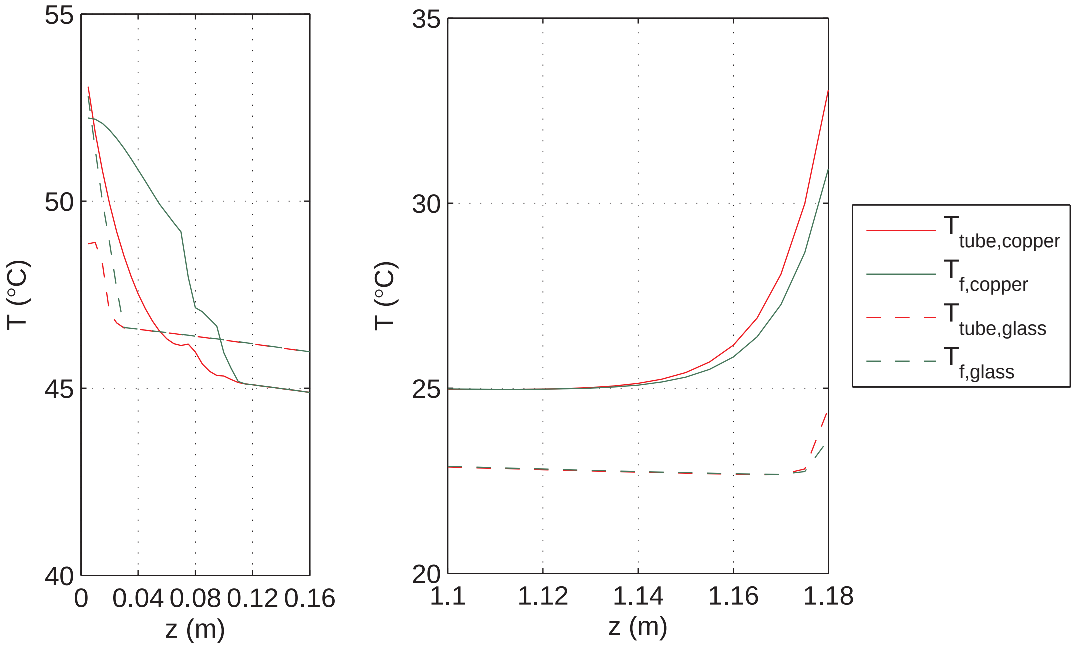

(a) at the beginning of the vapour line

(b) at the end of the liquid line

Figure 4.15: Comparison of the temperature profile between the copper tubes (solid lines) and the glass tubes (dashed lines) – $Q_{\text{in}} = 25\,\text{W}$

than with glass tubes, whatever the heat load. As a result, the transition to the constant conductance mode occurs at a lower heat load and for $Q_{\text{in}} > 33\,\text{W}$, the thermal performance is better with glass tubes than with copper tubes.

In conclusion, the thermal conductivity of the transport lines has an effect on the global behaviour of the LHP, and particularly on the subcooling of the liquid entering the condenser. It should therefore be taken into account when designing and optimising such a system. This simulation also shows the relevance of measuring the fluid temperature without an invasive thermocouple insertion, in the case of copper tubes. Indeed, with conductive tubes, the tube temperature is almost equal to the fluid temperature. In that case, a measurement on the tube wall enables an accurate estimation of the fluid temperature. This is, however, not the case for the first part of the vapour line (12 cm) for which the difference between T_{f} and T_{tube} is significant. In the case of glass tubes, such a measurement is not possible. The tube is thick and its thermal conductivity is low. Therefore, the radial thermal resistance of the tube, not considered in this model, is large and an invasive temperature measurement is necessary in this configuration.

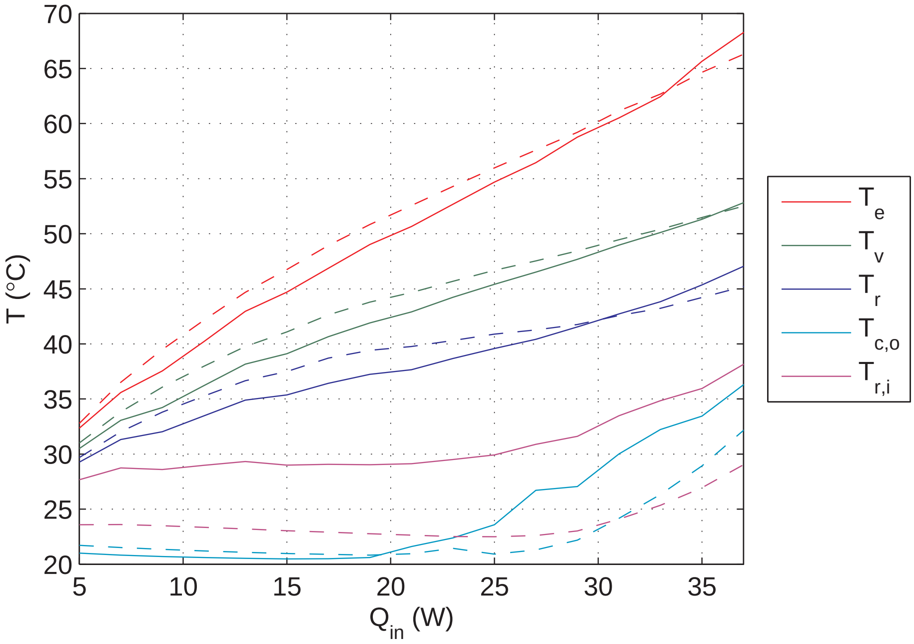

Figure 4.16: Comparison of the thermal performance between the copper tubes (solid lines) and the glass tubes (dashed lines)

4.3 Conclusion

A numerical model is developed. Based on a 1D discretisation of the transport lines and a 2D description of the evaporator/reservoir, the model takes accurately into account heat and mass transfer in both the wick, the evaporator casing, the transport lines and the condenser. An acceptable agreement is found between the model and the experimental results from the previous chapter and the experimental setup is characterised. The actual experimental results do not enable a thorough comparison with the theory due to experimental inaccuracies discussed in detail in chapter 3. The most significant discrepancy lies in the estimation of the pressure drops in the transport lines and the condenser, which may be due to inaccurate measurements or inadequate pressure drop correlations. A comparison is also presented concerning the influence of the heat sink temperature on the LHP behaviour. The temperature fields in the evaporator casing and in the wick are discussed. As it was expected, the conductivity of the casing material has a major influence on the heat and mass transfer in the evaporator, thus on the LHP operating temperature. Besides, a change of the heat transfer between the wick and the reservoir, for example in the case of boiling, results in a significant increase of the parasitic heat fluxes and the subcooling of liquid entering the reservoir. The temperature of the fluid and of the tube walls along the transport lines and the condenser are also studied. A simulation with copper tubes shows the necessity of considering the longitudinal thermal conduction in the design of LHPs to provide a correct estimation of the liquid subcooling at the entrance of the reservoir.

Conclusion

This thesis focuses on the study of the physical phenomena involved in loop heat pipes. After a thorough literature review, the investigation follows three complementary approaches. An analytical model is developed to highlight the main parameters of the system and their influence depending on the operating conditions. Then, a LHP is designed, built and tested with several sensors located at key locations inside the system. This system is partially transparent to provide observations of the liquid and vapour in operating conditions. Finally, a numerical model is developed, taking into account the geometry and the thermophysical properties of the experimental LHP in order to complete the experimental analysis.

First, an extensive literature study is undertaken. After mentioning the bases concerning the LHP operation, the investigation focuses on each component constituting this system. It shows the complexity of heat and mass transfer in LHPs, particularly in the evaporator/reservoir. Despite a large number of publications on the topic, an accurate evaluation of several parameters, such as the effective thermal conductivity of the wick, the compatibility of the working fluid with the LHP materials and the parasitic heat fluxes, remains challenging. A detailed analysis on the published modelling works on LHPs is also developed, showing the increasing number of models based on two-dimensional and three-dimensional descriptions, thanks to increasing computational resources. A discussion is presented regarding the location of the liquid-vapour interface inside the wick and the potential development of vapour pockets inside the capillary structure depending on the operating conditions. Despite interesting efforts to accurately predict the location of the interface, this phenomenon is still not well taken into account in LHP models since it depends on many unpredictable parameters such as a precise knowledge of the microscopic structure of the wick, the entrapment of vapour and gas inside the wick and the nucleate boiling phenomenon. Furthermore, such a consideration significantly increases the complexity of the modelling development. Therefore, it was chosen not to introduce this phenomenon in the present study.

In the second chapter, an analytical model is developed. It is based on a classical nodal description of the LHP, with the writing of an energy balance at each node and thermodynamic relationships between the interfaces. Its main originality lies in the consideration of heat and mass transfer in the evaporator, based on Fourier series. Such a method enables an accurate description of the parasitic heat fluxes and of the heat losses to the ambient that can be combined with the closed-form solution of the nodal network. The model is validated with experimental data from the literature, for both flat and cylindrical evaporators. After the definition of a standard case of study, a sensitivity analysis is undertaken to assess the influence of the accommodation coefficient a_{ev}, the thermal contact resistance R_{c}, the effective thermal conductivity λ_{eff} and the heat transfer coefficient with the ambient h_{ext} and with the heat sink h_{sink}. The major influence of the heat losses to the ambient is observed at very low heat loads. In variable conductance mode, the behaviour of the system is mainly controlled by the heat transfer inside the evaporator which depends on λ_{eff}, R_{c} and a_{ev}, whereas in fixed conductance mode, h_{sink} becomes the most influential parameter. This analysis shows that a sufficient number of sensors, well located inside a LHP should enable to estimate these parameters by comparison with the model. Finally, a parametric study is conducted to show and explain the behaviour of the system.

In the third chapter, the design of an experimental LHP, developed for research purposes is presented. Pressure and temperature measurements enable to characterise the operation of the LHP. Direct observations of the hydrodynamic phenomena are possible thanks to the use of glass for the transport lines and the condenser, as well as a window glass for the reservoir. The steady-state and transient operations of this LHP are investigated. These results are not exhaustive since the LHP was operational only a few weeks before the end of this PhD. Nevertheless, they constitute a first set of data that is useful to understand the behaviour of the system:

- A temperature hysteresis is observed between increasing and decreasing heat loads. The main explanation of this hysteresis is a partial dry-out of the capillary structure. A change of the ambient temperature or a potential increase of NCGs during the test of the system can increase this effect.

- In certain experimental conditions, boiling occurs inside the reservoir, inducing a sharp degradation of the system performance and a significant increase of the hysteresis. The nucleation in the reservoir is a complex phenomenon depending on various parameters and cannot be accurately predicted.

- The effect of non-condensable gases is also evaluated. NCGs induce an additional pressure in the reservoir and thus larger parasitic heat fluxes and a higher operational temperature. They also have a major influence on the boiling incipience in the reservoir, delaying the nucleation process.

- Contrarily to some experimental works of the literature, temperature overshoots are not observed during the start-up of the system. Nevertheless, the large thermal inertia of the set-up induces a long stabilisation time for the temperatures whereas the hydrodynamic regime is quite rapidly established.

- Temperature oscillations are observed in certain conditions and are strongly coupled with the hydrodynamics in the transport lines. Indeed, the condensation regime in the vapour line and the variation of the meniscus location during operation induce periodical variations of the main temperatures of the LHP.

- Observations of the condensation phenomena inside the tubes confirm previous investigations from the literature. Three regions can be distinguished at the end of the two-phase zone in the condenser: an annular zone with a quasi-hemispherical meniscus, a train of bubbles and isolated bubbles in the liquid phase. The detachment of Taylor bubbles occurs with fast and large deformation of the liquid vapour interface in the tube, inducing significant movements of liquid and vapour. The occurrence of drop-wise condensation in the vapour line leads to oscillating phenomena.

In the fourth chapter, a numerical model is developed. The two-dimensional heat and mass transfer is considered in the wick and the evaporator envelope. The model takes into account the accommodation coefficient for the modelling of the evaporation. The transport lines and the condenser are discretised and the temperatures of the wall and of the fluid are calculated separately. Such a feature enables the assessment of the longitudinal thermal conduction in the tubes as well as the calculation of the heat transfer and the pressure losses inside the tubes in both one-phase and two-phase flows. The model of the tubes is coupled with the 2D description of heat and mass transfer in the evaporator to determine the operation of the entire LHP. The numerical model is compared to the experimental data. A large discrepancy is observed regarding the pressure drops inside the vapour line and the condenser. This difference can be explained by the use of inadequate two-phase pressure drops correlations for the present experimental configuration. Furthermore, some temperature sensors may be not well representative of the real temperature of the system. This problem will be solved in a future work. The temperature field inside the evaporator is discussed. The numerical simulation confirms the increase of the evaporator temperature observed in the experiment after boiling incipience: a large increase of the heat transfer coefficient between the wick and the reservoir leads to a higher transversal parasitic heat flux and thus a higher temperature of the LHP. Finally, the temperature profiles of the fluid and of the tube wall along the transport lines and the condenser are investigated. The results highlight the importance the longitudinal thermal conduction inside the tube in the case of conductive materials such as copper.

Heat and mass transfer in LHPs being highly complex and a much investigated subject of research in the past decade, the present study does not claim to resolve and explain all of the key issues encountered in the operation of loop heat pipes and its prediction. However, the author hopes that the present investigation brings its own contribution to the understanding of the physical phenomena involved in such systems. Specific areas that should be given as a priority for future works in the continuity of this thesis are suggested below:

- Efforts should be directed towards a better control of the amount of NCGs inside the experimental setup. The airtightness of the system, as well as the purity of the working fluid should be enhanced. Such an improvement would enable a more accurate monitoring of the partial pressure of NCGs inside the reservoir. This should lead to more reproducible and comparable results and could result in a thorough quantitative investigation of the effect of non-condensable gases in LHPs.

- A further study of the pressure drops in the vapour line and in the condenser should be undertaken. Differential pressure measurements could enable a better choice of pressure drops correlations for the numerical model. Since the pressure drops set the temperature difference between the vapour line and the reservoir, such a feature would be of great interest regarding the determination of parasitic heat fluxes in the evaporator/reservoir. Furthermore, a better measurement of the reservoir temperature, with the insertion of a thermocouple inside the vapour zone of the reservoir, is essential. The analytical model should be improved to take into account the two-phase pressure drops inside the vapour line. Indeed, their significance is not negligible, in particular when the length of the vapour line is large and its diameter is small, inducing high flow velocities.

- The experimental data highlight the unpredictable boiling phenomenon in the reservoir and its major significance regarding the LHP operation and particularly the hysteresis of the evaporator temperature. A further parametric study should lead to a better understanding of this behaviour. This analysis could concern the amount of NCGs, the mass of working fluid in the system, the choice of working fluid and mainly the thermophysical and geometrical characteristics of the porous structure. Concerning the control of the mass of fluid inside the system, efforts should be directed towards a reduction of the dead volumes in the LHP and a better measurement of the level of liquid in the reservoir.

- The modularity of the new experimental setup should be put to good use to test various configurations. Various vapour groove designs, a more efficient condenser, thermal conductive transport lines would be interesting to test and to compare. Other working fluids should be tested and their performance evaluated, particularly fluids that are suitable candidates for avionics cooling applications.

- The experimental apparatus could be modified to test the LHP in various orientations and tilts. Indeed, in some applications like avionics, the LHPs are submitted to various environmental constraints like variable orientation, acceleration forces, etc. This investigation could increase the knowledge gained by the Cethil during the SYSHANG project (2010 – 2013), during which a commercial LHP was tested in various orientations for a future aeronautical application.

- The manufacture and the characterisation of the porous structure remain challenging issues in LHPs. An enhanced wick would improve the global performance of the LHP. A less conductive porous structure would also decrease the transversal parasitic heat transfer, thus preventing the boiling incipience in the reservoir. This is particularly important in the case of a low conductive evaporator envelope, for which the transversal parasitic heat flux is significant compared to the longitudinal heat losses. Furthermore, it is essential to characterise adequately the properties of the porous wick (effective thermal conductivity, permeability, pore size) in order to understand the heat transfer mechanisms in it and to provide reliable experimental data for the comparison with models. In that perspective, the Cethil and Mateis, a laboratory specialised in materials science, joined forces to launch the project 2MaTher. This project has various objectives. The first one is the development of new porous structures exclusively dedicated to LHPs, thanks to the expertise of the Cethil concerning LHPs and of Mateis regarding the design and manufacture of the materials. Innovative ceramics wicks and porous structure with thermal properties gradients will be tested. Besides, a characterisation bench will be designed to test the products and fine models will be developed regarding the permeability and the effective thermal conductivity of these porous structures. Finally, these wicks will be tested in the experimental bench designed in the present thesis and then in an industrial LHP.

- In the case of aeronautical applications, the use of water as working fluid is highly desirable because of its excellent thermo-physical characteristics, its environmental harmlessness and because it is free. However, in some particular storage conditions water may freeze, thus jeopardising the integrity of the LHP. To avoid this problem, the concept of an adsorption-based antifreeze solution was patented by the Cethil. The present experimental setup could be used to test the feasibility of this solution. The modularity of the apparatus enables the simple addition of an adsorbent reservoir which would adsorb the fluid during the shutdown of the system and desorb it prior to start-up. An experimental investigation would validate this concept and give essential data to understand the behaviour of such a modified LHP, investigate the start-up and shutdown phases, and choose the most appropriate adsorbent material. The modelling of the LHP behaviour and the comparison of experimental and predicted data could complete this analysis. This is a broad field of research, at both theoretical and experimental levels.

Bibliography

[1] Moore, G. E. Cramming more components onto integrated circuits. *Electronics*, 38(8): 114–117, 1965.

[2] Challis, K. Primae: Packaging of future intergrated modular avionics and electronics. In *Fibre Optics in Harsh Environments Conference*, number 13, Swindon, UK, 2012.

[3] Bonjour, J., Lefèvre, F., Sartre, V., Bertin, Y., Romestant, C., Ayel, V., and Platel, V. Systèmes diphasiques de contrôle thermique - thermosiphons et caloducs, 2010.

[4] Bonjour, J., Lefèvre, F., Sartre, V., Bertin, Y., Romestant, C., Ayel, V., and Platel, V. Systèmes diphasiques de contrôle thermique - boucles diphasiques gravitaires et capillaires, 2011.

[5] Bonjour, J., Lefèvre, F., Sartre, V., Bertin, Y., Romestant, C., Ayel, V., and Platel, V. Systèmes diphasiques de contrôle thermique - microcaloducs et caloducs oscillants, 2011.

[6] Launay, S., Sartre, V., and Bonjour, J. Analytical model for characterization of loop heat pipes. *Journal of Thermophysics and Heat Transfer*, 22(4):623–631, 2008.

[7] Rivière, N., Sartre, V., and Bonjour, J. Simulation of the operating characteristics of a cascaded LHP with thermal connector for on board electronic cooling. In 16^{th} *International Heat Pipe Conference*, Lyon, France, 2012.

[8] Lefèvre, F., Sartre, V., Siedel, B., and Bonjour, J. Dispositif amélioré de transport de chaleur en boucle fermée. *French patent*, FR2991031, 2011.

[9] Nikitkin, M. and Cullimore, B. CPL and LHP technologies: What are the differences, what are the similarities? *SAE paper*, 981587, 1998.

[10] Butler, D., Ku, J., and Swanson, T. Loop heat pipes and capillary pumped loops: An applications perspective. volume 608, pages 49–56, Albuquerque, New Mexico (USA), 2002.

[11] Lachassagne, L., Ayel, V., Romestant, C., and Bertin, Y. Experimental study of capillary pumped loop for integrated power in gravity field. *Applied Thermal Engineering*, 35:166–176, 2012.

[12] Lachassagne, L., Ayel, V., Romestant, C., and Bertin, Y. Steady-state modeling of capillary pumped loop for terrestrial application. In 15^{th} *International Heat Pipe Conference*, Clemson, South Carolina (USA), 2010.

[13] Lachassagne, L., Bertin, Y., Ayel, V., and Romestant, C. Steady-state modeling of capillary pumped loop in gravity field. *International Journal of Thermal Sciences*, 64: 62–80, 2013.

[14] Ayel, V., Lachassagne, L., Bertin, Y., Romestant, C., and Lossouarn, D. Experimental analysis of a capillary pumped loop for terrestrial application. *Journal of Thermophysics and Heat Transfer*, 25(4):561–571, 2011.

[15] Blet, N., Delalandre, N., Ayel, V., Bertin, Y., Romestant, C., and Platel, V. Transient thermohydraulic modeling of two-phase fluid systems. In *Journal of Physics: Conference Series*, volume 395, page 012177. IOP Publishing, 2012.

[16] Hoang, T., O'Connell, T., Ku, J., Khrustalev, D., and Norin, S. Cryogenic advanced loop heat pipe in temperature range of 20-30K. In 12^{th} *International Heat Pipe Conference*, Moscow, Russia, 2002.

[17] Zhao, X., Wang, Z., and Tang, Q. Theoretical investigation of the performance of a novel loop heat pipe solar water heating system for use in Beijing, China. *Applied Thermal Engineering*, 30(16):2526–2536, 2010.

[18] Singh, R., Akbarzadeh, A., and Mochizuki, M. Thermal potential of flat evaporator miniature loop heat pipes for notebook cooling. *IEEE Transactions on Components and Packaging Technologies*, 33(1):32–45, 2010.

[19] Dupont, V., Van Oost, S., and Barremaecker, L. Railways qualification tests of capillary pumped loop on a train. In 17^{th} *International Heat Pipe Conference*, Kanpur, India, 2013.

[20] Maydanik, Y. Loop heat pipes. *Applied Thermal Engineering*, 25:635–657, 2005.

[21] Wolf, D. A. and Bienert, W. B. Investigation of temperature control characteristics of loop heat pipes. *SAE paper*, 941576, 1994.

[22] Nikitkin, M., Kotlyarov, E., and Serov, G. Basics of loop heat pipe temperature control. *SAE Technical Paper*, page 01–2012, 1999.

[23] Nagano, H. and Ku, J. Capillary limit of a multiple-evaporator and multiple-condenser miniature loop heat pipe. *Journal of Thermophysics and Heat Transfer*, 21(4):694–701, 2007.

[24] Maydanik, Y. F. and Vershinin, S. Development and investigation of copper-water loop heat pipes with high operating characteristics. *Heat Pipe Science and Technology, An International Journal*, 1(2):151–162, 2010.

[25] Kim, J. and Golliher, E. Steady state model of a micro loop heat pipe. In 18^{th} *Annual IEEE Symposium , Semiconductor Thermal Measurement and Management*, pages 137–144, San Jose, California (USA), 2002.

[26] Hoang, T. T., O'Conne, T. A., Ku, J., Butler, C. D., and Swanson, T. D. Miniature loop heat pipes for electronic cooling. In *International Electronic Packaging Technical Conference and Exhibition*, Maui, Hawaii (USA), 2003.

[27] Chernysheva, M., Vershinin, S., and Maydanik, Y. F. Operating temperature and distribution of a working fluid in LHP. *International Journal of Heat and Mass Transfer*, 50:2704–2713, 2007.

[28] Chen, Y., Groll, M., Mertz, R., Maydanik, Y. F., and Vershinin, S. Steady-state and transient performance of a miniature loop heat pipe. *International Journal of Thermal Sciences*, 45:1084–1090, 2006.

[29] van Helden, P. G. M., den Ouden, M., dos Santos, N., and Riehl, R. R. Novel loop heat pipes development for ground and space applications. In 18^{th} *International Congress of Mechanical Engineering*, Ouro Preto, Brazil, 2005.

[30] Launay, S. and Vallée, M. State-of-the-art experimental studies on loop heat pipes. *Frontiers in Heat Pipes*, 2(1), 2011.

[31] Maydanik, Y., Vershinin, S., Korukov, M., and Ochterbeck, J. Miniature loop heat pipes - a promising means for cooling electronics. *IEEE Transactions on Components and Packaging Technologies*, 28(2):290–296, 2005.

[32] Launay, S., Sartre, V., and Bonjour, J. Parametric analysis of loop heat pipe operation: a literature review. *International Journal of Thermal Sciences*, 46(7):621–636, 2007.

[33] Kaya, T. and Goldak, J. Numerical analysis of heat and mass transfer in the capillary structure of a loop heat pipe. *International Journal of Heat and Mass Transfer*, 49: 3211–3220, 2006.

[34] Carey, V. P. *Liquid-vapor phase-change phenomena.* Hemisphere, New York, 1992.

[35] Ku, J. Operating characteristics of loop heat pipes. In 29^{th} *International Conference on Environmental System*, Denver, Colorado (USA), 1999.

[36] Maydanik, Y. F. Miniature loop heat pipes. In *13th International Heat Pipe Conference*, pages 23–35, 2004.

[37] Santos, P. H., Bazzo, E., and Oliveira, A. A. Thermal performance and capillary limit of a ceramic wick applied to LHP and CPL. *Applied Thermal Engineering*, 41:92–103, 2012.

[38] Wu, S.-C., Huang, C.-J., Chen, S.-H., and Chen, Y.-M. Manufacturing and testing of the double-layer wick structure in a loop heat pipe. *International Journal of Heat and Mass Transfer*, 56(1–2):709–714, 2013.

[39] Zhang, L., Xu, J., and Xu, H. Effect of inventory on the heat performance of copper–water loop heat pipe. *Experimental Thermal and Fluid Science*, 44:875–882, 2013.

[40] Becker, S., Vershinin, S., Sartre, V., Laurien, E., Bonjour, J., and Maydanik, Y. Steady state operation of a copper–water LHP with a flat-oval evaporator. *Applied Thermal Engineering*, 31(5):686–695, 2011.

[41] Vasiliev, L., Lossouarn, D., Romestant, C., Alexandre, A., Bertin, Y., Piatsiushyk, Y., and Romanenkovc, V. Loop heat pipe for cooling of high-power electronic components. *International Journal of Heat and Mass Transfer*, 52:301–308, 2009.

[42] Singh, R., Akbarzadeh, A., and Mochizuki, M. Operational characteristics of a miniature loop heat pipe with flat evaporator. *International Journal of Thermal Sciences*, 47:1504–1515, 2008.

[43] Chuang, P. *An improved steady-state model of loop heat pipes based on experimental and theoretical analyses*. PhD thesis, Pennsylvania State University, 2003.

[44] Hamdan, M. *Loop heat pipe (LHP) modeling and development by utilizing coherent porous silicon (CPS) wicks*. PhD thesis, University of Cincinnati, 2003.

[45] Singh, R., Akbarzadeh, A., and Mochizuki, M. Operational characteristics of the miniature loop heat pipe with non-condensable gases. *International Journal of Heat and Mass Transfer*, 53(17):3471–3482, 2010.

[46] Chernysheva, M. A. and Maydanik, Y. F. Simulation of thermal processes in a flat evaporator of a copper–water loop heat pipe under uniform and concentrated heating. *International Journal of Heat and Mass Transfer*, 55(25–26):7385–7397, 2012.

[47] Maydanik, Y. F., Chernysheva, M. A., and Pastukhov, V. G. Review: Loop heat pipes with flat evaporators. *Applied Thermal Engineering*, 2014.

[48] Singh, R., Akbarzadeh, A., and Mochizuki, M. Effect of wick characteristics on the thermal performance of the miniature loop heat pipe. *Journal of Heat Transfer*, 131 (8):082601, 2009.

[49] Boo, J. H. and Chung, W. B. Experimental study on the thermal performance of a small-scale loop heat pipe with polypropylene wick. *Journal of Mechanical Science and Technology*, 19:1052–1061, 2005.

[50] Ogushi, T., Yao, A., Xu, J. J., Masumoto, H., and Kawaji, M. Heat transport characteristics of flexible looped heat pipe under micro-gravity condition. *Heat Transfer Asian Research*, 32(5):381–390, 2003.

[51] Riehl, R. R. and dos Santos, N. Loop heat pipe performance enhancement using primary wick with circumferential grooves. *Applied Thermal Engineering*, 28:1745–1755, 2008.

[52] Santos, P., Bazzo, E., Becker, S., Kulenovic, R., and Mertz, R. Development of LHPs with ceramic wick. *Applied Thermal Engineering*, 30(13):1784–1789, 2010.

[53] Xu, J., Zou, Y., Yang, D., and Fan, M. Development of biporous Ti_3AlC_2 ceramic wicks for loop heat pipe. *Materials Letters*, 2012.

[54] Zimbeck, W., Slavik, G., Cennamo, J., Kang, S., Yun, J., and Kroliczek, E. Loop heat pipe technology for cooling computer servers. In 11^{th} *Intersociety Conference on Thermal and Thermomechanical Phenomena in Electronic Systems*, page 19–25, Orlando, Florida (USA), 2008.

[55] Silk, E. A. and Myre, D. Fractal loop heat pipe performance testing with a compressed carbon foam wick structure. *Applied Thermal Engineering*, 59(1–2):290–297, 2013.

[56] Pastukhov, V. and Maydanik, Y. Active coolers based on copper-water LHPs for desktop PC. *Applied Thermal Engineering*, 29(14-15):3140–3143, 2009.

[57] Li, J., Wang, D., and Peterson, G. P. Experimental studies on a high performance compact loop heat pipe with a square flat evaporator. *Applied Thermal Engineering*, 30(6-7):741–752, 2010.

[58] Wang, S., Huo, J., Zhang, X., and Lin, Z. Experimental study on operating parameters of miniature loop heat pipe with flat evaporator. *Applied Thermal Engineering*, 40: 318–325, 2012.

[59] Bartuli, E., Vershinin, S., and Maydanik, Y. Visual and instrumental investigations of a copper–water loop heat pipe. *International Journal of Heat and Mass Transfer*, 61: 35–40, 2013.

[60] Xu, J., Zhang, L., and Xu, H. Performance of LHPs with a novel design evaporator. *International Journal of Heat and Mass Transfer*, 55(23–24):7005–7014, 2012.

[61] Choi, J., Sung, B., Kim, C., and Borca-Tasciuc, D.-A. Interface engineering to enhance thermal contact conductance of evaporators in miniature loop heat pipe systems. *Applied Thermal Engineering*, 60(1–2):371–378, 2013.

[62] Singh, R., Nguyen, T., and Mochizuki, M. Capillary evaporator development and qualification for loop heat pipes. *Applied Thermal Engineering*, 63(1):406–418, 2014.

[63] Singh, R., Akbarzadeh, A., and Mochizuki, M. Experimental determination of wick properties for loop heat pipe applications. *Journal of Porous Media*, 12(8):759–776, 2009.

[64] Holley, B. and Faghri, A. Permeability and effective pore radius measurements for heat pipe and fuel cell applications. *Applied Thermal Engineering*, 26(4):448–462, 2006.

[65] Berti, L., Santos, P., Bazzo, E., Janssen, R., Hotza, D., and Rambo, C. Evaluation of permeability of ceramic wick structures for two phase heat transfer devices. *Applied Thermal Engineering*, 31(6-7):1076–1081, 2011.

[66] Nguyen, X. H., Sung, B. H., Choi, J., Ryoo, S. R., Ko, H. S., and Kim, C. Study on heat transfer performance for loop heat pipe with circular flat evaporator. *International Journal of Heat and Mass Transfer*, 55(4):1304–1315, 2012.

[67] Xu, J., Zou, Y., Fan, M., and Cheng, L. Effect of pore parameters on thermal conductivity of sintered LHP wicks. *International Journal of Heat and Mass Transfer*, 55 (9–10):2702–2706, 2012.

[68] Figus, C., Le Bray, Y., Bories, S., and Prat, M. Heat and mass transfer with phase change in a porous structure partially heated: continuum model and pore network simulations. *International Journal of Heat and Mass Transfer*, 42:1446–1458, 1999.

[69] Mo, S., Hu, P., Cao, J., Chen, Z., Fan, H., and Yu, F. Effective thermal conductivity of moist porous sintered nickel material. *International Journal of Thermophysics*, 27 (1):304–313, 2006.

[70] Li, C. and Peterson, G. P. The effective thermal conductivity of wire screen. *International Journal of Heat and Mass Transfer*, 49(21-22):4095–4105, 2006.

[71] Yeh, C., Chen, C., and Chen, Y. Heat transfer analysis of a loop heat pipe with biporous wicks. *International Journal of Heat and Mass Transfer*, 52(19):4426–4434, 2009.

[72] North, M. T., Sarraf, D. B., Rosenfeld, J. H., Maidanik, Y. F., and Vershinin, S. High heat flux loop heat pipes. In *AIP Conference Proceedings*, volume 387, pages 561–566. AIP Publishing, 1997.

[73] Yeh, C. C., Liu, B. H., and Chen, Y. M. A study of loop heat pipe with biporous wicks. *Heat and Mass Transfer*, 44(12):1537–1547, 2008.

[74] Lin, F.-C., Liu, B.-H., Huang, C.-T., and Chen, Y.-M. Evaporative heat transfer model of a loop heat pipe with bidisperse wick structure. *International Journal of Heat and Mass Transfer*, 54(21–22):4621–4629, 2011.

[75] Chen, B., Liu, W., Liu, Z., Li, H., and Yang, J. Experimental investigation of loop heat pipe with flat evaporator using biporous wick. *Applied Thermal Engineering*, 42: 34–40, 2012.

[76] Van Oost, S., Mullender, B., Bekaert, G., and Legros, J. C. Secondary wick operation principle and performance mapping in LHP and FLHP evaporators. In *AIP Conference Proceedings*, volume 608, page 94, 2002.

[77] Choi, J., Lee, Y., Sung, B., and Kim, C. Investigation on operational characteristics of the miniature loop heat pipes with flat evaporators based on diverse vapor removal channels. In 16^{th} *International Heat Pipe Conference*, Lyon, France, 2012.

[78] Altman, E., Mukminova, M., and Smirnov, H. The loop heat pipe evaporators theoretical analysis. In 12^{th} *International Heat Pipe Conference*, Moscow, Russia, 2002.

[79] Zhang, X., Li, X., and Wang, S. Three-dimensional simulation on heat transfer in the flat evaporator of miniature loop heat pipe. *International Journal of Thermal Sciences*, 54:188–198, 2012.

[80] Kiseev, V. M., Vlassov, V. V., and Muraoka, I. Experimental optimization of capillary structures for loop heat pipes and heat switches. *Applied Thermal Engineering*, 30 (11-12):1312–1319, 2010.

[81] Wei, Y., Jianyin, M., and Xingguo, S. Parametric analysis on lhp/cpl evaporator performance and critical heat flux by two-dimensional calculation. *China Academy of Space Technology*, 26:240–247, 2004.

[82] Vlassov, V. V. and Riehl, R. R. Modeling of a loop heat pipe with evaporator of circumferential vapor grooves in primary wick. In 36^{th} *International Conference on Environmental Systems*, Norfolk, Virginia (USA), 2006.

[83] Kuroi, M. and Nagano, H. The influence of groove shape on loop heat pipes' performance. In 16^{th} *International Heat Pipe Conference*, Lyon, France, 2012.

[84] Rivière, N., Sartre, V., and Bonjour, J. Fluid mass distribution in a loop heat pipe with flat evaporator. In 15^{th} *International Heat Pipe Conference*, Clemson, South Carolina (USA), 2010.

[85] Siedel, B., Sartre, V., and Lefèvre, F. Numerical investigation of the thermohydraulic behaviour of a complete loop heat pipe. *Applied Thermal Engineering*, 61(2):541–553, 2013.

[86] Wan, Z.-P., Wang, X.-W., and Tang, Y. Condenser design optimization and operation characteristics of a novel miniature loop heat pipe. *Energy Conversion and Management*, 64:35–42, 2012.

[87] Collier, J. G. and Thome, J. R. *Convective boiling and condensation,* 3^{rd} *edition.* Oxford University Press, Oxford, 1994.

[88] Thome, J. R. *Engineering Data Book III.* Wolverine Tube Inc., 2006.

[89] Dobson, M. K. and Chato, J. C. Condensation in smooth horizontal tubes. *Journal of Heat Transfer*, 120(1):193–213, 1998.

[90] Akers, W. W., Deans, H. A., and Crosser, O. K. Condensing heat transfer within horizontal tubes. *Chemichal Engineering Progress Symposium Series*, 59(29):171–176, 1958.

[91] Goncharov, K., Buz, V., and Kochetkov, A. Modeling and experimental researches of condensation in LHP. In 15^{th} *International Heat Pipe Conference*, Clemson, South Carolina (USA), 2010.

[92] Miscevic, M., Lavieille, P., and Piaud, B. Numerical study of convective flow with condensation of a pure fluid in capillary regime. *International Journal of Heat and Mass Transfer*, 52(21–22):5130–5140, 2009.

[93] El Achkar, G., Lavieille, P., and Miscevic, M. Loop heat pipe and capillary pumped loop design: About heat transfer in the isolated bubbles zone of condensers. *Applied Thermal Engineering*, 33-34:253–257, 2012.

[94] Soler, P. *Expérimentation et modélisation thermohydraulique des LHP*. PhD thesis, Université de Provence, 2009.

[95] Kaya, T. and Ku, J. A parametric study of performance characteristics of loop heat pipes. *SAE Technical Paper*, page 01–2006, 1999.

[96] Pauken, M. and Rodriguez, J. Performance characterization and model verification of a loop heat pipe. *American Society of Automotive Engineers, Paper*, page 01–2317, 2000.

[97] Hsu, C.-C., Kang, S.-W., and Hou, T.-F. Performance testing of micro loop heat pipes. *Tamkang Journal of Science and Engineering*, 8:123–132, 2005.

[98] Liu, Z., Gai, D., Li, H., Liu, W., Yang, J., and Liu, M. Investigation of impact of different working fluids on the operational characteristics of miniature LHP with flat evaporator. *Applied Thermal Engineering*, 31(16):3387–3392, 2011.

[99] Mishkinis, D., Ochterbeck, J., Sodtke, C., Ku, J., and Butler, D. Non-dimensional analysis and scaling issues in loop heat pipes. In 41^{st} *AIAA Aerospace Sciences Meeting and Exhibit*, Reno, Nevada (USA), 2003.

[100] Launay, S., Sartre, V., and Bonjour, J. Selection criteria for fluidic and geometrical parameters of a LHP based on analytical approach. In 15^{th} *International Heat Pipe Conference*, Clemson, South Carolina (USA), 2010.

[101] Mishkinis, D., Prado, P., Sanz, R., and Torres, A. Development of LHP for intermediate temperature range. In 15^{th} *International Heat Pipe Conference*, Clemson, South Carolina (USA).

[102] Anderson, W. G., Hartenstine, J. R., Sarraf, D. B., and Tarau, C. Intermediate temperature fluids for heat pipes and loop heat pipes. In 15th *International Heat Pipe Conference*, Clemson, South Carolina (USA), 2010.

[103] Nikitkin, M. N., Bienert, W. B., and Goncharov, K. A. Non condensable gases and loop heat pipe operation. In *International Conference on Environmental Systems*, Danvers, Massachusetts (USA), 1998. SAE International. (SAE Paper 981584).

[104] He, J., Lin, G., Bai, L., Miao, J., and Zhang, H. Effect of non-condensable gas on the operation of a loop heat pipe. *International Journal of Heat and Mass Transfer*, 70: 449–462, 2014.

[105] Baumann, J., Cullimore, B., Yendler, B., and Buchan, E. Noncondensible gas, mass, and adverse tilt effects on the start-up of loop heat pipes. In 29th *International Conference On Environmental Systems*, Denver, Colorado (USA), 1999.

[106] Kaya, T., Ku, J., Hoang, T. T., and Cheung, M. K. Mathematical modeling of loop heat pipes. In *37th AIAA Aerospace Sciences Meeting and Exhibit*, Reno, Nevada (USA), 1999.

[107] Douglas, D., Ku, J., and Kaya, T. Testing of the geoscience laser altimeter system (GLAS) prototype loop heat pipe. In 37th *AIAA Aerospace Sciences Meeting and Exhibit*, Reno, Nevada (USA), 1999. Goddard Space Flight Center, NASA. Paper 99-0473.

[108] Kaya, T. and Ku, J. Thermal operational characteristics of a small-loop heat pipe. *Journal of Thermophysics and Heat Transfer*, 17(4):464–470, 2003.

[109] Adoni, A., Ambirajan, A., Jasvanth, V., Kumar, D., Dutta, P., and Slinivasan, K. Thermohydraulic modeling of capillary pumped loop and loop heat pipe. *Journal of Thermophysics and Heat Transfer*, 21(2):410–421, 2007.

[110] El Hajal, J., Thome, J. R., and Cavallini, A. Condensation in horizontal tubes. part 1: two-phase flow pattern map. *International Journal of Heat and Mass Transfer*, 46(18): 3349–3363, 2003.

[111] Thome, J. R., El Hajal, J., and Cavallini, A. Condensation in horizontal tubes. part 2: new heat transfer model based on flow regimes. *International Journal of Heat and Mass Transfer*, 46(18):3365–3387, 2003.

[112] Friedel, L. Improved friction pressure drop correlations for horizontal and vertical two-phase pipe flow. In *European Two-Phase Flow Group Meeting*, volume 2, Ispra, Italy, 1979.

[113] Adoni, A. A., Ambirajan, A., Jasvanth, V. S., Kumar, D., and Dutta, P. Effects of mass of charge on loop heat pipe operational characteristics. *Journal of Thermophysics and Heat Transfer*, 23(2):346–355, 2009.

[114] Adoni, A., Ambirajan, A., Jasvanth, V., Kumar, D., and Dutta, P. Theoretical studies of hard filling in loop heat pipes. *Journal of Thermophysics and Heat Transfer*, 24(1): 173–183, 2010.

[115] Bai, L., Lin, G., Zhang, H., and Wen, D. Mathematical modeling of steady-state operation of a loop heat pipe. *Applied Thermal Engineering*, 29:2643–2654, 2009.

[116] Bai, L., Lin, G., and Wen, D. Parametric analysis of steady-state operation of a CLHP. *Applied Thermal Engineering*, 30(8-9):850–858, 2010.

[117] Singh, R., Akbarzadeh, A., Dixon, C., and Mochizuki, M. Theoretical modelling of miniature loop heat pipe. *Heat and Mass Transfer*, 46(2):209–224, 2009.

[118] Hodot, R., Sartre, V., Lefèvre, F., and Sarno, C. 3D modeling and optimization of a loop heat pipe evaporator. In 17th *International Heat Pipe Conference*, Kanpur, India, 2013.

[119] Cullimore, B. and Baumann, J. Steady-state and transient loop heat pipe modeling. In 30th *International Conference on Environmental Systems*, Toulouse, France, 2000.

[120] Hamdan, M., Gerner, F. M., and Henderson, H. T. Steady state model of a loop heat pipe (LHP) with coherent porous silicon (CPS) wick in the evaporator. In 19th *Annual IEEE Symposium , Semiconductor Thermal Measurement and Management*, pages 88–96, San Jose, California (USA), 2003.

[121] Ghajar, M., Darabi, J., and Crews Jr, N. A hybrid CFD-mathematical model for simulation of a MEMS loop heat pipe for electronics cooling applications. *Journal of Micromechanics and Microengineering*, 15:313–321, 2005.

[122] Li, Y.-Z., Wang, Y.-Y., and Lee, K.-M. Dynamic modeling and transient performance analysis of a LHP-MEMS thermal management system for spacecraft electronics. *IEEE Transactions on Components and Packaging Technologies*, 33(3):597–606, 2010.

[123] Hamdan, M. and Elnajjar, E. Thermodynamic analytical model of a loop heat pipe. *Heat and Mass Transfer*, 46(2):167–173, 2009.

[124] Coquard, T. *Transferts couplés de masse et de chaleur dans un élément d'évaporateur capillaire.* PhD thesis, Institut National Polytechnique de Toulouse, 2006.

[125] Louriou, C. *Modélisation instationnaire des transferts de masse et de chaleur au sein des évaporateurs capillaires.* PhD thesis, Institut National Polytechnique de Toulouse, 2010.

[126] Zhao, T. and Liao, Q. On capillary-driven flow and phase-change heat transfer in a porous structure heated by a finned surface: measurements and modeling. *International Journal of Heat and Mass Transfer*, 43(7):1141–1155, 2000.

[127] Chernysheva, M. and Maydanik, Y. Heat and mass transfer in evaporator of loop heat pipe. *Journal of Thermophysics and Heat Transfer*, 23(4):725–731, 2009.

[128] Li, J. and Peterson, G. 3D heat transfer analysis in a loop heat pipe evaporator with a fully saturated wick. *International Journal of Heat and Mass Transfer*, 54(1):564–574, 2011.

[129] Demidov, A. and Yatsenko, E. Investigation of heat and mass transfer in the evaporation zone of a heat pipe operating by the ' inverted meniscus' principle. *International Journal of Heat and Mass Transfer*, 37(14):2155–2163, 1994.

[130] Chernysheva, M. A. and Maydanik, Y. F. 3D-model for heat and mass transfer simulation in flat evaporator of copper-water loop heat pipe. *Applied Thermal Engineering*, 33-34:124–134, 2012. ISSN 13594311.

[131] Chernysheva, M. A., Pastukhov, V. G., and Maydanik, Y. F. Analysis of heat exchange in the compensation chamber of a loop heat pipe. *Energy*, 55:253–262, 2013.

[132] Maydanik, Y. F., Fershtater, Y. G., and Solodovnik, N. N. Loop heat pipes: Design, investigation, prospects of use in aerospace technics. Technical Report 941185, SAE International, Warrendale, PA, 1994.

[133] Cao, Y. and Faghri, A. Analytical solutions of flow and heat transfer in a porous structure with partial heating and evaporation on the upper surface. *International Journal of Heat and Mass Transfer*, 37(10):1525–1533, 1994.

[134] Furukawa, M. Model-based method of theoretical design analysis of a loop heat pipe. *Journal of Thermophysics and Heat Transfer*, 20(1):111–121, 2006.

[135] Boo, J. H. and Jung, E. G. A theoretical modeling of a loop heat pipe with a flat evaporator employing the thin-film theory. In 15th *International Heat Pipe Conference*, Clemson, South Carolina (USA), 2010.

[136] Delil, A., Baturkin, V., Gorbenko, G., Gakal, P., and Ruzaykin, V. Modelling of a miniature loop heat pipe with a flat evaporator. In *Proceedings of the* 32nd *International Conference on Environmental Systems*, 2002.

[137] Hoang, T. T. and Ku, J. Heat and mass transfer in loop heat pipes. In *ASME Summer Heat Transfer Conference*, pages 485–493, Las Vegas, Nevada (USA), 2003.

[138] Hoang, T. T., O'Connell, T., and Ku, J. Mathematical modeling of loop heat pipes with multiple capillary pumps and multiple condensers, Part I - steady state simulations. In 2nd *International Energy Conversion Engineering Conference*, AIAA Paper 2004-5577, Providence, Rhode Island (USA), 2004.

[139] Atabaki, N. *Experimental and computational studies of loop heat pipes.* PhD thesis, McGill University, Montréal, Québec, Canada, 2006.

[140] Jesuthasan, N. *Modeling of Thermofluid Phenomena in Segmented Network Simulations of Loop Heat Pipes*. PhD thesis, McGill University, Montréal, Québec, Canada, 2011.

[141] Bai, L., Lin, G., Mu, Z., and Wen, D. Theoretical analysis of steady-state performance of a loop heat pipe with a novel evaporator. *Applied Thermal Engineering*, 64(1–2): 233–241, 2014.

[142] Mishkinis, D. and Ochterbeck, J. Homogeneous nucleation and the heat-pipe boiling limitation. *Journal of Engineering Physics and Thermophysics*, 76(4):813–818, 2003.

[143] Launay, S. and Mekni, N. Specifically designd loop heat pipe for quantitative characterisation. In 15^{th} *International Heat Pipe Conference*, Clemson, South Carolina (USA), 2010.

[144] Lefèvre, F. and Lallemand, M. Coupled thermal and hydrodynamic models of flat micro heat pipes for the cooling of multiple electronic components. *International Journal of Heat and Mass Transfer*, 49(7-8):1375–1383, 2006.

[145] Lips, S. and Lefèvre, F. A general analytical model for the design of conventional heat pipes, *to be published. International Journal of Heat and Mass Transfer*, 2014.

[146] Eames, I., Marr, N., and Sabir, H. The evaporation coefficient of water: a review. *International Journal of Heat and Mass Transfer*, 40(12):2963–2973, 1997.

[147] Shabgard, H. and Faghri, A. Performance characteristics of cylindrical heat pipes with multiple heat sources. *Applied Thermal Engineering*, 31(16):3410–3419, 2011.

[148] Incropera, F. P. and DeWitt, D. P. *Fundamentals of heat and mass transfer*. John Wiley & Sons, Purdue University, Indiana (USA), 1996.

[149] Launay, S., Sartre, V., and Bonjour, J. Effect of fluid thermophysical properties on loop heat pipe operation. In 14^{th} *International Heat Pipe Conference*, Florianópolis, Brazil, 2007.

[150] Chuang, P.-Y. A., Cimbala, J. M., and Brenizer, J. S. Experimental and analytical study of a loop heat pipe at a positive elevation using neutron radiography. *International Journal of Thermal Sciences*, 77:84–95, 2014.

[151] Cheung, K. H., Hoang, T., Ku, J., and Kaya, T. Thermal performance and operational characteristics of loop heat pipe (NRL LHP). *SAE paper*, (981813), 1998.

[152] Vershinin, S. V. and Maydanik, Y. F. Hysteresis phenomena in loop heat pipes. *Applied Thermal Engineering*, 27(5-6):962–968, 2007.

[153] Rainey, K. N., You, S. M., and Lee, S. Effect of pressure, subcooling, and dissolved gas on pool boiling heat transfer from microporous, square pin-finned surfaces in FC-72. *International Journal of Heat and Mass Transfer*, 46(1):23–35, 2003.

[154] He, J., Lin, G., Bai, L., Miao, J., Zhang, H., and Wang, L. Effect of non-condensable gas on startup of a loop thermosyphon. *International Journal of Thermal Sciences*, 72: 184–194, 2013.

[155] Maydanik, Y., Vershinin, S., Chernysheva, M., and Yushakova, S. Investigation of a compact copper–water loop heap pipe with a flat evaporator. *Applied Thermal Engineering*, 31(16):3533–3541, 2011.

[156] Médéric, B., Miscevic, M., Platel, V., Lavieille, P., and Joly, J.-L. Experimental study of flow characteristics during condensation in narrow channels: the influence of the diameter channel on structure patterns. *Superlattices and Microstructures*, 35(3–6): 573–586, 2004.

[157] Médéric, B., Lavieille, P., and Miscevic, M. Void fraction invariance properties of condensation flow inside a capillary glass tube. *International Journal of Multiphase Flow*, 31(9):1049–1058, 2005.

[158] Louahlia-Gualous, H. and Mecheri, B. Unsteady steam condensation flow patterns inside a miniature tube. *Applied Thermal Engineering*, 27(8–9):1225–1235, 2007.

[159] Birdi, K. S., Vu, D. T., and Winter, A. A study of the evaporation rates of small water drops placed on a solid surface. *The Journal of physical chemistry*, 93(9):3702–3703, 1989.

[160] Bernardin, J. D., Mudawar, I., Walsh, C. B., and Franses, E. I. Contact angle temperature dependence for water droplets on practical aluminum surfaces. *International journal of heat and mass transfer*, 40(5):1017–1033, 1997.

[161] Churchill, S. W. and Chu, H. H. Correlating equations for laminar and turbulent free convection from a horizontal cylinder. *International Journal of Heat and Mass Transfer*, 18(9):1049–1053, 1975.

[162] Soliman, H. M. On the annular-to-wavy flow pattern transition during condensation inside horizontal tubes. *The Canadian Journal of Chemical Engineering*, 60(4):475–481, 1982.

[163] Hanlon, M. A. and Ma, H. B. Evaporation heat transfer in sintered porous media. *Journal of Heat Transfer*, 125(4):644–652, 2003.

[164] Miscevic, M., El Achkar, G., Lavieille, P., Kaled, A., and Dutour, S. About flow regime and heat transfer in low diameter condenser of LHP and CPL. In 16^{th} *International Heat Pipe Conference*, Lyon, France, 2012.

[165] Tavman, I. Effective thermal conductivity of granular porous materials. *International Communications in Heat and Mass Transfer*, 23(2):169–176, 1996.

[166] Živcová, Z., Gregorová, E., Pabst, W., Smith, D. S., Michot, A., and Poulier, C. Thermal conductivity of porous alumina ceramics prepared using starch as a pore-forming agent. *Journal of the European Ceramic Society*, 29(3):347–353, 2009.

[167] Carson, J. K., Lovatt, S. J., Tanner, D. J., and Cleland, A. C. Thermal conductivity bounds for isotropic, porous materials. *International Journal of Heat and Mass Transfer*, 48(11):2150–2158, 2005.

Appendix A

Effective thermal conductivity of a saturated porous medium

The effective thermal conductivity of a porous medium saturated with liquid is very difficult to predict theoretically since it depends on numerous parameters, such as the thermal properties of both phases and the microstructure geometry. Extensive studies have been conducted to develop correlations to predict the effective thermal conductivity λ_{eff} of a porous medium saturated with liquid, based on its thermophysic properties and its geometrical characteristics. Table A.1 summarizes some of these relationships.

Author/Name	Correlation	Validity
Parallel [165]	$\lambda_{\text{eff}} = \varepsilon\lambda_{\text{l}} + (1-\varepsilon)\,\lambda_{\text{w}}$	All geometries
Series [165]	$\lambda_{\text{eff}} = \dfrac{\lambda_{\text{l}}\lambda_{\text{w}}}{\varepsilon\lambda_{\text{l}} + (1-\varepsilon)\,\lambda_{\text{w}}}$	All geometries
Alexander [70]	$\lambda_{\text{eff}} = \lambda_{\text{l}}\left(\dfrac{\lambda_{\text{w}}}{\lambda_{\text{l}}}\right)^{(1-\varepsilon)^{0.59}}$	Layer of sintered wick screens
Maxwell [69]	$\lambda_{\text{eff}} = \lambda_{\text{l}}\dfrac{\lambda_{\text{w}} + 2\lambda_{\text{l}} + 2\varepsilon\,(\lambda_{\text{w}} - \lambda_{\text{l}})}{\lambda_{\text{w}} + 2\lambda_{\text{l}} - \varepsilon\,(\lambda_{\text{w}} - \lambda_{\text{l}})}$	Homogeneous particle suspension in a liquid
Zivcova [166]	$\lambda_{\text{eff}} = \lambda_{\text{w}}\exp\left(-\dfrac{1.5\varepsilon}{1-\varepsilon}\right)$	Ceramics with a pore-forming agent
EMT [167]	$\lambda_{\text{eff}} = \dfrac{1}{4}\Big((3\varepsilon-1)\,\lambda_{\text{l}} + [3\,(1-\varepsilon)-1]\,\lambda_{\text{w}} + \sqrt{((3\varepsilon-1)\,\lambda_{\text{l}} + [3\,(1-\varepsilon)-1]\,\lambda_{\text{w}})^2 + 8\lambda_{\text{l}}\lambda_{\text{w}}}\Big)$	All geometries

Lavochkin [94]	$\lambda_{\text{eff}} = \dfrac{(1-\varepsilon)\,\lambda_{\text{w}}}{1+11\varepsilon^2}$	Metallic meshes
Assad [69]	$\lambda_{\text{eff}} = \lambda_{\text{w}}\left(\dfrac{\lambda_{\text{l}}}{\lambda_{\text{w}}}\right)^{\varepsilon}$	Unconsolidated solids
Chaudhary-Bhandari[1] [69]	$\lambda_{\text{eff}} = \left(\varepsilon\lambda_{\text{l}} + (1-\varepsilon)\,\lambda_{\text{w}}\right)^n \left(\dfrac{\lambda_{\text{l}}\lambda_{\text{w}}}{\varepsilon\lambda_{\text{w}} + (1-\varepsilon)}\right)^{1-n}$	All geometries
Krupiczka [165]	$\lambda_{\text{eff}} = \lambda_{\text{l}}\left(\dfrac{\lambda_{\text{w}}}{\lambda_{\text{l}}}\right)^{0.28-0.757\log(\varepsilon)-0.057\log\frac{\lambda_{\text{w}}}{\lambda_{\text{l}}}}$	$0.215 \leq \varepsilon \leq 0.476$
Russell [69]	$\lambda_{\text{eff}} = \lambda_{\text{w}}\left[\dfrac{\varepsilon^{\frac{2}{3}} + \frac{\lambda_{\text{w}}}{\lambda_{\text{l}}}\left(1-\varepsilon^{\frac{2}{3}}\right)}{\varepsilon^{\frac{2}{3}} - \varepsilon + \frac{\lambda_{\text{w}}}{\lambda_{\text{l}}}\left(1-\varepsilon^{\frac{2}{3}}+\varepsilon\right)}\right]$	Continuous solid phase and $\varepsilon \leq 0.5$
Eucken [69]	$\lambda_{\text{eff}} = \lambda_{\text{w}}\dfrac{1+2\varepsilon\frac{1-\lambda_{\text{w}}/\lambda_{\text{l}}}{2\lambda_{\text{w}}/\lambda_{\text{l}}+1}}{1-\varepsilon\frac{1-\lambda_{\text{w}}/\lambda_{\text{l}}}{2\lambda_{\text{w}}/\lambda_{\text{l}}+1}}$	Continuous solid phase and $\varepsilon \leq 0.5$
Zehner-Schlünder [69]	$\lambda_{\text{eff}} = \lambda_{\text{l}}\left(1-(1-\varepsilon)^{\frac{1}{2}} + \dfrac{2(1-\varepsilon)^{\frac{1}{2}}}{1-\frac{\lambda_{\text{l}}}{\lambda_{\text{w}}}B} \times\left[\dfrac{\left(1-\frac{\lambda_{\text{l}}}{\lambda_{\text{w}}}\right)B}{\left(1-\frac{\lambda_{\text{l}}}{\lambda_{\text{w}}}B\right)^2}\ln\left(\dfrac{\lambda_{\text{w}}}{\lambda_{\text{l}}B}\right) - \dfrac{B+1}{2} - \dfrac{B-1}{1-\frac{\lambda_{\text{l}}}{\lambda_{\text{w}}}B}\right]\right)$ with $B = 1.25\left(\dfrac{1-\varepsilon}{\varepsilon}\right)^{\frac{10}{9}}$	Packed bed of spherical particles

Table A.1: Correlations for the effective thermal conductivity of a porous medium

Although these correlations were developed for various configurations and may not be valid for all geometrical characteristics nor for every liquid and solid material, a comparison is presented in Figure A.1. The results show an extremely large scattering of the numerical data. This shows the difficulty to chose a correlation in the case of LHP modelling. Indeed, the only valid method to determine the effective thermal conductivity of a porous medium remains the experimental analysis.

---

[1] For the correlation of Chaudhary and Bandhari, the value of the coefficient n is between 0.42 and 0.51. A value of $n = 0.51$ is chosen for the numerical applications.

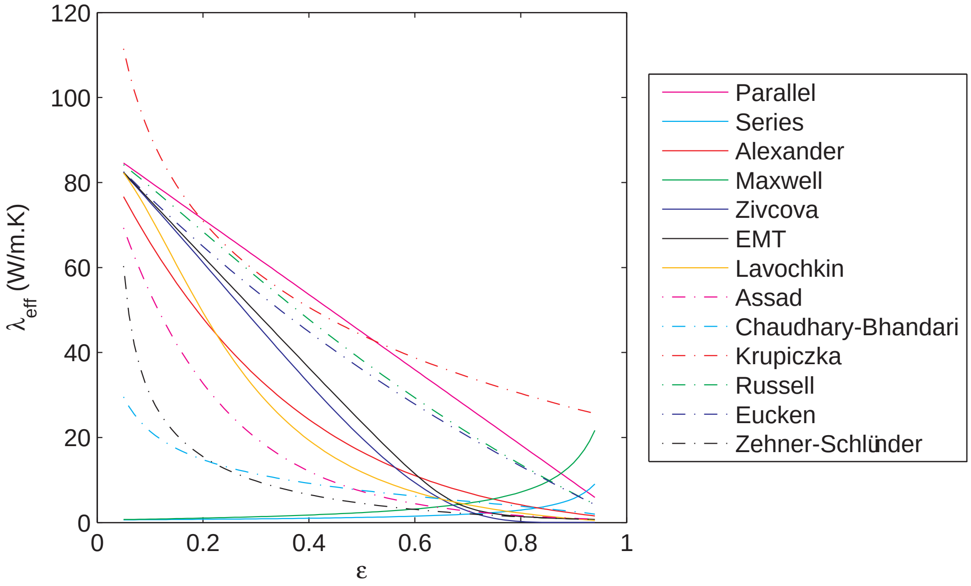

(a) Dependence on the wick porosity – $\lambda_\mathrm{l} = 0.6\,\mathrm{W \cdot m^{-1} \cdot K^{-1}}$ and $\lambda_\mathrm{w} = 89\,\mathrm{W \cdot m^{-1} \cdot K^{-1}}$

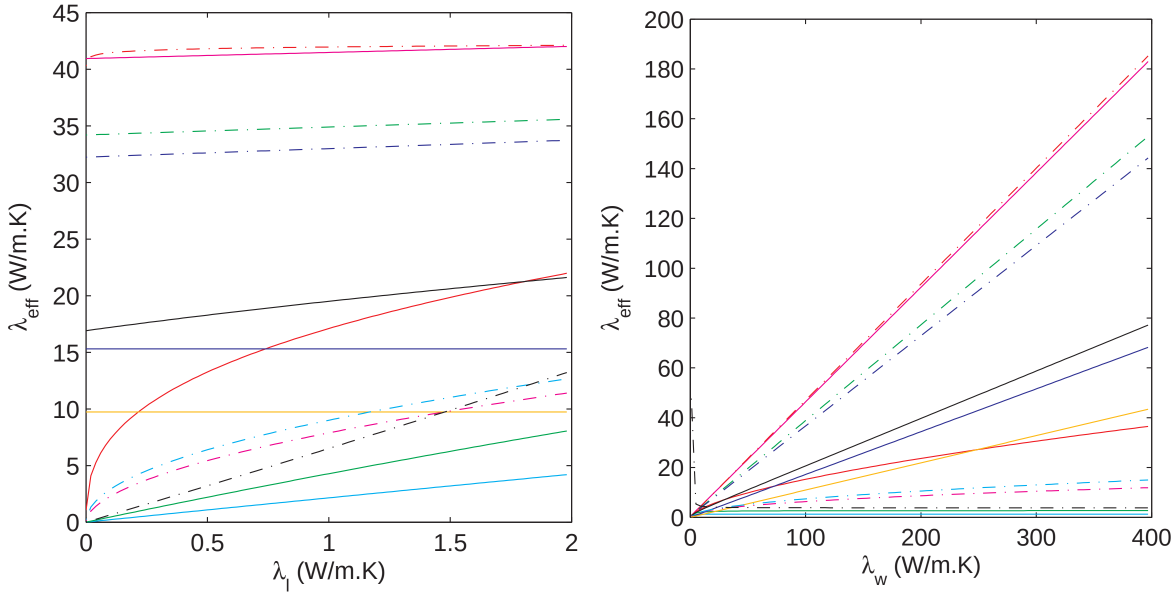

(b) Dependence on the liquid conductivity $\varepsilon = 54\,\%$ and $\lambda_\mathrm{w} = 89\,\mathrm{W \cdot m^{-1} \cdot K^{-1}}$

(c) Dependence on the solid conductivity $\varepsilon = 54\,\%$ and $\lambda_\mathrm{l} = 0.6\,\mathrm{W \cdot m^{-1} \cdot K^{-1}}$

Figure A.1: Comparison of the various correlations for the effective thermal conductivity

Appendix B

Detailed expression of the coefficients defined in the analytical model

Coefficients used in the 2D model of the wick

$$K_1 = S_{\mathrm{w}} \frac{a_0 + a_1}{2a} \left(-\frac{\lambda_{\mathrm{eff}}}{b} + \dot{m}_{\mathrm{l}} c_{\mathrm{p,l}} \frac{6}{\pi D_{\mathrm{w}}^2} \right) \tag{B.1}$$

$$\begin{aligned} K_2 = S_{\mathrm{w}} \Bigg[\sum_{m=1}^{\infty} & \left(2 \frac{\lambda_{\mathrm{eff}}}{a_1 - a_0} \frac{1}{m^2 \pi^2} \sin\left(m\pi \frac{a_0 + a_1}{2a} \right) \left(\cos\left(\frac{m\pi a_0}{a} \right) - \cos\left(\frac{m\pi a_1}{a} \right) \right) \right. \\ & \qquad \left. \left(\left(1 - e^{2m\pi B} \right)^{-1} - \left(1 - e^{-2m\pi B} \right)^{-1} \right) \right) \\ & + \frac{a_0 + a_1}{2a} \left(\frac{\lambda_{\mathrm{eff}}}{b} \left(1 - \frac{a_0 + a_1}{2a} \right) - \dot{m}_{\mathrm{l}} c_{\mathrm{p,l}} \frac{6}{\pi D_{\mathrm{w}}^2} \right) \Bigg] \end{aligned} \tag{B.2}$$

$$\begin{aligned} K_3 = -S_{\mathrm{w}} \Bigg[\sum_{m=1}^{\infty} & \left(2 \frac{\lambda_{\mathrm{eff}}}{a_1 - a_0} \frac{1}{m^2 \pi^2} \sin\left(m\pi \frac{a_0 + a_1}{2a} \right) \left(\cos\left(\frac{m\pi a_0}{a} \right) - \cos\left(\frac{m\pi a_1}{a} \right) \right) \right. \\ & \qquad \left. \left(\left(1 - e^{2m\pi B} \right)^{-1} - \left(1 - e^{-2m\pi B} \right)^{-1} \right) \right) \\ & - \frac{\lambda_{\mathrm{eff}}}{b} \left(\frac{a_0 + a_1}{2a} \right)^2 \Bigg] \end{aligned} \tag{B.3}$$

$$K_4 = S_{\mathrm{w}} \left(1 - \frac{a_0 + a_1}{2a} \right) \left(\frac{\lambda_{\mathrm{eff}}}{b} - \dot{m}_{\mathrm{l}} c_{\mathrm{p,l}} \frac{6}{\pi D_{\mathrm{w}}^2} \right) \tag{B.4}$$

$$\begin{aligned} K_5 = S_{\mathrm{w}} \Bigg[\sum_{m=1}^{\infty} & \left(2 \frac{\lambda_{\mathrm{eff}}}{a_1 - a_0} \frac{1}{m^2 \pi^2} \sin\left(m\pi \frac{a_0 + a_1}{2a} \right) \left(\cos\left(\frac{m\pi a_0}{a} \right) - \cos\left(\frac{m\pi a_1}{a} \right) \right) \right. \\ & \qquad \left. \left(\left(1 - e^{2m\pi B} \right)^{-1} - \left(1 - e^{-2m\pi B} \right)^{-1} \right) \right) \\ & - \left(1 - \frac{a_0 + a_1}{2a} \right) \left(\frac{\lambda_{\mathrm{eff}}}{b} \left(1 - \frac{a_0 + a_1}{2a} \right) - \dot{m}_{\mathrm{l}} c_{\mathrm{p,l}} \frac{6}{\pi D_{\mathrm{w}}^2} \right) \Bigg] \end{aligned} \tag{B.5}$$

$$
\begin{aligned}
K_6 = -S_{\mathrm{w}} \Bigg[\sum_{m=1}^{\infty} \bigg(& 2 \frac{\lambda_{\mathrm{eff}}}{a_1 - a_0} \frac{1}{m^2 \pi^2} \sin\left(m\pi \frac{a_0 + a_1}{2a} \right) \left(\cos\left(\frac{m\pi a_0}{a} \right) - \cos\left(\frac{m\pi a_1}{a} \right) \right) \\
& \left(\left(1 - e^{2m\pi B}\right)^{-1} - \left(1 - e^{-2m\pi B}\right)^{-1} \right) \\
+ \frac{\lambda_{\mathrm{eff}}}{b} \frac{a_0 + a_1}{2a} & \left(1 - \frac{a_0 + a_1}{2a} \right) \Bigg]
\end{aligned}
\tag{B.6}
$$

Coefficients used in the 2D model of the flat casing

$$
\begin{aligned}
K_7 = {} & h_{\mathrm{ext}} \pi \frac{c_1^2}{2} \left(\frac{-\frac{c_0 + c_1}{2c} + 1}{Bi_{\mathrm{b}} + 1} \right) \\
& - \sum_{m=1}^{\infty} \Bigg(2\lambda_{\mathrm{b}} \frac{c}{c_1 - c_0} \frac{1}{m^2 \pi^2} \left(\cos\left(\frac{m\pi c_0}{c} \right) - \cos\left(\frac{m\pi c_1}{c} \right) \right) \\
& \Bigg[\left(c_0 \pi \sin\left(\frac{m\pi c_1}{c} \right) \left(e^{m\pi D} - 1 \right) + \frac{\pi h_{\mathrm{ext}}}{\lambda_{\mathrm{b}}} \left(-\frac{c^2}{m^2\pi^2} + \frac{c^2}{m^2\pi^2} \cos\left(\frac{m\pi c_1}{c} \right) + \frac{c_1 c}{m\pi} \sin\left(\frac{m\pi c_1}{c} \right) \right) \right) \\
& \left(e^{m\pi D} + e^{-m\pi D} \frac{m\pi D + Bi_{\mathrm{b}}}{m\pi D - Bi_{\mathrm{b}}} \right)^{-1} \\
& + \left(-c_0 \pi \sin\left(\frac{m\pi c_1}{c} \right) \left(e^{-m\pi D} - 1 \right) + \frac{\pi h_{\mathrm{ext}}}{\lambda_{\mathrm{b}}} \left(-\frac{c^2}{m^2\pi^2} + \frac{c^2}{m^2\pi^2} \cos\left(\frac{m\pi c_1}{c} \right) + \frac{c_1 c}{m\pi} \sin\left(\frac{m\pi c_1}{c} \right) \right) \right) \\
& \left(e^{-m\pi D} + e^{+m\pi D} \frac{m\pi D - Bi_{\mathrm{b}}}{m\pi D + Bi_{\mathrm{b}}} \right)^{-1} \Bigg] \Bigg)
\end{aligned}
\tag{B.7}
$$

$$
\begin{aligned}
K_8 = {} & h_{\mathrm{ext}} \pi \frac{c_1^2}{2} \frac{c_0 + c_1}{2c} \frac{1}{Bi_{\mathrm{b}} + 1} \\
& + \sum_{m=1}^{\infty} \Bigg(2\lambda_{\mathrm{b}} \frac{c}{c_1 - c_0} \frac{1}{m^2 \pi^2} \left(\cos\left(\frac{m\pi c_0}{c} \right) - \cos\left(\frac{m\pi c_1}{c} \right) \right) \\
& \Bigg[\left(c_0 \pi \sin\left(\frac{m\pi c_1}{c} \right) \left(e^{m\pi D} - 1 \right) + \frac{\pi h_{\mathrm{ext}}}{\lambda_{\mathrm{b}}} \left(-\frac{c^2}{m^2\pi^2} + \frac{c^2}{m^2\pi^2} \cos\left(\frac{m\pi c_1}{c} \right) + \frac{c_1 c}{m\pi} \sin\left(\frac{m\pi c_1}{c} \right) \right) \right) \\
& \left(\left(e^{m\pi D} + e^{-m\pi D} \frac{m\pi D + Bi_{\mathrm{b}}}{m\pi D - Bi_{\mathrm{b}}} \right)^{-1} \right) \\
& + \left(c_0 \pi \sin\left(\frac{m\pi c_1}{c} \right) \left(e^{-m\pi D} - 1 \right) + \frac{\pi h_{\mathrm{ext}}}{\lambda_{\mathrm{b}}} \left(-\frac{c^2}{m^2\pi^2} + \frac{c^2}{m^2\pi^2} \cos\left(\frac{m\pi c_1}{c} \right) + \frac{c_1 c}{m\pi} \sin\left(\frac{m\pi c_1}{c} \right) \right) \right) \\
& \left(e^{-m\pi D} + e^{+m\pi D} \frac{m\pi D - Bi_{\mathrm{b}}}{m\pi D + Bi_{\mathrm{b}}} \right)^{-1} \Bigg] \Bigg)
\end{aligned}
\tag{B.8}
$$

$$
\begin{aligned}
K_9 &= h_{\mathrm{ext}}\pi\frac{c_1^2}{2}\left(\frac{\phi_0 d}{\lambda_{\mathrm{b}}}\frac{c_0\phi_{\mathrm{in}}}{c\phi_0}-\frac{1}{Bi_{\mathrm{b}}+1}T_{\mathrm{ext}}\right)\\
&\quad+\sum_{m=1}^{\infty}\Bigg(2\phi_{\mathrm{in}}c\frac{1}{m^2\pi^2}\sin\left(\frac{m\pi c_0}{c}\right)\\
&\quad\Bigg[\Bigg(-c_0\pi\sin\left(\frac{m\pi c_1}{c}\right)\left(e^{m\pi D}-1\right)-\frac{\pi h_{\mathrm{ext}}}{\lambda_{\mathrm{b}}}\Bigg(-\frac{c^2}{m^2\pi^2}+\frac{c^2}{m^2\pi^2}\cos\left(\frac{m\pi c_1}{c}\right)+\frac{c_1c}{m\pi}\sin\left(\frac{m\pi c_1}{c}\right)\Bigg)\Bigg)\\
&\quad\Bigg(\left(1+e^{2m\pi D}\right)^{-1}\Bigg)\\
&\quad+\Bigg(-c_0\pi\sin\left(\frac{m\pi c_1}{c}\right)\left(e^{-m\pi D}-1\right)+\frac{\pi h_{\mathrm{ext}}}{\lambda_{\mathrm{b}}}\Bigg(-\frac{c^2}{m^2\pi^2}+\frac{c^2}{m^2\pi^2}\cos\left(\frac{m\pi c_1}{c}\right)+\frac{c_1c}{m\pi}\sin\left(\frac{m\pi c_1}{c}\right)\Bigg)\Bigg)\\
&\quad\left(1+e^{-2m\pi D}\right)^{-1}\Bigg]\Bigg)
\end{aligned}
\tag{B.9}
$$

$$
\begin{aligned}
K_{10} &= h_{\mathrm{ext}}\pi\frac{c_1^2}{2}\left(\frac{-\frac{c_0+c_1}{2c}+1}{Bi_{\mathrm{b}}+1}\right)\\
&\quad-\sum_{m=1}^{\infty}\Bigg(2\lambda_{\mathrm{b}}\frac{c}{c_1-c_0}\frac{1}{m^2\pi^2}\left(\cos\left(\frac{m\pi c_0}{c}\right)-\cos\left(\frac{m\pi c_1}{c}\right)\right)\\
&\qquad\times\frac{\pi h_{\mathrm{ext}}}{\lambda_{\mathrm{b}}}\left(-\frac{c^2}{m^2\pi^2}+\frac{c^2}{m^2\pi^2}\cos\left(\frac{m\pi c_1}{c}\right)+\frac{c_1c}{m\pi}\sin\left(\frac{m\pi c_1}{c}\right)\right)\\
&\qquad\times\left[\left(e^{m\pi D}+e^{-m\pi D}\frac{m\pi D+Bi_{\mathrm{b}}}{m\pi D-Bi_{\mathrm{b}}}\right)^{-1}+\left(e^{-m\pi D}+e^{+m\pi D}\frac{m\pi D-Bi_{\mathrm{b}}}{m\pi D+Bi_{\mathrm{b}}}\right)^{-1}\right]\Bigg)
\end{aligned}
\tag{B.10}
$$

$$
\begin{aligned}
K_{11} &= h_{\mathrm{ext}}\pi\frac{c_1^2}{2}\frac{c_0+c_1}{2c}\frac{1}{Bi_{\mathrm{b}}+1}\\
&\quad+\sum_{m=1}^{\infty}\Bigg(2\lambda_{\mathrm{b}}\frac{c}{c_1-c_0}\frac{1}{m^2\pi^2}\left(\cos\left(\frac{m\pi c_0}{c}\right)-\cos\left(\frac{m\pi c_1}{c}\right)\right)\\
&\qquad\times\frac{\pi h_{\mathrm{ext}}}{\lambda_{\mathrm{b}}}\left(-\frac{c^2}{m^2\pi^2}+\frac{c^2}{m^2\pi^2}\cos\left(\frac{m\pi c_1}{c}\right)+\frac{c_1c}{m\pi}\sin\left(\frac{m\pi c_1}{c}\right)\right)\\
&\qquad\times\left[\left(e^{m\pi D}+e^{-m\pi D}\frac{m\pi D+Bi_{\mathrm{b}}}{m\pi D-Bi_{\mathrm{b}}}\right)^{-1}+\left(e^{-m\pi D}+e^{+m\pi D}\frac{m\pi D-Bi_{\mathrm{b}}}{m\pi D+Bi_{\mathrm{b}}}\right)^{-1}\right]\Bigg)
\end{aligned}
\tag{B.11}
$$

$$
\begin{aligned}
K_{12} &= h_{\mathrm{ext}}\pi\frac{c_1^2}{2}\left(\frac{\phi_0 d}{\lambda_{\mathrm{b}}}\frac{c_0\phi_{\mathrm{in}}}{c\phi_0}-\frac{1}{Bi_{\mathrm{b}}+1}T_{\mathrm{ext}}\right)\\
&\quad-\sum_{m=1}^{\infty}\Bigg(2\phi_{\mathrm{in}}c\frac{1}{m^2\pi^2}\sin\left(\frac{m\pi c_0}{c}\right)\frac{\pi h_{\mathrm{ext}}}{\lambda_{\mathrm{b}}}\left(-\frac{c^2}{m^2\pi^2}+\frac{c^2}{m^2\pi^2}\cos\left(\frac{m\pi c_1}{c}\right)+\frac{c_1c}{m\pi}\sin\left(\frac{m\pi c_1}{c}\right)\right)\\
&\qquad\times\left[\left(1+e^{2m\pi D}\right)^{-1}-\left(1+e^{-2m\pi D}\right)^{-1}\right]\Bigg)
\end{aligned}
\tag{B.12}
$$

Coefficients used in the 3D model of the cylindrical casing

$$
\begin{aligned}
K_7 &= \frac{Bi_{\mathrm{b}}}{Bi_{\mathrm{b}}+1}d\lambda_{\mathrm{b}}c_0\frac{2c-c_0-c_1}{2c}\\
&\quad+\sum_{m=1}^{\infty}\frac{2d}{m^2\pi^2}\lambda_{\mathrm{b}}\frac{c}{c_0-c_1}\frac{\cos\left(m\pi\frac{c_1}{c}\right)-\cos\left(m\pi\frac{c_0}{c}\right)}{\left(E\pi m+Bi_{\mathrm{b}}\right)e^{E\pi m}+\left(E\pi m-Bi_{\mathrm{b}}\right)e^{-E\pi m}}\\
&\qquad\times\left(-2Bi_{\mathrm{b}}\sin\left(m\pi\frac{c_0}{c}\right)+\sin\left(m\pi\frac{c_1}{c}\right)\left(2Bi_{\mathrm{b}}-\left(E\pi m+Bi_{\mathrm{b}}\right)e^{E\pi m}+\left(E\pi m-Bi_{\mathrm{b}}\right)e^{-E\pi m}\right)\right)
\end{aligned}
\tag{B.13}
$$

$$\begin{aligned}
K_8 = {} & \frac{Bi_\mathrm{b}}{Bi_\mathrm{b}+1} d\lambda_\mathrm{b} c_0 \frac{c_0+c_1}{2c} \\
& + \sum_{m=1}^{\infty} \frac{2d}{m^2\pi^2} \lambda_\mathrm{b} \frac{c}{c_0-c_1} \frac{\cos\left(m\pi\frac{c_1}{c}\right) - \cos\left(m\pi\frac{c_0}{c}\right)}{\left(E\pi m + Bi_\mathrm{b}\right) e^{E\pi m} + \left(E\pi m - Bi_\mathrm{b}\right) e^{-E\pi m}} \\
& \quad \times \left(2Bi_\mathrm{b} \sin\left(m\pi\frac{c_0}{c}\right) - \sin\left(m\pi\frac{c_1}{c}\right) \left(2Bi_\mathrm{b} - \left(E\pi m + Bi_\mathrm{b}\right) e^{E\pi m} + \left(E\pi m - Bi_\mathrm{b}\right) e^{-E\pi m}\right)\right)
\end{aligned} \tag{B.14}$$

$$\begin{aligned}
K_9 = {} & \frac{Bi_\mathrm{b}}{Bi_\mathrm{b}+1} \left(-\lambda_\mathrm{b} \frac{c_0 d}{e} T_\mathrm{ext} + \left(Bi_\mathrm{b}+1\right) \frac{c_0^2}{c} d_0 \phi_\mathrm{in}\right) \\
& - \sum_{m=1}^{\infty} \frac{2d_0}{m^3\pi^3} Bi_\mathrm{b} \phi_\mathrm{in} \frac{c^2}{e} \sin^2\left(m\pi\frac{c_0}{c}\right) \frac{1-e^{2E\pi m}}{1+e^{2E\pi m}} \\
& \quad + \frac{2cd_0}{m^2\pi^2} \phi_\mathrm{in} \sin\left(m\pi\frac{c_0}{c}\right) \sin\left(m\pi\frac{c_1}{c}\right) \left(1 - 2\frac{e^{E\pi m}}{1+e^{2E\pi m}}\right)
\end{aligned} \tag{B.15}$$

$$\begin{aligned}
K_{10} = {} & \frac{Bi_\mathrm{b}}{Bi_\mathrm{b}+1} d\lambda_\mathrm{b} c_0 \frac{2c-c_0-c_1}{2c} \\
& - \sum_{m=1}^{\infty} \frac{4d}{m^2\pi^2} \lambda_\mathrm{b} Bi_\mathrm{b} \frac{c}{c_0-c_1} \sin\left(m\pi\frac{c_0}{c}\right) \frac{\cos\left(m\pi\frac{c_1}{c}\right) - \cos\left(m\pi\frac{c_0}{c}\right)}{\left(E\pi m + Bi_\mathrm{b}\right) e^{E\pi m} + \left(E\pi m - Bi_\mathrm{b}\right) e^{-E\pi m}}
\end{aligned} \tag{B.16}$$

$$\begin{aligned}
K_{11} = {} & \frac{Bi_\mathrm{b}}{Bi_\mathrm{b}+1} d\lambda_\mathrm{b} c_0 \frac{c_0+c_1}{2c} \\
& + \sum_{m=1}^{\infty} \frac{4d}{m^2\pi^2} \lambda_\mathrm{b} Bi_\mathrm{b} \frac{c}{c_0-c_1} \sin\left(m\pi\frac{c_0}{c}\right) \frac{\cos\left(m\pi\frac{c_1}{c}\right) - \cos\left(m\pi\frac{c_0}{c}\right)}{\left(E\pi m + Bi_\mathrm{b}\right) e^{E\pi m} + \left(E\pi m - Bi_\mathrm{b}\right) e^{-E\pi m}}
\end{aligned} \tag{B.17}$$

$$\begin{aligned}
K_{12} = {} & \frac{Bi_\mathrm{b}}{Bi_\mathrm{b}+1} \left(-\lambda_\mathrm{b} \frac{c_0 d}{e} T_\mathrm{ext} + \left(Bi_\mathrm{b}+1\right) \frac{c_0^2}{c} d_0 \phi_\mathrm{in}\right) \\
& - \sum_{m=1}^{\infty} \frac{2d_0}{m^3\pi^3} Bi_\mathrm{b} \phi_\mathrm{in} \frac{c^2}{e} \sin^2\left(m\pi\frac{c_0}{c}\right) \frac{1-e^{2E\pi m}}{1+e^{2E\pi m}}
\end{aligned} \tag{B.18}$$

Coefficients used to express heat transfer in the condenser and the liquid line

$$K_{13} = \exp\left(\frac{-\pi\left(L_\mathrm{c} - L_{2\phi}\right)}{\dot{m}_\mathrm{l} c_\mathrm{p,l} \left(1/h_\mathrm{l} D_\mathrm{c,i} + 1/h_\mathrm{sink} D_\mathrm{c,o}\right)}\right) \exp\left(\frac{-\pi L_\mathrm{l}}{\dot{m}_\mathrm{l} c_\mathrm{p,l} \left(1/h_\mathrm{l} D_\mathrm{l,i} + 1/h_\mathrm{ext} D_\mathrm{l,o}\right)}\right) \tag{B.19}$$

$$\begin{aligned}
K_{14} = {} & \exp\left(\frac{-\pi L_\mathrm{l}}{\dot{m}_\mathrm{l} c_\mathrm{p,l} \left(1/h_\mathrm{l} D_\mathrm{l,i} + 1/h_\mathrm{ext} D_\mathrm{l,o}\right)}\right) \left(1 - \exp\left(\frac{-\pi\left(L_\mathrm{c} - L_{2\phi}\right)}{\dot{m}_\mathrm{l} c_\mathrm{p,l} \left(1/h_\mathrm{l} D_\mathrm{c,i} + 1/h_\mathrm{sink} D_\mathrm{c,o}\right)}\right)\right) T_\mathrm{sink} \\
& + \left(1 - \exp\left(\frac{-\pi L_\mathrm{l}}{\dot{m}_\mathrm{l} c_\mathrm{p,l} \left(1/h_\mathrm{l} D_\mathrm{l,i} + 1/h_\mathrm{ext} D_\mathrm{l,o}\right)}\right)\right) T_\mathrm{ext}
\end{aligned} \tag{B.20}$$

Second order equation for the determination of T_v

$$
\begin{aligned}
0 = {} & T_\mathrm{v}^2 \left[c_{\mathrm{p,l}} \left(1 - K_{13}\right) \left(K_6 \left(K_1 + K_2 + K_7\right) - \left(K_4 + K_5\right) \left(K_3 + K_8\right)\right.\right. \\
& \qquad \left.\left. + K_8 R_\mathrm{c}/S_\mathrm{c} \left(K_6 \left(K_1 + K_2\right) - K_3 \left(K_4 + K_5\right)\right)\right)\right] \\
& + T_\mathrm{v} \left[c_{\mathrm{p,l}} \left(1 - K_{13}\right) \left(\left(K_3 + K_8\right) K_4 \Delta T + \left(K_3 K_4 - K_1 K_6\right) K_8 \Delta T R_\mathrm{c}/S_\mathrm{c}\right.\right. \\
& \qquad \left. + K_6 \left(-K_1 \Delta T - K_7 \Delta T + K_9 - Q_\mathrm{in}\right)\right) \\
& \quad + \left(h_\mathrm{lv} - c_{\mathrm{p,l}} K_{14}\right) \left(K_6 \left(K_1 + K_2 + K_7 + K_8 \left(K_1 + K_2\right)\right)\right. \\
& \qquad \left. - \left(K_4 + K_5\right) \left(K_3 + K_8 + K_3 K_8 R_\mathrm{c}/S_\mathrm{c}\right)\right) \\
& \quad \left. + h_\mathrm{lv} \left(K_{11} \left(K_1 + K_2 + K_7 + K_3 K_7 R_\mathrm{c}/S_\mathrm{c}\right) - \left(K_3 + K_8 + K_3 K_8 R_\mathrm{c}/S_\mathrm{c}\right) \left(K_{10} + h_\mathrm{ext} S_\mathrm{r}\right)\right)\right] \\
& + c_{\mathrm{p,l}} K_{14} \left(K_6 \left(Q_\mathrm{in} - K_9\right) + \Delta T \left(K_6 \left(K_1 + K_7 + K_1 K_8 R_\mathrm{c}/S_\mathrm{c}\right) - K_4 \left(K_3 + K_8 + K_3 K_8 R_\mathrm{c}/S_\mathrm{c}\right)\right)\right) \\
& + h_\mathrm{lv} \Delta T \left(\left(K_3 + K_8\right) \left(K_4 + K_{10}\right) - \left(K_6 + K_{11}\right) \left(K_1 + K_7\right) + K_3 K_8 \left(K_4 + K_{10}\right) R_\mathrm{c}/S_\mathrm{c}\right. \\
& \qquad \left. - \left(K_3 K_7 K_{11} + K_1 K_6 K_8\right) R_\mathrm{c}/S_\mathrm{c}\right) \\
& + h_\mathrm{lv} \left(\left(K_3 + K_8 + K_3 K_8 R_\mathrm{c}/S_\mathrm{c}\right) \left(Q_\mathrm{in} - K_{12} + h_\mathrm{ext} S_\mathrm{r} \left(\Delta T + T_\mathrm{ext}\right)\right)\right. \\
& \qquad \left. - \left(K_6 + K_{11} + K_3 K_{11} R_\mathrm{c}/S_\mathrm{c}\right) \left(Q_\mathrm{in} - K_9\right)\right)
\end{aligned}
\tag{B.21}
$$

Appendix C

Alternative modelling of heat transfer between the wick and the reservoir

In the evaporator, heat transfer between the wick and the liquid bulk is not ideal and may thus be modelled using a heat transfer coefficient (Fourier's boundary condition). Therefore, the model of the wick is as presented in Figure C.1.

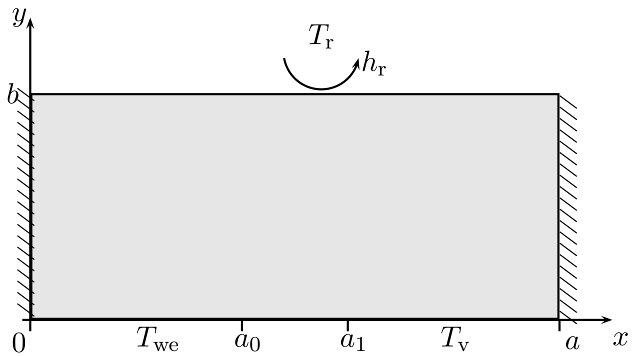

Figure C.1: Schematic of the alternative wick model

The boundary condition for $Y = 1$ is changed to:

$$\left.\frac{\partial T_\mathrm{w}^*}{\partial Y}\right|_{Y=1} = -Bi_\mathrm{w} T_\mathrm{w}^* \qquad \text{with} \qquad Bi_\mathrm{w} = \frac{b h_\mathrm{r}}{\lambda_\mathrm{eff}} \tag{C.1}$$

The other boundary conditions remain unchanged and the rest of the mathematical formulation is identical to the one presented in subsection 2.1.2.

A precise evaluation of the heat transfer coefficient h_r is very difficult. It depends on the thickness and the thermal conductivity of the liquid as well as the characteristics of the fluid flow in the liquid bulk (entrance of subcooled liquid from the liquid line, establishment of convective cells, presence of a bayonet). This parameter has then to be arbitrarily determined according to experimental results.

The non-dimensional temperature field is then:

$$\begin{aligned} T^*_{\mathrm{w}}(X,Y) &= A_{01}Y + A_{02} \\ &\quad + \sum_{m=1}^{\infty} \left(A_{\mathrm{m}1} e^{m\pi BY} + A_{\mathrm{m}2} e^{-m\pi BY} \right) \cos(m\pi X) \end{aligned} \tag{C.2}$$

with

$$A_{01} = -\frac{Bi_{\mathrm{w}}}{1+Bi_{\mathrm{w}}} \frac{\lambda_{\mathrm{eff}}}{\phi_0 b} \left(T_{\mathrm{v}} - T_{\mathrm{r}} + (T_{\mathrm{we}} - T_{\mathrm{v}}) \frac{a_0+a_1}{2a} \right) \tag{C.3}$$

$$A_{02} = \frac{\lambda_{\mathrm{eff}}}{\phi_0 b} \left(T_{\mathrm{v}} - T_{\mathrm{r}} + (T_{\mathrm{we}} - T_{\mathrm{v}}) \frac{a_0+a_1}{2a} \right) \tag{C.4}$$

$$A_{\mathrm{m}1} = 2\frac{\lambda_{\mathrm{eff}}}{\phi_0 b} \frac{T_{\mathrm{we}} - T_{\mathrm{v}}}{m^2\pi^2} \frac{a}{a_1 - a_0} \frac{\cos\left(m\pi \frac{a_0}{a}\right) - \cos\left(m\pi \frac{a_1}{a}\right)}{1 + \frac{m\pi B + Bi_{\mathrm{w}}}{m\pi B - Bi_{\mathrm{w}}} e^{2m\pi B}} \tag{C.5}$$

$$A_{\mathrm{m}2} = 2\frac{\lambda_{\mathrm{eff}}}{\phi_0 b} \frac{T_{\mathrm{we}} - T_{\mathrm{v}}}{m^2\pi^2} \frac{a}{a_1 - a_0} \frac{\cos\left(m\pi \frac{a_0}{a}\right) - \cos\left(m\pi \frac{a_1}{a}\right)}{1 + \frac{m\pi B - Bi_{\mathrm{w}}}{m\pi B + Bi_{\mathrm{w}}} e^{-2m\pi B}} \tag{C.6}$$

The K-coefficients K_1 to K_6 from Appendix B are then slightly modified to take into account h_{r}:

$$K_1 = S_{\mathrm{w}} \frac{a_0+a_1}{2a} \left(-\frac{\lambda_{\mathrm{eff}}}{b} \frac{Bi_{\mathrm{w}}}{1+Bi_{\mathrm{w}}} + \dot{m}_{\mathrm{l}} c_{\mathrm{p,l}} \frac{6}{\pi D_{\mathrm{w}}^2} \right) \tag{C.7}$$

$$\begin{aligned} K_2 = S_{\mathrm{w}} \Bigg[\sum_{m=1}^{\infty} & \left(2 \frac{\lambda_{\mathrm{eff}}}{a_1 - a_0} \frac{1}{m^2\pi^2} \sin\left(m\pi \frac{a_0+a_1}{2a} \right) \left(\cos\left(\frac{m\pi a_0}{a}\right) - \cos\left(\frac{m\pi a_1}{a}\right) \right) \right. \\ & \left. \left(\left(1 + e^{2m\pi B} \frac{m\pi B + Bi_{\mathrm{w}}}{m\pi B - Bi_{\mathrm{w}}} \right)^{-1} - \left(1 + e^{-2m\pi B} \frac{m\pi B - Bi_{\mathrm{w}}}{m\pi B + Bi_{\mathrm{w}}} \right)^{-1} \right) \right) \\ & + \frac{a_0+a_1}{2a} \left(\frac{\lambda_{\mathrm{eff}}}{b} \left(1 - \frac{a_0+a_1}{2a} \right) \frac{Bi_{\mathrm{w}}}{1+Bi_{\mathrm{w}}} - \dot{m}_{\mathrm{l}} c_{\mathrm{p,l}} \frac{6}{\pi D_{\mathrm{w}}^2} \right) \Bigg] \end{aligned} \tag{C.8}$$

$$\begin{aligned} K_3 = -S_{\mathrm{w}} \Bigg[\sum_{m=1}^{\infty} & \left(2 \frac{\lambda_{\mathrm{eff}}}{a_1 - a_0} \frac{1}{m^2\pi^2} \sin\left(m\pi \frac{a_0+a_1}{2a} \right) \left(\cos\left(\frac{m\pi a_0}{a}\right) - \cos\left(\frac{m\pi a_1}{a}\right) \right) \right. \\ & \left. \left(\left(1 + e^{2m\pi B} \frac{m\pi B + Bi_{\mathrm{w}}}{m\pi B - Bi_{\mathrm{w}}} \right)^{-1} - \left(1 + e^{-2m\pi B} \frac{m\pi B - Bi_{\mathrm{w}}}{m\pi B + Bi_{\mathrm{w}}} \right)^{-1} \right) \right) \\ & - \frac{\lambda_{\mathrm{eff}}}{b} \left(\frac{a_0+a_1}{2a} \right)^2 \frac{Bi_{\mathrm{w}}}{1+Bi_{\mathrm{w}}} \Bigg] \end{aligned} \tag{C.9}$$

$$K_4 = S_{\mathrm{w}} \left(1 - \frac{a_0+a_1}{2a} \right) \left(\frac{\lambda_{\mathrm{eff}}}{b} \frac{Bi_{\mathrm{w}}}{1+Bi_{\mathrm{w}}} - \dot{m}_{\mathrm{l}} c_{\mathrm{p,l}} \frac{6}{\pi D_{\mathrm{w}}^2} \right) \tag{C.10}$$

$$K_5 = S_\mathrm{w}\left[\sum_{m=1}^{\infty}\left(2\frac{\lambda_\mathrm{eff}}{a_1-a_0}\frac{1}{m^2\pi^2}\sin\left(m\pi\frac{a_0+a_1}{2a}\right)\left(\cos\left(\frac{m\pi a_0}{a}\right)-\cos\left(\frac{m\pi a_1}{a}\right)\right)\right.\right.$$
$$\left.\left(\left(1+e^{2m\pi B}\frac{m\pi B+Bi_\mathrm{w}}{m\pi B-Bi_\mathrm{w}}\right)^{-1}-\left(1+e^{-2m\pi B}\frac{m\pi B-Bi_\mathrm{w}}{m\pi B+Bi_\mathrm{w}}\right)^{-1}\right)\right) \tag{C.11}$$
$$\left.-\left(1-\frac{a_0+a_1}{2a}\right)\left(\frac{\lambda_\mathrm{eff}}{b}\left(1-\frac{a_0+a_1}{2a}\right)\frac{Bi_\mathrm{w}}{1+Bi_\mathrm{w}}-\dot{m}_\mathrm{l}c_\mathrm{p,l}\frac{6}{\pi D_\mathrm{w}^2}\right)\right]$$

$$K_6 = -S_\mathrm{w}\left[\sum_{m=1}^{\infty}\left(2\frac{\lambda_\mathrm{eff}}{a_1-a_0}\frac{1}{m^2\pi^2}\sin\left(m\pi\frac{a_0+a_1}{2a}\right)\left(\cos\left(\frac{m\pi a_0}{a}\right)-\cos\left(\frac{m\pi a_1}{a}\right)\right)\right.\right.$$
$$\left.\left(\left(1+e^{2m\pi B}\frac{m\pi B+Bi_\mathrm{w}}{m\pi B-Bi_\mathrm{w}}\right)^{-1}-\left(1+e^{-2m\pi B}\frac{m\pi B-Bi_\mathrm{w}}{m\pi B+Bi_\mathrm{w}}\right)^{-1}\right)\right) \tag{C.12}$$
$$\left.+\frac{\lambda_\mathrm{eff}}{b}\frac{a_0+a_1}{2a}\left(1-\frac{a_0+a_1}{2a}\right)\right]$$

Appendix D

Pre-design of the condenser

A rapid analysis is undertaken to pre-design the condenser for the experimental setup. The objective of the LHP is to be able to transport at least 30 W, which corresponds to heat loads that can be dissipated by common electronic chips. Furthermore, the evaporator temperature T_e is limited to 100 °C. In order to achieve this goal, the condenser needs do be sized adequately.

Figure D.1 presents a schematic of the condenser. L_c is its length and D_c its diameter, whereas D_i and D_o are the inner and outer diameters of the tube, respectively.

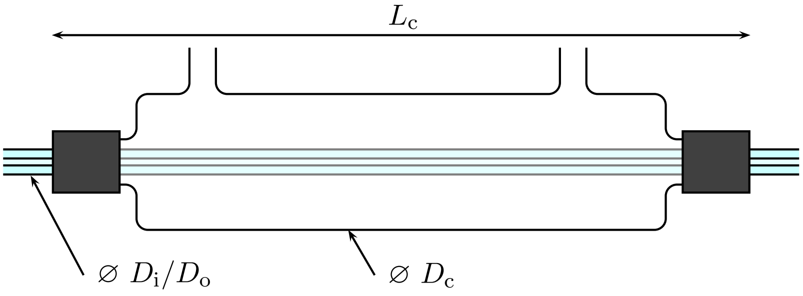

Figure D.1: Schematic of the condenser

To determine the heat transfer from the fluid flowing through the tube to the liquid coming from the heat sink, a thermal network is defined in Figure D.2. $R_{2\varphi}$, R_cond, $R_\mathrm{conv,c}$ and $R_\mathrm{conv,ext}$ are the thermal resistances associated to the condensation inside the tube, the thermal conduction in the tube wall, the convective heat transfer with the condenser liquid and the heat losses to the ambient, respectively. The condensation temperature inside the tube is equal to T_v, whereas the silicone oil flowing inside the condenser is at the heat sink temperature T_sink.

The following assumptions are made:

- Condensation is assumed in the entire length of the condenser

- The oil flowing inside the condenser is at a uniform temperature

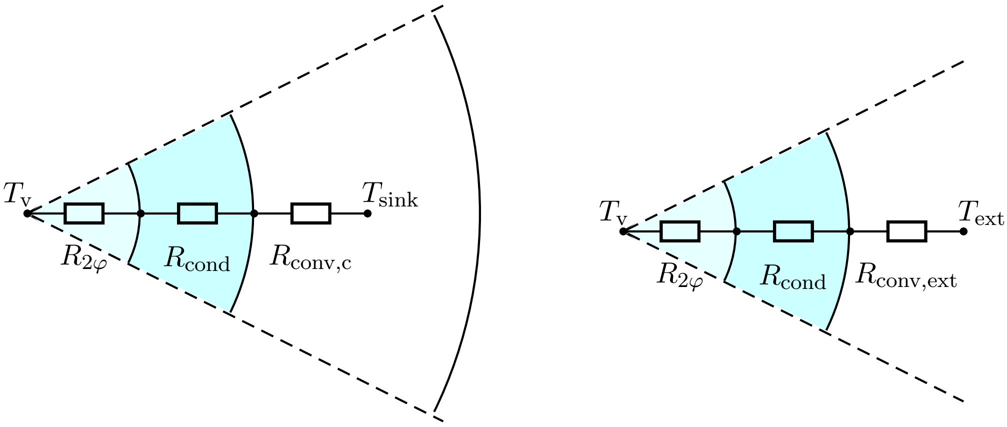

(a) Cross-section of the condenser

(b) Cross-section of the vapour line

Figure D.2: Modelling of the heat transfer in the condenser and in the vapour line

- The thermal resistance associated to the phase-change phenomenon can be neglected ($R_{2\varphi} = 0$)
- The heat sink is at $T_{sink} = 20\,°C$
- 80 % of the total heat load is dissipated through latent heat ($Q_{in}/Q_{ev} = 0.8$)

The thermal resistances of the evaporator and the condenser are:

$$R_e = \frac{T_e - T_v}{Q_{in}} \tag{D.1}$$

$$R_c = \frac{T_v - T_{sink}}{Q_{in}} \tag{D.2}$$

Assuming both resistances are equal:

$$T_v = \frac{T_e + T_{sink}}{2} \tag{D.3}$$

The liquid used for the cooling is silicone oil Kryo 51 manufactured by *Lauda*. The parameters used for the design are summarised in Table D.1.

The heat flux Q_{ev} is dissipated by condensation in the vapour line and in the condenser:

$$Q_{ev} = Q_v + Q_c \tag{D.4}$$

In the vapour line, the heat losses to the ambient are equal to:

$$Q_v = \frac{T_v - T_{ext}}{R_{cond} + R_{conv,ext}} \tag{D.5}$$

Parameter	**Value**
D_i	2 mm
D_o	6 mm
D_c	26 mm
L_v	685 mm
$h_\mathrm{conv,ext}$	$10\,\mathrm{W\cdot m^{-2}\cdot K^{-1}}$
λ_glass	$1\,\mathrm{W\cdot m^{-1}\cdot K^{-1}}$
λ_l[1]	$0.5\,\mathrm{W\cdot m^{-1}\cdot K^{-1}}$
ρ_l	$916\,\mathrm{kg\cdot m^{-3}}$
μ_l	$5\,\mathrm{mPa\cdot s}$
$\dot{m}_\mathrm{max}$	$20\,\mathrm{L\cdot min^{-1}}$
T_ext	20 °C
T_sink	20 °C
T_e	100 °C
T_v	60 °C
Q_in	0–30 W
$Q_\mathrm{in}/Q_\mathrm{ev}$	0.8
$R_\mathrm{e}/R_\mathrm{c}$	1

Table D.1: Parameters used in the pre-design

The conductive resistance in a cylindrical configuration is:

$$R_\mathrm{cond} = \frac{\ln\left(D_\mathrm{o}/D_\mathrm{i}\right)}{2\pi\lambda_\mathrm{glass}L_\mathrm{c}} \tag{D.6}$$

where λ_glass is the thermal conductivity of the glass tube. The convective resistance is calculated by:

$$R_\mathrm{conv,ext} = \frac{1}{h_\mathrm{conv,ext}\pi D_\mathrm{o}L_\mathrm{v}} \tag{D.7}$$

with L_v the length of the vapour line and $h_\mathrm{conv,ext}$ the heat transfer coefficient with the ambient.

The convective resistance in the condenser is:

$$R_\mathrm{conv,c} = \frac{1}{h_\mathrm{conv,c}\pi D_\mathrm{o}L_\mathrm{c}} \tag{D.8}$$

where $h_\mathrm{conv,c}$ is the heat transfer coefficient in the condenser.

In order to estimate $h_\mathrm{conv,c}$, one can use [148]

$$h_\mathrm{conv,c} = \frac{Nu\lambda_\mathrm{l}}{D_\mathrm{h}} \tag{D.9}$$

---

[1] No information is given by the manufacturer for the thermal conductivity of the silicone oil Kryo 51. An arbitrary value of $0.5\,\mathrm{W\cdot m^{-1}\cdot K^{-1}}$, slightly lower than that of water, is assumed for the present study.

where D_h is the hydraulic diameter:

$$D_\mathrm{h} = D_\mathrm{o} - D_\mathrm{i} \tag{D.10}$$

Since, the maximum mass flow rate of the chiller $\dot{m}_\mathrm{max}$ is equal to $20\,\mathrm{L}\cdot\mathrm{min}^{-1}$, the maximal flow velocity in the condenser is estimated to:

$$v_\mathrm{max} = \frac{4\dot{m}_\mathrm{max}}{\pi\left(D_\mathrm{o}^2 - D_\mathrm{i}^2\right)} \tag{D.11}$$

With $D_\mathrm{i} = 2\,\mathrm{mm}$ and $D_\mathrm{o} = 6\,\mathrm{mm}$, $v_\mathrm{max} = 0.79\,\mathrm{m}\cdot\mathrm{s}^{-1}$. The maximal Reynolds number:

$$Re_\mathrm{max} = \frac{\rho_\mathrm{l} v_\mathrm{max} D_\mathrm{h}}{\mu_\mathrm{l}} \tag{D.12}$$

is then equal to 2600. Therefore, a fully developed laminar flow is assumed and a constant Nusselt number, equal to 8 [148], is taken into account. The expected heat transfer coefficient is then:

$$h_\mathrm{conv,c} = 224\,\mathrm{W}\cdot\mathrm{m}^{-2}\cdot\mathrm{K}^{-1} \tag{D.13}$$

The maximal heat load that can be dissipated as a function of the condenser length is presented in Figure D.3. To ensure the dissipation of at least 30 W in the vapour line and in the condenser, without exceeding the temperature limit, a 250 mm-long condenser should be sufficient.

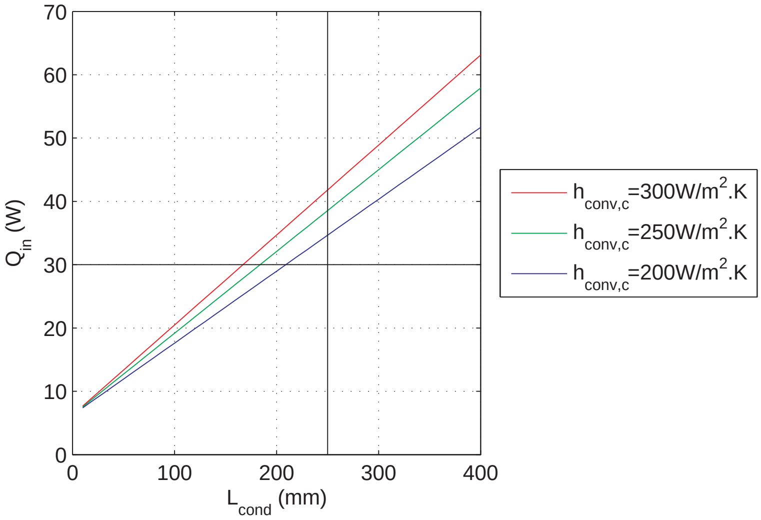

Figure D.3: Maximal dissipated heat load as a function of the condenser length

Although this pre-design study is based on many assumptions (heat losses to the ambient, saturation temperature, thermal conductivity of the silicone oil, heat transfer coefficient in the condenser), it gives a preliminary idea of the size of the condenser in order to meet the requirements.

Appendix E

Extended abstract (in french)

Analyse de la distribution des flux de chaleur et des écoulements au sein d'une LHP : modélisation par voies analytique et numérique et observations expérimentales

Résumé étendu en français

Depuis la fin du XX$^{\text{ème}}$ siècle, le développement et la miniaturisation des composants électroniques ont conduit à des contraintes grandissantes en ce qui concerne la gestion thermiques de ces derniers. La hausse continuelle des puissances de calcul et les restrictions en terme d'espace donnent lieu à des densités de chaleur à dissiper plus importantes, ainsi qu'à des fortes contraintes en ce qui concerne l'intégration des composants. Dans ce contexte, des solutions appropriées pour le contrôle thermique sont essentielles pour assurer la durabilité et la fiabilité de ces architectures électroniques.

En 2010, un consortium composé de partenaires européens, à la fois industriels et académiques, à lancé le projet FP7 PRIMAE. Son objectif est de développer des modules électroniques de nouvelle génération destinés à l'aéronautique commerciale. D'après le consortium, les contraintes thermiques sont la source principale de panne dans les modules avioniques. Dans ce contexte, des systèmes de gestion thermique fiables et efficaces doivent être dimensionnés, fabriqués et implémentés.

Les caloducs sont des systèmes de transfert de chaleur capables de transporter efficacement de la chaleur d'une source chaude vers un puits de chaleur. Ils ont gagné en importance depuis les années 1960 et leurs premières applications dans des programmes spatiaux pour devenir aujourd'hui des solutions utilisées dans de nombreuses applications telles que l'informatique, l'énergie nucléaire, l'automobile et l'aéronautique. Leur fonctionnement basé sur la pression capillaire, combiné aux transferts par chaleur latente, permet le transport de quantités d'énergie importante, passivement et avec des gradients de température minimums entre la source chaude et la source froide. Contrairement aux caloducs traditionnels, les boucles fluides à pompage capillaire, telles que les Loop Heat Pipes (LHP) et les Capillary Pumped Loops (CPL), disposent de canalisations séparées pour le transport du liquide et de la vapeur. Cette particularité réduit les pertes de charge et permet des transferts de chaleur sur des distances plus importantes, ainsi qu'une large flexibilité d'intégration.

Les nombreuses études théoriques et expérimentales de la littérature montrent la complexité des LHP et l'importance de phénomènes couplés sur leur fonctionnement. Ainsi, malgré des analyses détaillées, de nombreux phénomènes en jeu dans les LHP restent à ce jour mal compris et nécessitent des études plus poussées. Des données expérimentales supplémentaires et de nouvelles méthodes de modélisation peuvent offrir un nouvel éclairage concernant le comportement des LHP et des perspectives intéressantes à propos du dimensionnement de ces dernières.

L'objectif de cette étude et de proposer une étude complète du comportement des LHP par voies expérimentale, analytique et numérique. Basée sur les travaux présents dans la littérature, une étude théorique détaillée du système complet permet une analyse poussée des phénomènes couplés en jeu dans les LHP. De plus, les paramètres influents du systèmes sont évalués. Un nouveau banc expérimental avec des lignes de transport et un condenseur transparent est instrumenté. Les données expérimentales sont analysées et permettent une validation de l'étude théorique.

Premier chapitre : étude bibliographique

Le premier chapitre est une étude approfondie du comportement des boucles fluides de type LHP. Premièrement, les principes de fonctionnement sont décrits et les limites de fonctionnement du système sont expliquées. Ensuite, les éléments constituant les LHP sont étudiés en détail et leur influence sur le comportement global des boucles est analysé. L'accent est mis sur l'évaporateur/réservoir et particulièrement la structure capillaire. En effet, ses caractéristiques ont un impact majeur sur les phénomènes observés dans les boucles fluides. Une revue bibliographique des travaux de modélisation en régime stationnaire est ensuite proposée. Enfin, la position du front d'évaporation et le développement d'une poche de vapeur au sein de la structure poreuse sont étudiés.

Principes de fonctionnement des LHP

La figure E.1 présente un schéma d'une boucle fluide diphasique à pompage capillaire. Elle est principalement constituée d'un évaporateur comprenant une structure capillaire et d'un condenseur. Ils sont reliés entre eux par deux lignes de transport de fluide.

Un flux Q_{in} est apporté à l'évaporateur et est conduit à travers la paroi de l'évaporateur jusqu'aux cannelures de vapeur. L'évaporation du liquide circulant dans la mèche poreuse a lieu et la vapeur est évacuée à travers les cannelures. La vapeur circule ensuite dans la ligne de transport de vapeur jusqu'au condenseur, dans lequel elle se condense. Dans la deuxième partie du condenseur, le liquide est sous-refroidi, puis rejoint l'évaporateur par la ligne de transport de liquide. Le liquide entre dans la structure capillaire et remplace le fluide évaporé. Un accumulateur de liquide, appelé réservoir ou chambre de compensation, est soit

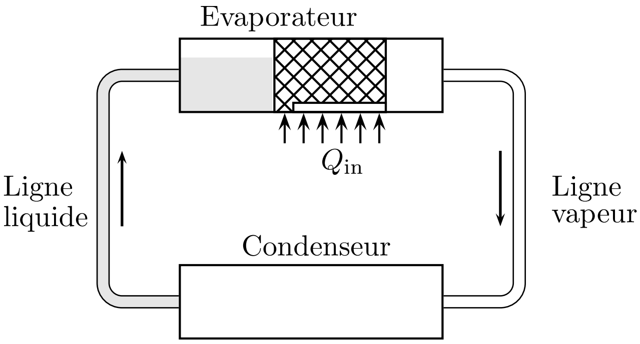

Figure E.1: Schéma d'une boucle fluide diphasique à pompage capillaire

connecté à la ligne liquide, soit intégré la structure de l'évaporateur. Il permet de compenser le déplacement de la masse de fluide dans le condenseur ainsi que l'expansion du fluide au cours du fonctionnement de la boucle.

La figure E.2 montre le diagramme classique pression-température du cycle thermodynamique d'une LHP en régime permanent. La position des points caractéristiques est détaillée sur la figure E.3.

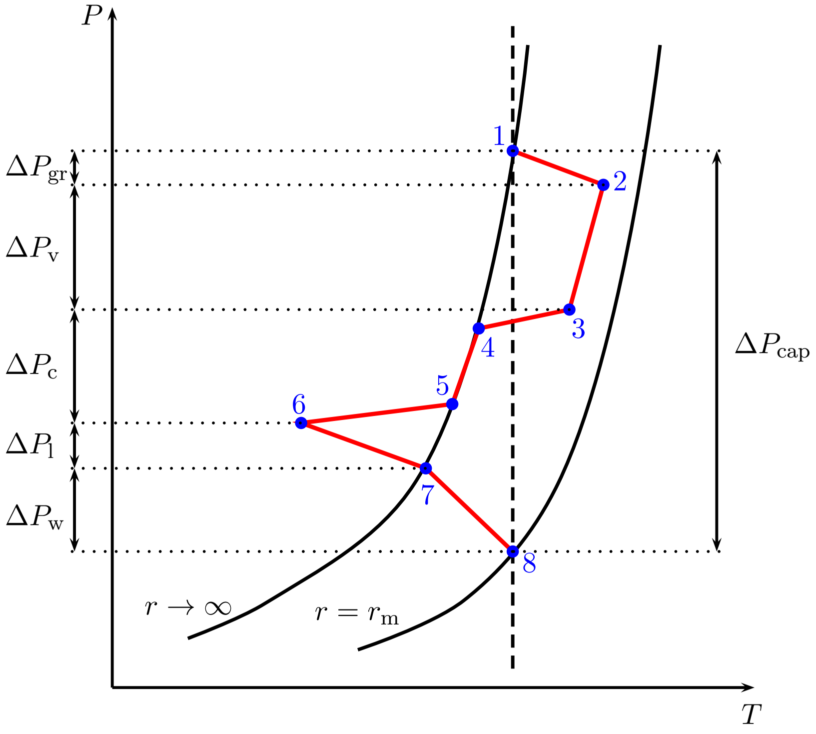

Figure E.2: Diagramme P-T du cycle de fonctionnement d'une LHP

Pour évaluer les performances du fonctionnement d'une LHP en régime permanent, on considère généralement sa température de fonctionnement ou sa résistance thermique en

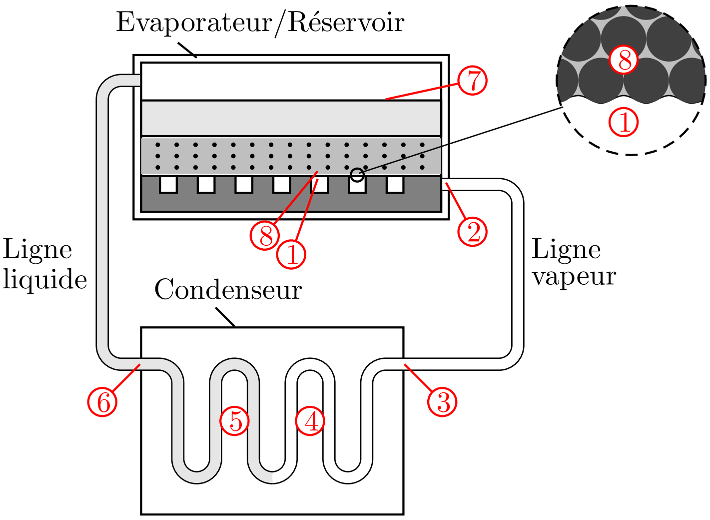

Figure E.3: Points caractéristiques d'une LHP

fonction de la charge appliquée. La température caractéristique est souvent définie comme étant la température de la vapeur dans les cannelures T_{v}, mais on trouve également dans la littérature l'utilisation de la température maximale de l'évaporateur T_{e} ou celle du réservoir T_{r}.

D'après Launay et al. [32], plusieurs limites peuvent restreindre le fonctionnement des LHP. Ces limites sont dépendantes des phénomènes physiques en jeu, ainsi que du cahier des charges de la LHP. La limite d'ébullition correspond à la nucléation dans le matériaux poreux, qui conduit au développement d'une poche de vapeur en son sein. La limite capillaire est atteinte lorsque la pression capillaire ne parvient plus à vaincre les pertes de charges du système. Dans ces conditions, la circulation du fluide n'est plus assurée. La pression capillaire maximale obtenue générée par la structure poreuse est:

$$\Delta P_{\mathrm{cap}} = \frac{2\sigma\cos\theta}{r_{\mathrm{m}}} \tag{E.1}$$

où σ est la tension de surface du fluide, r_{p} est le rayon de pore et θ l'angle de contact entre le liquide et la mèche poreuse. La limite de surchauffe est une contrainte définie par les propriétés des matériaux utilisés dans la LHP et les caractéristiques des éléments entourant le système. Dans le cadre du refroidissement de l'électronique, la température maximale admissible pour l'évaporateur est généralement de l'ordre de 100 °C.

Eléments constituant les LHP

Les LHP sont des systèmes complexes mettant en jeu de nombreux phénomènes couplés. Chaque élément d'une LHP exerce son influence sur le fonctionnement global du système:

- La structure évaporateur/réservoir est sans aucun doute le composant majeur d'une LHP. De forme variable suivant l'application (cylindrique, plat rectangulaire, plat circulaire), il est composé d'une partie réservoir accumulateur de fluide, d'une structure poreuse, de cannelures pour l'évacuation de la vapeur et d'une enveloppe généralement métallique. La mèche poreuse est un élément-clé du fonctionnement : elle permet d'approvisionner la zone d'évaporation en liquide et assure une pression capillaire suffisante pour la circulation du fluide dans la boucle. De nombreux paramètres caractérisent la mèche capillaire et jouent un rôle déterminant dans le comportement du système : le matériaux utilisé, le contact entre le poreux et le bâti de l'évaporateur, la porosité, la perméabilité, la taille des pores et la conductivité thermique équivalente. Malgré de nombreuses études sur le sujet, ces paramètres restent généralement difficiles à estimer. En ce qui concerne les cannelures, de nombreuses géométries existent dans la littérature.

- Les lignes de transport sont généralement des tubes de métal et doivent permettre la circulation du liquide et de la vapeur entre l'évaporateur et le condenseur tout en limitant les pertes de charge.

- Le condenseur permet la dissipation de chaleur du fluide de travail vers la source froide. De nombreuses configurations de condenseur existent, chacune ayant des caractéristiques différentes en terme de pertes de charge et de transferts thermiques.

- Le fluide utilisé doit répondre a de nombreux critères, les principaux étant : une forte chaleur latente d'évaporation, une tension de surface et une densité de vapeur importantes, une faible viscosité, une bonne stabilité chimique avec les matériaux des autres éléments.

Modélisation des LHP en régime permanent

Une étude approfondie des travaux de modélisation existant dans la littérature est menée. Celle-ci examine séparément les modèles numériques complets de LHP, les modèles numériques partiels d'évaporateur et les modèles analytiques.

Un tableau récapitulant les travaux de modélisation depuis 15 ans est présenté. La plupart des travaux parus sont des études numériques, basées sur des réseaux nodaux ou des méthodes aux différences finies. En revanche, peu de modèles analytiques existent à ce jour. De nombreux codes spécifiques pour les LHP ont été développés dans les dernières années, incluant de plus en plus de caractéristiques et de phénomènes. Cependant, il existe à ce jour peu de modèles capables de prédire le comportement global de la LHP tout en considérant précisément les transferts de chaleur et de masse au sein de l'évaporateur/réservoir, malgré leur importance significative sur le fonctionnement de la boucle.

Récemment, l'augmentation des ressources de calcul disponibles a permis le développement de plusieurs modèles tridimensionnels. De plus, les évaporateurs à géométrie plane sont de plus en plus étudiés. L'assèchement partiel du poreux et le fonctionnement avec réservoir rempli de liquide sont en revanche peu modélisés. Les transferts de chaleur et de masse sont généralement pris en compte de manière détaillée dans les modèles existants.

Position de l'interface liquide-vapeur

La position de l'interface liquide-vapeur dans l'évaporateur et la croissance éventuelle d'une zone de vapeur au sein de la structure capillaire ont été étudiés par divers auteurs. En effet, le déplacement du front d'évaporation dans la mèche change le profil de température dans le poreux, les caractéristique de l'évaporation et peut conduire, si la vapeur traverse complètement la mèche, à un arrêt du système.

Divers modèles existent, basés sur des descriptions continues de la structure poreuse ou bien sur des méthodes de type réseau de pore. Quelques études expérimentales sont également présentes dans la littérature. En revanche, peu d'observations en conditions réelles, c'est-à-dire dans le cas d'une LHP en fonctionnement, sont disponibles.

L'envahissement du poreux par une poche de vapeur et son influence sur le comportement global de la LHP restent peu connus. De plus, la modélisation de l'apparition de cette zone de vapeur passe par une compréhension fine du phénomène de nucléation au sein du poreux qui n'est à ce jour pas disponible. Enfin, la prise en compte de ce phénomène complexifierait grandement les modèles. La présente étude considère donc toujours une structure capillaire totalement saturée en liquide.

Second chapitre : modèle analytique de LHP et étude paramétrique

Ce second chapitre présente le développement et les résultats d'un modèle analytique complet de LHP. Un modèle analytique offre l'avantage d'une solution ne nécessitant pas de temps de calcul importants et qui peut être facilement implémentée dans le cadre du dimensionnement de LHP. Après avoir présenté les équations du modèle, une LHP standard est définie pour permettre une étude de sensibilité à certains paramètres importants du système. Enfin, quelques résultats montrent la complexité des boucles fluides et aident le lecteur à comprendre les phénomènes couplés au sein d'une LHP.

Détails du modèle

Le modèle est basé sur une description nodale de la LHP, comme cela est présenté figure E.4. L'état de la LHP peut ainsi être prédit à l'aide d'un bilan d'énergie à chaque nœud ainsi qu'en utilisant la relation thermodynamique reliant les états de saturation liquide-vapeur du système.

En combinant l'ensemble de ces bilans, une expression reliant la puissance totale Q_{in} aux température du système et au débit de fluide en son sein peut être déterminée:

$$Q_{\mathrm{in}} = f(T_{\mathrm{r}}, T_{\mathrm{r}}, T_{\mathrm{we}}, T_{\mathrm{e}}, \dot{m}_{\mathrm{f}}, T_{\mathrm{r,i}}) \tag{E.2}$$

Une méthode supplémentaire doit être implémentée afin de déterminer les transferts de chaleur au sein de l'évaporateur/réservoir. En effet, ceux-ci dépendent fortement de la géométrie et des propriétés thermo-physiques des matériaux utilisés, ainsi que des car-

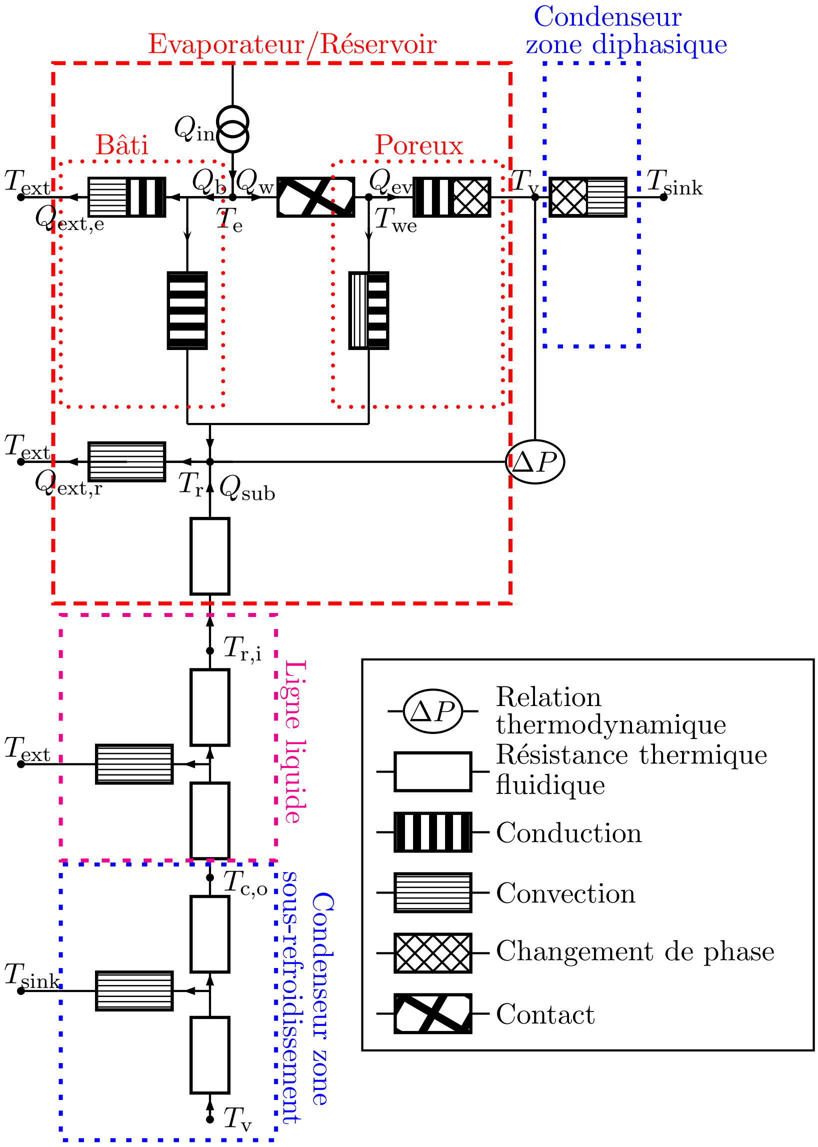

Figure E.4: Schéma nodal d'une LHP

actéristiques de transfert au sein du fluide et de l'environnement de la boucle (convection, évaporation, condensation).

L'équation de la chaleur bi-dimensionnelle dans le poreux est:

$$\frac{\partial^2 T_{\mathrm{w}}}{\partial x^2} + \frac{\partial^2 T_{\mathrm{w}}}{\partial y^2} = 0 \tag{E.3}$$

Cette équation peut s'exprimer sous la forme de séries de Fourier:

$$T^*_{\mathrm{w}}(X,Y) = \sum_{m=0}^{\infty} A_{\mathrm{m}}(Y)cos(m\pi X) + B_{\mathrm{m}}(Y)sin(m\pi X) \tag{E.4}$$

Les conditions aux limites sont définies et permettent de prendre en compte le coefficient d'accommodation qui détermine le taux d'évaporation dans les cannelures. Après calcul des coefficients de Fourier, le flux entrant dans le poreux Q_{w} et le flux dissipé par évaporation Q_{ev} peuvent être déterminés en intégrant le champ de température.

Une méthode analogue est développée pour les transferts thermiques dans le bâti de l'évaporateur. Cette méthode est appliquée en 2D dans le cas d'un évaporateur plat et en 3D pour les évaporateurs cylindriques. Comme précédemment, l'intégration des champs de température permet de calculer les puissances utiles pour résoudre le système d'équations d'un modèle général. La méthode complète de résolution du modèle est ensuite détaillée.

Etude de sensibilité

Afin de conduire une étude de sensibilité, un cas standard est défini. Celui-ci, basé sur des exemples courants de la littérature en ce qui concerne le refroidissement de l'électronique, permet de déterminer un cas de références pour l'étude de sensibilité. Des premiers résultats du modèle sont discutés à propos du cas standard.

Une étude de sensibilité est développée pour cinq paramètres du modèle qui sont particulièrement difficiles à estimer théoriquement. Ceux-ci sont: la conductivité équivalente du matériau poreux, la résistance de contact entre la mèche et le bâti, le coefficient d'accommodation et les coefficients d'échange avec la source froide d'une part et avec le milieu ambiant d'autre part. La sensibilité de chacun de ces paramètres sur le comportement de la LHP est étudié. Il apparait que ces paramètres agissent de manière découplée sur le fonctionnement de la boucle. Ainsi, ces paramètres peuvent être déterminés séparément par comparaison entre le modèle et des résultats expérimentaux, pour peu que la quantité de ces résultats (flux, températures) soit suffisante.

Validation du modèle

Le modèle analytique est validé à l'aide de résultats de la littérature publiés par Singh et al. [42]. Les simulations sont en très bon accord avec les données expérimentales. Le même modèle est également comparé à des résultats expérimentaux obtenus en configuration cylindriques et obtenus par Chuang et al. [150]. La comparaison est également satisfaisante. Les prédictions sont moins précises à très bas flux, conditions pour lesquelles les pertes vers l'ambiant jouent un rôle déterminant sur le fonctionnement global de la LHP.

Etude paramétrique

Une étude paramétrique complète est présentée ensuite. Celle-ci concerne le coefficient d'accommodation, la conductivité thermique équivalente du matériau poreux, la conductivité thermique du bâti de l'évaporateur, la résistance de contact entre le poreux et le bâti, la température ambiante, les échanges thermiques au niveau du condenseur, le fluide circulant dans la boucle et la quantité de gaz incondensables dans le système.

Conclusion

Ce modèle, développé à la fois pour des géométries d'évaporateur plane et cylindrique, a été validé dans différentes configurations expérimentales. Il met en évidence les paramètres d'influence de la LHP (conductivité thermique équivalente du poreux, résistance de contact, coefficient d'accommodation et coefficients d'échange avec la source froide et le milieu ambiant, respectivement) et leur influence sur le fonctionnement de la boucle. Les résultats montrent l'importante complexité du système dans lequel ces paramètres sont intimement liés les uns aux autres. Cependant, l'étude de sensibilité montre qu'une distinction de ces paramètres est possible à l'aide d'un dispositif expérimental associé à certaines mesures de température.

Troisième chapitre : étude expérimentale

Ce chapitre introduit une étude expérimentale de la conception, de la fabrication et du test d'une LHP. Un dispositif à vocation de recherche procure des éléments-clés en ce qui concerne les phénomènes thermiques et hydrauliques en jeu dans les LHP. De plus, des données expérimentales sont nécessaires pour valider les modèles développés dans le laboratoire. Ainsi, un banc expérimental à caractère modulaire est développé pour la première fois au laboratoire. Celui-ci est opérationnel depuis avril 2014. Les premiers résultats obtenus sont présentés dans ce chapitre. Premièrement, les éléments du dispositif expérimental sont présentés, ainsi que les différents capteurs et techniques utilisés pour caractériser le système. Ensuite, un cycle en puissance est étudié par une analyse des températures principales du dispositif. Une analyse plus poussée est entreprise pour évaluer les caractéristiques de la LHP en régime stationnaire et transitoire. Une étude par des observations est ensuite menée pour comprendre les phénomènes de condensation en jeu dans le condenseur et les lignes de transport de fluide et pour évaluer leur influence sur le fonctionnement du système.

Banc expérimental et procédures

Le dispositif expérimental a été conçu pour être le plus modulaire possible : les différents éléments (lignes de transport, structure poreuse, bloc de cuivre, etc.) sont interchangeable pour permettre des analyses expérimentales paramétriques avec plusieurs fluides. Les résultats présentés ici sont obtenus avec de l'eau. Certains des composants sont transparents pour permettre une meilleure compréhension des mécanismes en jeu dans les LHP. Ce banc est à vocation expérimentale et n'a donc pas comme objectif l'obtention de performances exceptionnelles.

La figure E.5 présente les différents éléments du dispositif expérimental : un évaporateur/réservoir circulaire incluant une structure capillaire, des lignes de transport de liquide et de vapeur et un condenseur droit. De plus, un réservoir permettant de gérer la mass de fluide dans le système est connecté à la ligne liquide et un dispositif de remplissage est également monté. Un hublot sur le réservoir et des tubes transparents pour les lignes et le condenseur permettent une observation visuelle du fonctionnement de la boucle.

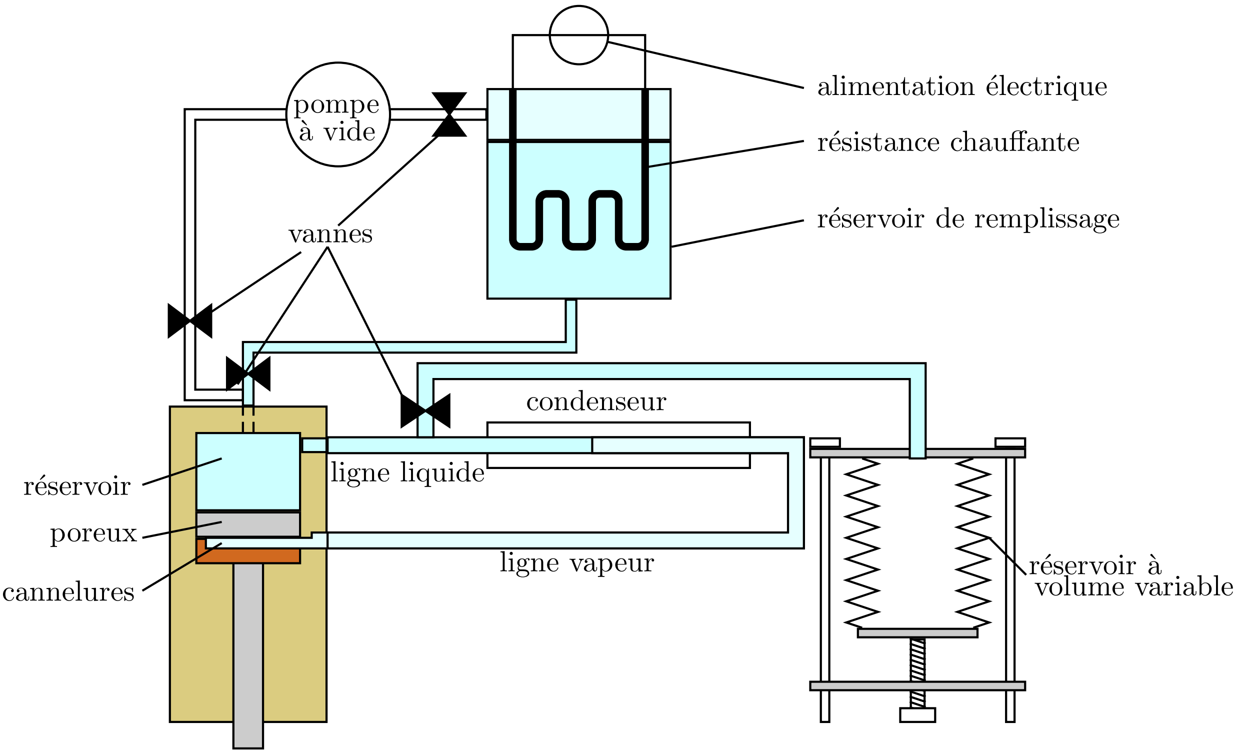

Figure E.5: Schéma du dispositif expérimental

Chaque élément du dispositif est ensuite décrit en détail : l'évaporateur/réservoir, les cannelures, la structure capillaire, les lignes de transport de fluide, le condenseur, le dispositif de remplissage, le réservoir de gestion de la charge, la source de chaleur et la source froide.

Dans un second temps, les techniques de mesures sont présentées. Un capteur de pression permet la mesure de la pression absolue dans le réservoir et des thermocouples de type K assurent l'acquisition de la température à plusieurs positions-clés de la LHP. De plus, la puissance totale dissipée et précisément mesurée et une caméra rapide permet d observer les écoulements dans les lignes et le condenseur. La position des thermocouple et du capteur de pression est détaillé sur la figure E.6.

Fiabilité des résultats expérimentaux

Une discussion détaillée concernant la fiabilité des résultats expérimentaux est présentée. En effet, le comportement de la LHP ne dépend pas uniquement des caractéristiques géométriques et thermo-physiques invariables du système. D'autres paramètres influencent le fonction-

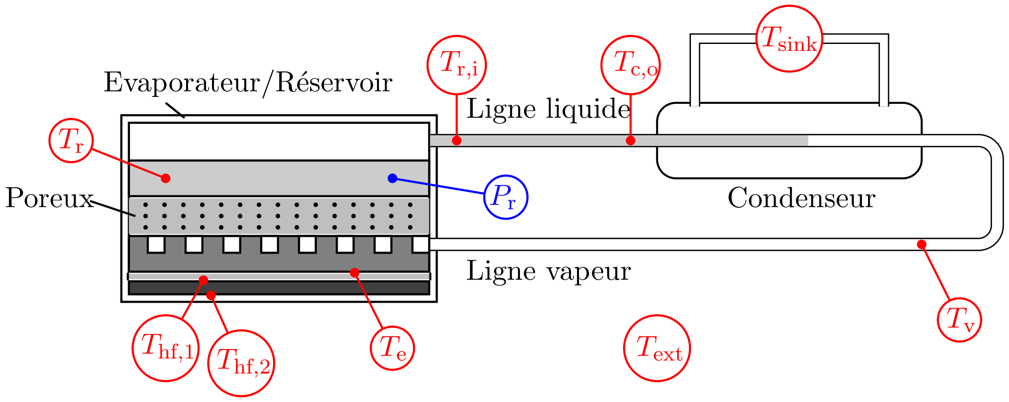

Figure E.6: Position des thermocouples et du capteur de pression

nement de la LHP en régimes stationnaire et transitoire : la quantité de gaz incondensables dans le dispositif et leur position, la variation de la température ambiante et la variation de la masse de fluide dans le système. Il est donc nécessaire de contrôler et d'estimer ces paramètres ainsi que d'évaluer leur importance sur le comportement de la LHP.

Les procédures de remplissage sont décrites et les problèmes d'étanchéité sont abordés. De plus, la reproductibilité des tests est évaluée. L'influence de le la position du thermocouple T_{r} est présentée.

Cette analyse montre une reproductibilité satisfaisante des résultats à flux faibles et modérés. Lorsque la puissance est plus importante, le déclenchement de l'ébullition, phénomène peu prévisible, modifie considérablement le comportement du système. La quantité de gaz incondensable et la variation de la température ambiante jouent également un rôle dans le fonctionnement de la LHP. Cependant, ces paramètres peuvent être partiellement contrôlés par des procédures expérimentales appropriées et mesurés à l'aide de capteurs et de thermocouples. La fiabilité du système est donc considérée suffisante pour les premiers résultats de ce dispositif, présentés dans cette thèse. Pour des études futures en revanche, il est impératif d'assurer une meilleure étanchéité de la LHP, ainsi que de permettre une mesure plus précise de la température du réservoir, à l'aide de l'insertion d'un thermocouple dans la zone de vapeur de celui-ci.

Comportement de la LHP au cours d'un cycle de puissance

Un cycle de puissance montée-descente de 0 W à 50 W est décrit (figure E.7). L'évolution des températures principales du système est analysée. Le démarrage et le fonctionnement à très faible puissance sont particulièrement discutés. Des temps de stabilisation particulièrement importants sont observés. Ceux-ci sont dus à la forte inertie thermique du banc expérimental. En effet, l'évaporateur/réservoir est de grande dimension et la masse de liquide présent dans le réservoir est importante.

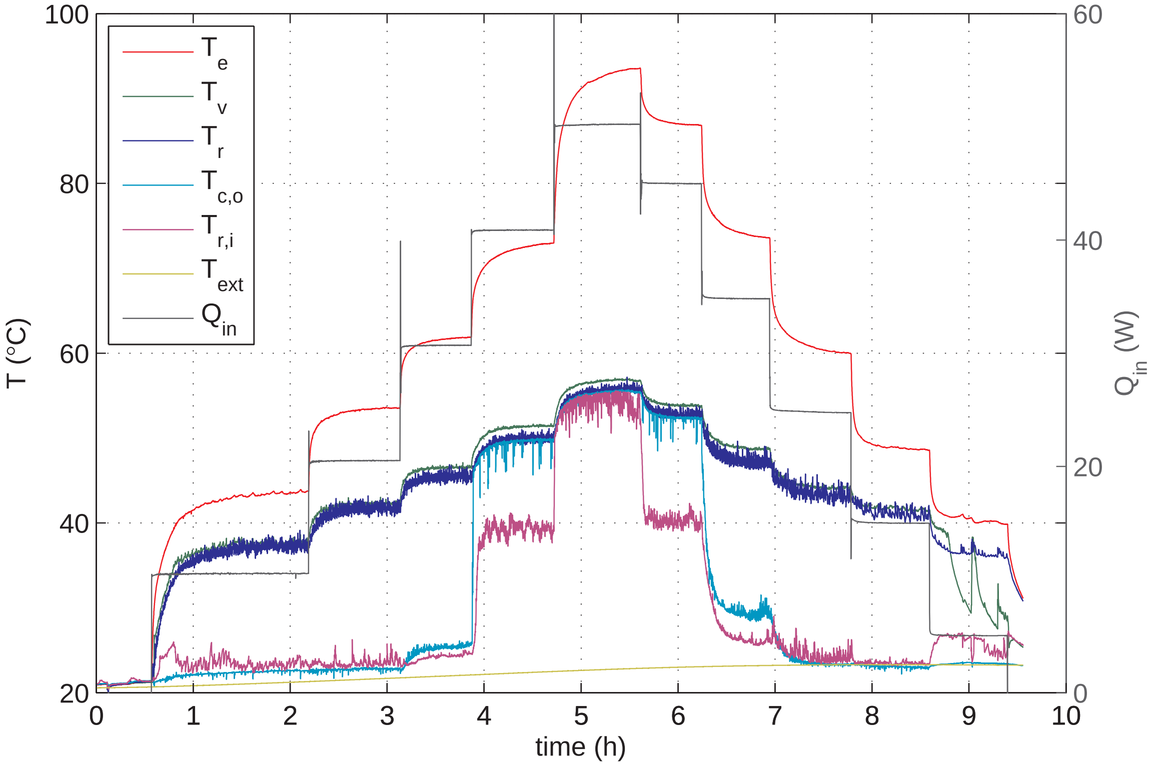

Figure E.7: Cycle montée-descente de la LHP – $T_{\text{sink}} = 20\,°\text{C}$

Fonctionnement en régime permanent

Divers tests tests sont présentés pour évaluer les performances de la LHP et estimer l'influence de certains paramètres (gaz incondensables, température de source froide, ébullition dans le réservoir) sur le fonctionnement en régime permanent du dispositif et sur les hystérésis observés.

La courbe caractéristique, représentant les températures principales en fonction de la puissance appliquée, est tracée. Une large différence de température entre T_{e} et T_{v} est observée. Celle-ci est en majorité induite par la résistance thermique de contact entre le matériaux poreux et le bâti de l'évaporateur.

Les performances thermiques de la LHP sont ensuite évaluées à l'aide des résistances thermiques de la boucles, calculées comme suit:

$$R_{\text{LHP}} = \frac{T_{\text{e}} - T_{\text{sink}}}{Q_{\text{in}}} \tag{E.5}$$

$$R_{\text{e}} = \frac{T_{\text{e}} - T_{\text{v}}}{Q_{\text{in}}} \tag{E.6}$$

$$R_{\text{c}} = \frac{T_{\text{v}} - T_{\text{sink}}}{Q_{\text{in}}} \tag{E.7}$$

où R_{LHP} est la résistance totale de la LHP, R_{e} la résistance thermique de l'évaporateur et R_{c} la résistance du condenseur. La résistance totale varie entre $1.1\,\text{K}\cdot\text{W}^{-1}$ à fortes puissances et plus de $3\,\mathrm{K}\cdot\mathrm{W}^{-1}$ à 10 W. La variation de la résistance globale de la LHP suit une courbe standard conforme à la littérature. La résistance est forte pour les faibles puissances pour lesquelles la proportion de chaleur dissipée par évaporation est faible et les pertes vers l'ambiant ont une forte influence sur le fonctionnement du système. En mode de conductance variable, la résistance diminue fortement avec l'augmentation de la puissance. En mode de conductance fixe, la résistance thermique de la LHP est quasi-constante. La contribution de la résistance au condenseur par rapport à la résistance de l'évaporateur est importante, particulièrement à faible puissance. Une telle contribution est attendue avec ce type de condenseur, puisque l'utilisation du verre combine à la fois une faible conductivité et une importante épaisseur de paroi, qui conduisent inévitablement à une dégradation nette des performances thermiques.

Un hystérésis est observé entre les phases de montée en puissance et celles de descente. Cet hystérésis est particulièrement prononcé pour la température de l'évaporateur. Après comparaison avec les hystérésis décrits dans la littérature, lesquels dépendent pour la plupart de mouvements hydrauliques dans le réservoir et de la présence de vapeur de celui-ci, l'hypothèse d'hystérésis capillaire est retenue pour expliquer les différences observées. Ainsi, le développement d'une poche de vapeur au sein de la structure capillaire entraîne un hystérésis du au mouvement de l'interface liquide-vapeur dans le poreux lors de l'augmentation et de la diminution de la puissance thermique.

De l'ébullition est observée dans le réservoir à la surface du poreux dans certaines conditions expérimentales. Ce phénomène a une influence significative sur le comportement de la LHP, particulièrement sur la température de l'évaporateur. La prédiction et la prévention du déclenchement de l'ébullition sont donc de grand intérêt. Cependant, de nombreux paramètres entrent en jeu dans le phénomène de nucléation : la taille des pores, la pureté du fluide, la présence de gaz incondensables ou de vapeur piégés a la surface du poreux, les propriétés thermo-physiques du fluide (tension de surface, masse volumique, chaleur latente de vaporisation), le flux parasite transversal, la charge de liquide dans le réservoir, etc.

L'influence des gaz incondensables sur le comportement de la LHP est ensuite présentée. Ceux-ci induisent une pression partielle supplémentaire dans le réservoir et donc une augmentation des flux parasites dans l'évaporateur. Ainsi, en présence de gaz incondensables, le fonctionnement de la boucle est dégradé et la LHP fonctionne à une température supérieur au cas sans gaz. Les gaz incondensables ont également un effet sur le déclenchement de l'ébullition dans le réservoir. En effet, la pression partielle augmente la température de nucléation à la surface du poreux, retardant assez significativement le déclenchement de l'ébullition dans le réservoir.

Une discussion concernant l'influence de la température de source froide sur le comportement de la boucle est menée. A faibles flux, l'influence de T_{sink} n'est pas significative. Une température de source froide inférieure permet d'augmenter légèrement les performances thermiques du système. Lorsque T_{sink} est supérieure à T_{ext} ($T_{\mathrm{sink}} = 30\,°\mathrm{C}$), le comportement de la LHP est modifié. La zone diphasique envahit la ligne liquide jusqu'à ce que le ménisque atteigne, à 30 W, le réservoir.

Fonctionnement en régime transitoire

Le démarrage de la LHP est discuté en détail. L'influence de la puissance de démarrage, de l'état du fluide dans la ligne vapeur (liquide ou vapeur) et des incondensables sont présentés.

Le comportement de la boucle en réponse à des échelons de puissance est ensuite étudié. Les résultats montrent la répétabilité des tests pour des échelons similaires. En revanche, la puissance totale à elle seule ne suffit pas à définir le fonctionnement du système. En effet, les états précédents de la boucle jouent également un rôle et peuvent modifier le comportement de la boucle (hystérésis capillaire, nucléation dans le réservoir, etc.).

Enfin, des phénomènes oscillatoires sont observés. Ceux-ci ont lieu dans deux configurations différentes : à très bas flux et lorsque la température de source froide est élevée.

Les oscillations observées à très faible puissance sont de trois types : forte amplitude et basse fréquence, faible amplitude et basse fréquence et faible amplitude et haute fréquence. Les deux premières sont une conséquence directe du phénomène de condensation en gouttes dans la ligne vapeur, ainsi que de la position du thermocouple T_{v}. La troisième est due à la position du thermocouple T_{r} dans la zone de liquide du réservoir.

Les observations observées à haute température de source froide sont une conséquence de la position du ménisque dans la ligne liquide et de son mouvement de va-et-vient au cours du fonctionnement. Ce mouvement du ménisque entraîne une variation du sous-refroidissement du liquide entrant dans le réservoir et modifie ainsi périodiquement les températures mesurée, principalement $T_{\mathrm{r,i}}$.

Visualisation des écoulements

L'observation directe des écoulements dans les lignes de transport et dans le condenseur est rendue possible par l'utilisation de tubes en verre. De plus, l'acquisition par caméra rapide permet d'étudier les mouvements rapides qui accompagnent le détachement des bulles.

Trois zones se distinguent dans le condenseur : une zone quasi-annulaire (légèrement stratifiée) se terminant par un ménisque hémisphérique, un train de bulles sphériques et une zone de liquide avec quelques bulles isolées. Le même type de structure d'écoulement à déjà été observé dans les travaux de Médéric et al. [156].

Le détachement d'une bulle dans le condenseur est décrit. Une légère stratification de l'écoulement existe, avec un film fin de liquide et une interface ondulée. Le ménisque quasi-hémisphérique avance dans le condenseur et conduit éventuellement à la coalescence de bulles entre elles ou avec la zone annulaire. L'interface liquide-vapeur du film se déforme progressivement et conduit finalement au détachement d'un bouchon de vapeur. Celui-ci se condense partiellement brutalement pour donner une bulle quasi-sphérique.

La condensation dans la ligne liquide est également étudiée, dans le cas où la température de source froide est supérieure à la température ambiante. Les résultats montrent des variations importantes de la position du ménisque au cours du fonctionnement. En effet, celui-ci se déplace de plus de 100 mm dans un intervalle d'une dizaine de secondes. Ces variations expliquent les oscillations de températures précédemment observées.

La condensation dans la ligne vapeur est observée. Les visualisations montrent la condensation en goutte sur les parois du verre. Les gouttelettes coalescent ensuite pour former les gouttes de plus grande taille. Enfin, la coalescence de ces gouttes donne naissance à un bouchon de liquide qui circule le long des lignes jusqu'au réservoir et emporte tout le condensat vers celui-ci. Ce régime intermittent explique en partie les oscillations précédemment décrites sur les températures du systèmes.

Conclusion

Un banc expérimental complet a été dimensionné, assemblé et instrumenté. Ses caractéristiques permettent de mesurer la pression dans le réservoir, la puissance dissipée par le système et la température de la LHP à des positions-clés. De plus, un hublot en verre et des tubes transparents permettent une observation directe des écoulements au sein des lignes de transport, du condenseur et du réservoir. Le comportement du dispositif expérimental en régimes permanent et transitoire est étudié et montre les paramètres influents du système. L'influence de l'ébullition nucléе sur le fonctionnement de la boucle et les effets des gaz incondensables sont évalués. Le couplage entre les oscillations thermiques et le comportement hydrodynamique de la LHP est mis en évidence. Enfin, des observations des écoulements dans les lignes et le condenseur sont analysées pour décrire les phénomènes physiques en jeu.

Quatrième chapitre : Modèle numérique du banc expérimental

Un modèle numérique est développé pour étudier plus en détail les résultats obtenus dans le chapitre 3, particulièrement les transferts de chaleur dans l'évaporateur et la condensation dans les lignes de transport. Contrairement à la méthode analytique présentée dans le chapitre 2 qui est un modèle de dimensionnement de pouvant pas prendre en compte les caractéristiques géométriques du banc expérimental, cette étude numérique tente de considérer ces paramètres. Après une description des hypothèses principales, le modèle est développé. Une comparaison entre les résultats numériques et les données expérimentale est présentée. Ensuite, les transferts thermiques dans l'évaporateur et dans les lignes de transports sont étudiés. Enfin, l'influence de certains paramètres (matériau du bâti, conduction thermique longitudinale dans les lignes, température de source froide, etc.) est discutée.

Développement du modèle numérique

Le modèle numérique instationnaire est basé sur une discrétisation 1D des lignes et du condenseur et une description 2D des transferts de chaleur et de masse dans l'évaporateur/réservoir. Le condenseur et les lignes vapeur et liquide sont discrétisées en petits éléments de volume comme indiqué sur la figure E.8.

Des corrélations d'écoulements monophasiques et diphasiques sont implémentées pour le

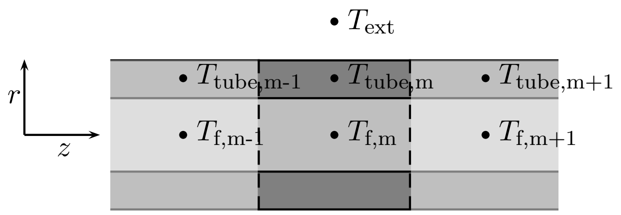

Figure E.8: Discrétisation des lignes de transport

calcul des coefficient de transfert de chaleur et pour la détermination des pertes de charges. Dans un premier temps, les pertes vers l'ambiant et le flux parasite longitudinal ne sont pas pris en compte. Un bilan d'énergie simplifié sur l'évaporateur donne donc :

$$Q_{\mathrm{in}} = Q_{\mathrm{ev}} + Q_{\mathrm{sen}} + Q_{\mathrm{sub}} \tag{E.8}$$

Les différents flux sont ensuite déterminés comme suit :

$$Q_{\mathrm{ev}} = \dot{m}_{\mathrm{f}} h_{\mathrm{lv}} \tag{E.9}$$

$$Q_{\mathrm{sen}} = \dot{m}_{\mathrm{f}} c_{\mathrm{p,l}} \left(T_{\mathrm{v}} - T_{\mathrm{r}}\right) \tag{E.10}$$

$$Q_{\mathrm{sub}} = \dot{m}_{\mathrm{f}} c_{\mathrm{p,l}} \left(T_{\mathrm{r}} - T_{\mathrm{r,i}}\right) \tag{E.11}$$

Le débit massique de fluide circulant dans la boucle ets, quant à lui, égal à :

$$\dot{m}_{\mathrm{f}} = \frac{Q_{\mathrm{in}}}{h_{\mathrm{lv}} + c_{\mathrm{p,l}} \left(T_{\mathrm{v}} - T_{\mathrm{r,i}}\right)} \tag{E.12}$$

Ensuite, une analyse bidimensionnelle des flux de chaleur et de masse dans la structure capillaire est entreprise. Un volume défini du matériaux poreux, une demi-cannelure et une partie du bloc de cuivre sont modélisés, comme indiqué sur la figure E.9. Les conditions aux limites sont exposées et la procédure de résolution est expliquée en détail.

Dans un second temps, un modèle bidimensionnel additionnel est ajouté, pour prendre en compte le flux parasite longitudinal et les pertes de l'évaporateur vers l'ambiant. Le bilan d'énergie du réservoir devient :

$$Q_{\mathrm{in}} = Q_{\mathrm{tube,v}} + Q_{\mathrm{tube,l}} + Q_{\mathrm{ev}} + Q_{\mathrm{sen}} + Q_{\mathrm{sub}} + Q_{\mathrm{ext}} \tag{E.13}$$

$$\dot{m}_{\mathrm{f}} = \frac{Q_{\mathrm{in}} - Q_{\mathrm{tube,v}} - Q_{\mathrm{tube,l}} - Q_{\mathrm{ext}}}{h_{\mathrm{lv}} + c_{\mathrm{p,l}} \left(T_{\mathrm{v}} - T_{\mathrm{r,i}}\right)} \tag{E.14}$$

$$-\lambda_{\mathrm{b}} \frac{\partial T}{\partial y} = \left(Q_{\mathrm{in}} - Q_{\mathrm{tube,v}} - Q_{\mathrm{b}}\right) \frac{1}{S_{\mathrm{w}}} \tag{E.15}$$

Le domaine modélisé est présenté sur la figure E.10 et les hypothèses et conditions aux limites sont détaillées.

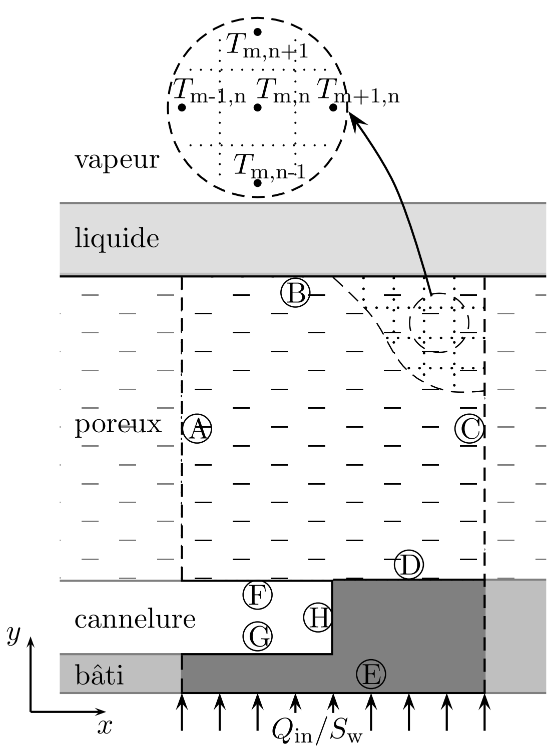

Figure E.9: Transferts de chaleur et de masse dans le poreux

Résultats numériques

Le modèle est comparé aux résultats expérimentaux, pour une température de source froide de 20 °C. Un bon accord existe entre les températures calculées et mesurées. Toutefois, une différence importante est observée en ce qui concerne les pertes de charge dans le système et donc la différence $T_{\text{v}} - T_{\text{r}}$. Cette différence peut être due à la fois à des mesures approximatives (position des thermocouples) et à l'utilisation de corrélations non adaptées. Une différence importante est également observée entre la longueur diphasique simulée par le modèles et les observations expérimentales. Ceci montre les limites du modèles en ce qui concerne la détermination des transferts de chaleur et de masse dans les lignes et le condenseur. L'influence de la température de source froide sur le système est ensuite présentée.

Les champs de température dans l'évaporateur sont discutés. Le champ de température dans la structure poreuse est modélisé à l'aide du modèle numérique et du modèle analytique. L'influence de la conductivité thermique du bâti et du déclenchement de l'ébullition dans le réservoir est ensuite présentée.

Enfin, le profil de température le long des lignes de transport et du condenseur est expliqué. Il confirme les résultats expérimentaux selon lesquels la condensation a lieu presque dès le début de la ligne vapeur. De plus, l'influence de la conductivité longitudinale dans les lignes est discutée. Il apparaît d'après les simulations que l'utilisation d'un matériau conducteur pour les tubes, tel que le cuivre, modifie significativement la température du liquide entrant dans le réservoir.

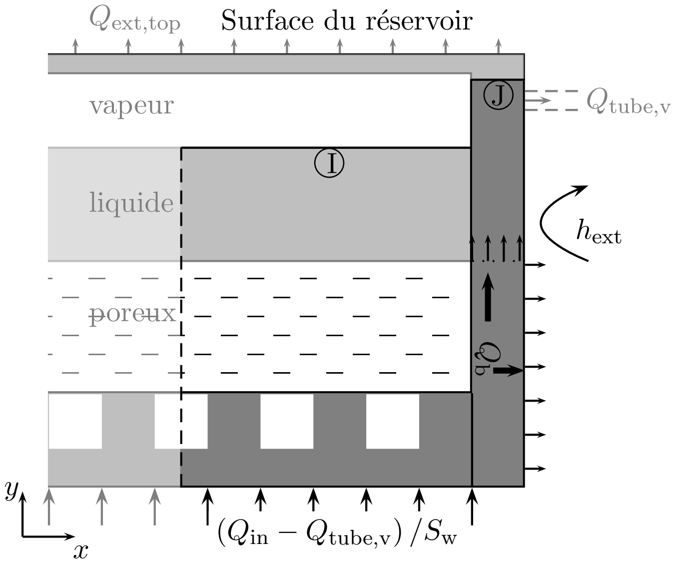

Figure E.10: Transferts thermique vers l'ambiant et à travers le bâti

Conclusion

Un modèle numérique complet est présenté. Basé sur une discrétisation 1D des lignes et 2D de l'évaporateur, le modèle prend précisément en compte les transferts de masse et de chaleur dans le poreux, le bâti, les lignes de transport et le condenseur. Un bon accord est trouvé avec les données expérimentales. La différence la plus significative concerne le calcul des pertes de charges. Une étude des champs de température dans l'évaporateur est menée. Les simulations avec des tubes en cuivre montrent la nécessité de prendre en compte la conductivité longitudinale dans les tubes dans le calcul du sous-refroidissement.

FOLIO ADMINISTRATIF

THESE SOUTENUE DEVANT L'INSTITUT NATIONAL DES SCIENCES APPLIQUEES DE LYON

NOM : SIEDEL DATE de SOUTENANCE : 26/09/2014

Prénoms : Benjamin

TITRE : Analyse de la distribution des flux de chaleur et des écoulements au sein d'une LHP : modélisation par voies analytique et numérique et observations expérimentales.

NATURE : Doctorat Numéro d'ordre :

Ecole doctorale : MEGA (Mécanique, Énergétique, Génie civil et Acoustique)

Spécialité : Thermique et Énergétique

RESUME : La miniaturisation toujours plus poussée des composants électroniques génère des contraintes thermiques de plus en plus importantes. Les systèmes diphasiques – et particulièrement les boucles diphasiques à pompage thermo-capillaire encore appelées Loop Heat Pipes ou LHP – suscitent actuellement un intérêt croissant en raison de leurs bonnes performances thermiques, de leur fiabilité et de leur géométrie permettant une grande souplesse d'implantation. Cependant, une meilleure compréhension des phénomènes en jeu dans ces systèmes est essentielle pour optimiser leur conception et prédire leur comportement de manière fiable.

Au cours de ce travail, un modèle analytique est développé qui intègre les paramètres de fonctionnement d'une LHP, afin d'étudier leur influence en fonction des conditions opératoires. Son originalité principale réside dans la détermination précise de la répartition des différents flux thermiques dans l'évaporateur. Une étude de sensibilité est menée pour évaluer les influences de la résistance de contact entre la structure capillaire poreuse et l'enveloppe de l'évaporateur, de la conductivité thermique équivalente du matériau poreux, du coefficient d'accommodation lié aux transferts de chaleur par évaporation et des coefficients de transfert thermique entre la paroi et le milieu ambiant ou la source froide. Cette analyse montre que les paramètres mentionnés ci-dessus peuvent être estimés individuellement, en comparant le modèle à des données expérimentales judicieusement choisies.

Un banc expérimental a également été conçu et fabriqué. L'instrumentation, qui comporte des thermocouples intrusifs, un capteur de pression et un capteur de flux, permet de caractériser le fonctionnement de la LHP. De plus, le système est partiellement transparent pour permettre l'observation de la position des phases liquide et vapeur dans le système au cours du fonctionnement. Les influences de la puissance thermique appliquée, de la présence de gaz incondensables et de la température de la source froide sont analysées. Aux puissances thermiques élevées, un régime d'ébullition nucléée est observé dans le réservoir. Ce phénomène a un effet significatif sur le comportement de la LHP, qui se traduit par une augmentation des flux parasites vers le réservoir donc une dégradation des performances de la LHP. Plusieurs phénomènes oscillatoires sont également observés et corrélés aux observations visuelles des écoulements dans les canalisations. Enfin, différents régimes de condensation sont observés et les mécanismes conduisant au détachement des bulles dans le condenseur sont décrits.

Un modèle numérique a été développé, afin de simuler le comportement du banc expérimental en se rapprochant au plus près de ses caractéristiques géométriques et thermophysiques. La comparaison entre les prédictions du modèle et les données expérimentales montre les carences des modèles de pertes de charges dans les écoulements diphasiques, pour la configuration étudiée. Les transferts de chaleur et de masse dans l'évaporateur sont analysés, ainsi que l'influence de l'apparition de l'ébullition dans le réservoir et celle de la conductivité thermique de l'enveloppe de l'évaporateur. Les résultats mettent également en évidence l'importance de la conduction thermique longitudinale dans les canalisations dans le cas d'un matériau conducteur, tel que le cuivre.

MOTS-CLES : loop heat pipe, modèle numérique, modèle analytique, régime permanent, banc expérimental, validation de modèle, analyse de sensibilité

Laboratoire (s) de recherche : Centre d'Énergétique et de Thermique de Lyon, CETHIL UMR5008

Directeurs de thèse: Pr. Frédéric LEFÈVRE, Dr. Valérie SARTRE

Président de jury :

Composition du jury : Pr. Yves BERTIN, Pr. Manfred GROLL, Dr. Vincent PLATEL, Pr. Marc PRAT